Design and Synthesis of Novel, Lead-reduced Piezo-/Ferroelectric Materials

by

Reagan Belan

Bachelor of Science, Simon Fraser University, 2009

Diploma of Technology, British Columbia Institute of Technology, 2007

Thesis Submitted in Partial Fulfillment of the

Requirements for the Degree of

Doctor of Philosophy

in the

Department of Chemistry

Faculty of Science

SIMON FRASER UNIVERSITY

Summer 2017

Approval

Name:	**Reagan Belan**
Degree:	**Doctor of Philosophy**
Title:	**Design and Synthesis of Novel, Lead-reduced Piezo-/Ferroelectric Materials**
Examining Committee:	**Chair:** **Corina Andreoiu** Associate Professor
	Zuo-Guang Ye Senior Supervisor Professor
	Byron Gates Supervisor Associate Professor
	Tim Storr Supervisor Associate Professor
	Gary Leach Internal Examiner Associate Professor
	Nazanin Bassiri-Gharb External Examiner Associate Professor
Date Defended/Approved:	August 24, 2017

Abstract

Relaxor-based piezo-/ferroelectric materials of complex perovskite structure, represented by (1-x)Pb($Mg_{1/3}Nb_{2/3}$)O_3-x$PbTiO_3$ (PMN-PT), have demonstrated excellent piezoelectric performance. However, they also exhibit some inherent drawbacks, such as a low Curie temperature, an even lower de-poling temperature due to the presence of a morphotropic phase boundary (MPB) region, a weak coercive field and a high content of lead, which make them unsuitable for high-temperature and high-field (power) applications and raise environmental concerns.

Bismuth-based complex perovskites, such as Bi($Zn_{1/2}Ti_{1/2}$)O_3 (BZT) seem to be an interesting candidate for the replacement of lead-based compounds because, like Pb^{2+} ion, Bi^{3+} also contains the $6s^2$ lone electron pair which is considered to be essential for the high piezo-/ferroelectric performance in lead-based perovskite. In addition, the solid solution between BZT and PT indeed exhibits larger structural distortion resulting in a higher Curie temperature than PT. However, its coercive field is too large for the material to be poled in order to make its potentially high piezo-/ferroelectric properties useful.

Faced with those issues and challenges, outcomes of this thesis are two-fold:

Firstly, addition of a non-stereochemically active ion and related complex compound, namely La($Zn_{1/2}Ti_{1/2}$)O_3 (LZT), as an end-member "softens" the structures, chemical bonding and electric properties of "hard" ferroelectric materials, to achieve improved electric properties, such as giant dielectric constant, smaller coercive field and switching polarization and excellent piezoelectricity and ferroelectricity.

Secondly, addition of BZT as the third component "hardens" the structures, chemical bonding and electric properties of PMN-PT binary system in order to increase its coercive field and to improve its piezo-/ferroelectricity. In particular, special efforts have been made to grow the single crystals of the PMN-PT-BZT ternary system. The studies of the single crystals provide invaluable information on the phase symmetry, domain structures, phase transitions and electric properties and allow to gain a better understanding of the relationship between crystal formation, chemical composition, phase symmetry and macroscopic properties.

Keywords: ferroelectric; single crystal; ceramic; relaxor; bismuth; lead-based

Dedication

This thesis is dedicated to my father, who unknowingly started me on the road to studying ferroelectrics when he taught me how to tell if a mare is ovulating by using ultrasound. It was a lesson I will never forget, because it was gross.

Acknowledgements

I would like to express my deepest gratitude to Dr. Zuo-Guang Ye for taking me on, first as an undergraduate researcher and then as a graduate student. It has been a long and challenging road and Dr. Ye has been there to help me weather the storm. The personal and professional growth I have experienced under his mentorship is immeasurable.

I would like to thank Dr. Byron Gates and Dr. Tim Storr for their guidance, suggestions and mentorship as my supervisory committee. I would like to thank Dr. Nazanin Bassiri-Gharb and Dr. Gary Leach for agreeing to be my external and internal examiners and Dr. Corina Andreoiu for acting as Chair for my defense. I would also like to express my gratitude to the staff of the SFU Chemistry Department, especially the tireless work of the Graduate Secretaries Ms. Nathalie Fournier and Ms. Lynn Wood.

I would like to thank the Ye Lab group members, past and present who have been an enormous source of strength, both academically and emotionally. I would like to specifically note the mentorship of Dr. Hamel Tailor and Dr. Alexei Bokov that has shaped the scientist I strive to be and the friendship of Dr. Bixia Wang and Dr. Zihe Ren that made long, late nights much more enjoyable. I would like to thank Ms. Erin Service, for contributing work which was used in completing the phase diagram in Chapter 5. I would like to thank Dr. Mandy Wu, Dr. Alisa Paterson, Mr. Brian Su, Ms. Cindy Wu, Ms. Maryam Bari, Ms. Xiaotong Wang, Ms. Yi Yuan and Ms. Sofia Pineda for their thoughtful comments and suggestions that have enhanced this work and for the friendship that they have extended to me, making my time in the lab memorable.

There are many, many people who have shown me love and support throughout this journey of graduate education. I want to thank my parents, Linda and Chris Belan, who have supported and encouraged me to pursue science as a career. Their love and support is felt daily. In addition, this would not have been possible without the love and friendship of Bonnie Belan, Emma Lawson, Meganne Sholdice and John Packman – I thank you with all my heart for being the best friends a person could ask for and always giving me laughter, a healthy dose of perspective and a shoulder to lean on when I needed it the most.

I have been very fortunate to form very close friendships with many of my colleagues, though none has been as important as the friendship and support of Finlay MacNab, who has welcomed me into his family and has pushed me to persevere, even when I most desperately wanted to quit. Thanks to Dr. Adam Barlev, Dr. Brandy Pilapil, Dr. C. Chad Warford, Dr. Chris Boyer and many others with whom I studied late into the night and shared many tears and even more beers.

Lastly, I would like to acknowledge and thank all the activists that I have gotten to know through my work at the Teaching Support Staff Union. Through this work, I have learned so much about the university, the way that it operates and how to best effect positive change. I would not have come through those challenges without struggling alongside Mr. Derek Sahota, Ms. Karen Dean and many, many others. Thank you for your passion and solidarity.

Table of Contents

List of Tables

List of Figures

List of Acronyms

a/b/c	Unit cell lattice parameters
α/β/γ	Unit cell lattice angles
AC	Alternating Current
AFM	Atomic Force Microscopy
BI	$BiInO_3$
BMT	$Bi(Mg_{1/2}Ti_{1/2})O_3$
BNT	$Bi(Ni_{1/2}Ti_{1/2})O_3$
BS	$BiScO_3$
BT	$BaTiO_3$
BZN	$Bi(Zn_{1/3}Nb_{2/3})O_3$
BZT	$Bi(Zn_{1/2}Ti_{1/2})O_3$
C	Cubic symmetry
δ	Diffuseness of dielectric permittivity (full width half maximum)
DFT	Density Functional Theory
d-spacing	Distance between lattice planes
D	Dipolar displacement

d_{33}	Piezoelectric coefficient
ε'	Real part of dielectric permittivity (Constant)
ε''	Imaginary part of dielectric permittivity
ε_A	Static permittivity maximum
ε_{max}	Permittivity maximum
ε_0	Permittivity of free space
E	Electric field
E_A	Activation energy
E_c	Coercive field
ER	Ergodic Relaxor
f_0	Onset frequency
Γ_o	Optical retardation
hkl	Miller Indices
LZT	$La(Zn_{1/2}Ti_{1/2})O_3$
M	Monoclinic symmetry
MBP	Morphotropic Phase Boundary
MEMS	Micro-electromechanical Systems

n	Refractive Index
n_e	Extraordinary ray
n_o	Ordinary ray
Δn	Birefringence
PLM	Polarized Light Microscopy
PMN	$Pb(Mg_{1/3}Nb_{2/3})O_3$
PNRs	Polar nano-regions
P	Polarization
P_r	Remanent polarization
P_s	Spontaneous polarization
P_{sat}	Saturation polarization
P(E)	Variation of polarization as a function of electric field
PT	$PbTiO_3$
PIN	$Pb(In_{1/2}Nb_{1/2})O_3$
PSN	$Pb(Sc_{1/2}Nb_{1/2})O_3$
PYN	$Pb(Yb_{1/2}Nb_{1/2})O_3$
PZT	$Pb(Zr_{1/2}Ti_{1/2})O_3$

Q	Charge
R	Rhombohedral symmetry
S	Strain
σ	Stress
T	Tetragonal symmetry
T_A	Temperature at maximum of static permittivity
T_B	Burns temperature
T_C	Curie-Weiss temperature
T_f	Temperature of dipole freezing
T_{max}	Temperature of maximum permittivity
T_{MPB}	Temperature of phase transition due to the morphotropic phase boundary
T_{RT}	Temperature of rhombohedral to tetragonal phase transition
T_{VF}	Vogel – Fulcher temperature
tanδ	Dielectric loss tangent
χ	Dielectric susceptibility
XRD	X-Ray Diffraction

ZFC	Zero Field Cooling
ZFH	Zero Field Heating

Chapter 1. **Introduction**

Piezoelectric and ferroelectric materials have been the subject of much scientific research and industrial development since the discovery of the piezoelectric effect in the late 1800s and its subsequent display in single crystals of Rochelle salt by Pierre and Jacques Curie [1]. Piezoelectrics are noncentrosymmetric crystals whereby application of pressure results in charge accumulation on its surface. A subgroup of piezoelectric materials shows the ferroelectric effect where the material's internal dipole occurs spontaneously and can be reoriented with an external electric field. The discovery of ferroelectric single crystals has enabled the piezoelectric effect to be utilized in polycrystalline ceramics and has allowed these materials to be used in a variety of technological applications that we interact with on a daily basis from high dielectric constant multilayered capacitors to the stage in an atomic force microscopy (AFM) probe [2]. Additionally, the piezo-/ferroelectric effects have been displayed in the tissues of living organisms and are of increasing promise as the key to understanding biological stimuli response and engineering biomimetic materials [3].

This thesis is about the design and synthesis of novel piezo-/ferroelectric materials and characterization of their crystal structures and physical properties in order to gain a better understanding of the structure-property relations of this important class of functional materials. In this section, the necessary background and theory will be introduced and discussed in order to establish the foundation for addressing the objectives, technical approaches and organization of this thesis.

1.1 Crystallographic symmetry and the criteria for piezo-/ferroelectricity:

When investigating solids that may display piezo-/ferroelectric activity, it is useful to start by looking at the crystallographic classes of solids as symmetry requirements are the primary constraint on these effects. The piezoelectric effect occurs in noncentrosymmetric crystal classes and is the generation of an electric charge with the application of pressure (direct effect) or the generation of deformation with an applied electric field (converse effect) as is shown in Figure 1.1.

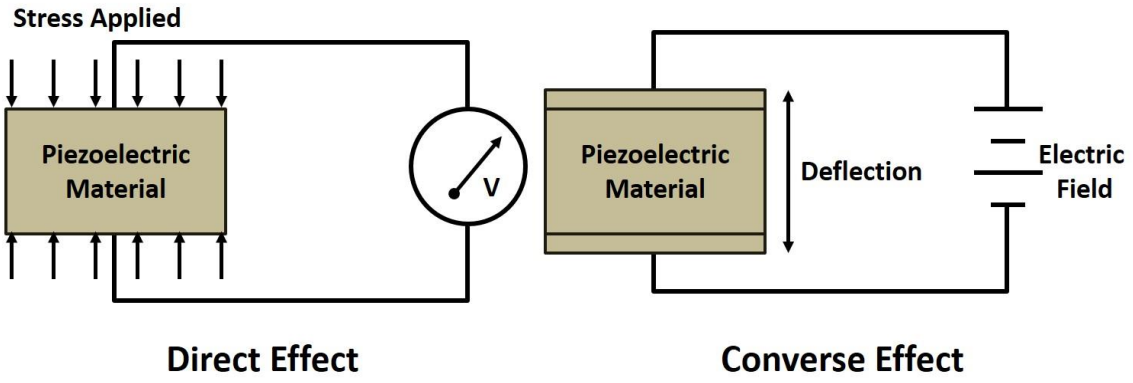

Figure 1.1 Schematics of the direct (left) and converse (right) piezoelectric effects.

The direct, or generator, effect can be described as follows:

$$D_i = d_{ijk}\sigma_{jk} \tag{1.1}$$

Whereby, the application of stress, σ_{jk}, alters the internal dipolar displacement vector, D_i, which manifests as charge on the surface of the material. The piezoelectric coefficient, d_{ijk}, is characteristic of the material and is expressed in C/N, *i.e.* the amount of charge generated per unit force applied.

The converse, or motor, effect can be described by the following equation:

$$S_{ij} = d_{kij}E_k \tag{1.2}$$

Whereby, an electric field, E_k, is applied to the material resulting in elongation (or compression) of the internal dipole inducing strain, S_{ij}. Again, this is characteristic of the material and the d_{kij} is expressed in m/V, *i.e.* the amount of deformation induced per unit of field applied [4].

As visualized in Figure 1.2, of the 32 crystallographic classes, only the 21 that are noncentrosymmetric can display the piezoelectric effect, with the exception of space group 432 in which polarization is cancelled out due to secondary symmetry operations. However, without additional symmetry constraints, the piezoelectric effect can only be displayed in single crystals due to the overlapping polarization directions and subsequent cancellation of those dipoles [1], [4].

Furthermore, of the 20 crystal classes that are noncentrosymmetric, 10 have a unique polar axis and display the pyroelectric effect, which is a change in internal dipole with a change in temperature. If the direction of that internal polarization can be reoriented with the application of an external electric field, it is said to be ferroelectric. Ferroelectric single crystalline materials inherently display both the pyroelectric and piezoelectric effects. The ceramic materials fall into four main categories of crystal structure: tungsten bronze, perovskite oxides, pyrochlores and perovskite-based layered structures.

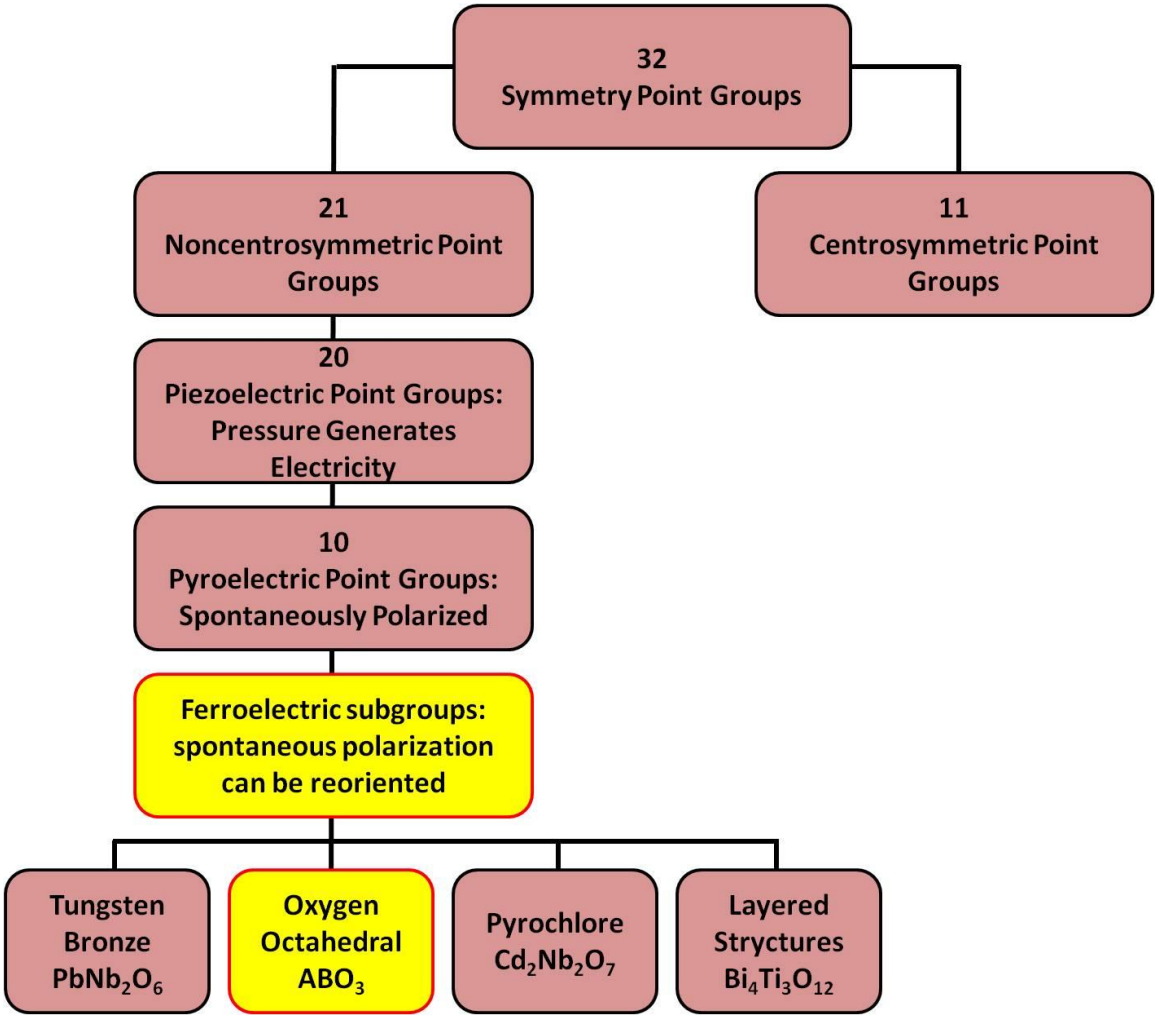

Figure 1.2: Symmetry requirements for piezo-/ferroelectric activities and commonly utilized ceramic ferroelectic subgroups (adapted from [1]**).**

1.2 The Perovskite Structure

Of the crystal structures that display the ferroelectric effect, the most versatile and well studied materials are perovskite oxides [2], [5]. The generic formula of this structure is ABO_3 and is shown in Figure 1.3 with the A-site cations occupying the corners of the unit cell, the B site cation sitting at the (1/2,1/2,1/2) body centre site and oxygen anions at the face centres of the unit cell, forming an octahedral cage around the B-site.

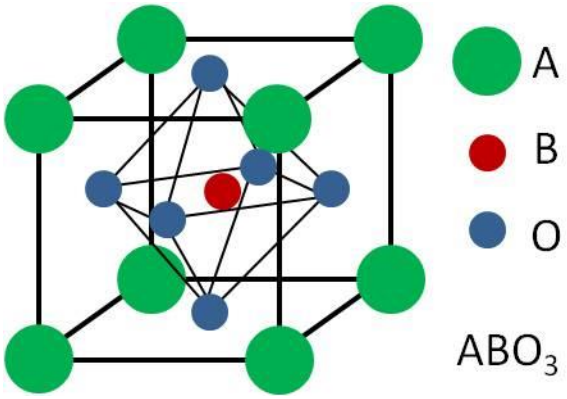

Figure 1.3: The perovskite unit cell, ABO_3, drawn with the B cation at the body centre position, oxygens occupying the face centres, creating an octahedra surrounding the B-site and the A cations occupying the corners of the unit cell.

In predicting the symmetry and stability of the perovskite structure, the tolerance factor is used:

$$t = \frac{r_A + r_O}{\sqrt{2}(r_B + r_O)} \tag{1.3}$$

where $(r_A + r_O)$ and $(r_B + r_O)$ are the interatomic distances between the A-site cation and oxygen anion and the B-site cation and oxygen anion, respectively. The unit cell can accommodate a range of the tolerance factor of $0.88 < t < 1.1$, while still maintaining coordination environments of the perovskite structures. Outside of those values, the perovskite structure is not stable and structures of other coordination environments are preferred, such as $GdFeO_3$ structure and the ilmenite structure $FeTiO_3$ [6]. Figure 1.4 shows the ideal cubic perovskite structure as well as the distortions from that structure to rhombohedral or tetragonal.

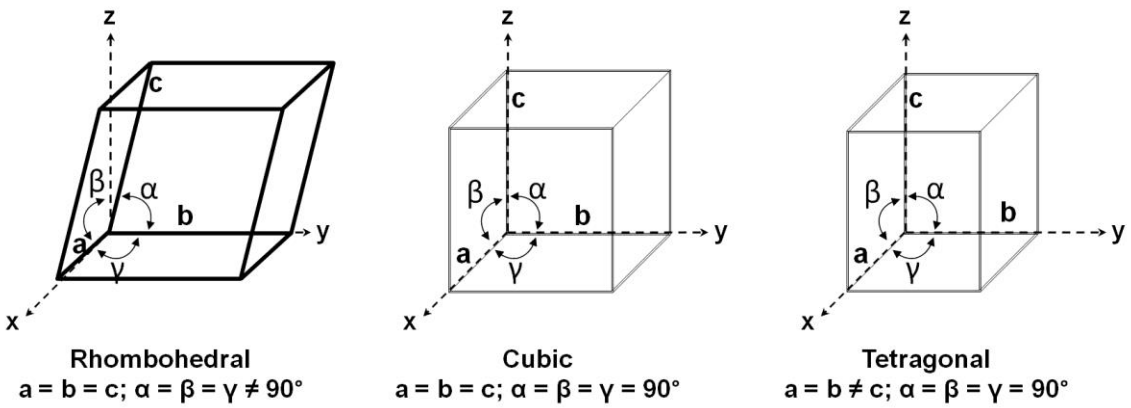

Figure 1.4 Relationship between unit cell symmetry, lattice parameters and bond angles for rhombohedral (R), cubic (C) and tetragonal (T) perovskite unit cells.

In order to display a spontaneous internal dipole, there are general considerations to be take into account when selecting A-site and B-site cations. A-site cations are usually of a large ionic radius and low valency, whereas the B-site cation is generally of a small ionic radius, high valency and a d^0 electronic configuration. It's the energy of the empty d-orbitals that are the primary mechanism of distortion leading to dipolar deformation. The low energy *n*d-states allow for partial mixing with the O-2p orbital, causing a displacement of the B-site cation toward one of the 6 oxygen atoms in the octahedral cage, resulting in a second order Jahn-Teller distortion away from the (1/2,1/2, 1/2) unit cell position [7].

The unit cell distortion is significantly enhanced when the A-site cation has a stereochemically active $6s^2$ lone electron pair, like Pb^{2+}. This causes different bond lengths to the two oxygen positions in the unit cell. This distortion is visualized two-dimensionally in Figure 1.5. This additional distortion can dramatically strengthen the ferroelectric properties. For example, $BaTiO_3$ has a paraelectric to ferroelectric phase transition temperature, *i.e.* a Curie Temperature, T_C, of ~ 120 °C, and a room-temperature spontaneous polarization, P_s, of 18 μC/cm^2, however, if we substitute Pb^{2+} for the Ba^{2+} on the A-site, we see an increase of the T_C to ~ 480 °C and an enhancement of room-temperature P_s to 30 μC/cm^2 in $PbTiO_3$ due to the additional distortion [6].

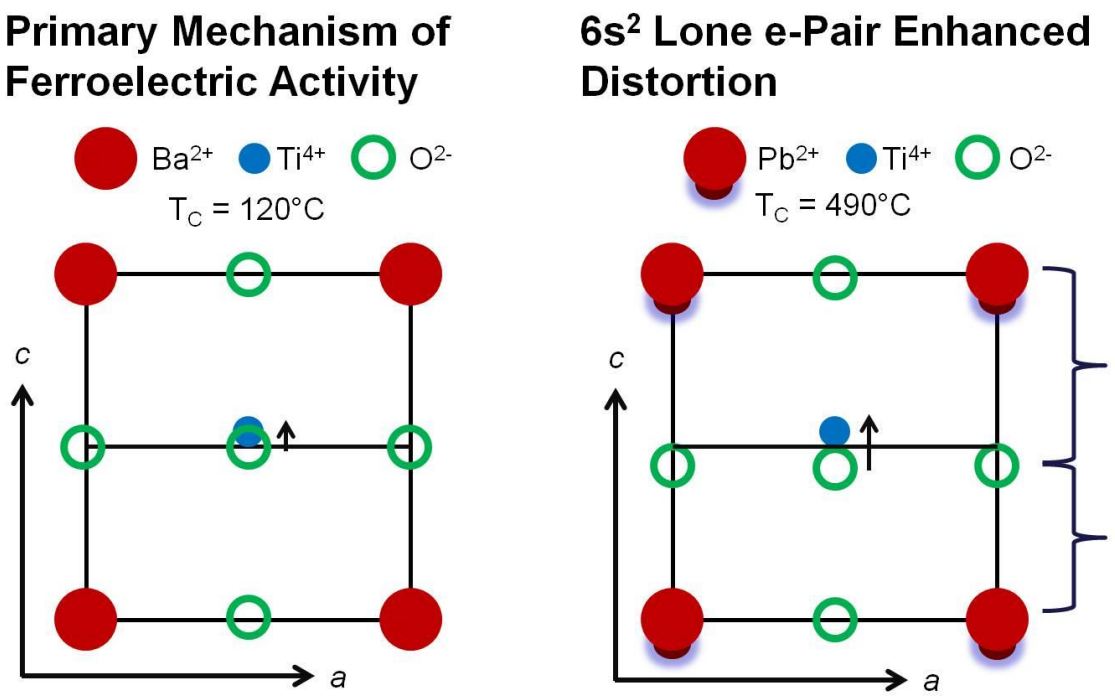

Figure 1.5: **A two-dimensional representation of the perovskite unit cell for $BaTiO_3$ (right) and $PbTiO_3$ (left) In $BaTiO_3$, the spontaneous internal dipole is due solely to B-site diaplacement. In $PbTiO_3$ there is enhanced tetragonal distortion through the presence of a $6s^2$ electron lone pair on the A-site.**

The spontaneous polarization direction of the unit cell is dependent of the symmetry it adopts. Polarization directions are described in Figure 1.6. For a tetragonal symmetry, there are 6 polarization directions that point to the face centre of the unit cell, along the <001> directions. In a rhombohedral unit cell, there are 8 polarization directions along the body diagonal <111> directions. For an orthorhombic unit cell, the polarization points to the unit cell edge, giving rise to 12 polarization directions along the <110> directions [8].

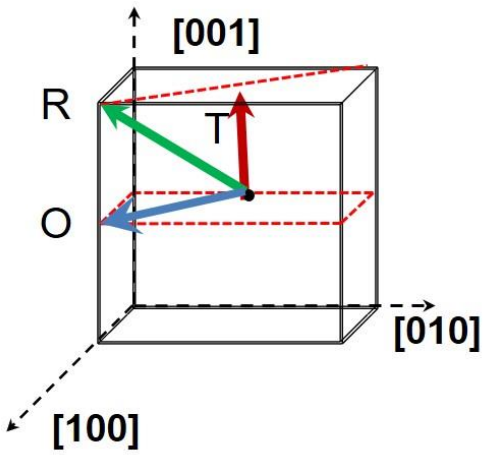

Figure 1.6 Polarization directions of the ferroelectric materials with tetragonal (T), rhombohedral (R) and orthorhombic (O) unit cells (adapted from [8]**).**

1.3 Ferroelectric activity

How a material's polarization behaves in an applied electric field largely determines the type of application it is suitable for. For this reason, the polarization vs. electric field, P(E), measurements provide an invaluable tool for describing that behaviour. In Figure 1.7, examples of the P(E) behaviour in an electric field for A) paraelectric, B) normal ferroelectric and C) antiferroelectric materials can be seen. In the P(E) relation of a high dielectric constant capacitor, as shown in Figure 1.7A, the material shows a large dipole distribution that is linearly dependent on the electric field and returns to the non-polar state once the field is removed.

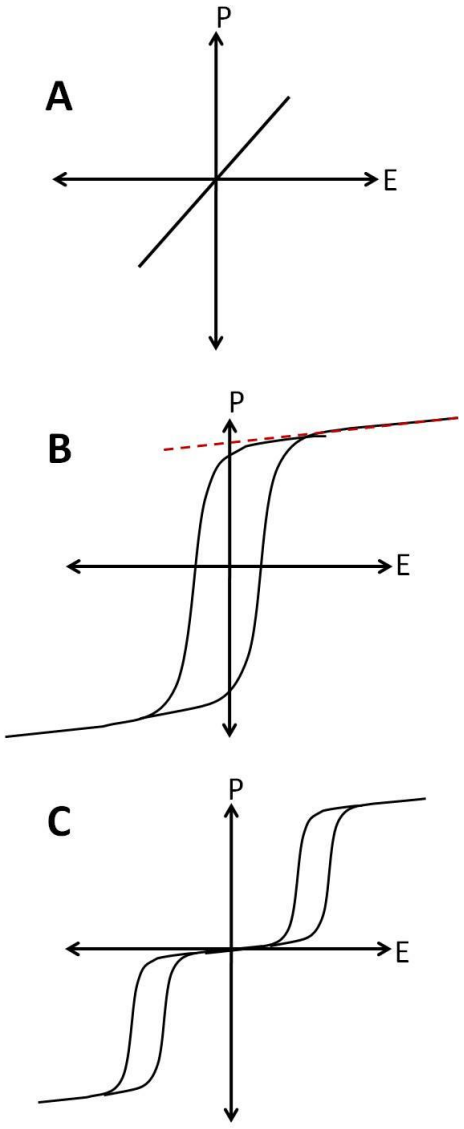

Figure 1.7 Polarization (P) behaviour as a function of bipolar electric field (E) for A) paraelectric materials, B) ferroelectric materials and C) antiferroelectric materials.

A normal ferroelectric P(E) hysteresis loop is shown in Figure 1.7B and contains valuable information about the material being studied. From inspection of the loop, it can be seen the material shows hysteretic behaviour as the forward applied field takes a different pathway than the reverse, giving the material two stable (remanent) states that can be used for memory devices. It can also be seen that with removal of the electric field, the majority of the polarization remains aligned in the direction of the previously applied electric field. Polarization in the opposite orientation is also a stable state, giving at least two equilibrium states of the system that are energetically equivalent and are

often represented as a double potential well (see Figure 1.8). Figure 1.7C shows an antiferroelectric P(E) hysteresis loop where at low fields there is no net polarization due to overlapping, opposite polar lattices. At high fields an induced ferroelectric state appears when the polar lattices align cooperatively, as seen by the opened 'sub-loop' at both high and low fields [4], [6], [9].

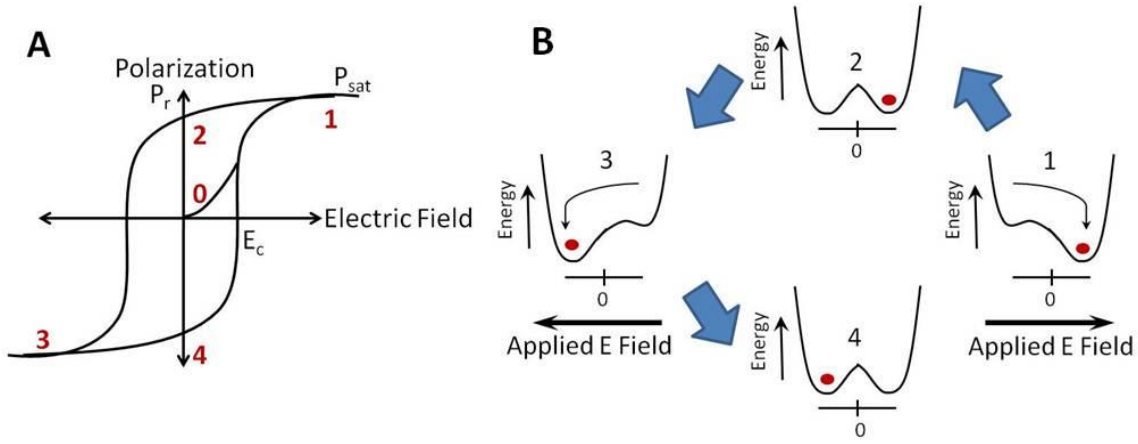

Figure 1.8 A) Polarization behaviour of a normal ferroelectric in a varying electric field and B) accompanying change in Gibbs free energy with applied electric field.

A closer look at the dipole interaction with an electric field is shown in Figure 1.8 where a more detailed representation of the ferroelectric hysteresis loop is shown in (Figure 1.8A), and the corresponding Gibbs free energy versus polarization plots (Figure 1.8B) represent the two opposite polarization states as a double potential energy well, with the red dot indicating the position of net polarization. At position 0, the dipoles in the material are randomly oriented and, due to overlap and cancellation, no net polarization is observed. The application of the field in a positive direction causes the dipolar displacement to respond linearly (similar to the capacitor pictured in Figure 1.7A). Once enough energy is supplied to the system, the dipoles begin to switch until all orientations are aligned with the electric field and the material is saturated at position 1. In a free energy sense (Figure 1.8B), the applied electric field is raising the energy of one of the displacement states until it is greater than that of the barrier separating the states, driving dipolar displacement to one orientation. Removal of the field returns that raised energy state to equilibrium position and the return of the barrier prevents dipoles from changing states. Some of the polarization is diminished due to the removal of the field, yet a net polarization remains as can be seen at position 2. To reorient the

polarization, a field greater than the coercive field can be applied in the reverse direction, raising the energy of the established polarization state to the point that the barrier of the well is, again, overcome so that the opposite position is now energetically favoured, leading to position 3. Subsequent removal of the electric field leaves that the net polarization now in the opposite configuration, position 4 [4], [6], [9].

Many factors, both intrinsic and extrinsic, affect the shape of the P(E) loop for a particular ferroelectric material. The remnant polarization, P_r, is a measure of how well the ferroelectric retains its polarization state without external energy input and is greatly influenced by extrinsic factors. For example, a polycrystalline ceramic will have random crystallographic directions and hence, internal dipoles are randomly oriented with respect to each other and the applied electric field. Once the field is removed, the dipoles will relax back to the most energetically favoured state that is best aligned with the crystallographic direction of the field applied, and not all the saturation polarization is retained, as seen in Figure 1.8A by the difference on the polarization axis between P_{sat} and P_r. In a single crystal of the same sample, the directionality of the structure can be exploited, whereby application of the electric field in the direction of the polar axis can yield better alignment with the field and a larger overall net dipole can be retained.

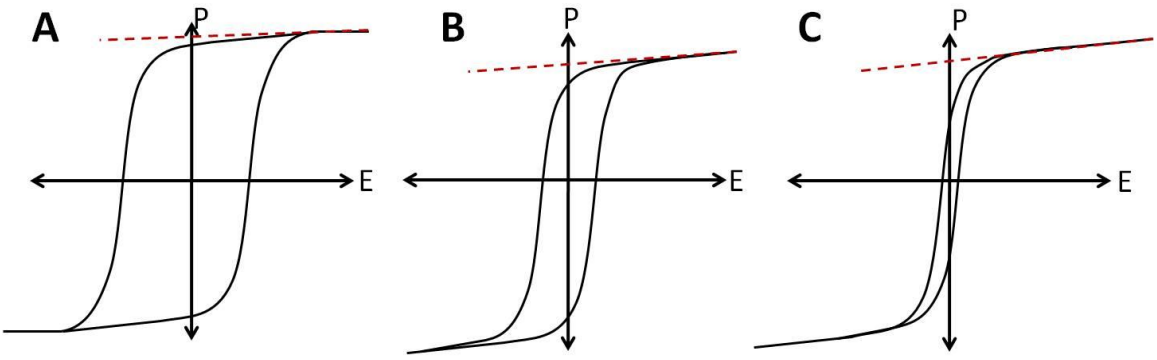

Figure 1.9 Different ferroelectric hysteresis loops which show A) a high coercive field i.e. 'hard' materials, B) a low coercive field, i.e. 'soft' materials and C) a material with a slim loop and very little hysteretic/memory behaviour.

Perhaps a greater influence on application suitability is the coercive field, E_C, i.e. the height of the barrier in the double potential well or the width of the P(E) loop, of which examples of different behaviour can be seen in Figure 1.9. The slimming of the hysteresis loop can be thought of in different ways. For instance, consider the three

loops A, B and C in Figure 1.9 to be the same material with varying temperature, and then the corresponding free energy vs. polarization plots can be presented in Figure 1.10. The loop in Figure 1.9A shows the material at some temperature that is far lower than that of its phase transition or Curie temperature, i.e. $T << T_C$, and it takes considerable energy input to overcome the barrier of the double potential well (Figure 1.10). As the temperature is elevated closer to the T_C yet still not approaching the phase transition, the input of thermal energy raises the energy of the two equilibrium states, lowering the energy barrier, and making the polarization easier to switch but still with significant hysteresis in the loop. As the temperature becomes very close to the T_C, the polarizability of the material becomes incredibly high as the double potential well appears to be flattened and very little energy is required to switch the polarization. This results in the slim loop seen in Figure 1.9C where there is very little hysteresis and an incredible ease of dipole reorientation [4].

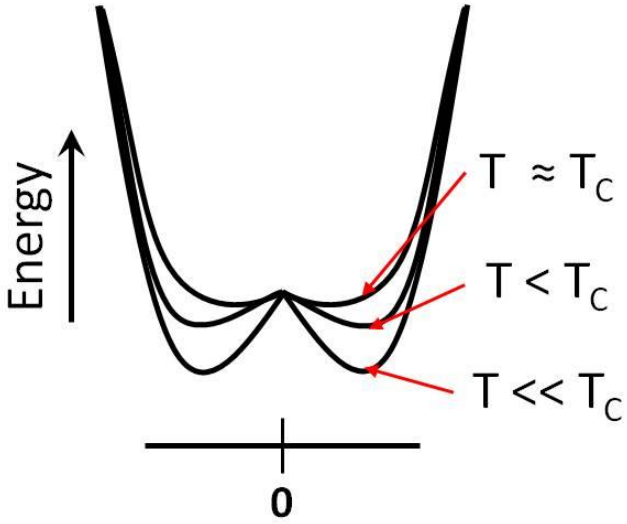

Figure 1.10 Schematic of Gibbs free energy vs. B-site displacement at $T \approx T_C$, $T < T_C$ and $T << T_C$ for a normal ferroelectric material.

An alternative approach to the three loops in Figure 1.9 is to look upon the center loop, Figure 1.9B, as an unaltered perovskite oxide ferroelectric system, ABO_3, that can be modified with dopants that will either “harden” (as in Figure 1.9A) or “soften” (as in Figure 1.9C) the material from its original state. Dopants introduce a cation with an off valent charge in either the A-site cation or B-site cation to obtain a desired effect in the P(E) behaviour of the system. Acceptor dopants are known as ‘hardening’ agent as they substitute a cation with a lower valence for a cation of a higher valence on either the A

site (i.e. K^+ for Pb^{2+}) or B site (i.e. Fe^{3+} for Zr^{4+}/Ti^{4+}). Introduction of these dopants (i.e. going from Figure 1.9B to Figure 1.9A) cause the chemical system to compensate for the lack of positive charge with oxygen vacancies, which 'pin' domain walls in the material by impeding domain wall motion, raising the energy required to switch the dipoles i.e. the height of the barrier in the double potential well (Figure 1.10), thus increasing the coercive field. The donor dopants are known as 'softening' agents and are utilized by substitution of cations of a higher valence for a cation of lower valence on the A site (i.e. La^{3+} for Pb^{2+}) or B site (i.e. Nb^{5+} for Zr^{4+}/Ti^{4+}) which leads to internal electric fields. The result of this substitution, going from Figure 1.9B to Figure 1.9C, is a material that can switch polarization with greater ease and has a lower coercive field as a result [1], [2], [6], [10]

The manipulation of ferroelectric properties through chemical modification is the basis for the vast majority of piezoelectric materials research and development. Being able to 'tune' these properties makes these materials versatile and practically useful for specific applications: some applications require a 'hard' material for high field or high temperature applications, while other devices require a 'soft' material that is easily switched and shows little memory. Continued understanding of how chemical composition alters these effects is key to understanding the underlying principles of piezoelectric and ferroelectric materials.

1.4 Dielectric Behaviour of Ferroelectric Materials

Examination of the dielectric permittivity with varying frequency and temperature of a particular material will indicate the temperature range at which ferroelectric materials may be utilized. An example of the variation of the dielectric permittivity (dielectric constant, ε') as a function of temperature for a typical ferroelectric material can be seen in Figure 1.11. At high temperatures, the ferroelectric material is in a non-polar, paraelectric phase and obeys Curie-Weiss behaviour:

$$\varepsilon' = \frac{C}{T - T_C} \tag{1.4}$$

Where C is the Curie constant and T_C is the Curie-Weiss temperature.

In this phase, there is no apparent net polarization as it is energetically favourable for the B-site cation to occupy the body centre site without distortion. As the material is cooled down, the dielectric properties diverge at the Curie temperature, T_C, where a large dielectric displacement is shown by a sharp peak in permittivity. As the material is cooled to temperatures well below the T_C, the sides of the potential energy well lower, resulting in off-centre, B-site distortion that yields the lowest energy state, and there is an energetic barrier to the switching of the polarization state [7], [11].

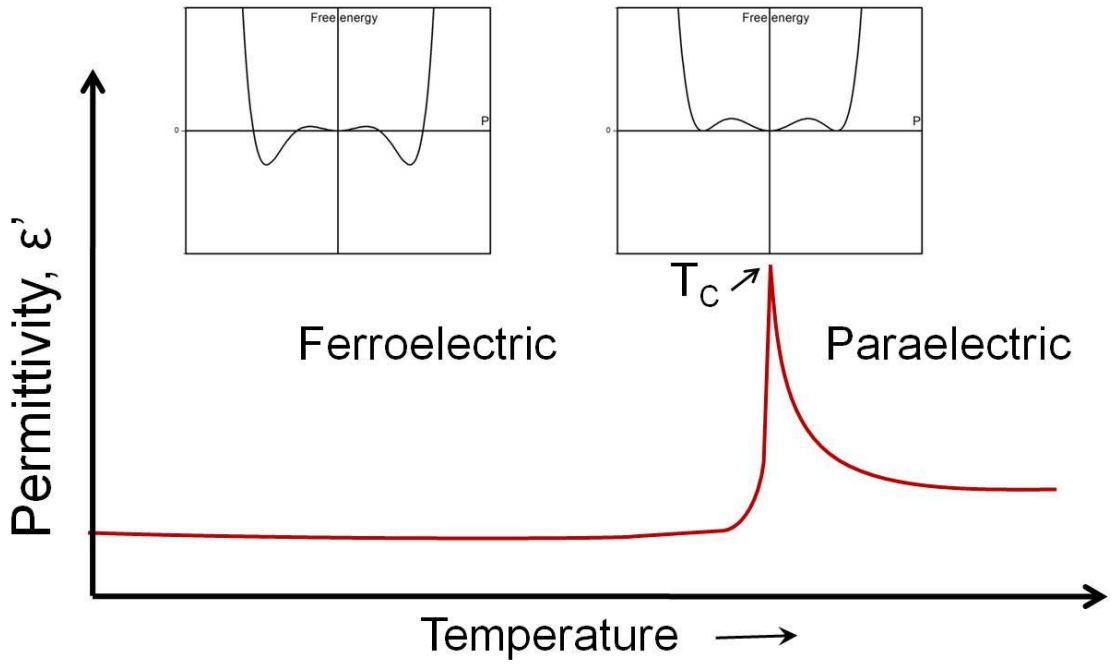

Figure 1.11: Variation of dielectric permittivity of a normal ferroelectric material as a function of temperature, measured at a specific frequency and accompanying potential energy diagrams, showing the paraelectric to ferroelectric phase transition at T_C upon cooling.

An additional feature of these types of systems is that T_C is frequency independent, and will not show dispersion with varying frequency of the measurement AC field. In addition, this transition in a normal ferroelectric is of first order and is accompanied by a measurable change in structure between the high temperature, paraelectric phase and the low temperature ferroelectric phase. When searching for a material useful for an application, the upper limit of the operational temperature should be at least 50° lower than the T_C in order to avoid de-poling the device during operation, which significantly restricts the temperature range of many materials whose T_C is not very high [12].

1.5 Dielectric Permittivity and Relaxor Ferroelectric Materials

The behaviour of normal ferroelectric materials with well-ordered compositions has been discussed in previous sections. However, relaxor perovskite materials of the generic formula $A(B,B')O_3$ introduce compositional disorder on the B-site of the unit cell. When the stoichiometry on the B-site is no longer 1:1, for example in $Pb(Mg_{1/3}Nb_{2/3})O_3$ (PMN), rather than a long range, ordered system, we see regions of short range polar order called polar-nano regions (PNRs) that are embedded in a disordered matrix. This ordering is depicted in Figure 1.12.

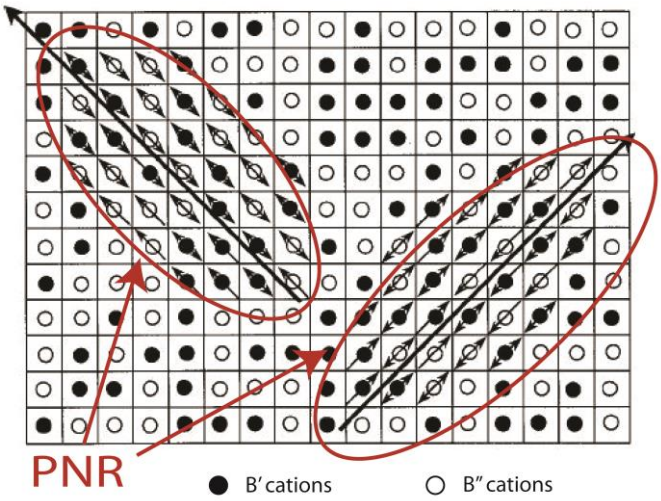

Figure 1.12 Schematic of polar-nano regions (PNRs), regions of local polar order in a disordered matrix, that exist in relaxor ferroelectric materials. The arrows on the atomic sites represent the switching direction of the individual PNR [adapted from [13] **– used with permission].**

At high temperatures, similarly to normal ferroelectrics, relaxor materials follow Currie-Weiss behavior and are in their paraelectric phase. This is visualized in Figure 1.13, which shows the dielectric response of a typical relaxor ferroelectric with varying temperature and frequency. As the material is cooled below the so-called Burns temperature, T_B, the material deviates from the Curie-Weiss behavior and transitions to the ergodic relaxor (ER) phase. It is in this phase where the dielectric properties exhibit a dependence on the frequency of the applied AC field which is not present for normal ferroelectric materials. This is evidenced in the dielectric curves with the appearance of

dispersion, i.e. variations of both the maximum permittivity, ε_{max}, and the temperature of maximum permittivity, T_{max}, as a function of the frequency applied.

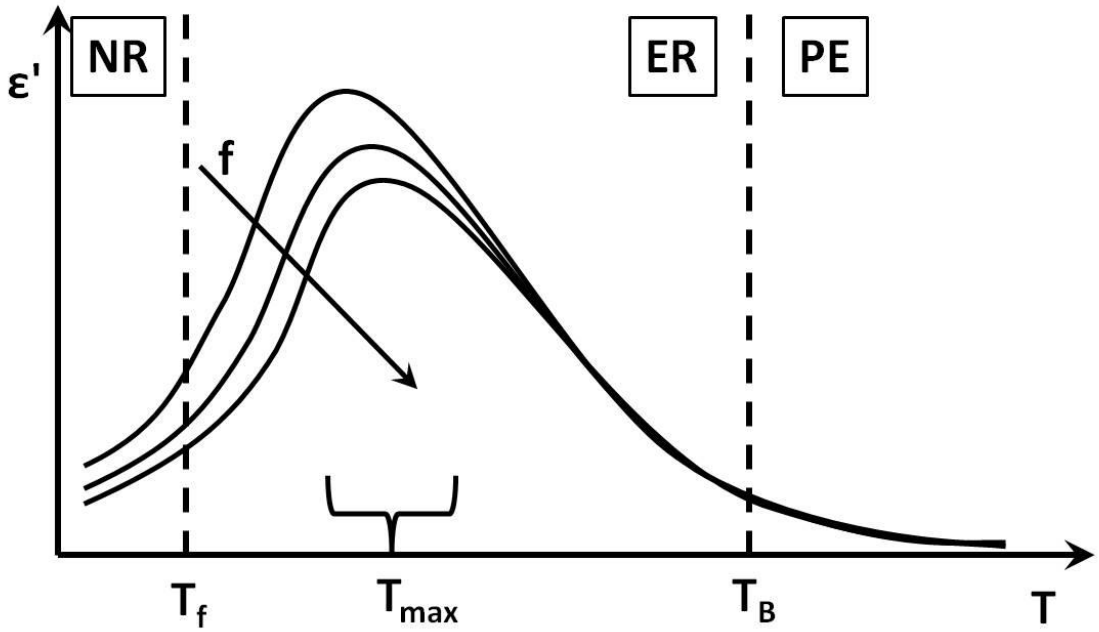

Figure 1.13: Dielectric response of a relaxor ferroelectric with varying temperature and frequency showing the transition from a high temperature paraelectric phase, to an ergodic relaxor phase below the Burns Temperature, T_B, where a frequency dispersion is observed. Futher cooling results in a non-ergodic relaxor state below the freezing temperature, T_f.

What causes this frequency dependence is the behavior of the PNRs. These small regions of polar order are rapidly reorienting with thermal energy at a particular frequency – the smaller the PNR, the higher frequency of response. As the material's temperature lowers, some PNRs stop switching, or "freeze out" when they approach the temperature of maximum permittivity, T_{max}, with the smaller, higher frequency PNRs freezing out at higher temperatures first, followed by the larger, lower frequency responding PNRs. The temperature of maximum permittivity and the varying frequencies can be related by the Vogel-Fulcher relationship:

$$f = f_0 exp\left(\frac{-E_A}{k_B(T_{max}-T_{VF})}\right) \quad (1.5)$$

By extracting the T_{max} for the full range of frequencies measured, we can then use this relationship to determine f_0, the onset frequency of dipolar switching, E_A, the energy barrier for the dipolar switching and T_{VF}, the freezing temperature at which dipolar switching ceases and the material is in a so-called glassy state [5]. The shape of the curve can also be evaluated to learn about the static properties of the system, i.e. when f→0. Such quadratic fitting is shown in Figure 1.14 and is performed according to the following equation:

$$\frac{\varepsilon_A}{\varepsilon} = 1 + \frac{(T-T_A)}{2\delta^2} \tag{1.6}$$

It applies to the ergodic relaxor data below T_B where all frequency curves coincide and have the same slope. By fitting the reciprocal of permittivity, ε, of this line to temperature, the temperature of the maximum static permittivity, T_A (*i.e.* $T_A \equiv T_{max}$ at f = 0), at the value of static permittivity, ε_A (*i.e.* $\varepsilon_A \equiv \varepsilon_{max}$ at f = 0) and the diffuseness of the transition, δ can be extracted.

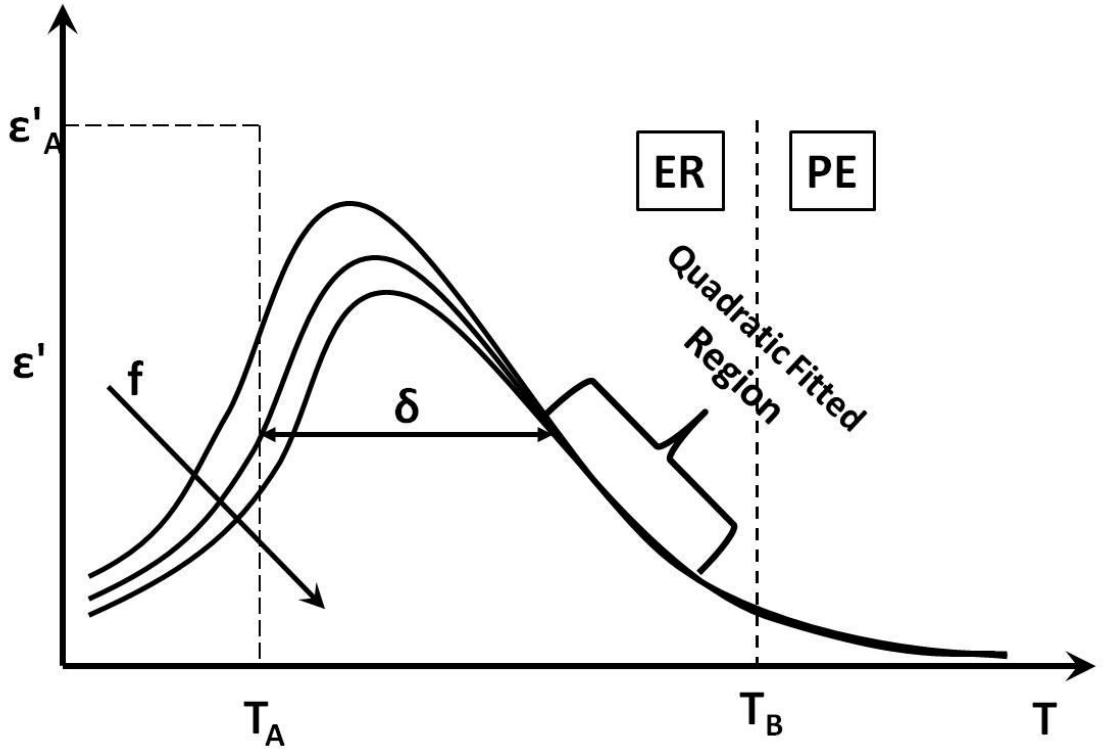

Figure 1.14 Quadratic fitting of the dielectric permittivity of a relaxor ferroelectric to Eq. 1.6 showing the behaviour of static permittivity characteristic of a relaxor system.

As additional components, or end members, are introduced into relaxor-type compound, a combination of properties begins to appear whereby, both relaxor behavior and normal ferroelectric phase transitions at T_C are evident in the dielectric spectra [5]. This occurs when the freezing of PNRs results in the coalescence into macroscopic ferroelectric domains rather than a glassy, disordered state.

1.6 Morphotropic Phase Boundaries and Piezoelectric Activity

While many combinations of cations could result in ferroelectric activity, there is particular interest in materials that contain a morphotropic phase boundary (MPB) region in a solid solution system. When represented on phase diagrams, the MPB is a demarcation of an abrupt change from one structure, or morphotrope, to another as the composition changes. In the previous section on dielectric behaviour of normal ferroelectrics, structural changes are addressed with respect to change in temperature. Here, we consider structural changes with respect to composition.

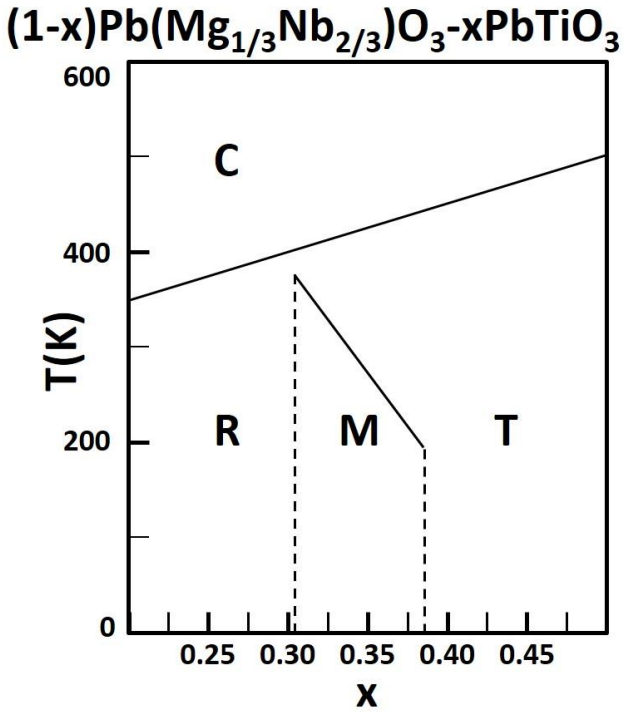

Figure 1.15 The composition – temperature phase diagram of the (1-x)Pb($Mg_{1/3}Nb_{2/3}$)O_3-x$PbTiO_3$ solid solution system showing different symmetry (R - rhombohedral; T - tetragonal; C - Cubic; M – monoclinic). The MPB region is outlined by dashed lines (Adapted from Noheda et al [14]**).**

The binary phase diagram of (1-x)Pb($Mg_{1/3}Nb_{2/3}$)O_3-x$PbTiO_3$ (PMN-PT) is shown in Figure 1.15. At x = 0, the system is of relaxor behaviour, pure PMN, with T_{max} below 300 K. As the mole fraction of PT, x, increases, the resulting change in the structure and Curie temperature are plotted. At compositions of high mole fraction of PMN, (x < 0.32) the structure is rhombohedral. In the MBP region (between the dashed lines), we see a monoclinic phase, that coexists with the rhombohedral and tetragonal phase, forming a region of coexistence of multiple phases, which is characteristic of MPB behaviour. Another feature of the MBP region is that an additional phase transition takes place at T_{RT} or T_{MPB}, which is below T_C, indicating a low-temperature structural transition from rhombohedral (and/or monoclinic phase) to tetragonal that occurs before transitioning into a high temperature paraelectric phase. The piezoelectric properties of a similar system, (1-x)Pb($Zn_{1/3}Nb_{2/3}$)O_3-x$PbTiO_3$ (PZN-PT), is presented in Figure 1.16, which shows a peak in d_{33} on the rhombohedral side of the MPB region [15]. This behaviour indicates that the MPB plays an important role in enhancing the piezoelectric performance of the solid solution system.

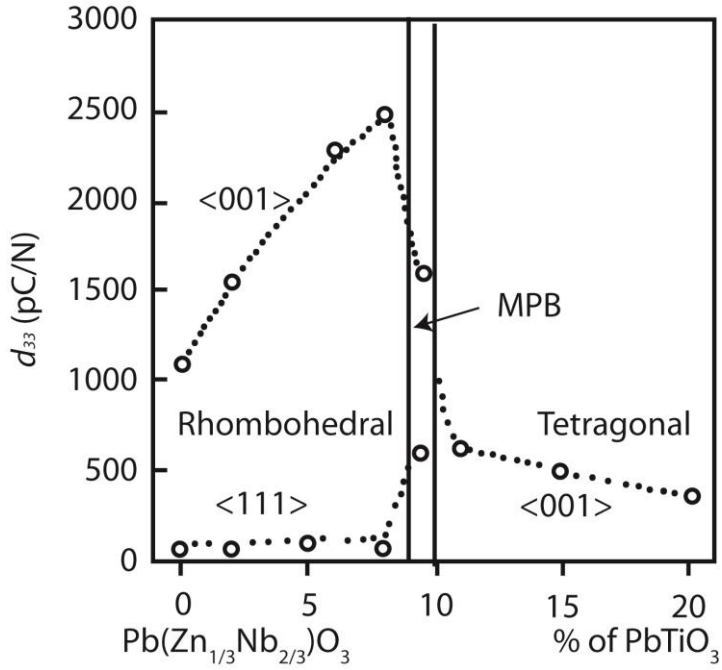

Figure 1.16 Variation of the piezoelectric coefficient, d_{33}, as a function of composition for the MPB-type $Pb(Zn_{1/3}Nb_{2/3})O$-$PbTiO_3$ binary solid solution system (adapted from [15]**).**

1.7 Interpreting Ternary Phase Diagrams

In addition to investigating piezo-/ferroelectric systems with two components, as seen in the PMN-PT binary phase diagram, it is necessary to examine systems that contain three components, or ternary systems. The addition of a third component could allow us to extend the composition range, the MPB regions and the properties of the binary systems, providing an effective way to design and synthesize new piezo-/ferroelectric materials. A generic ternary phase diagram is presented in Figure 1.17, where each corner of the triangle represents pure phase of components A, B and C, respectively, and the edges of the triangle are the binary phase lines of AB, BC and CA. Through the studies of the phase formation, crystal structures and properties, the solubility limits, phase symmetries and properties can all be overlaid on the blank diagram to establish a meaningful ternary phase diagram.

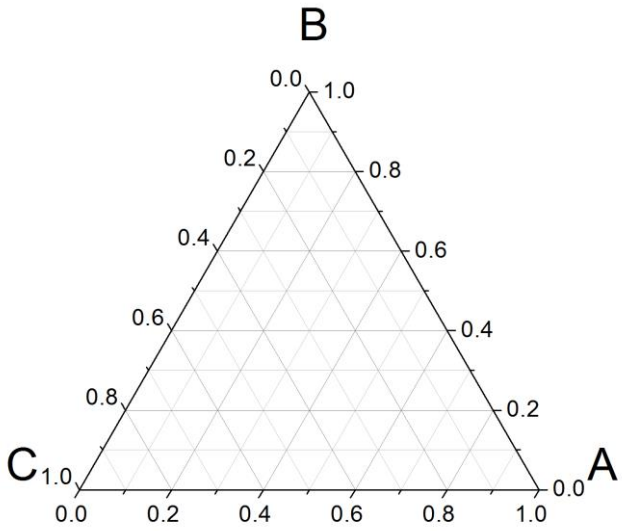

Figure 1.17 Generic ternary phase diagram for the system containing three components A, B, and C.

To determine the composition of a point on the chart, the three lines parallel to each of the edges must be drawn through that point. For example, in Figure 1.18a) a compound is marked on the phase diagram by the red dot. The percentage of A is read from the intersect of the line passing through the point parallel to the BC edge, at the CA edge (i.e. 20% A). The percentages of B and C can be read in the same way (Figure 1.18b), leading to the composition of 0.20A-0.40B-0.40C.

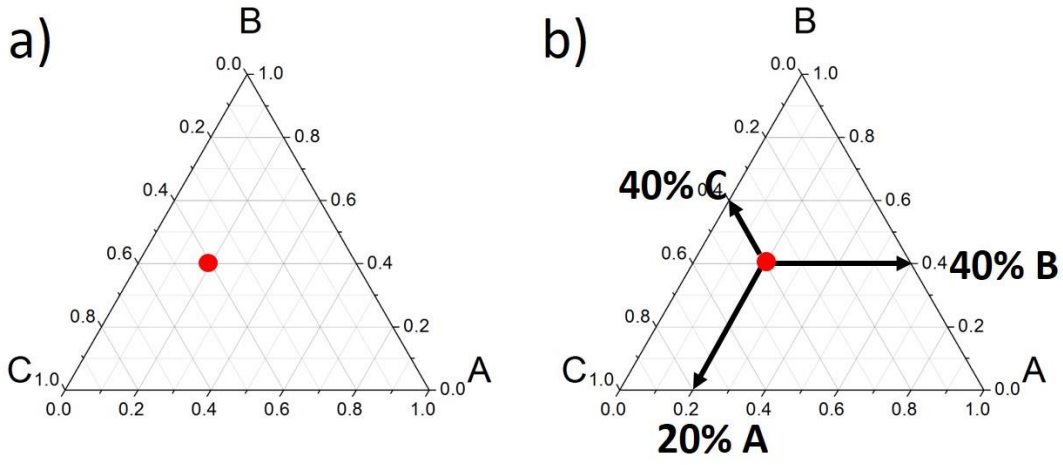

Figure 1.18 Composition identification of a point in a ternary phase diagram.

When establishing the phase diagram of an unknown ternary system, a methodical approach is used to establish symmetries, phase boundaries and solubility limits of some pertinent pseudo-binary systems. Two separate systems are shown in Figure 1.19.

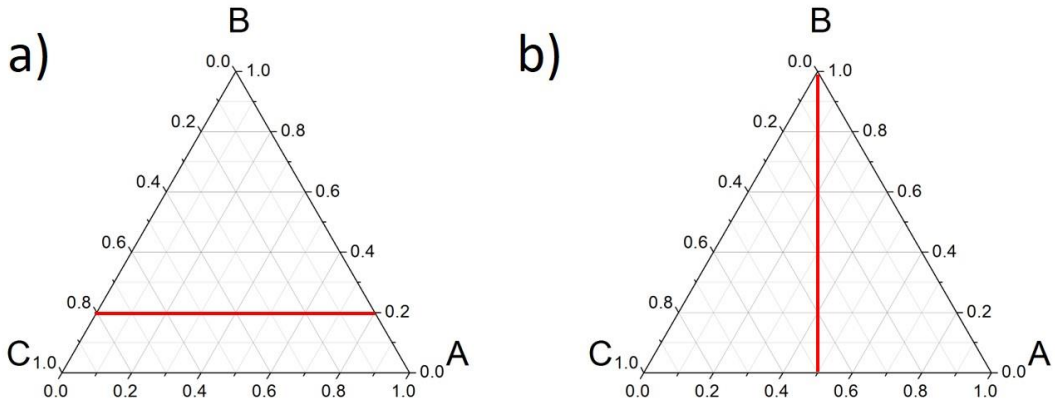

Figure 1.19 Pseudo-binary line (red) within a ternary phase diagram showing the compositions of a) 0.80[(1-x)C - xA]-0.20B and b) (1-x)B-x[0.50A-0.50C].

In the case of Figure 1.19a) along the pseudo binary line identified, the percentage of B stays constant across the line while the proportions of C and A are altered, *i.e.* moving from left to right across the phase diagram, the composition follows 0.80[(1-x)C - xA]-0.20B. In the case of Figure 1.19b), the ratio of A:C is constant while the proportion of (A+C) over B is varied, *i.e.* moving from the top to the bottom, the composition follows (1-x)B-x[0.50A-0.50C].

1.8 Single Crystal vs. Ceramic Materials

Currently, piezo-/ferroelectric materials are used broadly in single crystal and ceramic (polycrystalline) forms. Both types of materials present advantages and disadvantages in their synthesis and the resulting properties of the bulk material, and thereby in their specific applications.

Single crystals are characterized by their long-range periodicity of atomic and molecular arrangements, which gives rise to anisotropy, i.e. the dependence of the physical properties on the crystallographic directions (with the exception of the cubic space group). They offer the advantage of being able to exploit the spontaneous

polarization direction and to “engineer” it’s orientation in order to enhance the piezoelectric properties. Applying a poling field to the crystal along the polarization direction may achieve a monodomain state with all polarizations oriented in the same direction. While it may seem that a monodomain state with all dipoles aligned would give the highest piezoelectric output, this is not always the case, especially not for the relaxor-based piezoelectric single crystals like PMN-PT. Domain engineering is the technique of poling a ferroelectric crystal in a direction that is off their polar axis and in a direction where at least two of the original polarization directions are at an equal angle to the poling direction [16]. For example, Figure 1.20 shows a rhombohedral crystal with the polarization directions along the <111> pseudo-cubic diagonal direction. If a high enough poling field is applied along the $<001>_{cub}$ direction, the dipoles rotate to be oriented along the poling direction, resulting in an enhanced d_{33} arising from the intrinsic effects of the material. There may be a substantial increase in domain wall density which, in turn, creates internal electric fields that are thought to be the source of the increase in piezoelectric coefficient from the extrinsic contribution [4], [10].

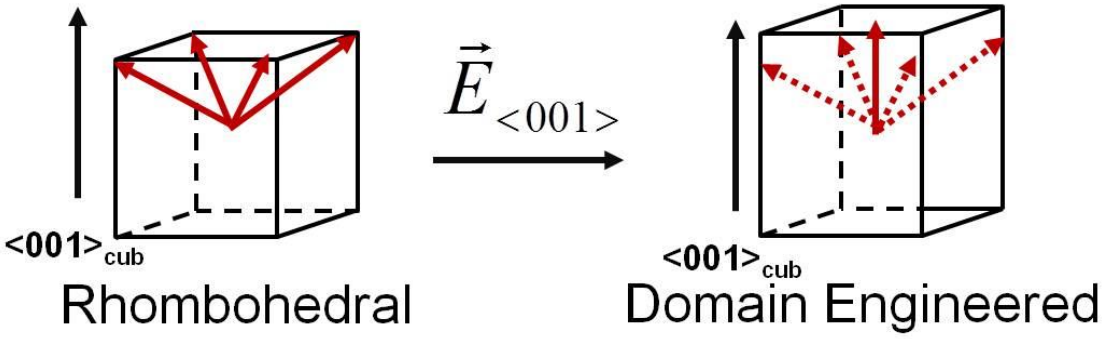

Figure 1.20 Schematic of polarization rotation that occurs when a rhombohedral single crystal is sufficiently poled off axis, along the <001> direction to achieve a domain engineered state in which the <111> polarization direction is rotated towards <001>.

These greatly enhanced piezoelectric properties make single crystal ferroelectric materials an attractive choice for many applications, yet there are drawbacks that should be considered. Namely, synthesis of single crystals can be more difficult and expensive in comparison to ceramics of the same material. Nowadays, large, lead-based ferroelectric single crystals are industrially grown by the Bridgman method, as shown in Figure 1.21, whereby a Pt crucible filled with a charge of stoichiometric metal oxides is

pulled through a heat gradient to melt the charge and then crystallize as the crucible moves through the gradient to cooler temperatures.

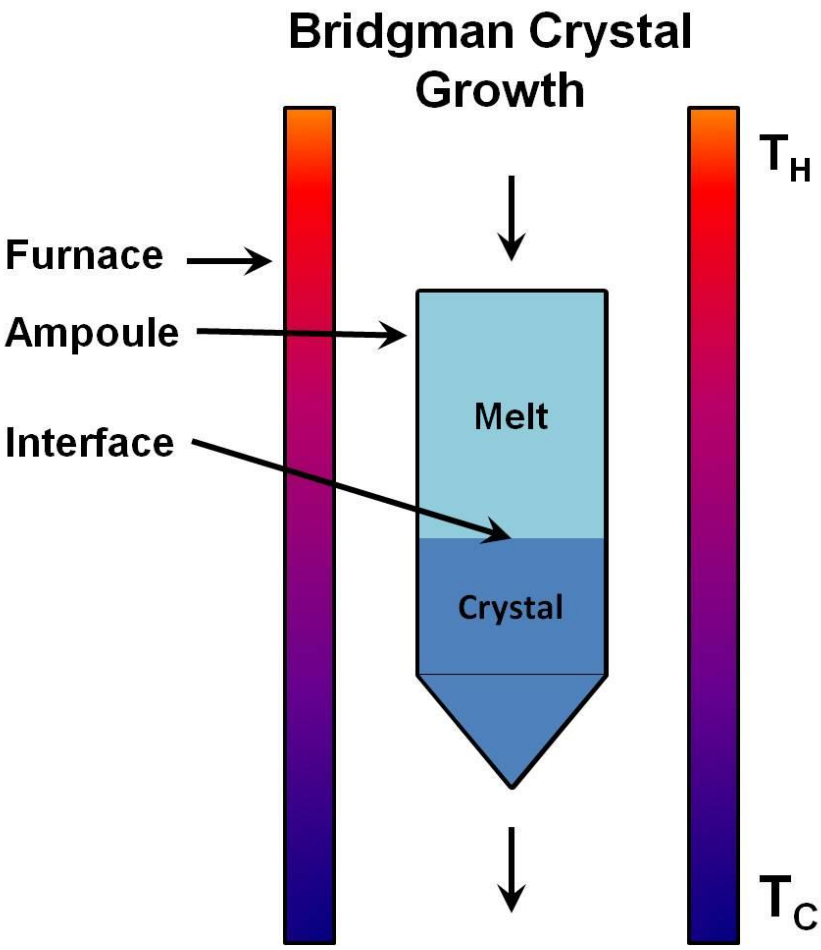

Figure 1.21 Schematic of an industrial Bridgman crystal growth furnace.

This methodology has allowed for more consistent fabrication of PMN-PT single crystals, however the crystals produced can suffer from compositional segregation along the length of the boule that is produced [2]. In addition, the radial composition of the cross-section experiences titanium migration, a phenomenon in which the Ti^{4+} atoms migrate to the exterior of the crystal [15]. In a practical sense, this method can be quite costly as each growth requires a Pt crucible that cannot be reused after the crystal growth. Another drawback of the Bridgman method is the difficulty of regulating the thermal gradient with the increase of crystal diameter [10], [15].

In order to reduce the temperatures needed to grow the desired crystals, a high temperature solution growth (or flux) method is utilized, akin to wet chemistry, but at

much higher temperatures. Here the flux (i.e. solvent) is chosen in which the charge (i.e. solute) is soluble at high temperatures and a specific flux:charge ratio (i.e. concentration) is selected to allow the desired compositions to precipitate out upon cooling. This principle is outlined in a generic binary piezocrystals – flux phase diagram in Figure 1.22. The flux method can lower the melting temperature by ~300 °C for the growth of PMN-PT piezocrystals and can be fine-tuned by altering the flux:charge ratio.

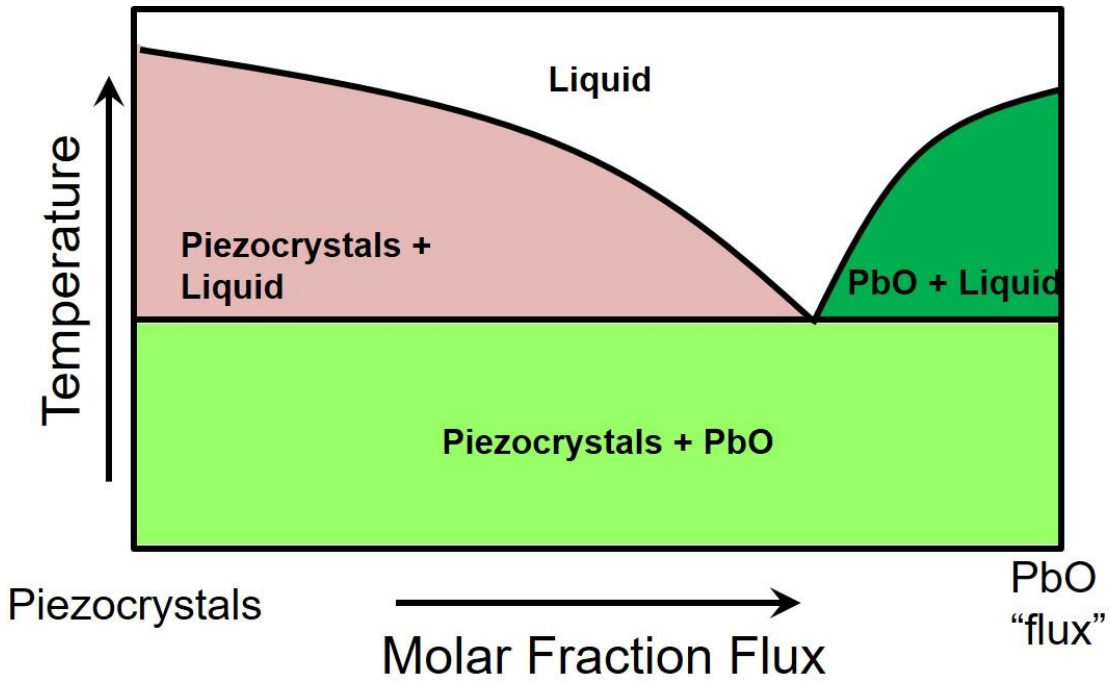

Figure 1.22 Generic binary phase diagram for the growth of piezocrystals (solute) from PbO flux (Adapted from [17]**).**

A schematic of the growth furnace set up is shown in Figure 1.23. In this method, the charge is composed of stoichiometric (nominal) amounts of the constituent metal oxide materials and then mixed with the flux in a ratio meant to obtain a super saturated solution at high temperature [17]. The solution is heated to above the melting temperature (~1100°C) and left to dwell for several hours in order to obtain a complete melt. The solution is slowly cooled over a period of several days or weeks for the desired piezocrystals to grow and obtain maximum crystal size. Nucleation can occur spontaneously upon cooling due to the internal thermal gradient of the furnace, or a seed crystal or wire can be introduced into the melt to provide a nucleation point.

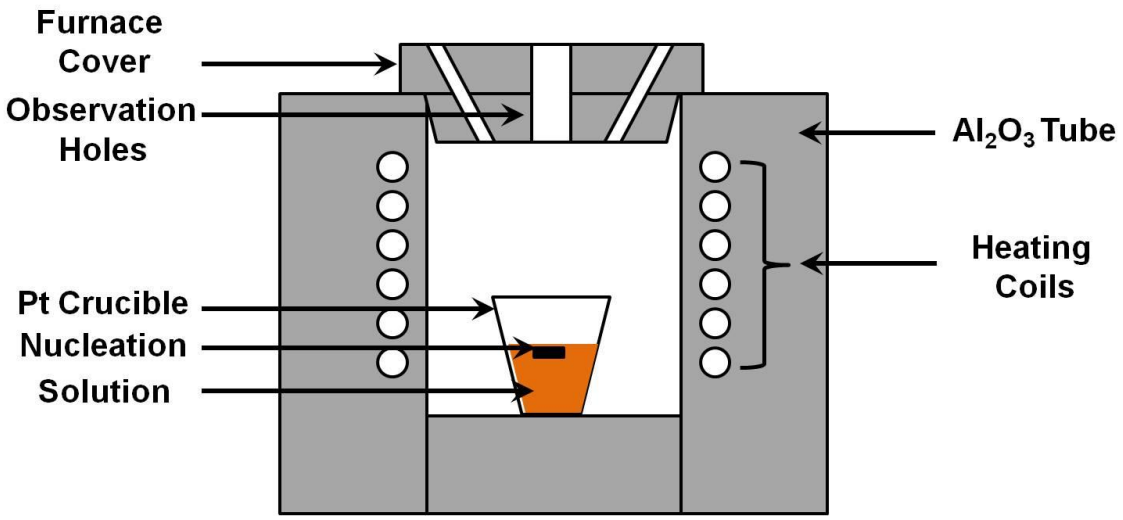

Figure 1.23 Schematic of a high-temerature furnace set up for the growth of piezocrystals by the flux method.

Ceramic materials are considerably inexpensive to make in comparison to their crystal counterparts and can be molded into a wide variety of shapes to suit the needs of the application. However, a polycrystalline ceramic, in the absence of an electric field, appears isotropic and has spherical symmetry due to the random orientations of grains and thereby the polarization vectors contained within the bulk [18]. In this case, if a material were piezoelectric, but not ferroelectric, its piezoelectric properties would remain unrealized due to a net cancellation of the overall change in dipole under pressure. By poling a ferroelectric ceramic, the piezoelectric properties can be displayed, as the external electric field orients the polarization vectors parallel to itself. This alignment cannot be complete and thus the piezoelectric coefficients of a ceramic are generally smaller than a single crystal of the same material.

1.9 A History of Lead-based Piezo-/Ferroelectric Materials

The field of piezo-/ferroelectric materials research has undergone continued growth since the first display of the direct piezoelectric effect by Jacques and Pierre Curie in 1880 when it was shown that the application of pressure resulted in surface charges in single crystals of both quartz and Rochelle's salt. It shortly followed that the converse effect, the application of an electric field to induce mechanical deformation, was demonstrated in 1881 by Gabriel Lippmann. After that discovery, it took more than 30 years until 1912 for the ferroelectric effect, a spontaneously occurring, reorientable

dipole, to be proposed and exactly 40 years until 1921 for that effect to be displayed in Rochelle's salt [19].

During World War I, there were efforts by the French Navy to use both quartz and Rochelle's salt as sonar transducers for underwater detection of German U-boats, as they were the only known piezoelectric materials. However, each of these materials presented unique obstacles: namely, the quartz crystals were difficult to grow in large sizes and of high quality at the time, and while Rochelle's salt crystals were easier to grow, they are also water soluble and subject to degradation with humidity [20]. No significant progress had been made until World War II, where concurrent research in the US, Japan and former Soviet Union allowed the discovery of $BaTiO_3$ (BT) for its potential as a high dielectric constant capacitor. Fortuitously, it was discovered that BT is also a ferroelectric material, and its ability to be poled while in ceramic form opened up a myriad of possibilities for potential applications as the material could be easily synthesized inexpensively and machined to a variety of shapes [1], [20]. However, BT is not without drawbacks – namely, its low Curie temperature, T_C = 120 °C - limiting its ability to operate in a broad range of temperatures.

The next significant leap forward for ferroelectrics research would come in the 1950s with the discovery of the solid solution between $PbTiO_3$ and antiferroelectric material $PbZrO_3$, namely $Pb(Zr,Ti)O_3$ (PZT). Though the phase diagram of PZT was proposed in 1953 by Sawaguchi, it was in 1954 [21], when Jaffe studied the behaviour of the morphotropic phase boundary (MPB) between the rhombohedral phase and tetragonal phases, and uncovered a marked increase in piezoelectric properties when approaching the compositionally induced phase change [20]. Since this discovery, lead-based perovskites have become the standard for high performance ferroelectric materials, particularly those possessing an MPB-type phase diagram. Many years after their discovery, BT and PZT ceramics are still among the most common commercially available piezo-/ferroelectric ceramics.

The applications of ferroelectric materials can be found in numerous areas and we interact with them on a daily basis. They are used as sensors where changes in pressure can be monitored by generating electricity, for example the knock sensor in a car's engine, and they can be used as motors or actuators where an electric field is applied to the material to cause deformation or displacement, for example an AFM probe

is moved finely and accurately by using a piezoelectric stage. If the material is behaving as a transducer, both the sensor and actuator effects are being utilized in the same application, e.g. in an ultrasound probe, an electric field is applied to a ferroelectric transducer, causing it to vibrate at the frequency of a soundwave, when the echo pulses comes back, the same material senses the change in pressure and converts it to an electric signal as the first step in generating an ultrasound image [1]. Since ferroelectric properties are hysteretic, they can be used for non-volatile memory devices. In addition, there is increased interest in looking at the ferroelectric effect in living systems, for example the shells of abalone have been shown to be made up of calcite and a ferroelectric polymer that shows ferroelectric bias [3].

1.10 Lead-Containing Relaxor-Based Piezo-/Ferroelectric Materials

Lead-based perovskite ferroelectric materials have become the standard for high-performance ferroelectric materials owing largely to the presence of a stereochemically active $6s^2$ lone electron pair when Pb^{2+} is on the 12-coordinate A-site. The molecular orbital diagram of Pb-O bonding based on density functional theory (DFT) calculations is shown in Figure 1.24. In bonding with oxygen, the Pb6s orbital displays partial mixing with the antibonding $O2p_z$ orbital, causing the electron density, and hence, the lattice to distort in order to reduce the overall energy of the system [22]. This lone pair is expected to create additional tetragonal distortion in the unit cell, leading to enhanced piezoelectric and ferroelectric properties in lead-based perovskites.

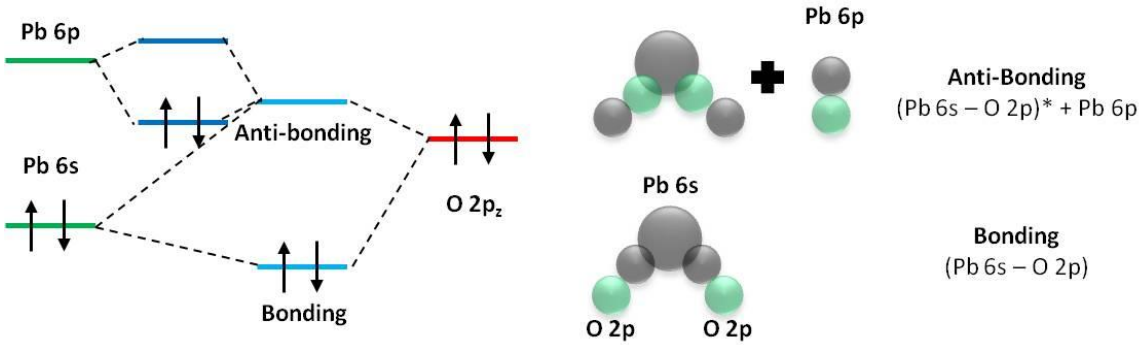

Figure 1.24 Molecular orbital diagram of Pb-O bonding resulting from a $6s^2$ lone electron pair (adapted from [22]**).**

Single crystals of lead-based relaxor ferroelectric systems which contain a morphotropic phase boundary region in their phase diagram have been extensively studied because of their enhanced properties. Many of these systems are based on the canonical relaxor ferroelectric $Pb(Mg_{1/3}Nb_{2/3})O_3$ (PMN) which has high dielectric permittivity, and high electrostriction at room temperature with very little hysteresis [13]. It was found that introducing $PbTiO_3$ as a second component resulted in a binary solid solution system with an MPB region. The phase diagram of $Pb(Mg_{1/3}Nb_{2/3})O_3$-$PbTiO_3$ (PMN-PT) solid solution system reported by Noheda can be seen in Figure 1.15 [14] with the MPB region starting at the PT mole fractions of 0.30 to 0.35. It is the pre-MPB compositions of the system that display the highest piezoelectric properties. In particular, when PT concentration is in the range of 29-32% (PMN-0.29PT and PMN-0.32PT), domain engineered single crystals of these materials exhibit very high piezoelectric constants, $d_{33} \cong 1500 – 2800$ pC/N [2], [10], [15]. However, these materials are not without their inherent drawbacks. Their Curie temperatures are relatively low, $T_C < 160$ °C and they have an additional low temperature phase transition from rhombohedral to tetragonal, T_{RT}, that ranges from 65 – 80 °C, which results in a loss of piezo-/ferroelectric properties due to de-poling. There is also a push to increase the field stability of these materials as their coercive fields of $E_C \cong 2.5$ kV/cm make these material prone to “over-poling” or de-poling, an effect that degrades the ferroelectric properties [23]. A comparison of properties of PMN-PT based piezo-/ferroelectric materials with PZT can be found in Table 1.1.

Table 1.1 Piezoelectric and Ferroelectric Properties of Selected Lead-based Ferroelectric Materials [1], [10]

Solid Solution System	Curie Temperature T_C (°C)	MPB phase change temperature T_{RT} (°C)	Coercive Field E_C (kV/cm)	Piezoelectric Coefficient d_{33} (pC/N)
PMN-0.29PT	135	96	2.3	1540
PMN-0.33PT	155	65	2.8	2800
PIN-PMN-PT (MPB)	197	96	5.5	2740
PZT Type II Ceramics	340	-	12	400
PZT Type IV Ceramics	250	-	8	650

There are several approaches that have been employed to mitigate these drawbacks to improve the ferroelectric properties of the system, yet to retain the high

piezoelectric coefficients that are desirable for applications. The most common approach being to add a third component to the established binary system with the aims of expanding the MPB region and enhancing the properties that near-MPB compositions display. Systems of interest include the second generation relaxor crystals $Pb(In_{1/2}Nb_{1/2})O_3$-$Pb(Mg_{1/3}Nb_{2/3})O_3$-$PbTiO_3$ (PIN-PMN-PT), $Pb(Yb_{1/2}Nb_{1/2})O_3$-$Pb(Mg_{1/3}Nb_{2/3})O_3$-$PbTiO_3$ (PYN-PMN-PT), $Pb(Sc_{1/2}Nb_{1/2})O_3$-$Pb(Mg_{1/3}Nb_{2/3})O_3$-$PbTiO_3$ (PSN-PMN-PT) and $Pb(Mg_{1/3}Nb_{2/3})O_3$-$PbZrO_3$-$PbTiO_3$ (PMN-PZ-PT). These materials have been shown to improve upon the thermal and electric field stability of PMN-PT, but have yet to reach commercialization as single crystals due to difficulties scaling up fabrication [2], [10].

There are additional issues presented by lead-based material systems that drive research to find lead-free alternatives, primarily the lead toxicity. What makes Pb^{2+} pernicious is that it acts as an ion mimic, due to its similar charge and size as ions such as Mg^{2+} and Ca^{2+}, displacing those needed metal ions in a variety of our bodily systems, causing poisonous effects. The potential of lead poisoning due to leaching from commercial goods has increased regulations that restrict and limit its usage [24]. Therefore, it is an urgent task to find lead-free or lead-reduced piezo-/ferroelectric materials as alternatives to the lead-based materials.

1.11 Bismuth as a Suitable Lead Replacement

From a chemical point of view, an intuitive replacement of lead is bismuth. Like the Pb^{2+} ion, Bi^{3+} also contains a stereochemically active $6s^2$ lone electron pair that is expected to contribute to the high tetragonal distortion, and therefore high polarization, of Pb^{2+}-based materials [25], but contrary to lead, bismuth is relatively non-toxic. Bismuth-based perovskite-like compounds such as $BiMO_3$ (M = Al, Ga) have been predicted theoretically to exhibit high T_C and high polarization, but require high pressures (≥ 6 GPa) to synthesize due to the smaller size of Bi^{3+} which prefers an 8-coordinate site over the 12-coordinate A-site of the perovskite unit cell [26]. Using the solid solution approach, several $Bi(M,M')O_3$ components have been stabilized in $PbTiO_3$. For example, the $Bi(Zn_{1/2}Ti_{1/2})O_3$-$PbTiO_3$ (BZT-PT) binary system shows a consistent increase in Curie temperature, T_C, with increasing mole fraction of BZT [27], whereas solid solutions containing $Bi(Zn_{1/3}Nb_{2/3})O_3$ (BZN), $BiInO_3$ (BI), $BiScO_3$ (BS), $Bi(Ni_{1/2}Ti_{1/2})O_3$ (BNT) and $Bi(Mg_{1/2}Ti_{1/2})O_3$ (BMT) show an increase in T_C with a small mole fraction of Bi^{3+} [25]. To

date piezo-/ferroelectric properties of these Bi-based solid solutions, particularly the BZT-PT system, have not been reported due to a coercive field that is higher than the dielectric breakdown field, rendering them useless for device applications.

Our interest in bismuth as a replacement for lead has multiple facets. Firstly, stabilizing Bi^{3+} in a lead-based solid solution will allow for the examination of how the two metal ions behave differently in the same coordination site. By using chemical substitution for the Bi^{3+}, it will give us insight into how to best take advantage of the high tetragonal distortion that results from Bi^{3+}substitution while ideally mitigating the problem of high coercive fields preventing ferroelectric behaviour from being displayed. With the understanding of these two problems, it will give us insight into how to better design and synthesize lead-reduced and lead-free materials.

1.12 Objectives of This Work

Relaxor-based piezo-/ferroelectric materials of complex perovskite structure, represented by $(1-x)Pb(Mg_{1/3}Nb_{2/3})O_3$-$xPbTiO_3$ (PMN-PT), that were developed in the last decade, have demonstrated excellent piezoelectric performance potentially useful for high-end electromechanical transducer applications. However, they also exhibit some inherent drawbacks, such as low a Curie temperature, an even lower de-poling temperature due to the presence of a MPB, a weak coercive field and a high content of lead, which make them unsuitable for high-temperature and high-field (power) applications and raise environmental concerns [2], [10], [28].

On the other hand, bismuth-based complex perovskites such as $Bi(Zn_{1/2}Ti_{1/2})O_3$ (BZT) seem to be an interesting candidate for the replacement of lead-based compounds because like Pb^{2+} ion, Bi^{3+} also contains the $6s^2$ lone electron pair which is considered to be essential for the high piezo-/ferroelectric performance in lead-based perovskite. In addition, the solid solution between BZT and PT indeed exhibits larger structural distortion and thereby higher Curie temperature than PT. However, its coercive field is too large for the material to be poled in order to make its potentially high piezo-/ferroelectric properties useful [25], [27], [29], [30].

Faced with those issues and challenges, the objectives of this thesis work are mainly of two-fold:

1) Use a non-stereochemically active ion and related complex compound, namely $La(Zn_{1/2}Ti_{1/2})O_3$ (LZT) as an end-member to "soften" the structures, chemical bonding and electric properties of "hard" ferroelectric materials, including the canonical ferroelectric PT and the solid solution of PT-BZT, by reducing the overall tetragonal distortion. In doing so, we seek to achieve improved electric properties such as giant dielectric constants, smaller coercive fields, switching polarizations and excellent piezoelectricity and ferroelectricity.

2) Use BZT as the third component to "harden" the structures, chemical bonding and electric properties of the PMN-PT binary system in order to increase its coercive field and to improve its piezo-/ferroelectricity. In particular, special efforts have been made to grow the single crystals of the PMN-PT-BZT ternary system. The studies of the single crystals are expected to provide invaluable information on the phase symmetry, domain structures, phase transitions and electric properties and to gain a better understanding of the relationship between crystal formation, chemical composition, phase symmetry and macroscopic properties.

1.13 Organization of This Thesis

This thesis is written in 8 chapters, with the 5 research chapters written in the style of manuscripts for publication, and are intended to be self contained units.

Chapter 1 contains the necessary background and theory will be introduced and discussed in order to establish the foundation for addressing the objectives, technical approaches and organization of this thesis.

Chapter 2 will introduce and discuss briefly the principles and applications of various synthesis, analytical and measurement techniques utilized to characterize the crystal structure and physical properties of the material synthesized in order to better understand the structure/property relationship. This will include diffraction techniques for structural analysis and optical and electric characterization methods for studies of domain structure, phase transitions and, dielectric, ferroelectric and piezoelectric properties.

In Chapter 3, Chapter 4 and Chapter 5, the approach of using chemical substitution to “soften” a ferroelectric material in order to lower or display ferroelectric properties is explored.

Chapter 3 highlights the binary system of $La(Zn_{1/2}Ti_{1/2})O_3$-$PbTiO_3$. The new solid solution system of (1-x)$La(Zn_{1/2}Ti_{1/2})O_3$-x$PbTiO_3$ (LZT-PT) was successfully synthesized with complete solubility throughout the series. At low concentrations of LZT x = 0.00 – 0.30, the material is in a tetragonal phase with diffuse ferroelectric phase transitions that lower in Curie temperature, T_C from T_C = 490 °C at x = 0.00 to nearly room temperature, T_C = 39 °C at x = 0.30, effectively “softening” the ferroelectric properties by chemical substitution. As the concentration of LZT increases to x = 0.40 – 0.70, the material transforms to a non-ferroelectric pseudo-cubic phase and at high concentrations of LZT, x = 0.80 – 1.00, the material is in a monoclinic $P2_1/n$ phase. Most interesting about this binary system is that at mole fractions of x = 0.30 – 0.40, the material shows giant dielectric constants on the order of $\varepsilon' > 10^6$, making these compositions promising for high energy density storage and MEMS applications.

Chapter 4 expands upon the binary system of LZT-PT by incorporating $Bi(Zn_{1/2}Ti_{1/2})O_3$. The 0.20$Bi(Zn_{1/2}Ti_{1/2})O_3$-0.80$PbTiO_3$ (BZT-PT) solid solution, [27] is unique in that it exhibits a higher Curie temperature (T_C) than the bench mark ferroelectric end member, $PbTiO_3$. However, BZT-PT experiences too large a coercive field (E_c), *i.e.* too “hard”, for its polarization to switch thereby preventing its potentially promising piezo-/ferroelectric properties to be explored for practical applications. In this work, we have found an unconventional way to “soften” the character of BZT-PT by lanthanum substitution for Bi^{3+}. The new solid solution system of 0.20[x$La(Zn_{1/2}Ti_{1/2})O_3$ – (1-x)$Bi(Zn_{1/2}Ti_{1/2})O_3$] - 0.80$PbTiO_3$ (LZT-BZT-PT) ceramics are successfully synthesized with x = 0.0 – 1.0 showing complete solubility for the series. Powder x-ray diffraction of the ceramics reveals a tetragonal, P*4mm* structure that shows decreased tetragonal distortion (c/a) with increasing mole fraction of LZT. The measurement of dielectric permittivity as a function of temperature measured at varying frequency also revealed a decrease in T_C as the fraction of LZT increases. More interestingly, E_C is reduced as the LZT mole fraction increases. At the high bismuth end of the pseudo-binary line, E_C is greater than the dielectric breakdown field at x = 0 – 0.3, whereby saturated P(E) loops are not obtained. As the mole fraction of LZT increases, dipolar switching is realized with the lowered E_C > 70 kV/cm at x = 0.40 to E_C = 22 ± 0.5 kV/cm at x = 1.0. Therefore, this

‘softening’ of the BZT-PT binary system allows for the display of bipolar states in the polarization vs. electric field hysteresis loops for mole fractions of LZT $x \geq 0.40$ making this solid solution series promising materials for future high field applications.

Chapter 5 brings together the work performed exploring the solubility limits, phase symmetry and properties of the $La(Zn_{1/2}Ti_{1/2})O_3$-$Bi(Zn_{1/2}Ti_{1/2})O_3$-$PbTiO_3$ (LZT-BZT-PT) solid solution system and proposes its ternary phase diagram which maps out the various phases, their structures and associated properties. It includes the new results obtained from the investigation of the (1-x)PT-x[50LZT-50BZT] pseudo-binary system and the $0.30[(1-x)Bi(Zn_{1/2}Ti_{1/2})O_3$-$xLa(Zn_{1/2}Ti_{1/2})O_3]$-$0.70PbTiO_3$ pseudo-binary line. These results are combined with the results previously presented in Chapter 3 and Chapter 4 to determine the areas of interest within the ternary system.

In the areas of high PT concentration, there is a tetragonal, ferroelectric phase that is further divided into two regions: a region of “hard” ferroelectricity where high BZT concentration leads to high Curie temperatures, T_C, and coercive field, E_C, and a region of “soft” ferroelectricity where high LZT concentrations lead to lower T_C and E_C. This high PT region is of interest for high field ferroelectric applications. Outside of that region of ferroelectric activity, along the (1-x)LZT-xPT binary system, the region of $x = 0.30 – 0.40$ displays giant dielectric constants, making them materials of interest for high-density energy storage and MEMS applications. The high BZT concentration region of the phase diagram does not show a single phase in ambient synthesis conditions.

Chapter 6 and Chapter 7 take the same chemical substitution approach to “harden” the PMN-PT system in order to increase Curie temperatures, T_C, and coercive fields, E_C.

In Chapter 6 single crystals of the $Pb(Mg_{1/3}Nb_{2/3})O_3$–$PbTiO_3$–$Bi(Zn_{1/2}Ti_{1/2})O_3$ [PMN–PT–BZT] ternary complex perovskite system have been grown by a high temperature solution method using the mixture of PbO and H_3BO_3 as flux (in a molar ratio of 4:2) and an optimum flux:charge molar ratio of 6:1. It is found that the addition of BZT into the relaxor ferroelectric PMN–PT system reduces the number of spontaneous nucleations, resulting in large single crystals (5mm x 5mm x 14mm) of good quality. The grown crystals exhibit a pseudo-cubic morphology and show evidence of two-dimensional growth mechanism. Examination by polarized light microscopy (PLM)

reveals the formation of striation, which can be reduced by changing the growth conditions. The domain structure and phase transition of the PMN–PT–BZT crystals are investigated by PLM. The temperature and frequency dependences of the dielectric permittivity of the grown crystals show typical relaxor ferroelectric behavior, with the frequency dependence of the temperature of maximum permittivity (T_{max}) following the Vogel-Fulcher law. The ferroelectric and piezoelectric properties are displayed and compared to both the parent and next generation relaxor materials for comparison.

In Chapter 7 single crystals of the nominal composition $0.61Pb(Mg_{1/3}Nb_{2/3})O_3–0.312PbTiO_3–0.078Bi(Zn_{1/2}Ti_{1/2})O_3$ (PMN-PT-BZT) have been grown by high temperature solution (flux) growth in order to attain crystals of morphotropic phase boundary (MPB) type compositions. The large crystal block which resulted has many twinning points that served as separation planes for the individual crystals. The individual crystals and the group of crystals, as a whole, had a high degree of compositional segregation due to changing melt concentration throughout the growth process. This segregation allowed for mechanistic insight into the growth of the PMN-PT-BZT crystal solid solution system, namely that early-stage crystals have a rhombohedral, more PMN-like character, showing relaxor ferroelectric behaviour, and late-stage crystals having more PT- like character, showing normal ferroelectric behaviour. The crystals in the as-grown block cross over the MPB region, due to the presence of rhombohedral, tetragonal and monoclinic phases. Evaluating the ferroelectric behaviour, the incorporation of BZT achieved the goal of “hardening” the PMN-PT binary solid solution system as both remnant polarization, P_r, and coercive field, E_C, showed improvement over the parent system.

Chapter 8 brings together general conclusions about the two systems studied in order to put the work of this thesis in broader context as well as future outlook for these projects.

Chapter 2. Experimental Principles and Techniques

This chapter will introduce and discuss briefly the principles and applications of various analytical and measurement techniques utilized to characterize the crystal structure and physical properties of the material synthesized in order to better understand the structure/property relationship. This will include solid state synthesis, diffraction techniques for structural analysis and optical and electric characterization methods for studies of domain structure, phase transitions and, dielectric, ferroelectric and piezoelectric properties.

2.1 Conventional Ceramic Synthesis by Solid State Reaction

The ceramics prepared and reported within this work were synthesized *via* a conventional, two-step solid state reaction synthesis method whereby the materials are first calcined to obtain pure-phase perovskite materials and then sintered to obtain dense ceramics for characterization.

In this methodology, stoichiometric amounts of the component metal oxides are weighed and combined to make a 10g charge. The powders are then hand ground in acetone for 1hr and then pressed into two ~5g pellets for calcination. The muffle furnace is ramped to the dwell temperature at a rate between 50 - 300 °C/hr to reach the dwell temperature. The dwell temperature is varied between 700 – 950 °C and dwell time is varied between 2 – 12hr to obtain ideal synthesis conditions. Once pure phase perovskite powders are obtained, the pellets are reground in acetone for 1hr and then pressed into ~0.5g, 1 cm diameter discs for sintering between 1050 – 1200 °C. Those dense ceramics are then polished to achieve flat, parallel surfaces for electrode application and subsequent characterization.

2.2 Structural Characterization by Powder X-Ray Diffraction (XRD)

Due to the crystalline nature of perovskite piezo-/ferroelectric materials, structural information can predict and explain the properties that result. Powder x-ray diffraction is

utilized to monitor reaction progress and determine phase purity and crystal structure of the materials synthesized. Upon refinement of the XRD diffraction patterns, the symmetry, lattice parameters (*a*, *b* and *c*), bond angles (*α*, *β* and *γ*) and atomic positions can be extracted as well as the local bond lengths and bonding angles. A generic unit cell with bond lengths and angles is shown in Figure 2.1. The symmetry criteria for the seven crystallographic classes are outlined in Table 2.1.

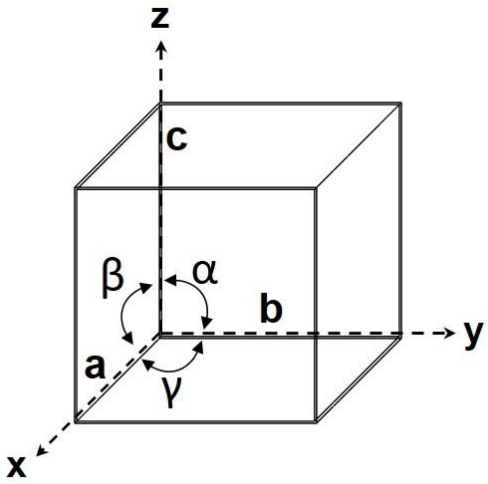

Figure 2.1: Representation of a generic unit cell with bond lengths, a, b and c and bond angles, α, β, and γ labelled.

Table 2.1 Seven Crystallographic Systems

Crystal Class	Axis System
Cubic	a = b = c; α = β = γ = 90°
Tetragonal	a = b ≠ c; α = β = γ = 90°
Hexagonal	a = b ≠ c; α = β = 90°, γ = 120°
Rhombohedral	a = b = c; α = β = γ ≠ 90°
Orthorhombic	a ≠ b ≠ c; α = β = γ = 90°
Monoclinic	a ≠ b ≠ c; α = β = 90°, γ ≠ 90°
Triclinic	a ≠ b ≠ c; α ≠ β ≠ γ ≠ 90°

2.2.1 Generation of X-rays

To generate x-rays, we must first bombard a source material with an electron beam of sufficiently high energy to eject an inner shell electron, creating a hole. Once the hole is created, an upper shell electron will fall into the hole and emit an x-ray of a characteristic wavelength. To be utilized experimentally, monochromatic x-rays must be

generated. There are a variety of metals that are used as the x-ray source, the two most common being copper and molybdenum. This phenomenon will be looked at in closer detail using copper as the x-ray source.

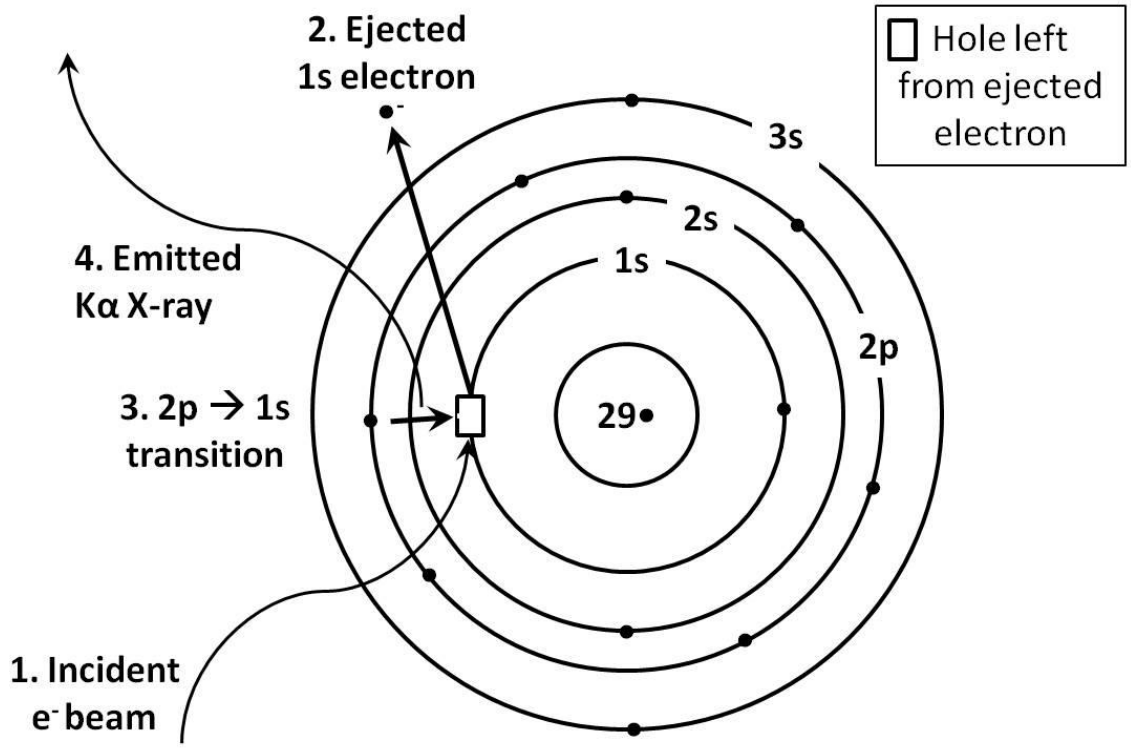

Figure 2.2: Emission of x-rays from a copper source whereby: 1. An incident electron beam collides with a 1s electron; 2. The electron is ejected, leaving a hole; 3. A 2p electron falls into the 1s hole; 4. A Kα X-ray is emitted.

When a copper foil is struck with an electron beam under a high accelerating voltage, a 1s electron is ejected from the shell. Rapidly, a higher shell electron falls into the hole left behind, emitting a short wavelength on the order of 10^{-10} m. The wavelength that will be emitted is dependent on the energy level of the electron that will fill that hole. If the transition is 2p → 1s, depending on the spin state of the electron, there will be a transition at either wavelength $K_{\alpha 1}$ = 1.54051 Å or $K_{\alpha 2}$ = 1.54433 Å. If the transition is 3p → 1s, its transition wavelength is K_{β} = 1.3922 Å. The resulting diffraction pattern is most intense at the $K_{\alpha 1}$ wavelength, so nickel foil is used to act as a filter for lower wavelength emissions, allowing the K_{α} beams to pass through to interact with the sample material. However, $K_{\alpha 1}$ and $K_{\alpha 2}$ are too similar in energy to be effectively filtered out from each other and, in some cases, difficult to resolve in the resulting diffraction pattern. In order

to address this issue, the $K_{\alpha 2}$ is removed from the analyzed spectrum with software in the post diffraction analysis [6].

2.2.2 Bragg's Law and X-ray Diffraction in Crystalline Materials

The approach to evaluating diffraction from a crystalline material is to view the atoms in the crystal structure as sets of planes of regular spacing that have a degree of transparency to X-ray, separated by an interplanar distance, *d*. When the x-ray beam collides with the sample, some of the x-rays are transmitted through the sample, and others are reflected (diffracted) at the angle of (180° - Incident angle). Figure 2.3 outlines the pathway of diffraction.

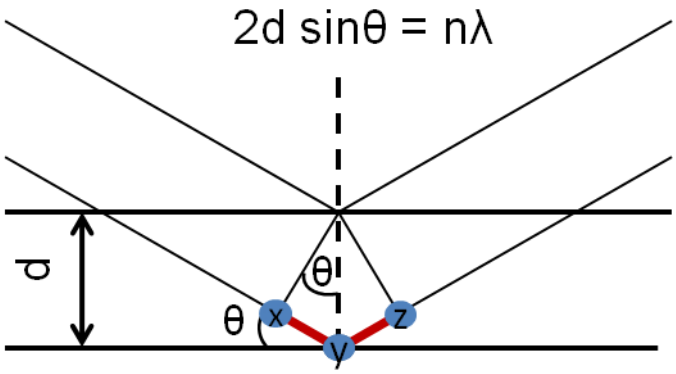

Figure 2.3 The path of x-ray diffraction by crystal planes to derive the Bragg's Law.

Using the rules of similar triangles, the path length in Figure 2.3 is related to the Bragg Angle, θ, by the following equation:

$$xy = yz = dsin\theta \tag{2.1}$$

Yielding the path length difference as:

$$xyz = 2dsin\theta \tag{2.2}$$

For the diffracted intensity to be detected in the detector, the path length difference must satisfy the conditions for constructive interference of the two diffracted beams, *i.e.* must be a multiple (n = 1, 2, 3, …, n) times of the incident wavelength:

$$xyz = n\lambda \tag{2.3}$$

Thus, the condition to satisfy Bragg's Law is as follows:

$$2dsin\theta = n\lambda \tag{2.4}$$

The resulting constructive reflections are captured either by a moving detector that captures reflections at each angle 2θ, or by an image plate that detects the entire reflection pattern [31]. This image is then converted to a diffraction pattern in terms of intensity and the angle 2θ. When looking at the lattice planes within the unit cell of a material, their positions and orientations are conventionally described using Miller indices. The Miller indices, (*hkl),* are determined as the reciprocal of the fraction of the lattice parameter where the plane intersects the unit cell axis. For example, cubic unit cells are pictured in Figure 2.4 showing two different shaded planes. In the case of example a), the plane intersects the *a* and *b* lattice axes at infinity and the *c* axis at ½ of the *c* parameter, giving a Miller index of (002), *i.e. h* = 0, *k* =0, *l* = 2. In example b), the plane intersects the *a* and *b* axes at 1 and the *c* axis infinity, giving a Miller index of (110), *i.e.* h = 1, *k* = 1, *l* = 0.

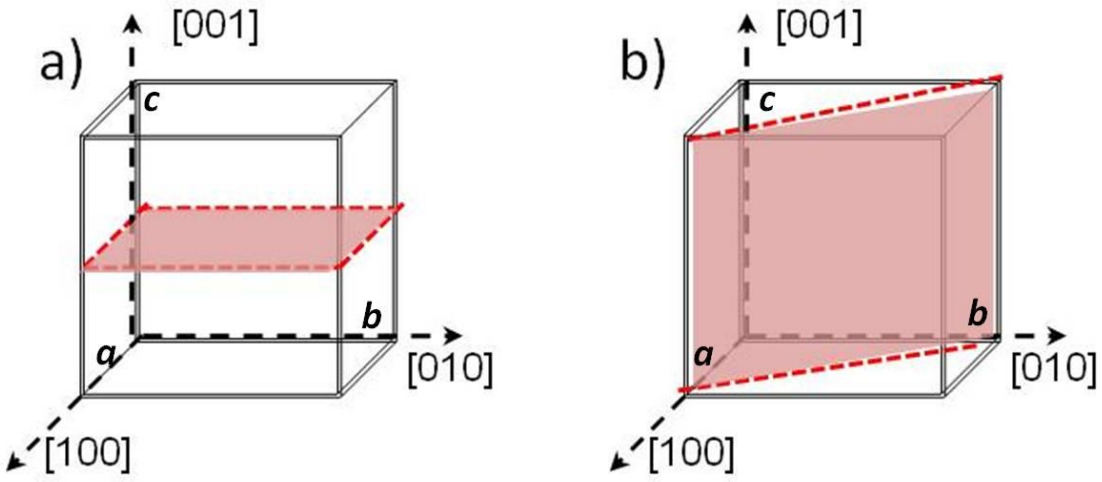

Figure 2.4 Miller indices for a) (002) and b) (110) planes in a cubic unit cell.

The Miller indices are related to the d-spacing of the unit cell in an orthogonal crystal (*i.e. α* = *β* = *γ* = 90°) in the following way:

$$\frac{1}{d_{hkl}^2} = \frac{h^2}{a^2} + \frac{k^2}{b^2} + \frac{l^2}{c^2} \tag{2.5}$$

Typical, indexed powder diffraction patterns of perovskite materials are shown in Figure 2.5, which demonstrate the peak positions and profiles (shapes) characteristic of

rhombohedral (R) symmetry and tetragonal (T) symmetry, respectively. Peak positions are refined to determine symmetry and lattice parameters of the unit cell. Peak widths are analyzed to give information about the average crystallite size in the polycrystalline material. Peak intensities indicate the electron density at a particular atomic site allowing for determination of site occupancy. In these two diffraction patterns, there are differences in peak symmetry and splitting, e.g. (200) and (210), based on whether the symmetry is rhombohedral or tetragonal.

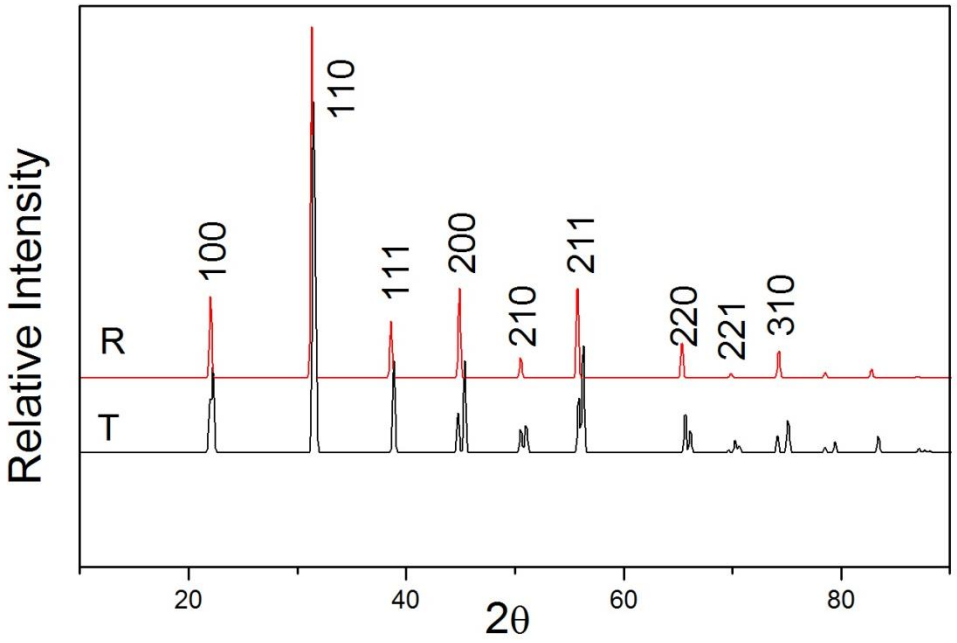

Figure 2.5 Indexed powder XRD patterns for $0.91Pb(Mg_{1/3}Nb_{2/3})O_3$ - $0.09PbTiO_3$ with rhombohedral (R) symmetry and $0.64Pb(Mg_{1/3}Nb_{2/3})O_3$ - $0.36PbTiO_3$ with tetragonal (T) symmetry.

Since the perovskite structure shows its characteristic diffraction pattern, analyzing the splitting at characteristics sets of peaks can reveal the deviation (lowering) of symmetry from the ideal, cubic structure and determine the resultant symmetry. In Figure 2.6, the variations of the indexed peaks of (111), (200) and (220) with decreasing symmetry in the perovskite structure are illustrated. For example, for cubic and tetragonal unit cells, the (111) peak is as singlet because all the (111) d-spacings are overlapping, whereas in a rhombohedral unit cell, the (111) peak splits as a result of lattice distortion along the <111> direction. Similarly, the tetragonal phase is associated with the characteristic splitting of such peaks as (100), (110), (200), etc. In lead-based perovskites, the highest intensity peak belongs to the (110) set of planes due to the high electron density of Pb^{2+} on the A-site [6], [31].

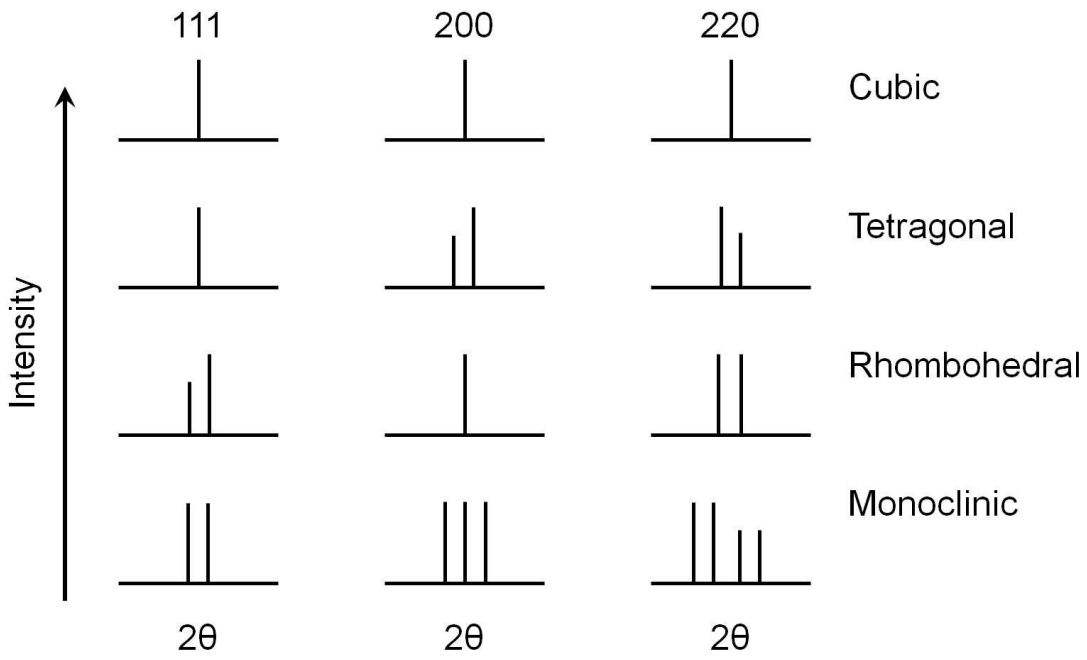

Figure 2.6 Schematic XRD patterns for the (111), (200) and (220) peak sets for a cubic perovskite structure and their characteristic splitting in tetragonal, rhombohedral and monoclinic symmetries.

The Rietveld method is an important tool for refining the crystal structure and lattice parameters. In the Rietveld refinement of XRD data, an ideal pattern is calculated from what is known about the material, *e.g.* symmetry, site occupancies, and is fit to the experimental data using a least squares method. From this comparison, more accurate lattice parameters, bond angles and atomic positions/displacements can be extracted. In addition, the method corrects the background of the specific instrument used and can account for a preferred orientation of the sample [32]. TOPAS Academic software is utilized to refine the lattice parameters and unit cell specifications using the Rietveld method. In this way, lattice parameters, bond lengths and bond angles can be determined as well as the ionic displacements.

2.3 Optical Characterization by Polarized Light Microscopy (PLM)

Polarized light microscopy is used on single crystal samples to observe and analyze their domain structures and phase transition, to measure birefringence and to investigate how those properties vary with changes in temperature and/or electric field. In an isotropic crystal, light will travel at the same speed, regardless of direction of

propagation. However, due to their high degree of anisotropy, ferroelectric single crystals are highly birefringent, *i.e.* the refractive index is dependent on the direction in which light propagates through the material. This phenomenon is described in a uniaxial crystal by the following equation:

$$\Delta n = n_e - n_o \tag{2.6}$$

where n_o is the refractive index of the ordinary ray whose polarization is perpendicular to the optic axis and n_e is the refractive index of the extraordinary ray whose polarization is parallel to the optic axis. This is represented visually as an ellipsoidal figure shown in Figure 2.7 called the optical indicatrix. The crystal is said to be positively uniaxial when $n_e > n_o$ and negatively uniaxial when $n_e < n_o$ [33].

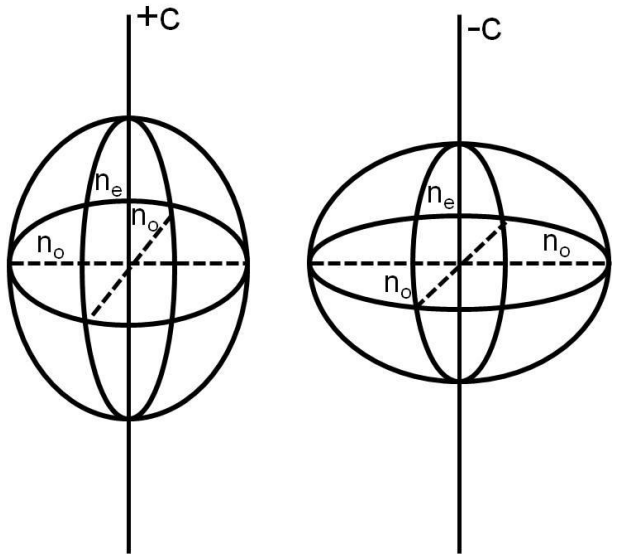

Figure 2.7 The optical indicatrix of a uniaxial crystal when it is positively uniaxial (left) or negatively uniaxial (right).

The experimental set up of a polarized light microscope can be seen in Figure 2.8 in which the directions of the polarizer and analyzer are perpendicular to each other. Light is emitted from the source and passed through the polarizer, to become linearly polarized light. If there is no sample in the light's path, or the sample is isotropic, when the light reaches the analyzer (*i.e.* a perpendicular polarizer), no light passes though and the image appears dark. If a birefringent crystal is placed between the polarizer and analyzer, the image will be in either transmission (or diagonal) (bright) or extinction (dark) depending on the orientation of the optic axis with respect to the crossed polarizer and analyzer. If the optic axis is parallel to the polarizer, light passes along that axis

unimpeded, yielding extinction at that angle. When the sample is rotated off that axis, due to the variance in refractive index, the extraordinary ray experiences a phase shift from the ordinary ray. When the extraordinary ray is recombined with the ordinary ray after exiting the sample at a rotated angle from the polarizer, light is allowed to transmit through the analyzer, giving rise to a specific interference colour. The path difference between the extraordinary and ordinary beams due to phase shift is called the optical retardation of the sample.

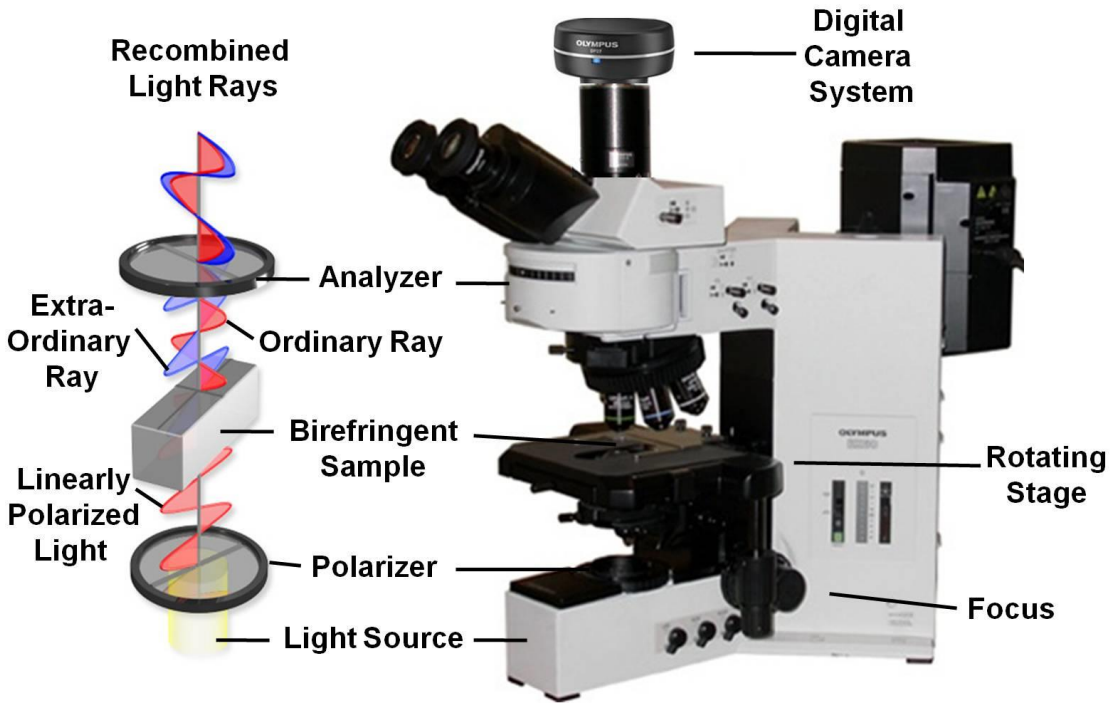

Figure 2.8 **A schematic of a polarized light microscope. (Adapted from** [34], [35]**).**

Optical retardation or phase shift, Γ_0, is quantified in the following equation:

$$\Gamma_0 = \Delta n * d \tag{2.7}$$

where the phase shift is determined by the birefringence, Δn and the thickness of the sample, d. The phase shift is a measurable quantity, thereby rearranging this equation gives a basis to calculate the birefringence of a sample

$$\Delta n = \frac{\Gamma_0}{d} \tag{2.8}$$

Using a U-CBE tilting compensator (e - line; λ = 546.1 nm), the phase shift can be measured based on the tilt angle to bring the crystal sample to extinction at its brightest transmission (diagonal) position. In a practical sense, the sample is positioned at 45° to the extinction position between crossed polarizers. The compensator's tilt is adjusted to bring the sample to extinction, *i.e.* to compensate exactly the optical retardation, and the angle at which the phase is adjusted to "compensation" is recorded. The angle of compensation is converted to the optical retardation (in nm) of the phase shift by using the e-line at 546.1 nm, as shown in Figure 2.9.

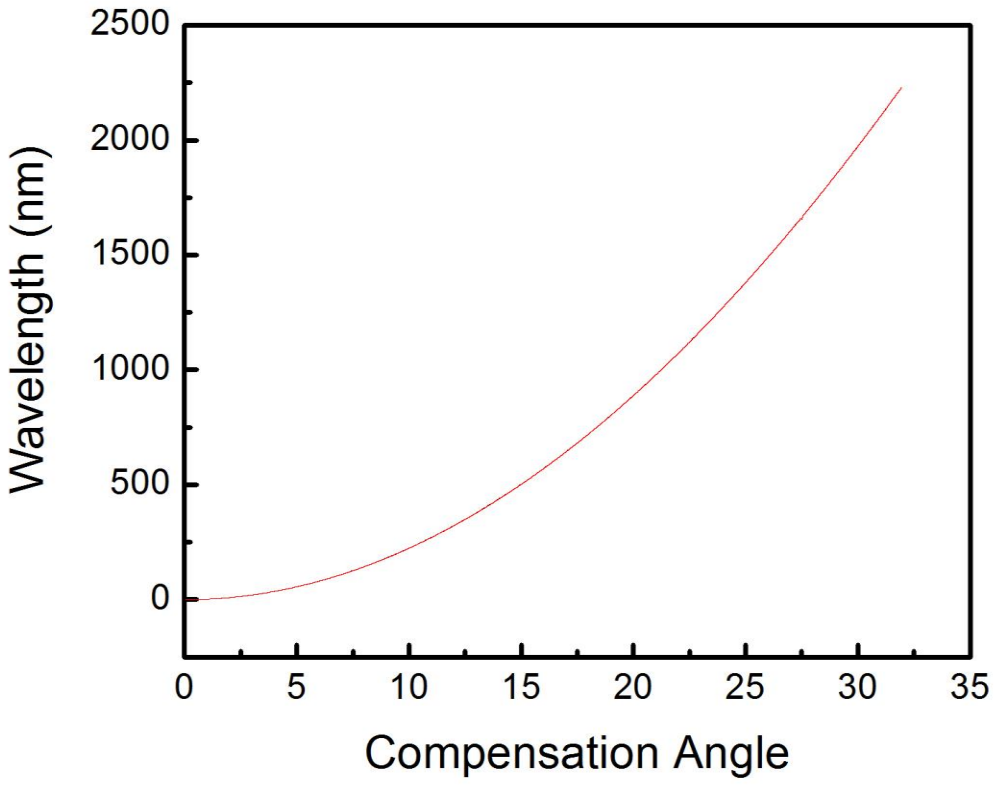

Figure 2.9 Wavelength for opical retardation vs. compensation angle for e-line transmission at 546.1 nm for a U-CBE tilting compensator.

Perovskite single crystals generally grow with a pseudo-cubic morphology, with regular, (100) crystal faces [36]. What makes this type of analysis particularly convenient and useful when studying perovskite-type ferroelectric single crystals is that the optic axis is coincident with the polarization axis. This means that by examining the extinction angle of individual domains with respect to the crystal's grown face and edge, one can determine the symmetry of the bulk crystal, analyze the phase components and map out

their distribution across the crystal [8][36]. Figure 2.10 shows the extinction angles with respect to the as-grown crystal face and edges for tetragonal and rhombohedral symmetries for a (001)-oriented platelet. For the tetragonal symmetry whose polarization is along the <001> direction, the crystal shows extinction when the crossed polarizers are parallel (or at 90°) to the <100> direction and in transmission when they are at 45° to the <100>, i.e. along the <110> direction. For rhombohedral crystals whose polarization is along the <111> directions, the crystal shows transmission when the crossed polarizers are parallel (or at 90°) to the <100> direction and extinction when they are at 45° to <100>, i.e. along the <110> direction [8], [36].

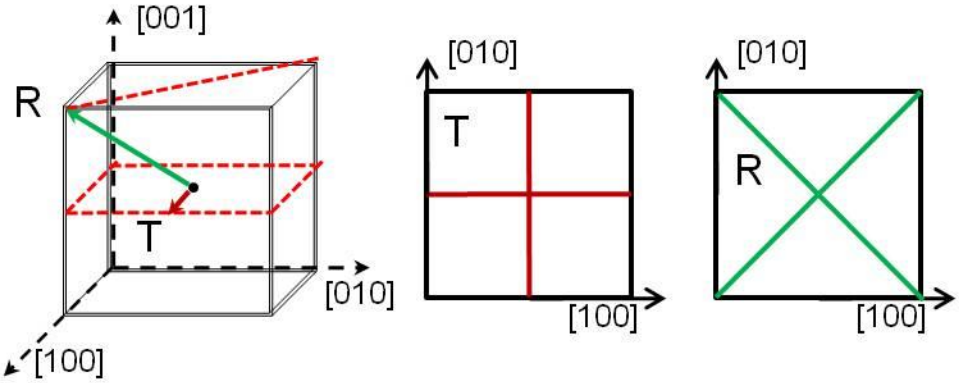

Figure 2.10 Extinction directions and angles with respect to as-grown crystal edges of the tetragonal and rhombohedral perovskite single crystals when observed in (001) platelets.

In addition to extinction angles, domain patterns can be observed through PLM due to the different deformation and polarization directions permitted by the polar symmetry (lower than the cubic prototype symmetry). Domains form in order to reduce both the elastic and electrostatic energy of the system and are regions of congruent polarization in the crystal that are separated by domain walls. Domain walls enhance internal electric fields and make a significant contribution to the extrinsic piezo-/ferroelectric properties of the material. High domain wall density is desirable to enhance the piezoelectric and ferroelectric properties [37].

Crystals of rhombohedral symmetry can develop 180°, 71° and 109° domain walls. Due to their small sized domains, ferroelectric crystals generally exhibit fine patterns when observed under PLM, because of the existence of a large number of overlapping, lamellar domains. Tetragonal domain patterns are of a larger size and are

more easily visualized with PLM. The two ways tetrahedral domain walls form is shown in Figure 2.11. For the formation of 180° domain walls, neighboring polarizations exist antiparallel to each other, whereas 90° domain walls form due to polarizations that develop perpendicular to each other. Both 180° and 90° domain walls form to reduce the effect of electrostatic energy due to surface charge and depoling fields. In addition, 90° domain walls serve to reduce mechanical stresses through the reduction of elastic energy, making them both ferroelectric and ferroelastic domains [4], [16].

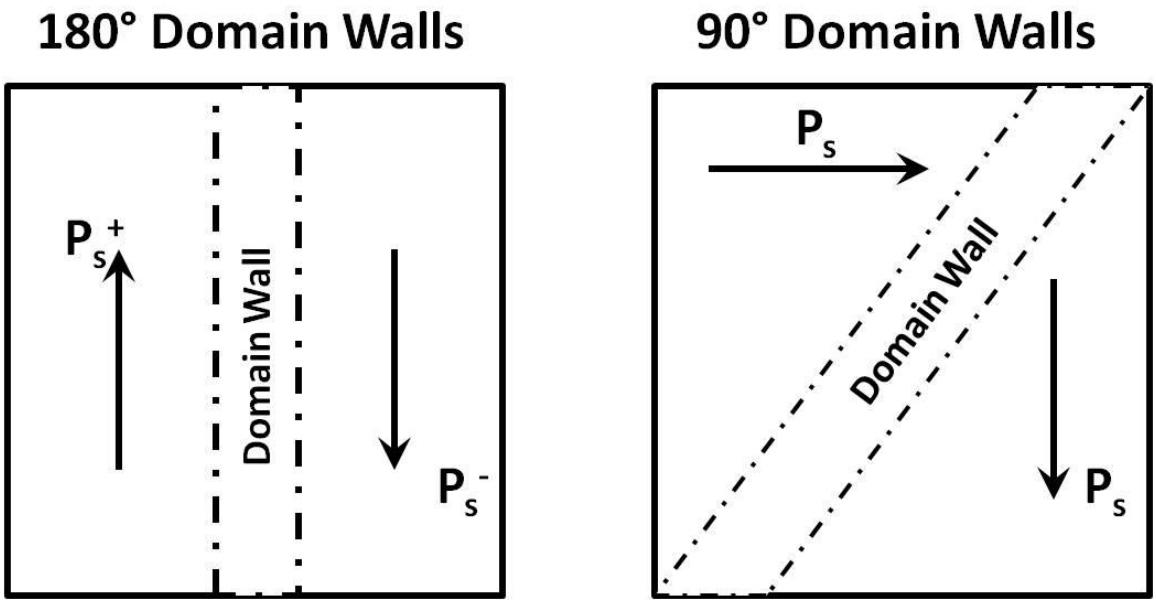

Figure 2.11 Illustration of 180 ° domain walls in which polarizations form antiparallel to each other to reduce electrostatic interactions energy and 90° domain walls that arise to reduce both electrostatic and mechanical interactions for tetragonal ferroelectric crystals.

2.4 Dielectric Property Measurements

Impedance spectroscopy is used to characterize the dielectric permittivity of a material. Dielectric permittivity is a measure of the polarizability of a material and its ability to hold charge (i.e. to store energy). There are several contributions to the polarization of a material under an applied electric field: 1) electronic contributions occur as the electron cloud surrounding an atom shifts to align with an applied field; 2) ionic contributions occur when ions shift their relative atomic position in response to an electric field; 3) orientational contributions are possible when a molecule has the ability

to rotate to align with an applied field and 4) any mobile charge carriers present can migrate to give space charge polarization [18].

The measurement of dielectric permittivity is performed by comparing the dipolar displacement of the sample material to that of permittivity in a vacuum. The dipolar displacement, D, in a vacuum is described by the following equation:

$$D = \varepsilon_0 E \tag{2.9}$$

where ε_0 is the permittivity of free space and E is the applied electric field. When a sample is placed in the cell, the polarization of the material, P, is induced with:

$$D = \varepsilon_0 E + P \tag{2.10}$$

$$D = \varepsilon_0 E + \chi \varepsilon_0 E \tag{2.11}$$

where χ is the dielectric susceptibility of the material. The susceptibility and the permittivity of free space can be combined to simplify the equation and give a single value for dielectric permittivity:

$$D_i = \varepsilon_{ij} E_j \tag{2.12}$$

To determine the real part of permittivity (dielectric constant), ε', the following equation is used:

$$C = \varepsilon' \varepsilon_0 \left(\frac{A}{d}\right) \tag{2.13}$$

where the capacitance, C, is measured of a dielectric sample that is between two electrodes of an area, A, and a thickness, d. The permittivity of free space is represented by ε_0.

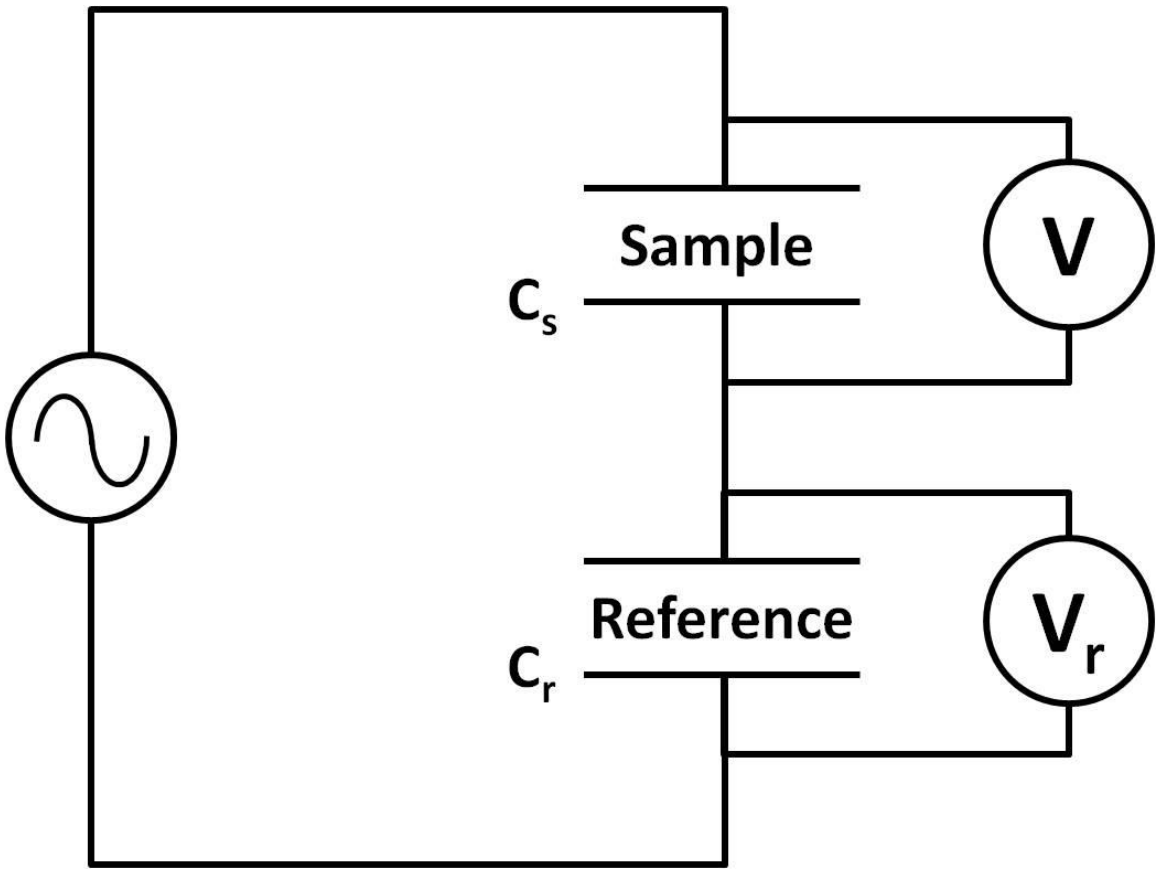

Figure 2.12 Simplified circuit schematic of the experimental set up to perform dielectric spectroscopic measurements, where C_r is the capacitance of a reference material, V_r is the voltage applied to the reference, C_s is the capacitance of the sample and V is the voltage applied to the sample.

Figure 2.12 shows a simplified circuit for measuring dielectric permittivity. In this set up, the capacitance of a sample, C_s, with electrodes of an area, A, and a thickness, d, is connected in series with the capacitance of a reference, C_r. By applying a voltage to the capacitors in series the charge on the reference, Q_r, is the same as the charge on the sample, Q_s (i.e. $Q_r = Q_s$). The charge on the sample is given by:

$$Q_r = Q_s = C_r V_r \tag{2.14}$$

The voltage is measured across the sample, allowing for the determination of capacitance by rearranging Equation 2.14:

$$C_s = \frac{Q}{V_s} = \frac{C_r V_r}{V_s} \tag{2.15}$$

The capacitance is then used to determine the dielectric constant by Equation 2.13 [38].

When taking these measurements in an AC field, the charge density of the material of a capacitance, C_s, will also have to respond to the frequency, ω, of that field:

$$Q = C_s V_0 \sin(\varpi t) \tag{2.16}$$

In order to obtain the frequency dependence of current, I, with respect to time, we must take the derivative of Equation 2.16 with respect to time:

$$I = \varpi C_s V_0 \cos(\varpi t) \tag{2.17}$$

$$I = \varpi C_s V_0 \sin(90 - \varpi t) \tag{2.18}$$

In an ideal capacitor, the generated current will lead the voltage by a 90° phase shift. However, real materials cannot always respond to the field when the frequency being applied is alternating at a rate faster than the polarization of a material can respond, resulting in dielectric relaxation. Different types of polarization will experience this at different frequencies: the dipolar response cannot follow the AC field at frequencies beyond the microwave region near 10^{10} Hz; the ionic polarization loses AC field response in the infrared region near 10^{13} Hz; and the electronic polarization loses AC field response in the UV region near 10^{15} Hz [18].

Dielectric loss can result from either leakage current or dielectric relaxation and must be accounted for. The full expression for permittivity, ε*, is a complex number with a real part, ε', and an imaginary part, ε'', that is expressed as a function of frequency:

$$\varepsilon^*(\varpi) = \varepsilon'(\varpi) - i\varepsilon''(\varpi) \tag{2.19}$$

The real part of permittivity, ε', is what is referred to as the dielectric constant, and the imaginary part, ε'', contains the in-phase contributions. The dielectric loss tangent, tanδ, is a description of the angle between the real and imaginary parts, i.e. the angle at which the current leads the applied field [4]:

$$tan\delta = \frac{\varepsilon''}{\varepsilon'} \tag{2.20}$$

In this work, dielectric constants, ε', and dielectric loss tangents, tanδ, are measured and reported as a function of temperature at various frequencies for the materials synthesized. To perform Vogel-Fulcher fitting analysis, 35 frequencies are

measured between 10^1 – 10^6 Hz. The T_{max} of each frequency is extracted from the curves and then fit to equation 1.15.

2.5 Ferroelectric Property Measurements

The measurement of ferroelectric properties is performed by recording the variation of polarization as a function of a bipolar electric field. In this work, the measurement is performed using an RT66A Standard Ferroelectric Testing System (Radiant Technologies). The polarization of a material is defined as:

$$P = \frac{Q}{A} \tag{2.21}$$

where Q is the charge developed and A is the surface area of the electrodes. In order to perform this measurement, a modified Sawyer-Tower circuit is used, shown schematically in Figure 2.13. In this measurement, the step voltage, V, is applied to the sample of an unknown capacitance, C_s, a known thickness, d, and a known area, A. where the field applied, E, is defined by:

$$E = \frac{V - V_r}{d} \tag{2.22}$$

The sample is connected in series to a parallel resistor – capacitance circuit where the reference voltage, V_r, and capacitance, C_r, are used to determine the charge on the reference *via* $Q = C_rV_r$ and hence the charge on the sample, owing to the capacitors being connected in series. Polarization can then be determined from the known charge, Q, using Equation 2.21 [11], [39], [40].

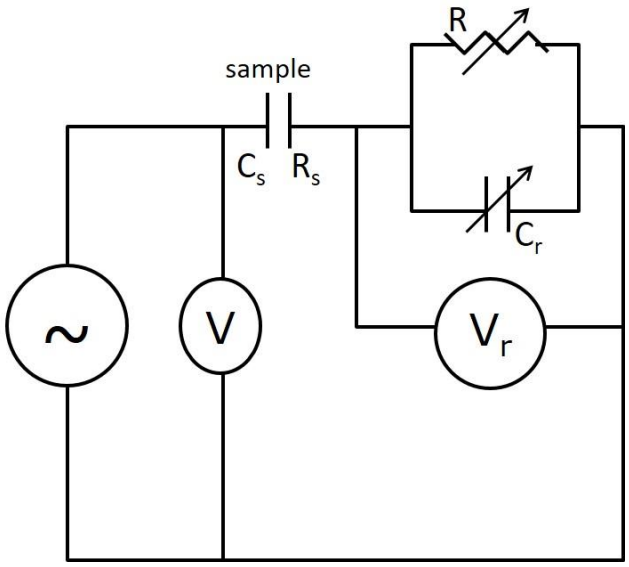

Figure 2.13 A modified Sawyer-Tower circuit utilized for measuing polarization (P) as a function of bipolar electric field (E), where C_r is the capacitance of a reference, R_s is the resistance of the sample, R is the resistor, V is the step voltage applied and V_r is the voltage across C_r.

2.6 Piezoelectric Property Measurements

In this work, piezoelectric coefficients, d_{33}, are measured directly by a quasi-static method using a Piezo-d_{33}/d_{31} Meter (ZJ-6B). First the sample must be poled by applying a poling field three times that of the coercive field, E_C. The piezoelectric coefficient is a measure of the material's ability to couple electrical and mechanical energy and, when considering the direct piezoelectric effect, it is defined by the relationship between charge density, D_3 (C/m^2), and mechanical stress applied, σ_3 (N/m^2) in the following way:

$$d_{33} = \left(\frac{D_3}{\sigma_3}\right) \tag{2.23}$$

$$d_{33} = \left(\frac{Q/A}{F/A}\right) = \frac{Q}{F} = \frac{C*V}{F} \tag{2.24}$$

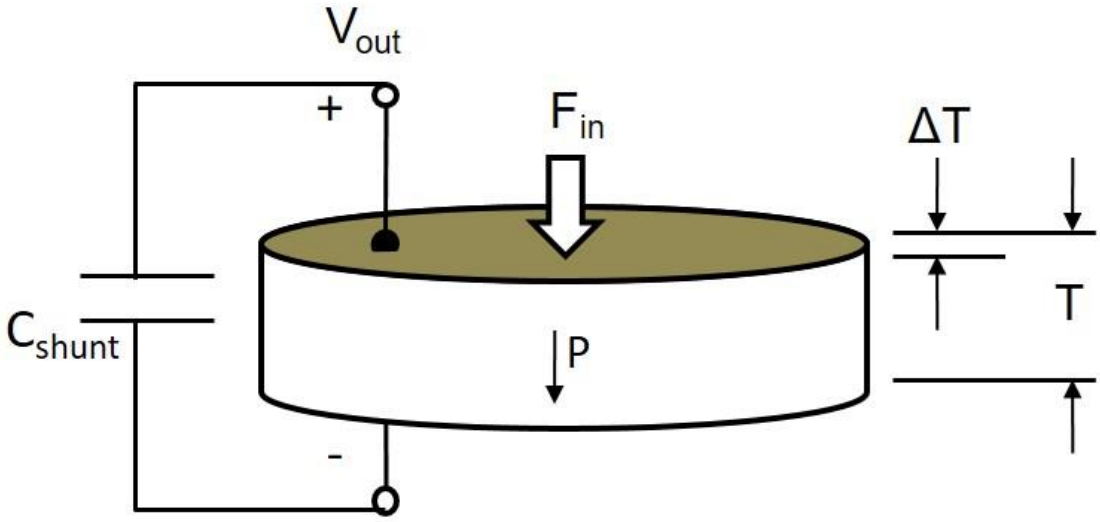

Figure 2.14 Schematic of the Berlincourt method of determining piezoelectric coefficient, d_{33} where F_{in} is the force applied, ΔT is the change in thickness and V_{out} is the resulting voltage.

A schematic representation of the measurement set up is provided in Figure 2.14. In this method, a force, F_{in}, is applied to an area, A, by probes (electrodes) on both sides of the sample. Due to the change in the dipole vector, charge, Q, is accumulated on the surface of the sample. The piezometer measures the potential difference, V_{out}, across the shunt capacitor, C_{shunt}, and uses that to calculate the d_{33} value in pC/N [1]. The d_{33} values that are reported are an average of several measurements and the error values are the standard deviation from that average.

Chapter 3. Synthesis and Characterization of the New Binary $PbTiO_3$ - $La(Zn_{1/2}Ti_{1/2})O_3$ Solid Solution System – A Giant Dielectric Constant Material for Energy Storage

3.1 Abstract

The new solid solution system of $(1-x)La(Zn_{1/2}Ti_{1/2})O_3$-$xPbTiO_3$ (LZT-PT) was successfully synthesized with complete solubility throughout the series. At low concentrations of LZT x = 0.00 – 0.30, the material is in a tetragonal phase with diffuse ferroelectric phase transitions that lower in Curie temperature, T_C from T_C = 490 °C at x = 0.00 to nearly room temperature, T_C = 39 °C at x = 0.30, effectively "softening" the ferroelectric properties by chemical substitution. As the concentration of LZT increases to x = 0.40 – 0.70, the material transforms to a non-ferroelectric pseudo-cubic phase and at high concentrations of LZT, x = 0.80 – 1.00, the material is in a monoclinic $P2_1/n$ phase. Most interesting about this binary system is that at mole fractions of x = 0.30 – 0.40, the material shows giant dielectric constants on the order of $\varepsilon' > 10^6$, making these compositions promising for high energy density storage and MEMS applications.

3.2 Introduction

Since their discovery in the 1950s, $PbTiO_3$-based ferroelectric materials have been of great interest due to their high Curie temperatures, (T_C), and good piezoelectric and ferroelectric properties attributed to the presence of a stereochemically active $6s^2$ lone electron pair that cause high tetragonal distortion in the unit cell. $PbTiO_3$ (PT) has a T_C = 490 °C and yet, PT is limited in its applications due to the difficulty in obtaining dense ceramic materials and its high leakage current [1], [10]. As a result, PT is often stabilized in solid solution with another component, for example the solid solution $PbTiO_3$-$PbZrO_3$ (PZT) is a widely studied piezo-ferroelectric material with a morphotropic phase boundary (MPB) [20]. This ferro-/antiferroelectric binary solid solution system whereby the substitution of the B-site cation yields dense ceramics, shows high electromechanical coupling with compositions near MPB. While this material was much easier to produce than PT, for many years its synthesis was proprietary and the material itself suffers from property degradation under high field applications. In addition, the

presence of Pb^{2+} in PZT has raised concerns due to lead toxicity. Therefore, it is necessary to reduce the lead content in commercially available piezo-/ferroelectric materials.

In addition to seeking materials of high ferroelectric performance, there is also a considerable drive to discover materials with a very high dielectric constant that can be used to make giant capacitors for high-density energy storage applications, and for use in miniaturization of capacitors for micro-electronic mechanical systems (MEMS). These materials require a high dielectric constant ($\varepsilon' > 10^3$) that is frequency independent in a wide temperature range, low dielectric loss tangent ($\tan\delta < 0.1$), and good thermal stability [41]. So far, these capacitors are mainly made of the following types of materials: $CaCu_3Ti_4O_{12}$ (CCTO), doped NiO-compounds, e.g. A_xSr_yNiO (A = La, Nd, Sm) and (In + Nb) co-doped rutile TiO_2, e.g. $Ti_{0.9}In_{0.05}Nb_{0.05}O_2$. All of these materials have dielectric constants of 10^4 - 10^6 with goof temperature stability (between temperatures of 0 to 200 °C) and applied field (over frequencies on the order of MHz to GHz), but they suffer from high dielectric loss tangents [41]. Ferroelectric materials, by their polar nature, are among the top choice for high capacitance applications. However, long-range polar order, such as that in PZT, prevents their internal dipoles from switching easily, making it difficult to achieve higher dielectric constants. Relaxor ferroelectrics, on the other hand, could exhibit high dielectric constants due to the presence of polar nanoregions which are formed as a result of chemical order/disorder arising from aliovalent cations on the B-site of the complex perovskite, such as $Pb(Mg_{1/3}Nb_{2/3})O_3$ (PMN) [13]. Inspired by this phenomenon, we propose here an original concept to develop new materials with high dielectric constants based on $PbTiO_3$ (PT). Our approach is to prepare a solid solution of PT with a non-ferroelectric compound, namely $La(Zn_{1/2}Ti_{1/2})O_3$.

La-based, hexagonal perovskites, such as $La_{1.2}Sr_{2.7}IrO_{7.33}$ and $La_{1.2}Sr_{2.7}RuO_{7.33}$, have been reported to display gigantic dielectric coefficients $\varepsilon' > 10^5$, though dielectric loss is a significant impediment to their commercial use [42], [43]. In addition, lanthanum has been effectively utilized in the past as a substitution for lead and was found to be useful for electrooptic materials. Previous work has shown that $Pb_{(1-x)}La_xTiO_3$ with mole fractions of lanthanum from x = 0.0 – 0.30 can be synthesized in solid solutions with normal, ferroelectric phase transitions that soften the material as evidenced by a decrease in Curie temperature as x increases [44]. However, since La^{3+} is heterovalent

to Pb^{2+}, this substitution leads to A-site vacancies to keep the overall solid solution system charge neutral. This, in turn, leads to oxygen octahedral tilting and compositional inhomogeneity yielding diffuse ferroelectric phase transitions at high concentrations of La^{3+} [44], [45]. $La(Zn_{1/2}Ti_{1/2})O_3$ (LZT) is a centrosymmetric dielectric perovskite of monoclinic $P2_1/n$ symmetry that is of interest for microwave resonance applications due to its high dielectric constant and low dielectric losses [46].

It is expected that by forming the solid solution of $(1\text{-}x)PbTiO_3\text{-}xLa(Zn_{1/2}Ti_{1/2})O_3$ (PT-LZT), we will be able to break down the long-range ferroelectric order of PT to make it more polarly active and to reduce its Curie temperature, T_C, so as to bring its dielectric peak to room temperature, and to maintain the stoichiometry by the coupled substitution on both the A-site and B-site: La^{3+} for Pb^{2+} and $(Zn_{1/2}Ti_{1/2})^{3+}$ for Ti^{4+}. The resulting chemical and structural effects would lead to a new material system that could exhibit giant dielectric constants. Therefore, in this work, the new solid solution system of $(1\text{-}x)PbTiO_3 - xLa(Zn_{1/2}Ti_{1/2})O_3$ will be synthesized by solid state reaction and ceramic sintering process and investigated in terms of the binary system's solubility limits, phase symmetry, ferroelectric and dielectric properties in order to characterize the material's suitability for both ferroelectric and giant dielectric capacitor applications.

3.3 Experimental

3.3.1 Solid Solution Synthesis

The solid solution of the pseudo-binary system $(1\text{-}x)\ PbTiO_3 - xLa(Zn_{1/2}Ti_{1/2})O_3$ (PT-LZT) was synthesized in the form of ceramics by solid state reaction and sintering process, with x = 0.0 to 1.0 in increments of 0.05 - 0.1 mole fraction. Stoichiometric amounts of the constituent metal oxides (PbO, heat treated La_2O_3, ZnO, 99.9%, Aldrich; and TiO_2, 99.5%, Alfa Aesar) were hand milled (1 hr, in the presence of acetone) and the resulting powder was dried, pressed into pellets and calcined in a muffle furnace (ramp = 300 °C/hr to 900 °C, dwell = 4hr) to form the solid solution of PT-LZT. The pellets were crushed and reground by hand (1 hr, in the presence of acetone) to yield a fine powder that was then pressed into discs of 10 mm diameter and sintered (ramp = 300 °C/hr to 1100 °C, dwell = 4 hr) to yield dense ceramics for structural and dielectric characterization.

3.3.2 Structural Analysis

The crystal structure of the as-sintered ceramics is examined at room temperature by X-ray diffraction (Rigaku Diffractometer, 46 mA, 42 kV, 2θ = 10 ° - 80 °, Ω = 200 °, Φ = 270 °, χ = 45 ° and Bruker D8 Advance Diffractometer, 40 mA, 40 kV, step size = 0.02 °/step, 2θ = 10 ° - 80 °). The resulting patterns were analyzed using JADE XRD pattern processing software to determine the symmetry and TOPAS Academic software to refine the lattice parameters and atomic positions.

3.3.3 Dielectric Characterization

To perform electrical characterization, the sintered ceramics were polished with a series of silicon carbide sand papers (220, 400, and 600 grit) successively to achieve parallel, flat surfaces on the circular faces of the ceramics, with various thicknesses (1000 – 200 μm). The polished ceramics were then sputtered with gold layers (Anatech Hummer Sputter-Coater 6.2, 12 min., 15 mA plasma discharge current) and gold wires were attached to both surfaces of the samples using colloidal silver paste. The dielectric properties (permittivity, ε', and loss tangent, tanδ) were measured as a function of temperature (in the low temperature range from -50 ºC to 350 ºC) at frequencies varying from 1 to 10^6 Hz using a Novacontrol Alpha high-resolution broadband dielectric analyzer. The measurements were performed under zero-field-cooling (ZFC) conditions.

3.4 Results and Discussion

3.4.1 Structural Analysis

The powder XRD patterns of the (1-x) $PbTiO_3 - xLa(Zn_{1/2}Ti_{1/2})O_3$ solid solution are shown in Figure 3.1- Figure 3.3 with the compounds of the LZT mole fraction of x = 0.10 – 0.30 (Figure 3.1), x = 0.40 - 0.60 (Figure 3.2) and x = 0.70 – 0.90 (Figure 3.3), respectively. At low concentrations of LZT, x = 0.05 – 0.10, the XRD patterns show discernable tetragonal symmetry with P4mm space group, as evidenced by splitting of the {001}, {110} and {002} sets of peaks, and a lack of splitting at the {111} peaks (Figure 3.1). The presence of tetragonal distortion suggests that the ferroelectric property of PT is preserved. As the concentration of LZT increases to x = 0.20 – 0.30, the {001}, {110} and {002} sets of peaks begin to merge and superimpose with each

other, suggesting that the tetragonal distortion has been significantly reduced. Nevertheless, some visible shoulders and the asymmetry of the peaks indicate some degree of tetragonal distortion still exists in the crystal lattice. As the mole fraction of LZT increases to x = 0.40 – 0.60, the solid solution remains in pure perovskite phase, but the structure has transitioned from the tetragonal symmetry to a pseudo-cubic one, as evidenced by the merging and sharpening of the (001)/(100), (110)/(010) and (002)/(200) peaks with no discernable splitting of the (111) peak (Figure 3.2).

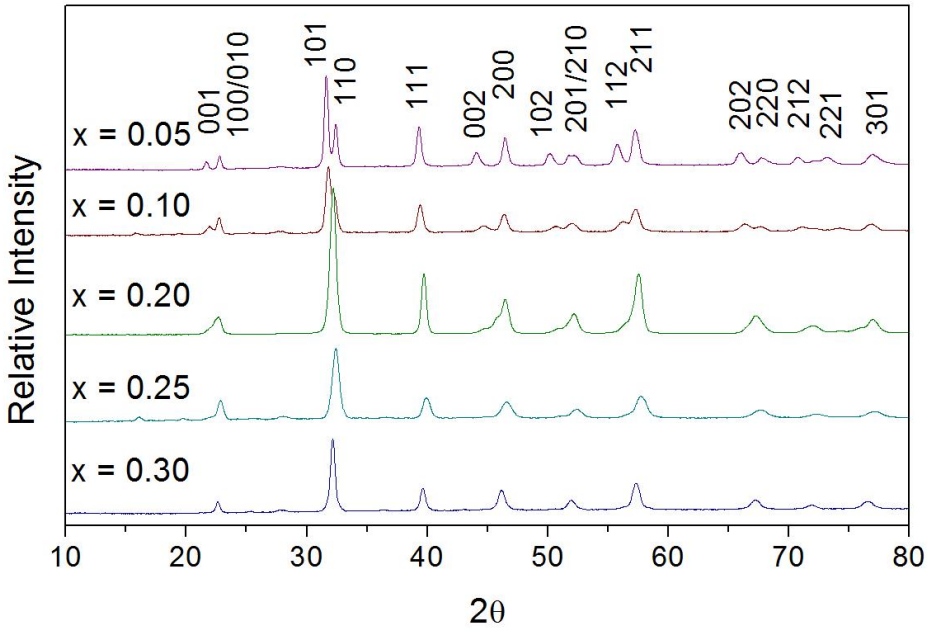

Figure 3.1 Indexed powder XRD patterns for the (1-x)$PbTiO_3$ - x$La(Zn_{1/2}Ti_{1/2})O_3$ solid solution system with the mole fraction of LZT x = 0.05 - 0.30.

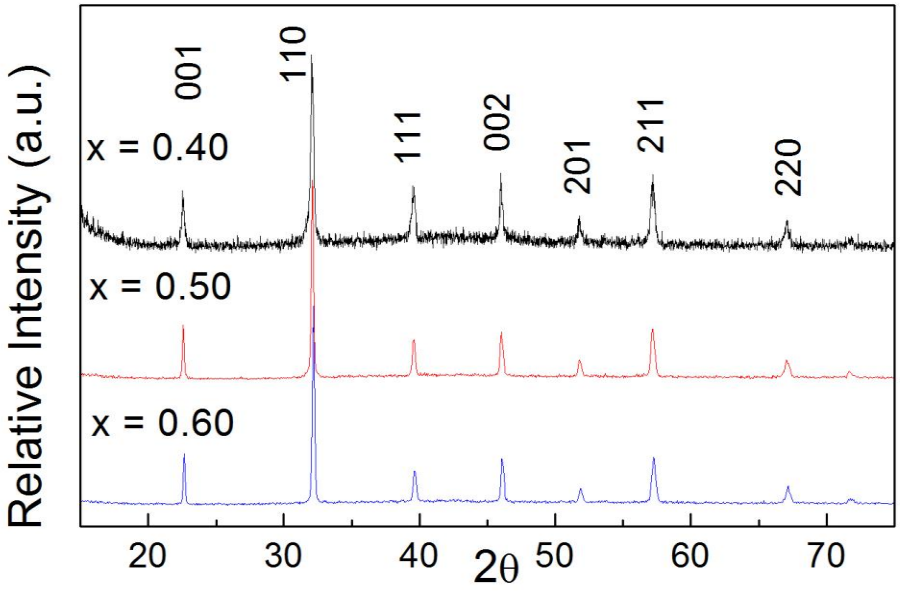

Figure 3.2 Indexed powder XRD patterns for the (1-x)$PbTiO_3$ - x$La(Zn_{1/2}Ti_{1/2})O_3$ solid solution system with the mole fraction of LZT x = 0.40 - 0.60.

At higher concentrations of LZT, x = 0.70 – 0.90, a weak superlattice peak appears at 2θ = 25.2 (Figure 3.3). The appearance of this peak indicates a change in symmetry from pseudo-cubic to monoclinic with the space group $P2_1/n$, which originates from the structure of pure $La(Zn_{1/2}Ti_{1/2})O_3$ [46].

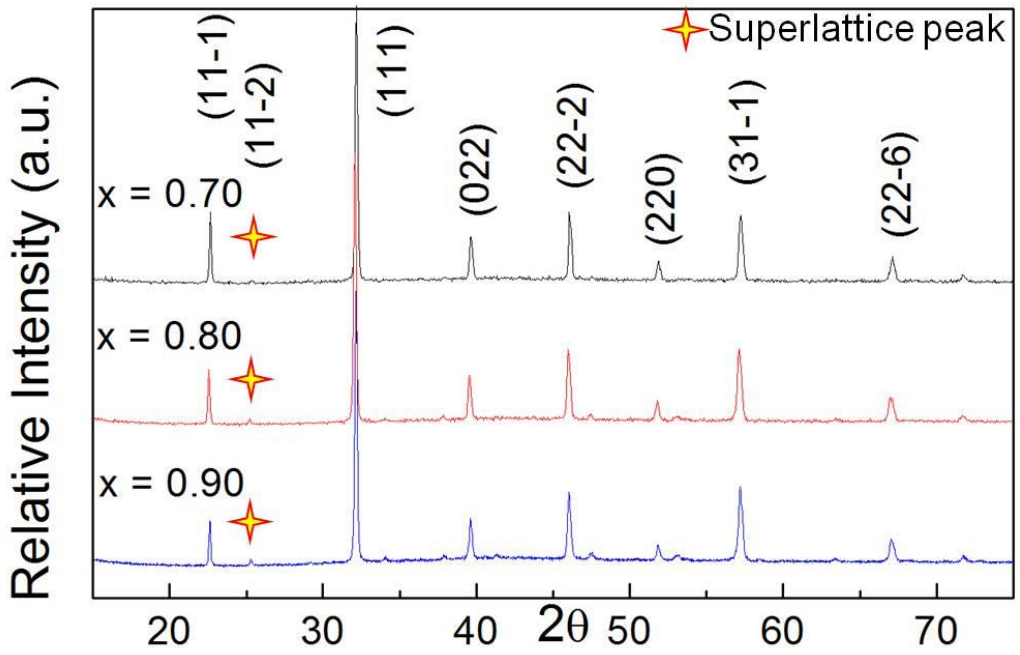

Figure 3.3 Indexed powder XRD patterns for the (1-x)$PbTiO_3$ - x$La(Zn_{1/2}Ti_{1/2})O_3$ solid solution system with the mole fraction of LZT x = 0.70 - 0.90.

Lattice parameters are calculated from the above XRD patterns and ploted in Figure 3.4 as a function of the molar concentration of LZT. It can be seen from Figure 3.4 and Table 3.1 that as LZT content increases, the tetragonal distortion, represented by tetragonality, c/a, decreases and enters a pseudo-cubic phase when $x \geq 0.40$, and when $x > 0.70$, it transforms to the monoclinic phase. Therefore, Figure 3.4 also illustrates the binary phase diagram of the new PT-LZT solid solution with respect to symmetry and structure.

Table 3.1 **Lattice Parameters and Bond Angles of (1-x)$PbTiO_3$ - x$La(Zn_{1/2}Ti_{1/2})O_3$ Solid Solution**

x	0.05	0.1	0.2	0.3	0.4	0.5	0.6	0.7	0.8	0.9
Space Group	P4mm	P4mm	P4mm	P4mm	Pm3m	Pm3m	Pm3m	Pm3m	$P2_1/n$	$P2_1/n$
Beta (°)	90	90	90	90	90	90	90	90	90.111	89.82
a (Å)	3.9087	3.9144	3.9273	3.9164	3.9446	3.9472	3.9369	3.9395	7.9122	7.9117
error	0.0003	0.0005	0.0014	0.0004	0.0010	0.0017	0.0007	0.0007	0.0022	0.0005
b (Å)	-	-	-	-	-	-	-	-	5.5947	5.5839
error	-	-	-	-	-	-	-	-	0.0015	0.0005
c (Å)	4.1106	4.0730	4.0162	4.0554	3.9454	3.9458	3.9276	3.9272	5.5835	5.5857
error	0.0005	0.0009	0.0033	0.0007	0.0019	0.0030	0.0014	0.0012	0.0018	0.0092
c/a	1.0516	1.0405	1.0226	1.0354	1.0001	0.9996	0.9976	0.9968	-	-

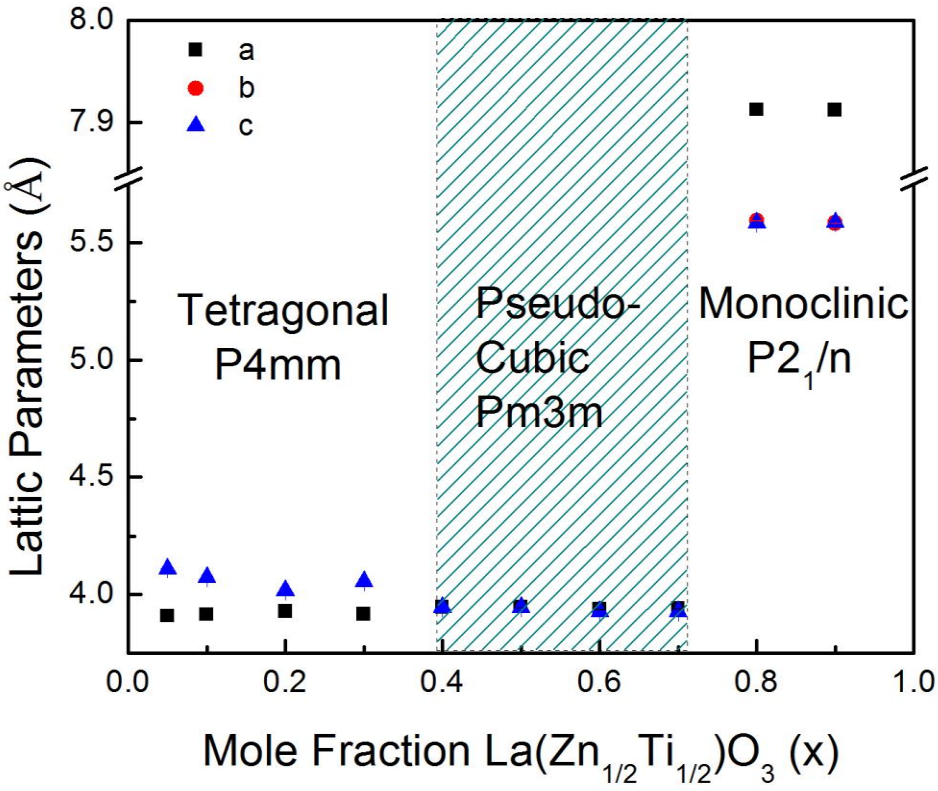

Figure 3.4 **Variation of the lattice parameters of the (1-x)$PbTiO_3$ - x$La(Zn_{1/2}Ti_{1/2})O_3$ solid solution system as a function of mole fraction of LZT, x, showing three phase regions: tetragonal, pseudo-cubic and monoclinic.**

3.4.2 Dielectric Characterization

The dielectric measurements can not only give us the variation of dielectric properties, but also allow us to determine the Curie temperature, T_C. The variations of the real part of dielectric permittivity (dielectric constant), ε', as a function of temperature, measured at frequencies of 10 – 10^5 Hz for (1-x)$PbTiO_3$-x$La(Zn_{1/2}Ti_{1/2})O_3$ with compositions of x = 0.20 – 0.40 are shown in Figure 3.5. The composition of x = 0.20 (Figure 3.5(a)) exhibits a dielectric peak for all measurement frequencies, which indicates the ferroelectric to paraelectric phase transition at T_C = 178 °C. The sample of x = 0.25 (Figure 3.5(b)) shows a dielectric peak at a lower temperature of T_C = 114 °C. It is interesting to note that as the LZT content changes from x = 0.20 to 0.25, not only does T_C decrease, but also the maximum dielectric constant, ε'_{max} decreases while the room temperature dielectric constant at 1 kHz increases slightly from ~ 500 to ~ 800. With the LZT content increased to x = 0.30 (Figure 3.5(c)), the dielectric peak temperature continues to decrease to 39 °C. More interestingly, the maximum dielectric constant increases sharply to over 7.5 x 10^6, giving rise to a giant dielectric constant of $\varepsilon' \cong 7 \times 10^6$ at room-temperature. With further increase of x to 0.40 (Figure 3.5(d)), the dielectric peak temperature seems to decrease to below room temperature with strong dispersion appearing at high temperature, likely due to conduction effects. The temperature of maximum permittivity, T_{max} or T_C, shows no dispersion with frequency, indicating that these peaks are not due to relaxor ferroelectric behaviour but rather normal ferroelectric transitions which become diffuse due to inhomogeneity in the local structure, giving rise to overlapping phase transitions rather than one cooperative transition. This is similar to the behaviour reported for $Pb_{(1-x)}La_xTiO_3$ [44], [45] though the A-site and B-site disorders are more likely the cause of inhomogeneity in PT-LZT rather than the site vacancies in the former. The x = 0.40 compound exhibits a pseudo-cubic structure at room temperature, which is consistent with the XRD analysis where the *a* and *c* lattice parameters approach each other, as shown in Figure 3.4.

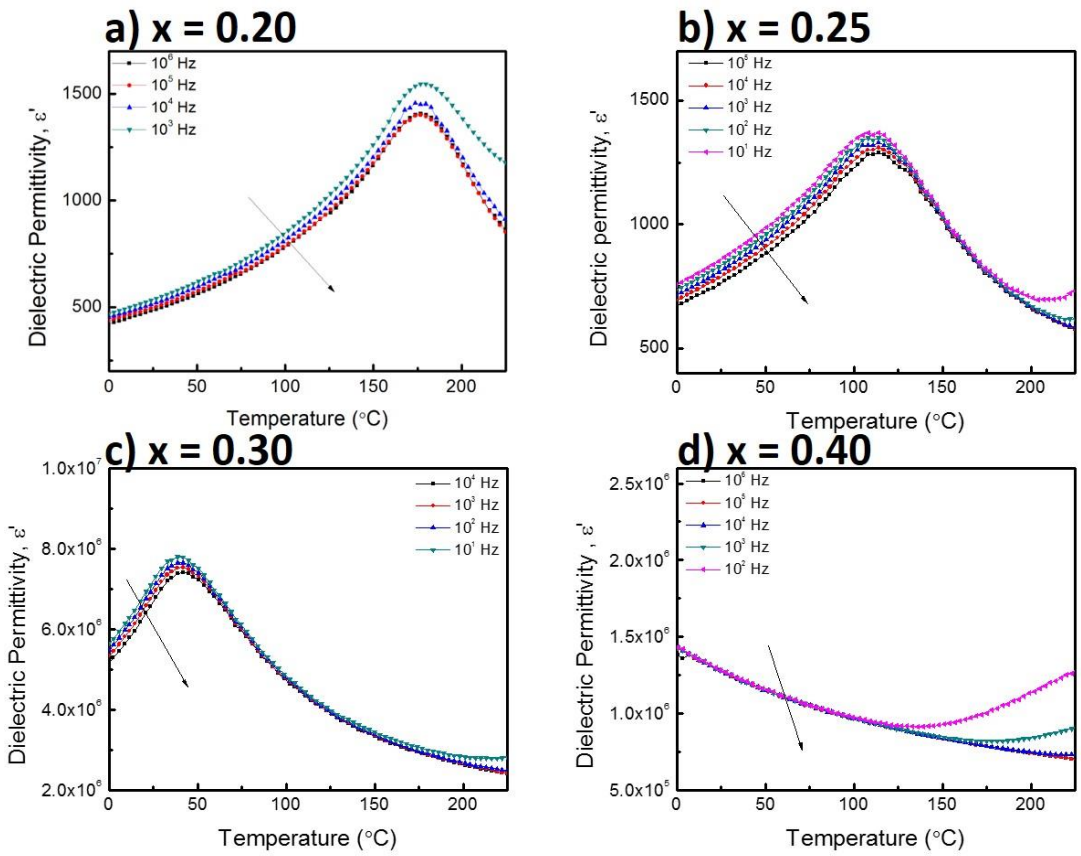

Figure 3.5 Variation of the dielectric permittivity (constant) of (1-x)$PbTiO_3$-x$La(Zn_{1/2}Ti_{1/2})O_3$ as a function of temperature and frequency for the compositions of x = 0.20 (a), 0.25 (b), 0.30 (c) and 0.40 (d).

Based on the dielectric measurements, the variation of the Curie temperature, T_C, is plotted in Figure 3.6 as a function of the mole fractions of LZT for x = 0.0 – 0.30. The end member of pure PT has a T_C = 490 °C [1], and as the concentration of LZT is increased, T_C decreases almost linearly to T_C = 39 °C at x = 0.30. From linear extrapolation, the T_c (or T_{max}) of x = 0.40 can be estimated to be ~ -110 °C. This sharp decrease in T_c by the substitution of LZT for PT, is due to the reduction of tetragonal distortion, and thereby strength of the ferroelectric order, by the A-site substitution of La^{3+} for Pb^{2+} as La^{3+} does not have a stereochemically active $6s^2$ lone pair and plays a role in diminishing the ferroelectric interactions. Therefore, by substitution of LZT for PT, we have achieved the electric "softening" of PT and shifted the dielectric constant peak to close to room temperature with x = 0.30.

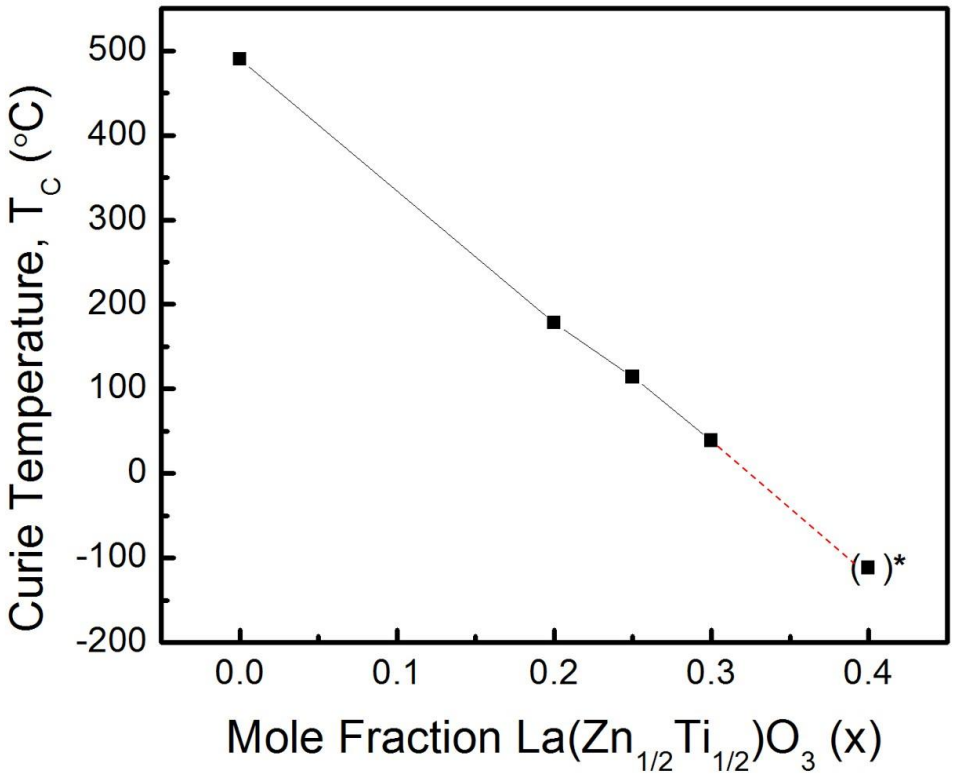

Figure 3.6 **Variation of the Curie temperature, T_C, for the (1-x)$PbTiO_3$ - x$La(Zn_{1/2}Ti_{1/2})O_3$ solid solution as a function of the mole fraction of LZT for x = 0.0 – 0.3, with a speculative value for x = 0.40 (marked with *).**

The room-temperature values of dielectric constant, ε', are shown in Figure 3.7 for (1-x)$PbTiO_3$ - x$La(Zn_{1/2}Ti_{1/2})O_3$ as a function of LZT concentration x = 0.20 – 0.30 with a speculative value included for x = 0.40. It is interesting to note that the dielectric constant undergoes a dramatic jump of almost four orders of magnitude with the LZT content x varying from 0.25 to 0.30. The dielectric constant at room temperature is in the order of ε' ≅ 800 for x = 0.25. It jumps drastically to the order of ε' ≅ 6.5 x 10^6 for x = 0.30, and slightly decreases but still remains in the order of 10^6 when the mole fraction of LZT is increased to x = 0.40. In addition, Figure 3.8 shows the variation of the dielectric loss tangent, tanδ, with the compositions of x = 0.20 – 0.40. For all the compositions studied, tanδ < 0.03 and, more interestingly, it shows a decreasing trend with increasing LZT content. Therefore, we have found that the (1-x)PT-xLZT solid solution ceramics with the composition of 0.30 ≤ x ≤ 0.40 exhibit giant dielectric constant at room temperature, coupled with low dielectric loss. These excellent dielectric properties of ε' >

10^6, three orders of magnitude higher than that of PMN-PT single crystals (ε' = 5400 – 8200 [10]) make these materials promising for making giant dielectric constant capacitors useful for miniaturization of ferroelectric devices, and high energy density storage.

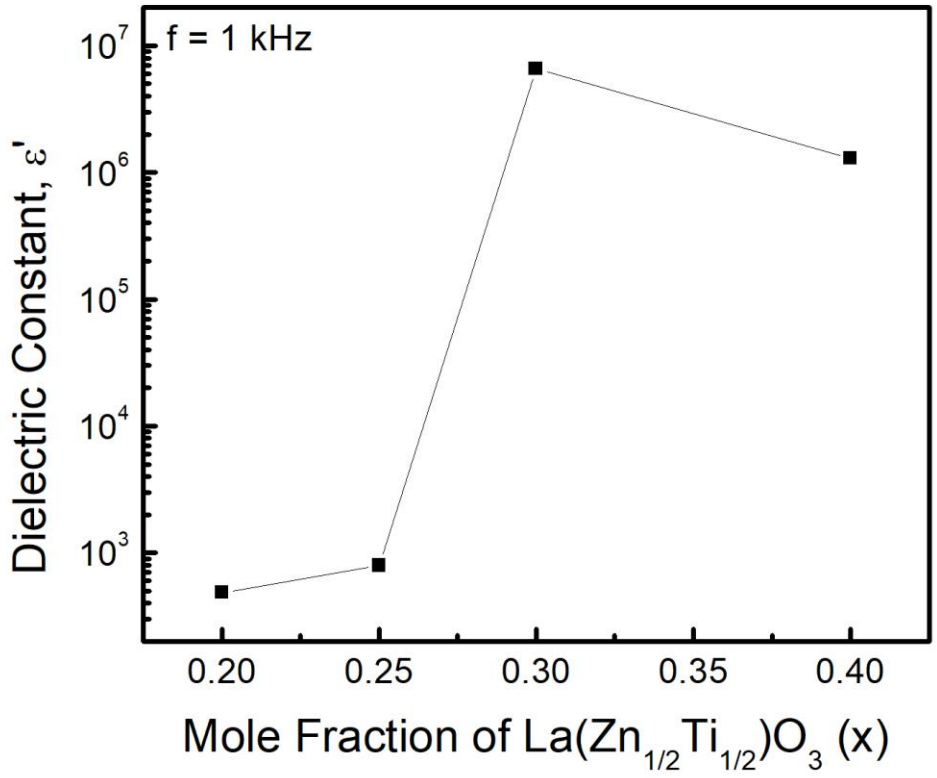

Figure 3.7 Room-temperature dielectric constant, ε', of the (1-x) $PbTiO_3$ - x$La(Zn_{1/2}Ti_{1/2})O_3$ solid solution as a function of mole fraction LZT, x, measured at the frequency f = 1 kHz.

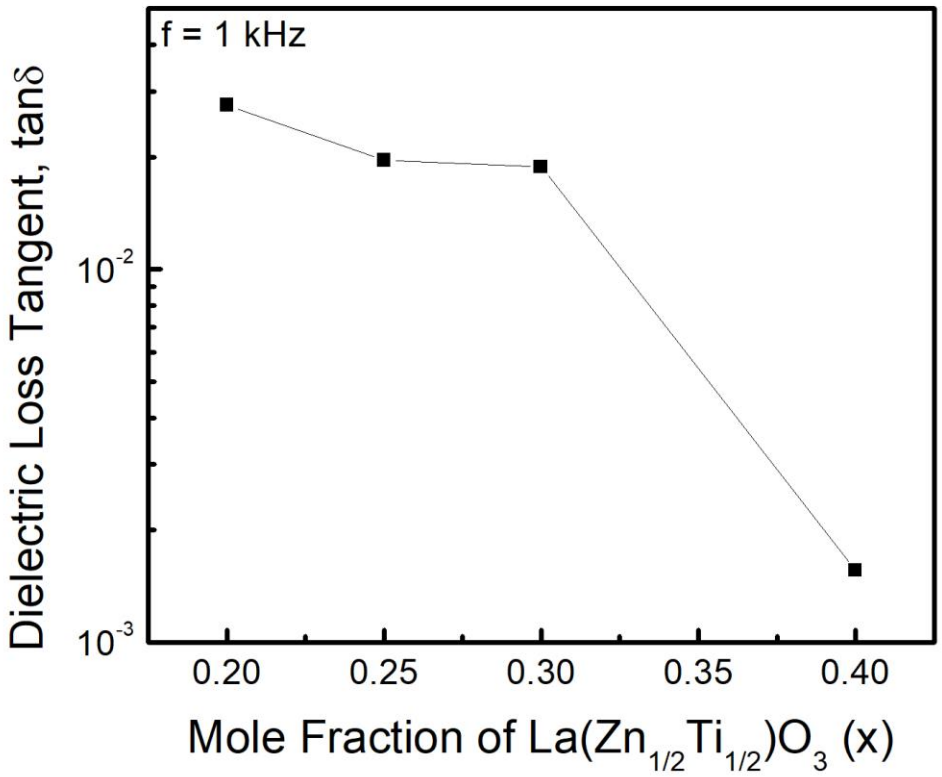

Figure 3.8 Room-temperature dielectric loss tangent, tanδ, of the (1-x) $PbTiO_3$ - x$La(Zn_{1/2}Ti_{1/2})O_3$ solid solutionas a function of mole fraction LZT, x, measured at the frequency f = 1 kHz.

3.4.3 Ferroelectric Properties

The variation of polarization (P) with the application of a bipolar electric field (E) is shown for the composition of 0.20$La(Zn_{1/2}Ti_{1/2})O_3$-0.80$PbTiO_3$ can be seen in Figure 3.9. What can be seen is that there is hysteresis behaviour that is characteristic of ferroelectric materials with a coercive field of E_c = 22 kV/cm and a remanent polarization of P_r = 13 μC/cm^2. This confirms the peaks seen in the dielectric spectra are diffuse ferroelectric phase transitions.

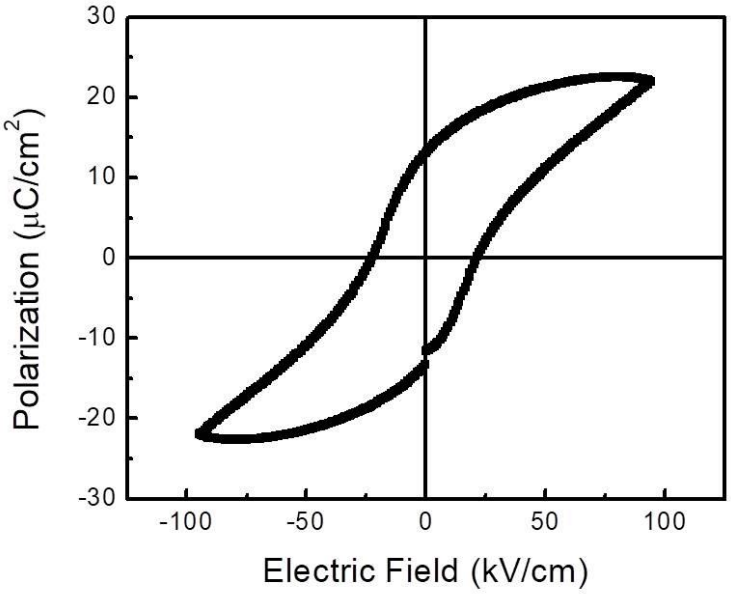

Figure 3.9 Variation of polarization (P) as a function of bipolar electric field (E) for $0.20La(Zn_{1/2}Ti_{1/2})O_3$-$0.80PbTiO_3$ showing characteristic ferroelectric behaviour.

3.5 Conclusions

Through crystal the chemistry concept of solid solution softening to create a high dielectric constant material, the formation of the new binary solid solution of $(1-x)PbTiO_3 – xLa(Zn_{1/2}Ti_{1/2})O_3$ has been synthesized with complete and continued solubility for the concentrations of LZT of x = 0.0 – 1.0. At low concentrations of LZT, x = 0.0 – 0.3, the solid solution is a tetragonal perovskite, which transitions to a pseudo-cubic phase for compositions of $0.40 \leq x \leq 0.70$, and at high concentrations of x = 0.8 - 1.0, the solid solution is of a monoclinic $P2_1/n$ symmetry. A binary phase diagram has been established illustrating these phase regions.

It is found from the dielectric characterization that the Curie temperature, T_C, decreases with the increased concentration of x, demonstrating an actual softening of the ferroelectric order and strength. The dielectric peaks become more diffuse, with T_C approaching room temperature for the composition x = 0.30. Giant dielectric constants are found at room temperature for x = 0.30 - 0.40 with low dielectric loss, forming a new family of giant dielectric constant materials very promising for high-density energy storage and MEMS applications.

Chapter 4. The "Softening" of Piezo-/Ferroelectric Properties in the Binary Ceramic System $Bi(Zn_{1/2}Ti_{1/2})O_3 – PbTiO_3$ via Lanthanum Substitution

4.1 Abstract:

The $0.20Bi(Zn_{1/2}Ti_{1/2})O_3$-$0.80PbTiO_3$ (BZT-PT) solid solution [25] is unique in that it exhibits a higher Curie temperature (T_C) than the bench mark ferroelectric end member, $PbTiO_3$. However, BZT-PT experiences too large a coercive field (E_c), *i.e.* too "hard", for its polarization to switch thereby preventing its potentially promising piezo-/ferroelectric properties to be explored for practical applications. In this work, we have found an unconventional way to "soften" the character of BZT-PT by lanthanum substitution for Bi^{3+}. The new solid solution system of $0.20[xLa(Zn_{1/2}Ti_{1/2})O_3 – (1-x)Bi(Zn_{1/2}Ti_{1/2})O_3] - 0.80PbTiO_3$ (LZT-BZT-PT) ceramics are successfully synthesized with x = 0.0 – 1.0 showing complete solubility for the series. Powder x-ray diffraction of the ceramics reveals a tetragonal, P*4mm* structure that shows decreased tetragonal distortion (c/a) with increasing mole fraction of LZT. The measurement of dielectric permittivity as a function of temperature measured at varying frequency also revealed a decrease in T_C as the fraction of LZT increases. More interestingly, E_C is reduced as the LZT mole fraction increases. At the high bismuth end of the pseudo-binary line, E_C is greater than the dielectric breakdown field at x = 0 – 0.3, whereby saturated P(E) loops are not obtained. As the mole fraction of LZT increases, dipolar switching is realized with the lowered E_C > 70 kV/cm at x = 0.40 to E_C = 22 ± 0.5 kV/cm at x = 1.0. Therefore, this 'softening' of the BZT-PT binary system allows for the display of bipolar states in the polarization vs. electric field hysteresis loops for mole fractions of LZT x ≥ 0.40 making this solid solution series promising materials for future high field applications.

4.2 Introduction:

High performance piezo-/ferroelectrics find their applications in many aspects of our everyday lives from a car's accelerometer to a medical ultrasound transducer. Some of the highest piezo-/ferroelectric response materials consist of lead-based solid solution

systems (i.e. $Pb(Mg_{1/3}Nb_{2/3})O_3$-$PbTiO_3$ [PMN-PT]; $PbZrO_3$-$PbTiO_3$ [PZT]) which are characterized by the existence of a morphotropic phase boundary (MPB) in their respective phase diagrams [47]. This boundary indicates a compositionally induced phase transition, typically from a rhombohedral (R) phase, through a monoclicnic (M) phase and then to a tetragonal (T) phase as the concentration of PT increases [14], [47]. There is evidence of a coexistence of R/M and M/T phases on either side of the MPB line and it has become commonly accepted to include those extended mixed phase areas as a part of the MPB region [47]–[49]. Interestingly, the dielectric and piezoelectric properties of these systems all peak at the near-MPB compositions on the rhombohedral side due, in part, to polarization rotation favoured by the MPB phases [47]–[49]. However, these systems present some inherent drawbacks *e.g.* PMN-PT suffers from a low phase transition temperature ($T_{R-T} \approx 100°C$) where the material undergoes a symmetry change from rhombohedral to tetragonal, losing its polarization state and thereby deteriorating its piezo-/ferroelectric performance [2], [14]. Moreover, its low coercive field (E_c = 2 - 3 kV/cm) limits the suitability of these materials for high-field, bi-stable applications [2], [14]. Increasing the Curie temperature (T_C) and the coercive field (E_C) of PMN-PT material and related materials could potentially broaden the scope of their applications in both the high temperature and high electric field regime. Additionally, lead oxide (PbO) is a large component in most high-performance piezo-/ferroelectric materials and there is a large drive to discover lead-free or lead-reduced materials that have equivalent or better piezo-/ferroelectric performance in order to reduce the amount of lead present in consumer goods, which could be harmful to the environment and health [24].

From a chemistry point of view, a natural replacement for lead is bismuth. Like the Pb^{2+} ion, Bi^{3+} also contains a stereochemically active $6s^2$ lone pair that is expected to contribute to the high tetragonal distortion, and therefore high polarization, of Pb^{2+}-based materials [7], but contrary to lead, bismuth is relatively non-toxic. Bismuth-based perovskite-like compounds such as $BiMO_3$ (M = Al, Ga) were predicted theoretically to exhibit high T_C and high polarization, but require high pressures (≥ 6 GPa) to synthesize due to the smaller size of Bi^{3+} which prefers a lower coordination site [50]. Using the solid solution approach, several $Bi(M,M')O_3$ components have been stabilized in $PbTiO_3$. For example, the $Bi(Zn_{1/2}Ti_{1/2})O_3$-$PbTiO_3$ (BZT-PT) binary system shows a consistent increase in Curie temperature, T_C, with increasing mole fraction of Bi^{3+} [27], [29],

whereas solid solutions containing $Bi(Zn_{1/3}Nb_{2/3})O_3$ (BZN), $BiInO_3$ (BI), $BiScO_3$ (BS), $Bi(Ni_{1/2}Ti_{1/2})O_3$ (BNT) and $Bi(Mg_{1/2}Ti_{1/2})O_3$ (BMT) show an increase in T_C with a small mole fraction of Bi^{3+} [25]. To date piezo-/ferroelectric properties of these Bi-based solid solutions, particularly the BZT-PT system, have not been reported due to a coercive field that is higher than the dielectric breakdown field, rendering them useless for device applications.

In this work, we show that by chemical substitution it is possible to 'soften' the binary system of BZT-PT to display the piezo-/ferroelectric properties locked within while maintaining a high Curie temperature. The chemical substitution is achieved by introducing a third component, $La(Zn_{1/2}Ti_{1/2})O_3$ (LZT), into the binary system. The cationic substitution of lanthanum, La^{3+} for Bi^{3+}, was chosen as it has the same charge and ionic radius (r = 117 Å) as Bi^{3+} but does not contain the $6s^2$ lone pair which is believed to cause the high tetragonal distortion and high coercivity [27]. Starting with the binary solid solution of $0.20Bi(Zn_{1/2}Ti_{1/2})O_3$-$0.80PbTiO_3$, which has been shown to retain high Curie temperatures (T_C = 535 °C) while keeping sintering temperatures low, we have investigated the pseudo-binary solution series of $0.20[xLa(Zn_{1/2}Ti_{1/2})O_3$-$(1-x)Bi(Zn_{1/2}Ti_{1/2})O_3]$-$0.80PbTiO_3$. The substitution of the non-ferroelectrically active La^{3+} cation for Bi^{3+} is expected to reduce the overall tetragonality of the system and the energy potential separating the polar states, so as to "soften" the ferroelectricity, allowing for the resulting piezo-/ferroelectric properties of the system that have not been seen before to be characterized and explored for potential applications as high-temperature and high-field electromechanical transducers.

4.3 Experimental:

4.3.1 Solid Solution Synthesis

The solid solution of the pseudo-binary system $0.20[xLa(Zn_{1/2}Ti_{1/2})O_3 – (1-x)Bi(Zn_{1/2}Ti_{1/2})O_3] - 0.80PbTiO_3$ (LZT-BZT-PT) were synthesized in the form of ceramics by solid state reaction and sintering process. Stoichiometric amounts of the constituent metal oxides (PbO, La_2O_3, ZnO, Bi_2O_3; 99.9%, Aldrich; and TiO_2, 99.5%, Alfa Aesar; with x=0.0 to 1.0 in increments of 0.1 mole fraction) were hand milled (1 hr, in the presence of acetone) and the resulting powder was dried, pressed into pellets and calcined in a muffle furnace (ramp = 300 °C/hr to 900 °C, dwell = 4hr) to form the solid solution of

LZT-BZT-PT. The pellets were crushed and reground by hand (1 hr, in the presence of acetone) to yield a fine powder that was then pressed into discs of 10 mm diameter and sintered (ramp = 300 °C/hr to 1100 °C, dwell = 4 hr) to yield dense ceramics for characterization.

4.3.2 Structural Analysis

The crystal structures of the as-sintered ceramics were examined by X-ray powder diffraction (Rigaku Diffractometer, 46 mA, 42 kV, 2θ = 10 ° - 80 °, Ω = 200 °, Φ = 270 °, χ = 45 °and Bruker D8 Advance Diffractometer, 40 mA, 40 kV, step size = 0.02 °/step, 2θ = 10 ° - 80 °). The resulting patterns were analyzed using JADE XRD pattern processing software to confirm the symmetry and TOPAZ Academic software to refine the lattice parameters and atomic positions.

4.3.3 Dielectric, Piezoelectric and Ferroelectric Measurements

To perform electrical characterization, the sintered ceramics were polished with a series of silicon carbide sand papers (220, 400, and 600 grit successively) to achieve parallel, flat surfaces on the circular faces of the ceramics, with various thicknesses (1000 – 200 μm). The polished ceramics were then sputtered with gold layers (Anatech Hummer Sputter-Coater 6.2, 12 min., 15 mA plasma discharge current) and gold wires were attached to both surfaces of the samples using colloidal silver paste. Ceramics were further painted with colloidal silver paste to cover the electrode surfaces for high temperature measurements to prevent the loss of gold. The dielectric properties (permittivity, ε', and loss, tanδ) were measured as a function of temperature (from -50 ºC to 350 ºC, high temperatures from 30 °C – 700 °C, at intervals of 3 °C) at varying frequencies from 1 to 10^6 Hz using a Novacontrol Alpha high-resolution broadband dielectric analyzer. The measurements were performed under zero-field-cooling (ZFC) conditions. Ferroelectric hysteresis loops were displayed using a Radiant Technologies RT66A testing system, connected to a Trek 609E-6 high voltage bipolar amplifier. The same samples were subsequently poled in silicon oil at an electric field of E = 3(E_C) and at temperatures T = 25 °C, 100 °C, 200 °C (see Section 3.3) using a Stanton PS350 high voltage source, and then their piezoelectric coefficient, d_{33}, was measured using an IACAS Model ZJ-6B d_{33} meter based on the Berlincourt method.

4.4 Results and Discussion

4.4.1 Structural Analysis

The powder XRD patterns for the compounds with x = 0.0 – 1.0 are shown in Figure 4.1. These patterns indicate that a single phase of perovskite structure is obtained for the full pseudo-binary series, indicating the formation of solid solution. As expected, the compound with x = 0.0 is of tetragonal symmetry, as evidenced by the clean splitting of the {001}, {110}, {200}, *etc.* peaks. As the mole fraction of LZT increases, the splitting of the peaks weaken, until the set of peaks (001)/(100), (002)/(200), *etc.* eventually merge together at a composition near the molar fraction of LZT, x = 0.7. At compositions of x > 0.7, the merged {100}, {110}, {200}, etc. peaks are broadened and asymmetric, with shoulders still visibly retaining some degree of tetragonal symmetry though appearing more pseudo-cubic, reflecting the symmetry of the LZT end member of P$2_1/n1$. The lattice parameters were refined based on the tetragonal space group *P*4*mm*.

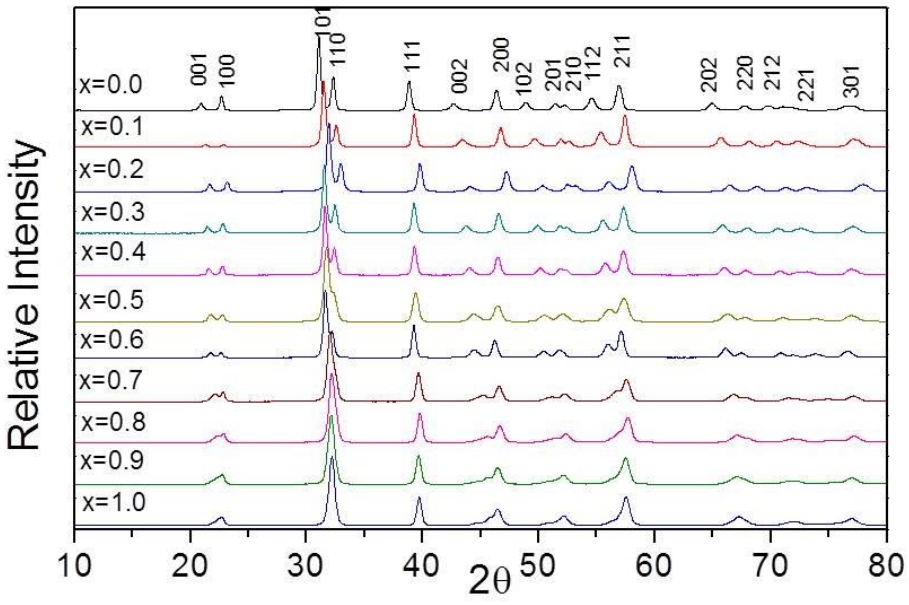

Figure 4.1 Powder XRD patterns of the 0.2[xLa($Zn_{1/2}Ti_{1/2}$)O_3-(1-x)Bi($Zn_{1/2}Ti_{1/2}$)O_3]-0.8$PbTiO_3$ series with x = 0.0 – 1.0.

The variation of the lattice parameters of the system as a function of the molar fraction LZT can be seen in Figure 4.2a. While the *a* parameter does not vary significantly across the series, there is a dramatic decrease in the *c* parameter with increasing molar LZT content. This gives rise to a decrease in the *c/a* values, as shown in Figure 4.2b. The decrease in tetragonality indicates a reduction of the tetragonal distortion of the unit cell by the substitution of LZT.

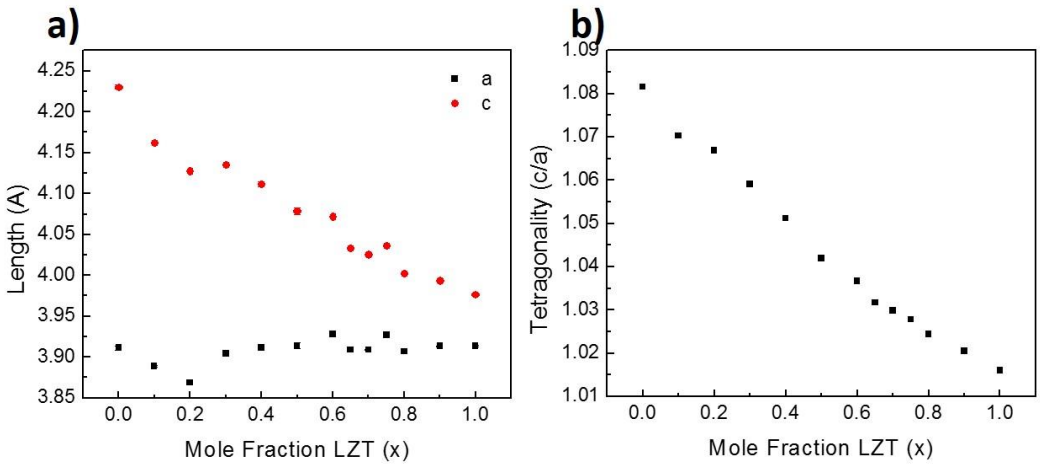

Figure 4.2 Variation of a) the lattice parameters a and c of the tetragonal symmetry as a function of the $La(Zn_{1/2}Ti_{1/2})O_3$ [LZT] concentration for the $0.2[xLa(Zn_{1/2}Ti_{1/2})O_3\text{-}(1\text{-}x)Bi(Zn_{1/2}Ti_{1/2})O_3]\text{-}0.8PbTiO_3$ solid solution and b) the tetragonal distortion (c/a) as a function of the LZT concentration.

To reveal the crystal chemistry origin of the effect, we further examine the local structure and bonding environments based on XRD symmetry analysis. Figure 4.3 shows the average bond length between the A site cation and the two different coordinating oxygen anions O1 and O2 (the two differing oxygen sites are shown in the unit cell pictured in Figure 4.4). The average bond length between A-O2 is consistently longer than that of A-O1, especially for the BZT-PT binary solid solution. This anisotropy in bonding environments of A-O is believed to be the origin of the enhanced tetragonality, high polarization and high T_C. As the mole fraction of LZT increases, the bond lengths A-O1 and A-O2 tend to converge, as shown by a decrease in their difference. This confirms that the stereochemically active $6s^2$ lone pair is responsible for the high tetragonal distortion of the initial binary BZT-PT system and its systematic substitution by La^{3+} reduces that effect, making the structure more isotropic.

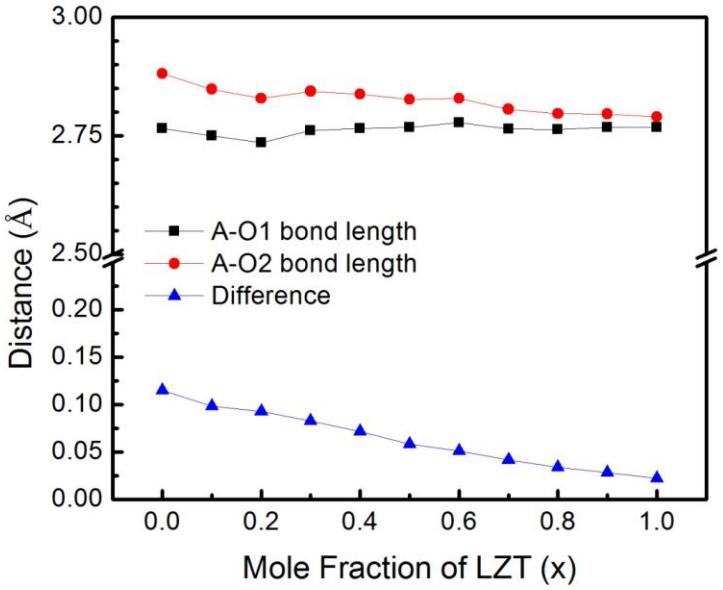

Figure 4.3 **Average bond lengths of A-O1 and A-O2 in the perovskite unit cell of $0.20[xLa(Zn_{1/2}Ti_{1/2})O_3 – (1\text{-}x)Bi(Zn_{1/2}Ti_{1/2})O_3] - 0.80PbTiO_3$ and the difference in these two bond lengths indicating the distortion (anisotropy) in the oxygen coordination environment.**

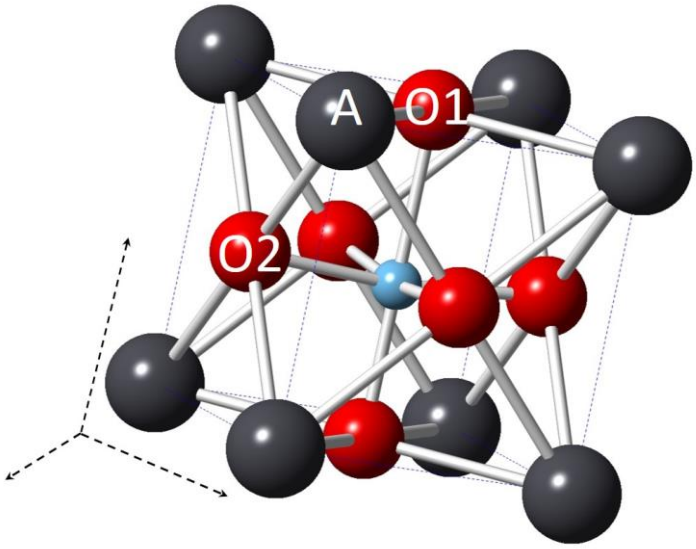

Figure 4.4 **3D view of the perovskite crystal structure showing the anisotropic A-O1 and A-O2 bond lengths. It is this difference in bond length that yeilds high tetragonal distortion, as evidenced by the splitting of the (100)/(001), (101)/(110) and (200)/(002) peaks shown in Figure 4.1.**

4.4.2 Dielectric Properties

The dielectric properties were measured to determine the phase transition behavior and the Curie temperature (T_C). The variations of the dielectric permittivity (ε') and dielectric dissipation factor, tanδ as a function of temperature at the selected frequency of 10^3 Hz are presented in Figure 4.5 for the compositions of x = 0.30, x = 0.60 and x = 1.0. The peaks in dielectric permittivity associated with a minimum in loss tangent indicate a ferroelectric phase transition at T_C. The values of T_C decrease steadily with increasing mole fraction of LZT, as shown in Figure 4.6. This follows the trend shown in Figure 4.2a) and b), indicating that as the influence of the stereochemically active $6s^2$ lone pair on the A-site cation is reduced, the ferroelectric state becomes less stable against thermal effects and it transforms into the non-polar paraelectric phase at lower temperatures [51]. This variation also reveals a phase boundary between the pseudo-cubic, paraelectric phase and the tetragonal, ferroelectric phase.

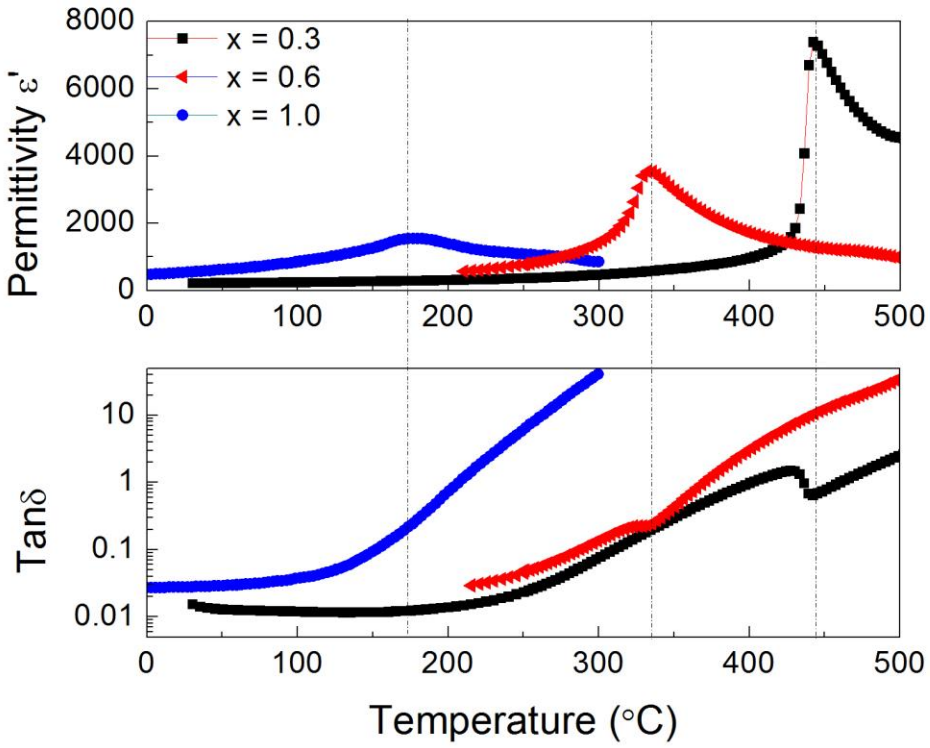

Figure 4.5 **Variation of the real part of dielectric permittivity (ε') and loss tangent (tanδ) as a function of temperature measured at 10^3 Hz of $0.2[xLa(Zn_{1/2}Ti_{1/2})O_3$- $(1-x)Bi(Zn_{1/2}Ti_{1/2})O_3]$-$0.8PbTiO_3$ for the compositions with the LZT (x) concentration of x = 0.3, x = 0.6 and x = 1.0.**

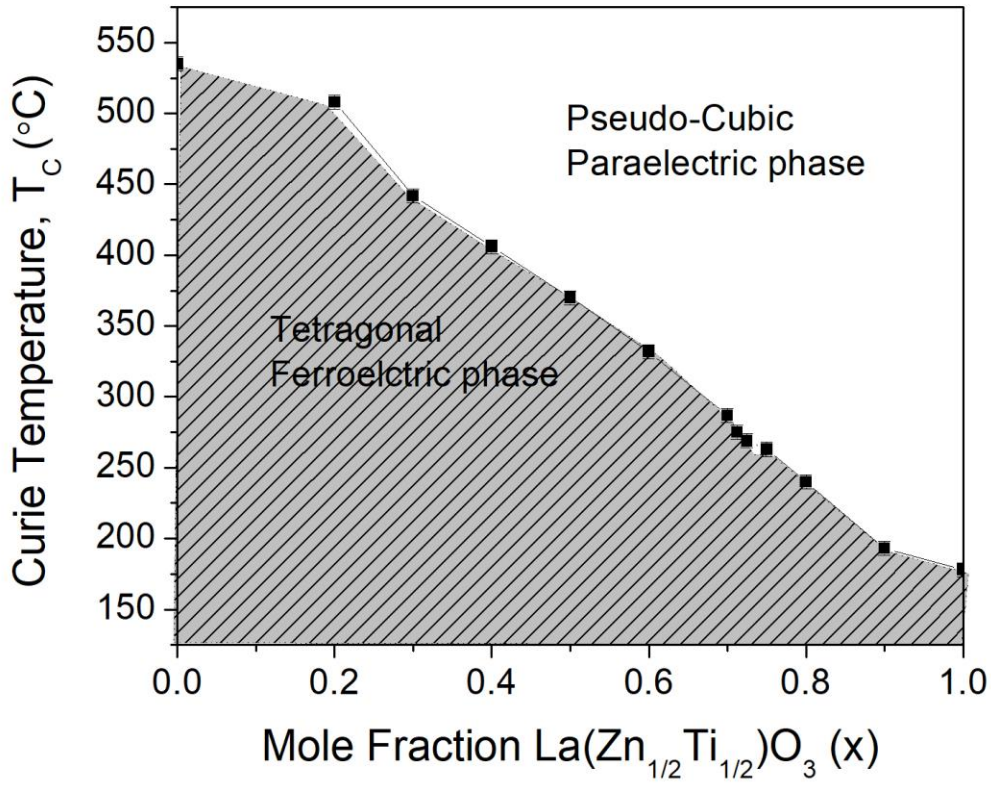

Figure 4.6 Variation of the Curie temperature, T_C, extracted from the dielectric curves for the $0.2[xLa(Zn_{1/2}Ti_{1/2})O_3$- $(1-x)Bi(Zn_{1/2}Ti_{1/2})O_3]$-$0.8PbTiO_3$ solid solution as a function of mole fraction of LZT (x). It also reveals a pseudo-binary phase diagram delimiting the cubic paraelectric and tetragonal ferroelectric phases and their phase boundary.

From the dielectric plots, values of the room temperature permittivity (ε'_{RT}) and the maximum permittivity (ε'_{max}) were extracted and shown in Figure 4.7. It can be seen that ε'_{RT} shows a steady increase with the increasing mole fraction of LZT owing to the increasing closeness of the T_C to room temperature. On the other hand, with the increase in mole fraction LZT, the maximum permittivity of the system decreases, indicating that the reduction of the $6s^2$ lone pair and the decreased anisotropy makes the material less polarizable at the T_C, the ferroelectric phase transition. Another interesting feature is that as the mole fraction of LZT increases, the shape of the dielectric peak becomes broader and more diffuse, suggesting a less cooperative phase transition due to the increased chemical disorder and polar inhomogeneity in the structural lattice [51].

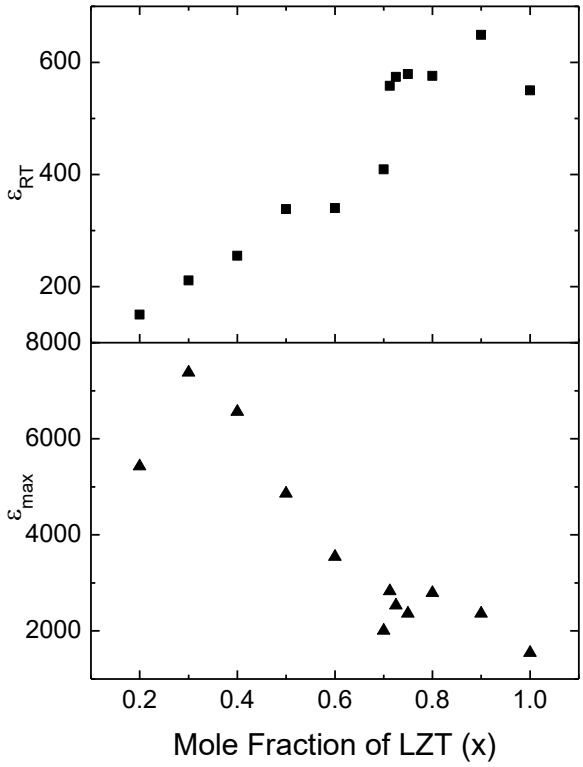

Figure 4.7 Variations of the room temperature permittivity (ε'_{RT}) and maximum permittivity (ε'_{max}) as a function of composition for the series of $0.2[xLa(Zn_{1/2}Ti_{1/2})O_3\text{-}(1\text{-}x)Bi(Zn_{1/2}Ti_{1/2})O_3]\text{-}0.8PbTiO_3$ solid solution.

The dielectric dissipation factor, *i.e.* loss tangent, tanδ, at room temperature is shown in Figure 4.8. The dielectric loss at this temperature is quite low for all mole fractions of x. While the value increases with increasing mole fraction of LZT, it remains within the same order of magnitude. This type of behaviour is consistent with that of other lanthanum-doped ferroelectric materials, such as $(La_xPb_{1-x})(Zr_{1/2}Ti_{1/2})O_3$ where the substitution of lanthanum has altered the band gap of the material to be more semi-conducting [6], [38], [51].

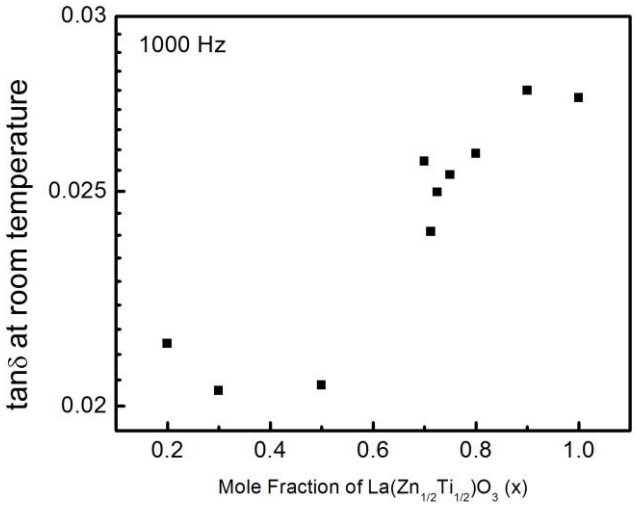

Figure 4.8 Dielectric dissipation factor or loss tangent, tanδ, at room temperature for $0.2[xLa(Zn_{1/2}Ti_{1/2})O_3\text{-}(1\text{-}x)Bi(Zn_{1/2}Ti_{1/2})O_3]\text{-}0.8PbTiO_3$ solid solution as a function of mole fraction of LZT (x).

4.4.3 Piezoelectric and Ferroelectric Properties.

The polarization vs. electric field, P(E), hysteresis loops were measured for the series of solid solutions. Those of the compositions of x = 0.30 (a), x = 0.60 (b) and x = 1.0 (c) are displayed in Figure 4.9. At low mole fractions of LZT (x < 0.40), the coercive field is still too high to yield a saturated P(E) loop, as can be seen in Figure 4.9(a), indicating that the coercive field is greater than the material's dielectric breakdown field. As the mole fraction of LZT increases, saturated loops can be displayed up to the mole fraction of x = 1.0. The coercive fields (E_C) and the remanent polarization (P_r) for the compositions showing saturated P(E) loops (x = 0.40 – 1.0) and are displayed in Figure 4.10. Coercive field (E_C) was shown to reduce as the LZT mole fraction increased, from E_C > 70 kV/cm at x = 0.40 to E_C = 22 ± 0.5 kV/cm at x = 1.0. The variation in E_C with composition follows the trends of the tetragonal distortion (Figure 4.2b) and of Curie temperature (Figure 4.6). The substitution of La^{3+} for Bi^{3+} has made polarization switching easier, which indicates that the reduction of the $6s^2$ lone pair has lowered the energy barrier separating the bipolar states. This is consistent with the reduced tetragonality and Curie temperature, confirming the "softening" effects of La-substitution. The room temperature remnant polarization (P_r) of the series slightly increases with increasing LZT fraction, reaching a maximum at x = 0.70 and then decreasing, as shown in Figure 4.10.

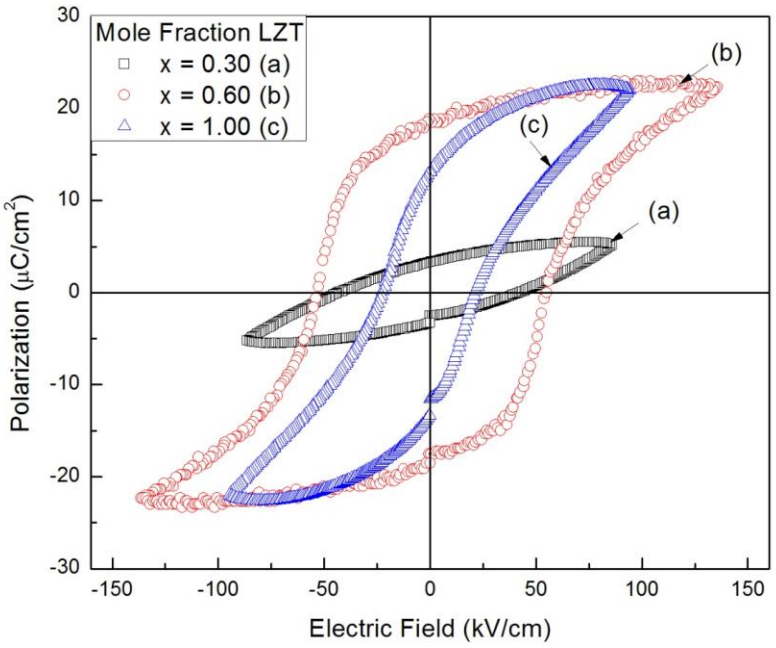

Figure 4.9 **Polarization vs. electric field hysteresis loops displayed for $0.2[xLa(Zn_{1/2}Ti_{1/2})O_3$- $(1-x)Bi(Zn_{1/2}Ti_{1/2})O_3]$-$0.8PbTiO_3$ with compositions of x = 0.3 (a), 0.6 (b) and 1.0 (c).**

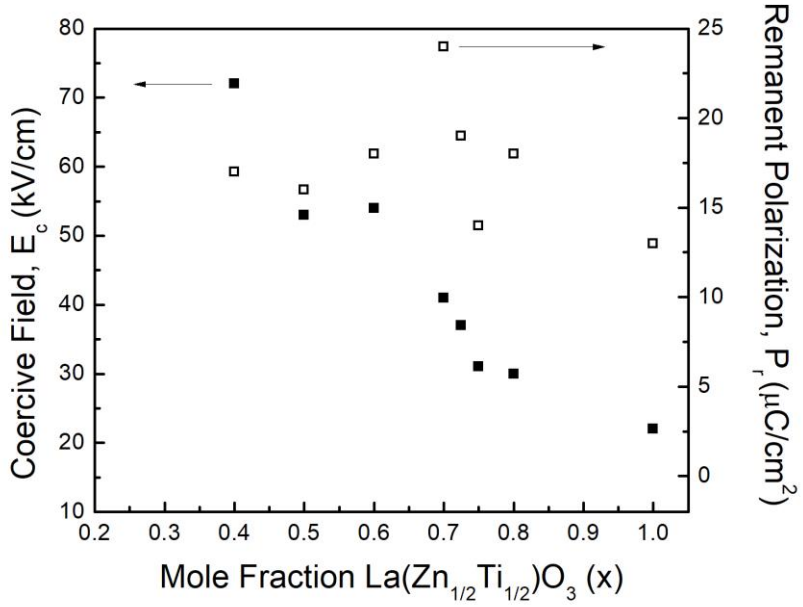

Figure 4.10 **Variations of the coercive field, E_c, and the remnant polarization, P_r, as a function of the mole fraction of LZT (x) in the $0.2[xLa(Zn_{1/2}Ti_{1/2})O_3$-$(1-x)Bi(Zn_{1/2}Ti_{1/2})O_3]$-$0.8PbTiO_3$ system.**

Piezoelectric measurements were performed on the same set of ceramics poled at 25 °C, 100 °C and 200 °C, respectively, and the results are presented in Figure 4.11. The ceramics poled at room temperature show piezoelectric coefficients d_{33} < 40 pC/N. Poling at 100 °C and 200 °C results in an increase in d_{33} by up to 3 times that of the room temperature poling. These d_{33} values show a peak at x = 0.7 in agreement with the peak in P_r.

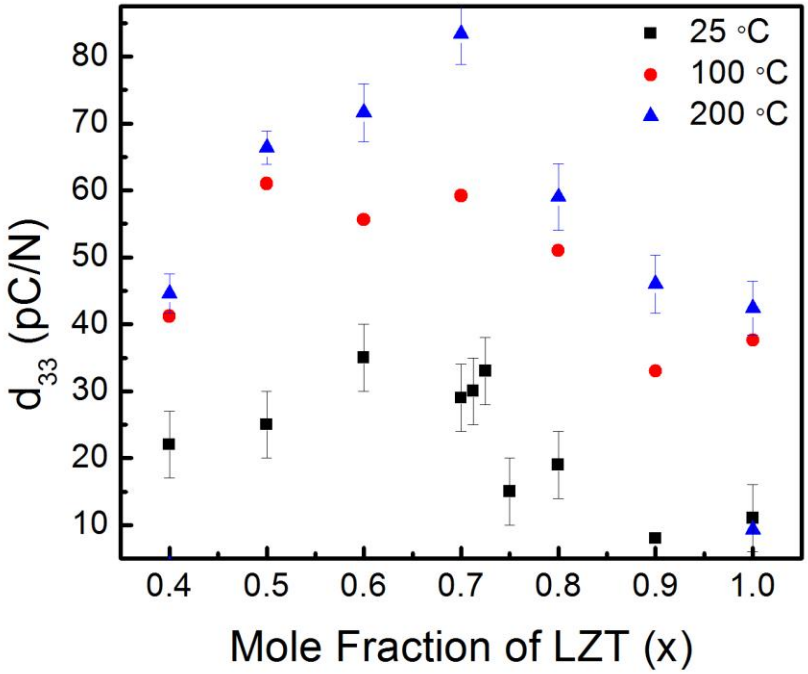

Figure 4.11 Variation of the piezoelectric coefficient (d_{33}) as a function of the mole fraction of LZT (x) for the ceramics of 0.2[x$La(Zn_{1/2}Ti_{1/2})O_3$- (1-x)$Bi(Zn_{1/2}Ti_{1/2})O_3$]-0.8$PbTiO_3$, poled at 25 °C, 100 °C and 200 °C, respectively.

This peak in the piezo-/ferroelectric properties can be attributed to two factors: i) A higher concentration of La^{3+} (LZT, x > 0.7) in the overall composition. The non-ferroelectric nature of the La^{3+} cation disrupts the long-range ferroelectric order, diminishing the piezo-/ferroelectric output. This is also evidenced in the dielectric behavior shown Figure 4.5 where at higher concentrations of LZT, the dielectric peak becomes more diffuse, suggesting the overlapping of a large number of local polarizations with different T_C. ii) At compositions with lower LZT content (x ≤ 0.6), the increased softening of the polarization (with reduced coercive fields) with increased concentration of LZT makes the effective poling of the ceramics stronger, revealing an

increased d_{33}. This trend of variation of d_{33} makes the region of LZT fraction from x = 0.6 – 0.7 of interest for application where remanent polarization and d_{33} are at a peak and Curie temperatures are still quite high (300 - 350 °C). Further improvement on piezoelectricity is expected if the poling can be optimized for compositions of a lower LZT mole fraction.

4.5 Conclusions

Through design by crystal chemistry concepts and preparation by solid state reaction and ceramic sintering process, a new pseudo-binary system $0.20[xLa(Zn_{1/2}Ti_{1/2})O_3 – (1\text{-}x)Bi(Zn_{1/2}Ti_{1/2})O_3] - 0.80PbTiO_3$ (LZT-BZT-PT) has been successfully synthesized with compositions x = 0.0 – 1.0 with complete solubility throughout the series. The highly tetragonally distorted structure in BZT-PT, which had prevented its piezo-/ferroelectricity from being revealed, shows a consistent decrease in tetragonality (c/a) with increasing mole fraction of LZT (x). This reduction of tetragonal distortion indicates that the structural 'softening', indeed, is realized by the substitution of La^{3+} for Bi^{3+} with a lone electron pair, as evidenced by the decreases in the ferroelectric Curie temperature and coercive field with increasing LZT content. More interestingly, this structural softening also leads to the softening of the polar order. These results show the presence of the $6s^2$ lone pair on Bi^{3+} has contributed to the high tetragonality and high Curie temperatures in the BZT-PT binary system in particular and in other ferroelectric materials in general. The 'softening' effect, realized by the substitution of LZT, allows for the realization of stable, bipolar states as displayed in the polarization vs. electric field hysteresis loops for mole fractions of LZT $x \geq 0.40$. The variations of remnant polarization and piezoelectric coefficients as a function of composition shows a peak at compositions x = 0.6 – 0.7 making those materials potentially useful for electromechanical transduction applications with high temperature applications.

Chapter 5. Composition, Structure and Properties of the New Ternary System $La(Zn_{1/2}Ti_{1/2})O_3$-$Bi(Zn_{1/2}Ti_{1/2})O_3$-$PbTiO_3$

5.1 Abstract

This chapter brings together the work performed exploring the solubility limits, phase symmetry and properties of the $La(Zn_{1/2}Ti_{1/2})O_3$-$Bi(Zn_{1/2}Ti_{1/2})O_3$-$PbTiO_3$ (LZT-BZT-PT) solid solution system and proposes its ternary phase diagram which maps out the various phases, their structures and associated properties. It includes the new results obtained from the investigation of the (1-x)PT-x[50LZT-50BZT] pseudo-binary system and the $0.30[(1-x)Bi(Zn_{1/2}Ti_{1/2})O_3$-$xLa(Zn_{1/2}Ti_{1/2})O_3]$-$0.70PbTiO_3$ pseudo-binary line. These results are combined with the results previously presented in Chapter 3 and Chapter 4 to determine the areas of interest within the ternary system.

In the areas of high PT concentration, there is a tetragonal, ferroelectric phase that is further divided into two regions: a region of “hard” ferroelectricity where high BZT concentration leads to high Curie temperatures, T_C, and coercive field, E_C, and a region of “soft” ferroelectricity where high LZT concentrations lead to lower T_C and E_C. This high PT region is of interest for high field ferroelectric applications. Outside of that region of ferroelectric activity, along the (1-x)LZT-xPT binary system, the region of x = 0.30 – 0.40 displays giant dielectric constants, making them materials of interest for high-density energy storage and MEMS applications. The high BZT concentration region of the phase diagram does not show a single phase in ambient synthesis conditions.

5.2 Introduction

In Chapter 3, it was demonstrated that $La(Zn_{1/2}Ti_{1/2})O_3$ (LZT) forms a stable solid solution with $PbTiO_3$ (PT) and has complete solubility throughout the binary system. The addition of LZT was shown to soften the structure and properties of the PT end member by lowering the Curie temperature, T_C, and disrupting the long-range ferroelectric order to achieve giant dielectric constant at concentrations of LZT where x = 0.30 – 0.40. In Chapter 4, the addition of LZT to the $Bi(Zn_{1/2}Ti_{1/.2})O_3$ - $PbTiO_3$ binary system was found to lower the Curie temperature, T_C, and the coercive field, E_c, and to soften the binary

system such that ferroelectric and piezoelectric properties could be realized that previously was restricted by coercive fields greater than that of dielectric breakdown.

In this chapter, the pseudo-binary systems of i) $0.30[(1-x)Bi(Zn_{1/2}Ti_{1/2})O_3$-$xLa(Zn_{1/2}Ti_{1/2})O_3]$-$0.70PbTiO_3$ and ii) (1-x)PT-x[50LZT-50BZT] (shown in Figure 5.1) are explored in order to determine the solubility limits and piezo-/ferroelectric properties of the ternary $La(Zn_{1/2}Ti_{1/2})O_3$-$Bi(Zn_{1/2}Ti_{1/2})O_3$-$PbTiO_3$ system and to determine the compositions that will be most suitable for potential applications.

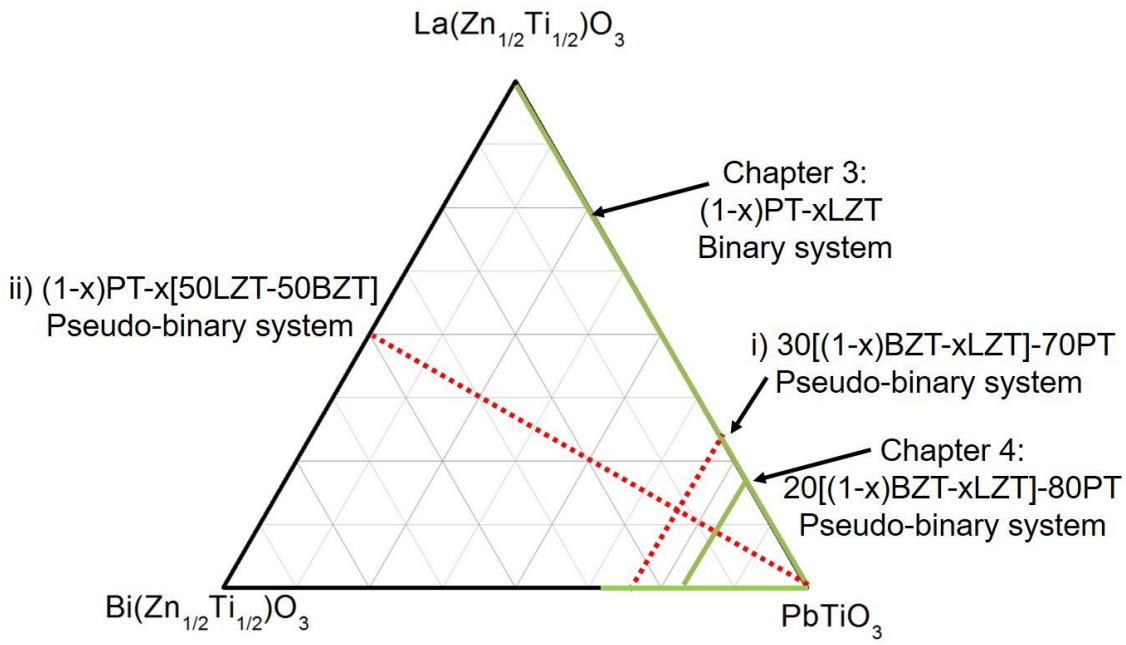

Figure 5.1 Previously studied pseudo-binary lines (solid green lines) and proposed pseudo-binary lines (dashed red lines) for further investigation. i) $0.30[(1-x)Bi(Zn_{1/2}Ti_{1/2})O_3$-$xLa(Zn_{1/2}Ti_{1/2})O_3]$-$0.70PbTiO_3$ and, ii) (1-x)PT-x[50LZT-50BZT] within the $La(Zn_{1/2}Ti_{1/2})O_3$-$Bi(Zn_{1/2}Ti_{1/2})O_3$-$PbTiO_3$ ternary solid solution system.

5.3 Experimental

5.3.1 Solid Solution Synthesis

The pseudo-binary solid solution systems of i) $0.30[(1-x)Bi(Zn_{1/2}Ti_{1/2})O_3$ - $xLa(Zn_{1/2}Ti_{1/2})O_3]$ - $70PbTiO_3$ and ii) $(1-x)PbTiO_3$-$x[50La(Zn_{1/2}Ti_{1/2})O_3$-$50Bi(Zn_{1/2}Ti_{1/2})O_3]$ were synthesized in the form of ceramics by solid state reaction and sintering process. Stoichiometric amounts of the constituent metal oxides (PbO, heat-treated La_2O_3, ZnO,

Bi_2O_3; 99.9%, Aldrich; and TiO_2, 99.5% Alfa Aesar) were hand milled (1hr, in the presence of acetone) and the resulting powder was dried, pressed into pellets and calcined in a muffle furnace (ramp = 300 °C/hr to 900 °C, dwell = 4hr) to form the solid solutions. The pellets were crushed and reground by hand (1 hr, in the presence of acetone) to yield a fine powder that was then pressed into discs of 10 mm diameter and sintered (ramp = 300 °C/hr to 1100 °C, dwell = 4 hr) to form dense ceramics for characterization.

5.3.2 Structural Analysis

The crystal structures of the materials synthesized were examined by X-ray powder diffraction on as-sintered ceramics (Rigaku Diffractometer, 46 mA, 42 kV, 2θ = 10 ° - 80 °, Ω = 200 °, Φ = 270 °, χ = 45 ° and Bruker D8 Advance Diffractometer, 40 mA, 40 kV, step size = 0.02 °/step, 2θ = 10 ° - 80 °). The resulting patterns were analyzed using JADE XRD pattern processing software to confirm the symmetry and TOPAS Academic software to refine the lattice parameters and atomic positions.

5.3.3 Dielectric and Ferroelectric Measurements

To perform electrical characterization, the sintered ceramics were polished with a series of silicon carbide sand papers (220, 400, and 600 grit successively) to achieve parallel, flat surfaces on the circular faces of the ceramics, with various thicknesses (1000 – 200 μm). The polished ceramics were then sputtered with gold layers (Anatech Hummer Sputter-Coater 6.2, 12 min., 15 mA plasma discharge current) and gold wires were attached to both surfaces of the samples using colloidal silver paste. Ceramics were further painted with colloidal silver paste to cover the electrode surfaces during high temperature measurements to prevent the loss of gold. The dielectric properties (permittivity, ε', and loss, tanδ) were measured as a function of temperature (from -50 ºC to 350 ºC, and high temperatures from 30 °C – 700 °C, at intervals of 3 °C) at frequencies varying from 1 to 10^6 Hz using a Novocontrol Alpha high-resolution broadband dielectric analyzer. The measurements were performed under zero-field-cooling (ZFC) conditions. Ferroelectric hysteresis loops were displayed using a Radiant Technologies RT66A testing system, connected to a Trek 609E-6 high voltage bipolar amplifier.

5.4 Results and Discussion

5.4.1 Structural Analysis

The XRD patterns for 30[(1-x)Bi($Zn_{1/2}Ti_{1/2}$)O_3-xLa($Zn_{1/2}Ti_{1/2}$)O_3]-70$PbTiO_3$ ceramics with the mole fraction of LZT, x = 0.1 – 0.9, are shown in Figure 5.2. As was seen in Chapter 4, as x increases, the splitting of the {100} and {110} sets of peaks, which is characteristic of tetragonal symmetry, gradually reduces such that at the compositions of x = 0.4 – 0.6, the {110} peaks are no longer resolved, but a shoulder is still visible, indicating there is still some degree of tetragonal distortion. At compositions of x ≥ 0.7 the shoulder is no longer discernable, indicating a complete transition to a pseudo-cubic phase.

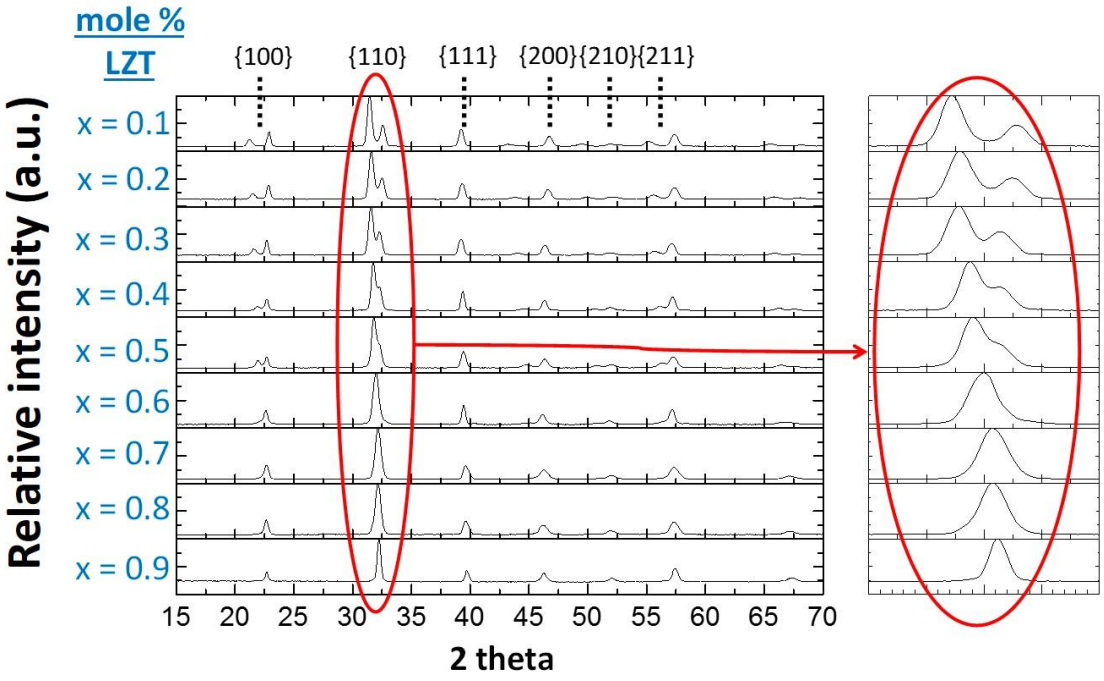

Figure 5.2 XRD powder diffraction patterns for the 30[(1-x)Bi($Zn_{1/2}Ti_{1/2}$)O_3-xLa($Zn_{1/2}Ti_{1/2}$)O_3]-70$PbTiO_3$ for ceramics with mole fractions of LZT, x = 0.1 - 0.9. The enlargement of the (110) peak is shown on the right-hand side.

The diffraction patterns were fit to the P4*mm* space group, using TOPAS Academic software to extract the lattice parameters. Figure 5.3 shows the variation of the tetragonal lattice parameters for 30[(1-x)Bi($Zn_{1/2}Ti_{1/2}$)O_3-xLa($Zn_{1/2}Ti_{1/2}$)O_3]-70$PbTiO_3$ system as a function of mole fraction of LZT for x = 0.1 – 0.9. It can be seen that as the mole fraction

of LZT increases, the lattice parameter *a* stays relatively constant, with only a slight increase over the series, and the lattice parameter *c* decreases significantly. The variations of *a* and *c* lattice parameters indicate a reduced tetragonal distortion, which is due to a decrease in the concentration of the cations with $6s^2$ electron lone pair as a result of substitution of La^{3+} for Bi^{3+} on the A-site.

To further depict this trend, the tetragonality, *c/a*, is plotted as a function of mole fraction of LZT, x = 0.1 – 1.0, for both 20[(1-x)$Bi(Zn_{1/2}Ti_{1/2})O_3$-x$La(Zn_{1/2}Ti_{1/2})O_3$]-80$PbTiO_3$ and 30[(1-x)$Bi(Zn_{1/2}Ti_{1/2})O_3$-x$La(Zn_{1/2}Ti_{1/2})O_3$]-70$PbTiO_3$ systems. In Figure 5.4 it can be seen that both pseudo-binary systems show a decrease in tetragonality with the increase in mole fraction of LZT. Moreover, the 30[(1-x)BZT-xLZT]-70PT pseudo-binary line exhibits a much steeper slope, owing to a greater overall proportion of La^{3+} substitution on the A-site as x increases. These consistent variations of the structural features with composition of these two systems confirm the explanation given in Chapter 4 for the 20[(1-x)BZT-xLZT]-80PT system, and further proves the concept of chemical softening by substitution of LZT for BZT.

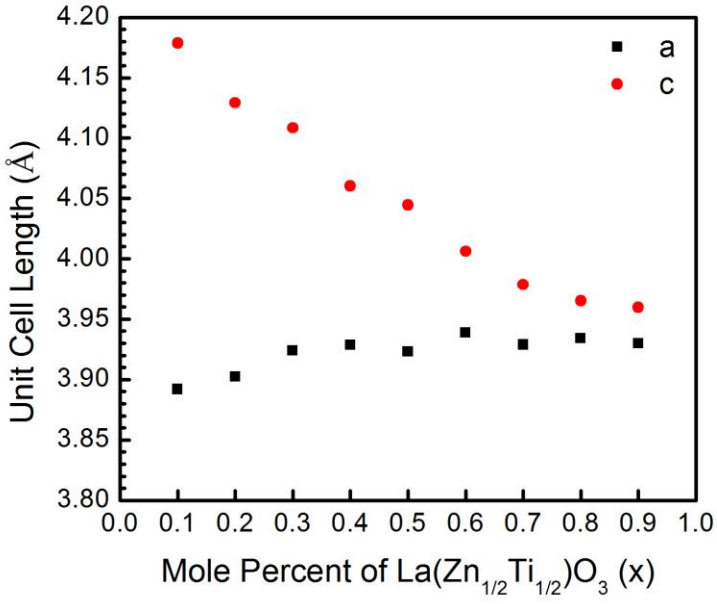

Figure 5.3 Variations of the tetragonal lattice parameters *a* and *c* for 30[(1-x)$Bi(Zn_{1/2}Ti_{1/2})O_3$ -x$La(Zn_{1/2}Ti_{1/2})O_3$]-70$PbTiO_3$ as a function of the mole fraction of LZT for x = 0.1 - 0.9.

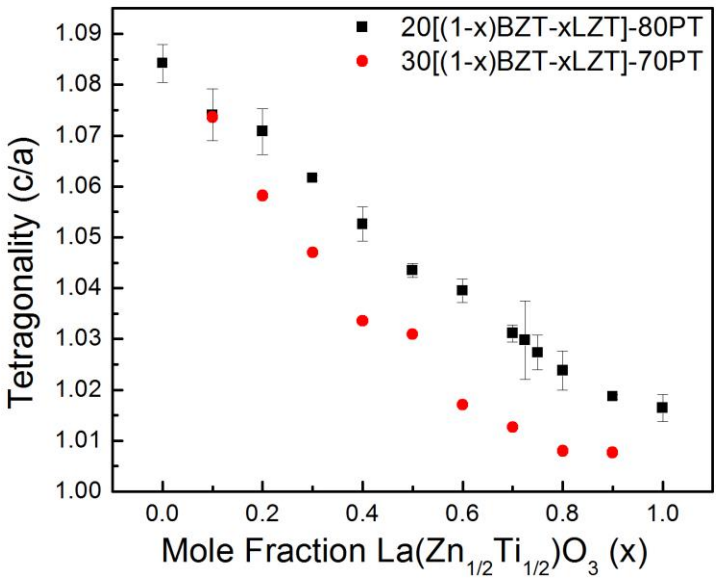

Figure 5.4 **Variation of the tetragonality (*c/a*) for 20[(1-x)Bi($Zn_{1/2}Ti_{1/2}$)O_3-xLa($Zn_{1/2}Ti_{1/2}$)O_3]-80$PbTiO_3$ and 30[(1-x)Bi($Zn_{1/2}Ti_{1/2}$)O_3-xLa($Zn_{1/2}Ti_{1/2}$)O_3]-70$PbTiO_3$ as a fucntion of the mole fraction of LZT x from x = 0.0 - 1.0.**

The powder XRD patterns for the (1-x)$PbTiO_3$ - x[0.50La($Zn_{1/2}Ti_{1/2}$)O_3 - 0.50Bi($Zn_{1/2}Ti_{1/2}$)O_3] pseudo-binary system with mole fractions of x = 0.1 - 0.5 are shown in Figure 5.5. It can be seen that a pure perovskite phase is formed for x = 0.1 – 0.4. For the composition of x = 0.50, pyrochlore impurity peaks appear (as marked by the stars), indicating that the solubility limit of the pseudo-binary system is about x =0.40.

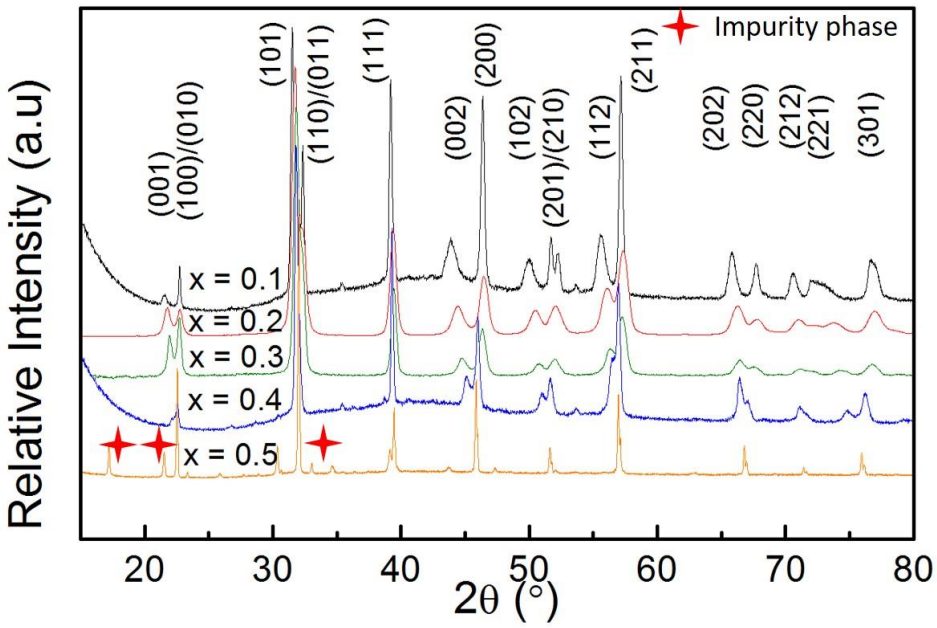

Figure 5.5 **Powder XRD patterns of the (1-x)$PbTiO_3$ - x[0.50$La(Zn_{1/2}Ti_{1/2})O_3$ - 0.50$Bi(Zn_{1/2}Ti_{1/2})O_3$] system for mole fractions of x = 0.1 - 0.5. The stars indicate peaks attributed to a secondary, imputity phase in x = 0.50.**

5.4.2 Dielectric and Ferroelectric Characterizations

Figure 5.6 shows the variation of dielectric permittivity as a function of temperature measured at 1kHz for the ceramics of the 30[(1-x)$Bi(Zn_{1/2}Ti_{1/2})O_3$ - x$La(Zn_{1/2}Ti_{1/2})O_3$] - 70$PbTiO_3$ pseudo-binary solid solution system with mole fractions of LZT x = 0.20 - 0.75. The first thing to note is that all the compositions studied show a dielectric peak indicating the paraelectric to ferroelectric phase transition at T_C. As the mole fraction of LZT, x, increases, the Curie temperature, T_C, decreases, following the trend of decreasing tetragonal distortion of the unit cell. Although T_c decreases, the dielectric peak becomes sharper and higher as x increases and reaches a maximum value at ε' = 4500 with x = 0.50. With x = 0.75, the peak value has decreased and the peak becomes broader, however, the T_C stays constant with changing frequencies, indicating a normal ferroelectric transition with diffuseness.

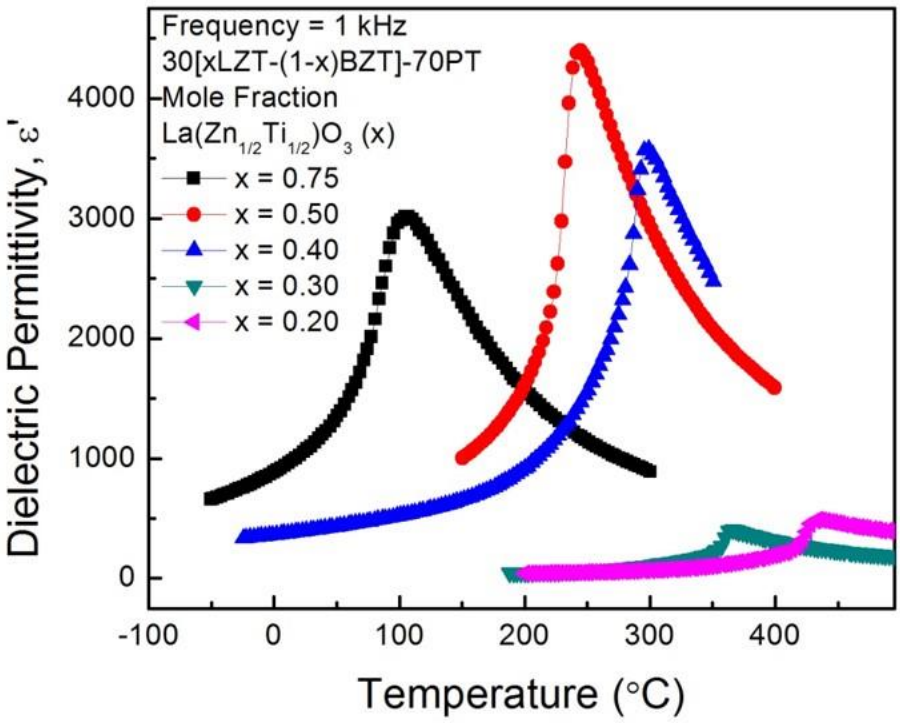

Figure 5.6 Variation of dielectric permittivity as a function of temperature measured at 1 kHz for the 30[(1-x)Bi($Zn_{1/2}Ti_{1/2}$)O_3-xLa($Zn_{1/2}Ti_{1/2}$)O_3]-70$PbTiO_3$ pseudo-binary solid solutions system with mole fractions of LZT, x = 0.20 - 0.75.

The variations of the Curie temperature, T_C, for both the 20[(1-x)Bi($Zn_{1/2}Ti_{1/2}$)O_3 - xLa($Zn_{1/2}Ti_{1/2}$)O_3] - 80$PbTiO_3$ and 30[(1-x)Bi($Zn_{1/2}Ti_{1/2}$)O_3 - xLa($Zn_{1/2}Ti_{1/2}$)O_3]-70$PbTiO_3$ systems as a function of mole fraction of LZT, x = 0.0 - 1.0, are shown in Figure 5.7. Similar to the variation of their tetragonality (see Figure 5.4), both pseudo-binary systems show a decrease in T_C as the mole fraction of LZT, x, is increased. Additionally, 30[(1-x)Bi($Zn_{1/2}Ti_{1/2}$)O_3 - xLa($Zn_{1/2}Ti_{1/2}$)O_3]-70$PbTiO_3$ shows a steeper slope in the trendline, indicating that with a higher fraction of initial $6s^2$ lone-pair cations (30% Bi^{3+} vs 20% Bi^{3+}) substituted by La^{3+}, a non-lone-pair cation, for PT, the more pronounced the effect of chemical “softening” can be achieved, giving rise to a sharper decrease in the tetragonality and the Curie temperature.

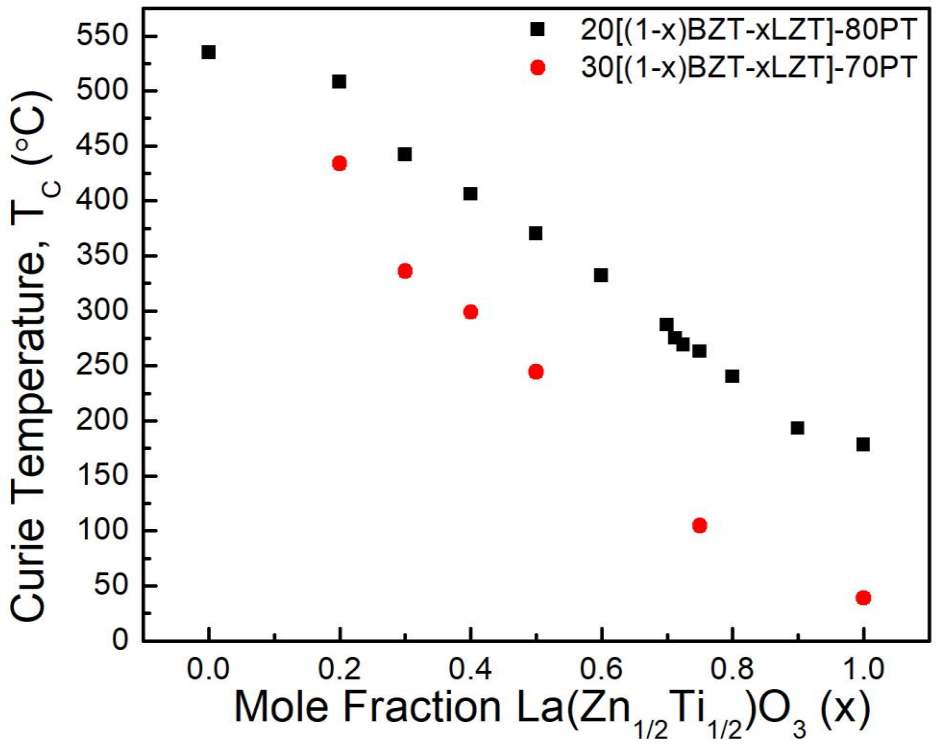

Figure 5.7 **Variations of the Curie temperature, T_C, for the $20[(1-x)Bi(Zn_{1/2}Ti_{1/2})O_3 - xLa(Zn_{1/2}Ti_{1/2})O_3]$-$80PbTiO_3$ and $30[(1-x)Bi(Zn_{1/2}Ti_{1/2})O_3 - xLa(Zn_{1/2}Ti_{1/2})O_3]$-$70PbTiO_3$ systems as a function of the mole fraction of LZT, x = 0.0 - 1.0.**

5.4.3 Mapping of the Composition, Structure and Properties for the Ternary $La(Zn_{1/2}Ti_{1/2})O_3$-$Bi(Zn_{1/2}Ti_{1/2})O_3$-$PbTiO_3$ Solid Solution System – A summary

Based on the structural and property data obtained in Chapter 3, Chapter 4 and above, a preliminary ternary phase diagram is established for LZT-BZT-PT ternary solid solution system as presented in Figure 5.8. This ternary phase diagram shows the following features. In the region of high PT concentration, a ferroelectric perovskite phase of tetragonal symmetry is formed. Interestingly, this area can be further divided into two sub-regions: The compositions with low LZT concentration (green area) that behave like hard ferroelectrics with high T_C and high coercive fields, making the material suitable for high-field and high-power applications. With the substitution of LZT for BZT, the ferroelectricity is softened (maroon area) with the tetragonality, coercive field and

Curie temperatures decreased as the proportion of LZT is increased, making these materials suitable for electromechanical transducers and memory devices. Moreover, room temperature dielectric constants are increased with increasing LZT concentration, leading to giant dielectric constants along the LZT-PT binary side with 30 – 40 mole percent of LZT. Increasing the mole fraction of LZT along the LZT-PT binary line, the pseudo-cubic phase transitions to a $P2_1/n$ monoclinic phase at $x > 0.70$, a dielectric material. On the BZT side of the phase diagram, there is a large area where no single-phase perovskite can be formed under ambient, solid state reaction conditions. This reflects the low chemical stability of the BZT end member. High pressure may be required to prepare a single perovskite phase in that region of the phase diagram.

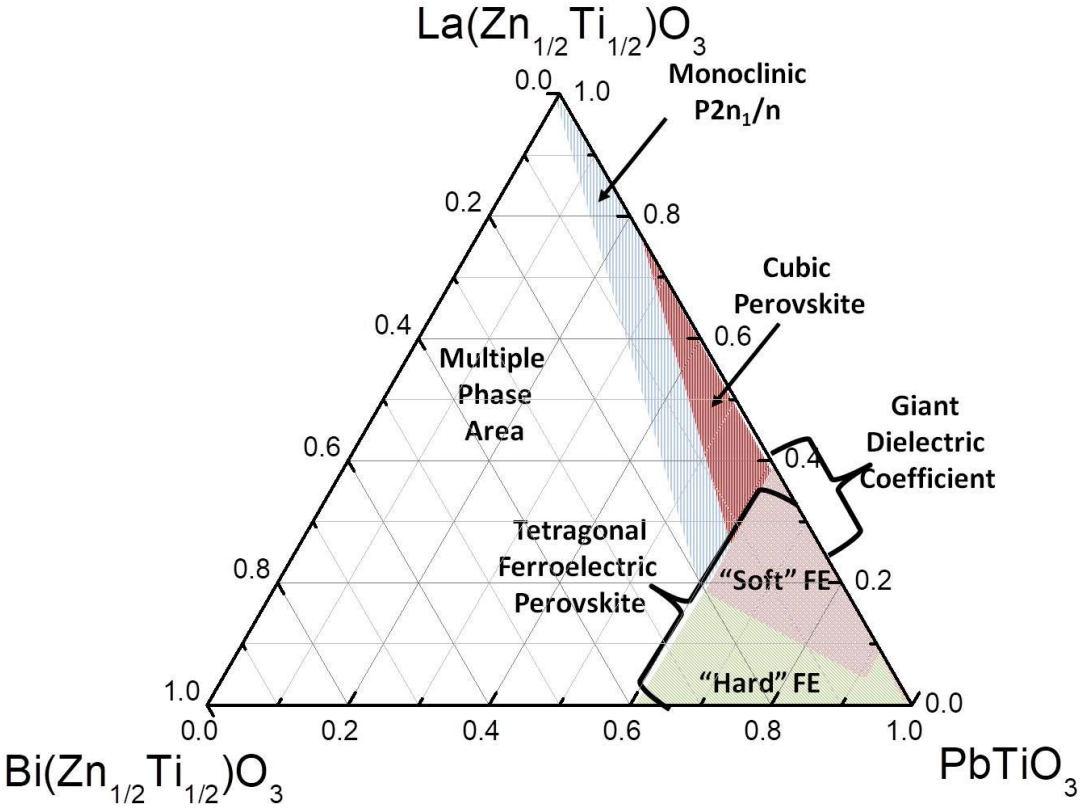

Figure 5.8 **Established phase diagram of the $La(Zn_{1/2}Ti_{1/2})O_3$-$Bi(Zn_{1/2}Ti_{1/2})O_3$-$PbTiO_3$ ternary system, showing various phases of tetragonal, cubic and monoclinic symmetries and the associated functional properties, namely "hard" and "soft" ferroelectricity and giant dielectric constant.**

Chapter 6. Growth, Characterization and the Unconventional "Hardening" of Piezo-/Ferroelectric $Pb(Mg_{1/3}Nb_{2/3})O_3$-$PbTiO_3$-$Bi(Zn_{1/2}Ti_{1/2})O_3$ Ternary Single Crystals

The work in this chapter is presented as published, with minor modifications from the following publication: R. A. Belan, H. N. Tailor, X. Long, A. A. Bokov, and Z.-G. Ye, "Growth and characterization of piezo-/ferroelectric $Pb(Mg_{1/3}Nb_{2/3})O_3$–$PbTiO_3$–$Bi(Zn_{1/2}Ti_{1/2})O_3$ ternary single crystals," *J. Cryst. Growth*, vol. 318, no. 1, pp. 839–845, Mar. 2011. (All experiments and analysis were performed by R. A. Belan, the primary author on the publication, co-authors facilitated the discussion sections.)

6.1 Abstract

In order to develop new piezo-/ferroelectric materials, single crystals of the $Pb(Mg_{1/3}Nb_{2/3})O_3$–$PbTiO_3$–$Bi(Zn_{1/2}Ti_{1/2})O_3$ [PMN–PT–BZT] ternary complex perovskite system have been grown by a high temperature solution method using the mixture of PbO and H_3BO_3 as flux (in a molar ratio of 4:2) and an optimum flux:charge molar ratio of 6:1. It is found that the addition of BZT into the relaxor ferroelectric PMN–PT system reduces the number of spontaneous nucleations, resulting in large single crystals (5mm x 5mm x 14mm) of good quality. The grown crystals exhibit a pseudo-cubic morphology and show evidence of two-dimensional growth mechanism. Examination by polarized light microscopy (PLM) reveals the formation of striation, which can be reduced by changing the growth conditions. The domain structure and phase transition of the PMN–PT–BZT crystals are investigated by PLM. The temperature and frequency dependences of the dielectric permittivity of the grown crystals show typical relaxor ferroelectric behavior, with the frequency dependence of the temperature of maximum permittivity (T_{max}) following the Vogel-Fulcher law. The ferroelectric and piezoelectric properties are displayed and compared to both the parent and next generation relaxor materials for comparison.

6.2 Introduction:

Relaxor ferroelectrics-based solid solution single crystals, namely $Pb(Mg_{1/3}Nb_{2/3})O_3$–$PbTiO_3$ [PMN-PT] and $Pb(Zn_{1/3}Nb_{2/3})O_3$–$PbTiO_3$, exhibit extraordinary piezoelectric performance, making them the materials of choice for the next generation of electromechanical transducers for a broad range of advanced applications [2], [14]. PMN crystallizes in a complex perovskite $A(B'B'')O_3$-type structure and exhibits typical relaxor behavior with a diffuse maximum of dielectric permittivity (ε'), the temperature of which (T_{max}) increases with increasing frequency. The relaxor behavior is believed to arise from the relaxation of polar nanoregions (PNRs) that form as a result of chemical order/disorder that prevents long-range polar order from developing as in normal ferroelectric materials.

However, there are some drawbacks to the (1-x)PMN-xPT single crystals. They suffer from relatively low Curie temperatures (T_C), which limits the operational range of the manufactured devices. They also have lower coercive fields (E_C), making the material unsuitable for high-field bipolar applications. The phase diagram of the solid solution system shows a morphotropic phase boundary (MPB) region within x = 0.32-0.37 where the piezo-/ferroelectric properties are at maximum [14]. Single crystals with $x \leq 0.32$ show a rhombohedral polar symmetry. Their optimum piezoelectric performance is exploited through domain engineering and polarization rotation by poling the material in the $<001>_{cub}$ direction instead of the $<111>_{cub}$ polar direction [14], [52], [53]. These materials are also susceptible to over-poling that leads to a degradation of those desired properties [23].

Bismuth zinc titanate, $Bi(Zn_{1/2}Ti_{1/2})O_3$ [BZT], is a good candidate to form a solid solution with PMN-PT because Bi^{3+} and Pb^{2+} both have large atomic numbers and contain a stereochemically active $6s^2$ lone electron pair that makes their host lattice more polarizable and thereby introduces an additional component of asymmetry into the unit cell. The addition of BZT was shown to increase the Curie temperature (T_C) of the canonical ferroelectric $PbTiO_3$ [27], a rare occurrence when forming solid solutions with lead titanate [54]. This was thought to be due to the high tetragonality created by the addition of the Bi^{3+} cation into the solid solution. However, the high tetragonality also has the disadvantage of increasing the coercive field to a value higher than that of dielectric

breakdown, making it impossible to pole the material at room temperature and to realize the potential of the material in devices.

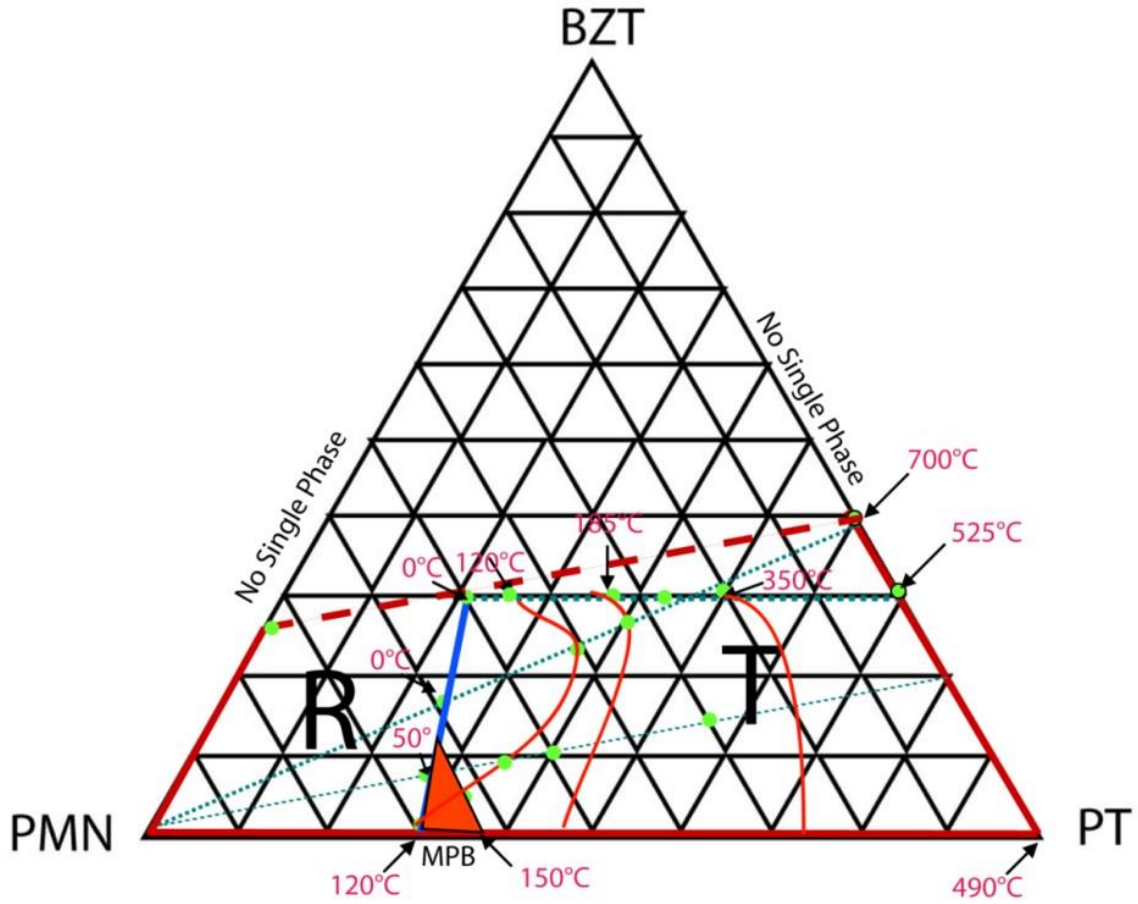

Figure 6.1 **$Pb(Mg_{1/3}Nb_{2/3})O_3$-$PbTiO_3$-$Bi(Zn_{1/2}Ti_{1/2})O_3$ ternary phase diagram, as established based on ceramic materials of varying compositions. The red lines indicate the Curie Temperature, and the orange triangle indicates the MPB region (**[55]–[57]**Used with permission).**

In order to develop new materials with higher Curie temperatures and larger coercive fields, ceramics of the ternary solid solution of $Pb(Mg_{1/3}Nb_{2/3})O_3$–$PbTiO_3$–$Bi(Zn_{1/2}Ti_{1/2})O_3$ were recently studied in our Laboratory and their structure and dielectric and piezo-/ferroelectric properties were characterized as a function of temperature and composition, the resulting phase diagram is shown in Figure 6.1. It was found that the inclusion of bismuth into the PMN-PT system indeed leads to an increased coercive field, “hardening” the system to high field applications, with high piezoelectric properties occurring along the pseudo-binary line of (1-x)$Pb(Mg_{1/3}Nb_{2/3})O_3$–x[0.80$PbTiO_3$–0.20$Bi(Zn_{1/2}Ti_{1/2})O_3$], x = 0.38-0.40 [55], [56]. In order to retain this increased field stability and increase piezoelectric output, exploration of the

behavior of the PMN-PT-BZT ternary system as single crystal piezo-/ferroelectrics is of great interest. In this work, we grow single crystals of $xPb(Mg_{1/3}Nb_{2/3})O_3 - yPbTiO_3 - zBi(Zn_{1/2}Ti_{1/2})O_3$ by the high temperature solution (flux) method, and characterize the structure and the dielectric, optical and piezo-/ferroelectric properties of the grown crystals.

6.3 Experimental

6.3.1 Crystal Growth

The high temperature solution (flux) method was employed for the growth of the ternary crystals of a nominal charge composition of $0.61Pb(Mg_{1/3}Nb_{2/3})O_3–0.078PbTiO_3–0.312Bi(Zn_{1/2}Ti_{1/2})O_3$. Stoichiometric amounts of high purity constituent metal oxides, PbO, TiO_2, MgO, Nb_2O_5, ZnO, and Bi_2O_3 were mixed in a mortar with a 4:1 mole ratio of $PbO:H_2BO_3$ as flux, at a flux:charge molar ratio of 6:1 (total flux + charge = 100g). The resulting mixture was loaded into a 50 cc platinum crucible that was then placed in a cylindrical crystal growth furnace. The temperature was raised to 1070 °C over a period of 6 h and held for 24 h. The molten solution was then slowly cooled at two different rates: 0.4 °C/h (Growth A) and 0.2 °C/h (Growth B), down to 900 °C, followed by natural furnace cooling to room temperature. The melt was inspected regularly to observe the formation of nuclei and monitor the progress of growth. The resulting crystals were then leached from the solidified melt using a hot 15% acetic acid solution.

6.3.2 Structural Characterization

The crystal structure of the as-grown crystals was examined by x-ray powder diffraction by grinding a portion of the crystal to a fine powder and recording its diffraction pattern (Bruker D8 Advance Diffractometer, 40 mA, 40 kV, step size = 0.02°/step, 2θ = 10°-80°). The resulting pattern was analyzed using JADE XRD pattern processing software and TOPAZ Academic to confirm the symmetry and refine the lattice parameters.

6.3.3 Optical Studies by Polarized Light Microscopy

The grown crystals were cut perpendicular to the (001) crystallographic face using a Fine #1 Diamond Wheel (0.006') and then polished with silicon carbide sand paper (220, 400, 600 grit) followed by 3M Al_2O_3 lapping sheets (5 to 3 μm) down to optical transparency (400-50 μm thick). Polarized light microscopy (PLM) was performed using an Olympus BX60 microscope equipped with Olympus UC30 digital camera to study the growth mechanism, domain structure, phase symmetry and phase transition. Optical retardation (and birefringence) of the crystals was determined using an Olympus U-CBE compensator (e = line; λ = 546.1 nm) and a green filter 9-U150 (λ = 546 nm) at varying temperatures (25 - 300 °C, at 0.5°/min) using a Linkham THMS600 heating stage controlled and monitored by Linkham TMS93 and LNP temperature control interfaces.

6.3.4 Dielectric, Piezoelectric and Ferroelectric Measurements

To perform electrical characterization, the polished, parallel crystal surfaces were first sputtered with gold layers (Anatech Hummer Sputter-Coater 6.2, 12 min., 15 mA plasma discharge current) and gold wires were then attached to both surfaces of the samples using colloidal silver paste. The dielectric properties (permittivity, ε', and loss, tanδ) were measured as a function of temperature (from -50 ºC to 350 ºC at intervals of 3 ºC) at varying frequencies from 1 to 10^6 Hz using Novacontrol Alpha high-resolution broadband dielectric analyzer. The measurements were performed under zero-field-heating (ZFH) conditions on both an unpoled sample and a sample poled using an electric field three times the coercive field (E_C) applied at room temperature. Ferroelectric hysteresis loops were displayed using a Radiant Technologies RT66A testing system, connected to a Trek 609E-6 High Voltage Bipolar Amplifier. Samples were subsequently poled in silicon oil using a Stanton PS350 high voltage source prior to piezoelectric measurements of the Berlincourt method with an IACAS Model ZJ-6B d_{33} meter to obtain the piezoelectric coefficient, d_{33}.

6.4 Results and Discussion:

6.4.1 Crystal Growth

During the slow cooling process of the thermal cycle, a spontaneous nucleation was observed at the surface of the melt at the temperature of 1041 °C and the nucleus appeared to be a square, indicating a single nucleation for each of the two batches (Batch A and Batch B). Upon further cooling, this nucleus grew into a larger crystal of pseudo-cubic morphology on top of the melt, as shown in Figure 6.2a. Figure 6.2b and Figure 6.2c show the two large crystals obtained from Batch A and Batch B, respectively, after leaching. Upon inspection of Crystal A, a regular, cubic morphology is observed with 90° corners at the edge of the crystal. The steps and kinks visible on the (001) face indicate a layered growth mechanism [58]. Crystal B appears to be twinned and exhibits faceted growth, as in Batch A, although the corner facets are found to be only approximately 90º. It also shows a higher degree of transparency than Crystal A.

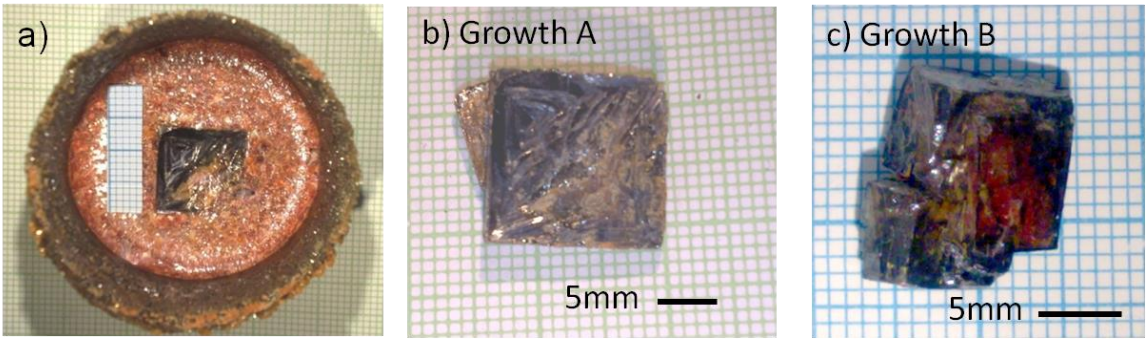

Figure 6.2 (a) As-grown crystal obtained from Growth A after cooling, (b) crystal from Growth A after leaching and (c) crystal from Growth B after leaching.

Further insight into the growth mechanism of Crystal A is gained from the optical examination of the crystal platelet by PLM, as seen in Figure 6.3. The (001) platelet shows a clear striped pattern parallel to the $<100>_{cub}$ direction that could either be domain structure or growth striation. Upon heating the crystal up to 250 ºC, no visible change to the pattern is observed except for the decrease of birefringence. This confirms that the observed striped pattern corresponds to the growth striation, a phenomenon frequently encountered in crystal growth from high temperature solution, which can be caused by temperature instability during the growth process, or a concentration variation at the interface between the growth face and the solution [59].

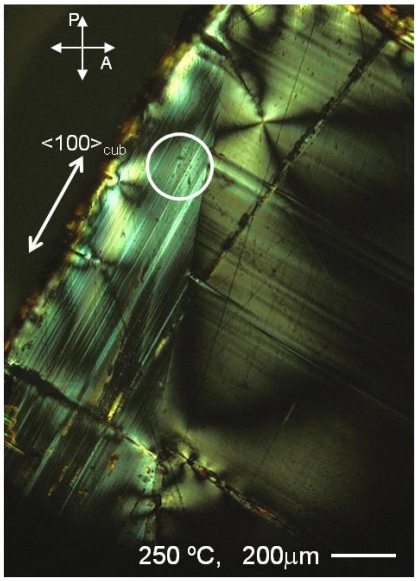

Figure 6.3 **Crystal A cut perpendicular to the (0 0 1) face and observed under crossed polarizers at 250 °C, showing growth striation.**

In contrast, Crystal B grown at a slower cooling rate does not exhibit such striation patterns, as shown in Figure 6.4a, suggesting that a more stable thermal environment was achieved which prevented striation from developing in the crystal. Note that while the striation pattern is absent, Crystal B contains many more inclusions, which deteriorates the dielectric and ferroelectric properties.

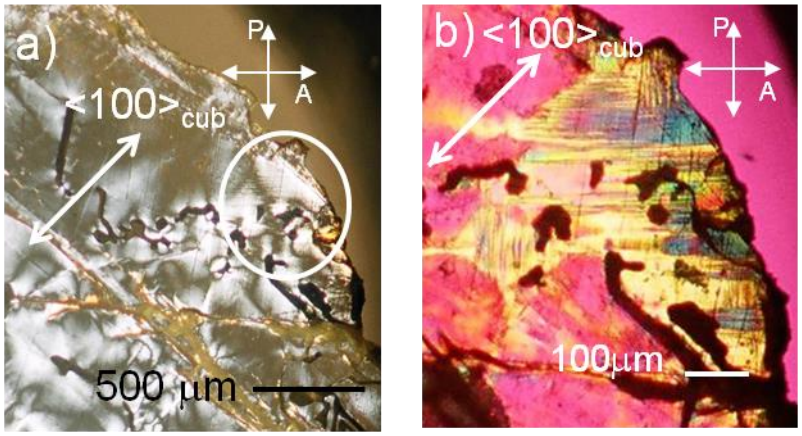

Figure 6.4 **(a) Crystal B cut perpendicular to (0 0 1) face and observed under crossed polarizers at room temperature, showing reduced striation and coexistence of rhombohedral and tetragonal (circled) phases. (b) Close-up of the tetragonal region with a first order red plate superimposed to reveal domain structure.**

6.4.2 Crystal Structure

Further examination of the crystal platelets by PLM reveals the symmetry of the grown crystals, which is confirmed by XRD powder patterns. Figure 6.5a and Figure 6.5b show the (001) platelet with respect to the crystal growth edge of Crystal A with crossed polarizers (A-P) at 45º, and parallel, to the $<100>_{cub}$ direction, respectively, between crossed polarizers, whereas Figure 6.5c and Figure 6.5d show the circled area of the (001) platelet of Crystal B (see Figure 6.4a and Figure 6.4b) at the same respective positions. Platelet A is in extinction with crossed polarizers at 45º to the $<100>_{cub}$ direction and in diagonal position with crossed polarizers parallel to the $<100>_{cub}$ direction, which suggests a rhombohedral (or pseudo-cubic) symmetry.

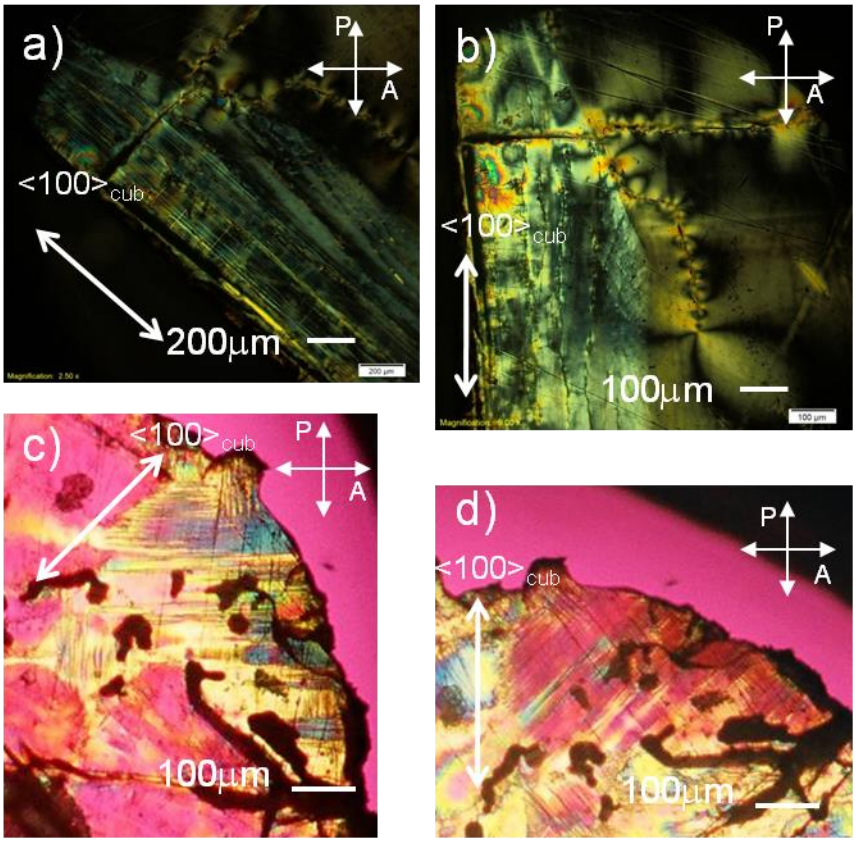

Figure 6.5 **(a) Crystal Platelet A in extinction under crossed polarizers at 45° to 〈1 0 0〉 cub and (b) crystal Platelet A in diagonal position with polarizers parallel to 〈1 0 0〉 cub. (c) Crystal Platelet B with the tetragonal region in diagonal position with crossed polarizers at 45° to 〈1 0 0〉 cub and (d) Crystal Platelet B with the tetragonal region in extinction with crossed polarizers parallel to 〈1 0 0〉 cub.**

The platelet of Crystal B also shows large regions of extinction at a 45° angle to the $<001>_{cub}$ direction, indicating a rhombohedral or pseudo-cubic structure, as seen in Figure 6.4a. In addition to large areas where stress-induced birefringence can be measured, there are also regions with well-defined domain structure (as circled on Figure 6.4a, enlarged in Figure 6.4b), indicating that the edge region of the crystal exhibits a different symmetry, which arises from some degree of phase segregation within the crystal, a typical situation for solid solutions. These domains show extinction directions parallel to $<001>_{cub}$, indicating a tetragonal symmetry. The coexistence of the tetragonal domains and rhombohedral (or pseudo-cubic) regions suggests that the composition of Crystal B lies near or within the morphotropic phase boundary (MPB) region. MPB is a common phenomenon occurring in many ferroelectric solid solutions like the previously studied PMN-PT system [60]. Figure 6.6a gives the x-ray powder diffraction patterns for both Crystal A and B, which indicate the predominantly rhombohedral (or pseudo-cubic) phase for both crystals as no splitting in the $(100)_{cub}$, $(110)_{cub}$ and $(200)_{cub}$ peaks can be observed, (splitting would indicate a tetragonal phase) These results are consistent with the crystal symmetry deduced from the observations by PLM.

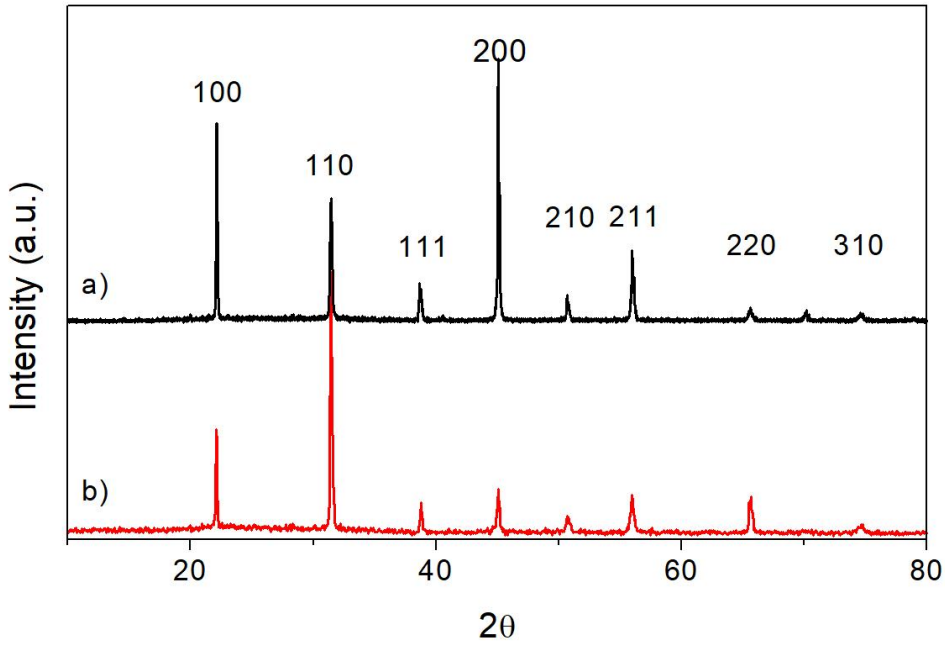

Figure 6.6 Powder XRD patterns of Crystal A (a) and Crystal B (b), respectively.

6.4.3 Dielectric Properties and Phase Transitions

The dielectric properties (ε', tanδ) of Crystal A as a function of temperature (-50 ºC to 300 ºC) were measured at varying frequencies between 1 and 10^6 Hz, as presented in Figure 6.7. The crystal exhibits typical relaxor behavior with a diffuse permittivity peak whose temperature (T_{max}) varies from 87 to 101 ºC with frequency increasing from 1 to 10^4 Hz. The crystal was then poled using an applied field of 10.5 kV/cm, three times that of the coercive field (E_C) at room temperature and the dielectric properties are measured upon heating at zero electric field. As shown in Figure 6.8, a dielectric anomaly is observed at the depoling temperature, T_d = 56 ºC, corresponding to a phase transition from the poled macro-polar phase to an ergodic relaxor state, as reported in other relaxor ferroelectrics [5], [61], [62]. Below T_d, the dielectric dispersion is significantly attenuated (compared with the unpoled crystal), while above T_d, the relaxor state is restored with typical dispersion of the permittivity maximum and its temperature (T_{max}).

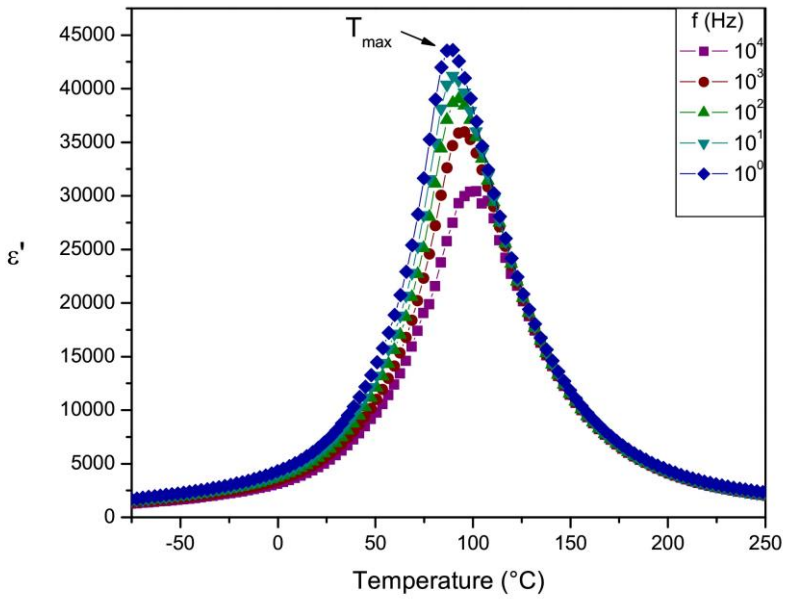

Figure 6.7 Temperature dependence of the dielectric permittivity (*ε'*) of Crystal A measured at various frequencies, showing typical relaxor behavior.

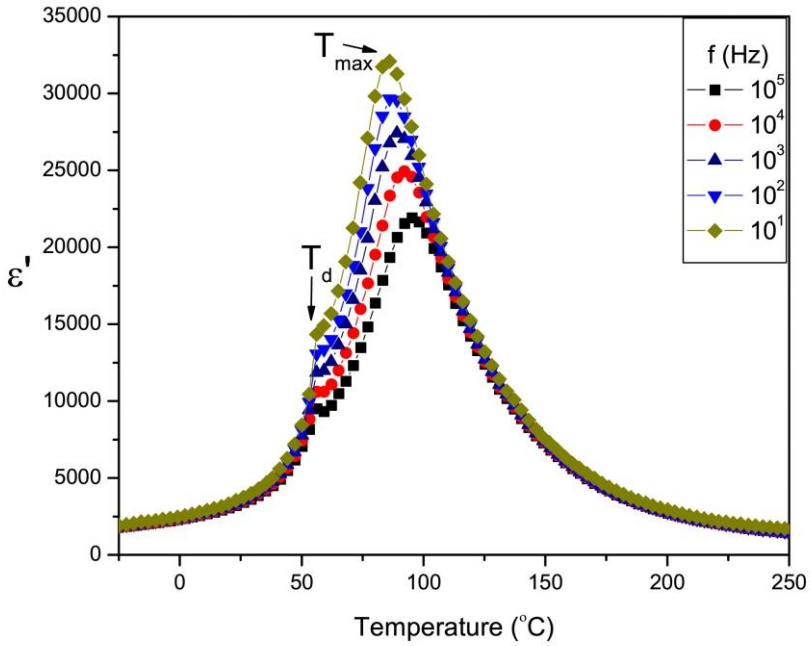

Figure 6.8 Temperature dependence of dielectric permittivity (*ε'*) of Crystal A, measured at various frequencies upon zero-field-heating after poling, showing an anomaly at T_d=56 °C, which corresponds to the transformation from the ferroelectric phase to the relaxor state.

The dispersive T_{max} of unpoled crystal (Figure 6.7) was fitted to the Vogel-Fulcher (V-F) law [5], [61], [62]:

$$f = f_0 \, exp\left[\frac{-E_a}{k_B(T_{max} - T_{VF})}\right],$$

where f is the frequency of T_{max}, f_0 is the Debye frequency, E_a is the activation energy and T_{VF} is the temperature at which the relaxation process freezes out or ceases to be displayed in the solid. The fitting results are presented in Figure 6.9, which shows a good fit to the V-F law (red line), confirming the relaxor ferroelectric behavior. The fitting parameters are presented in Table 6.1:

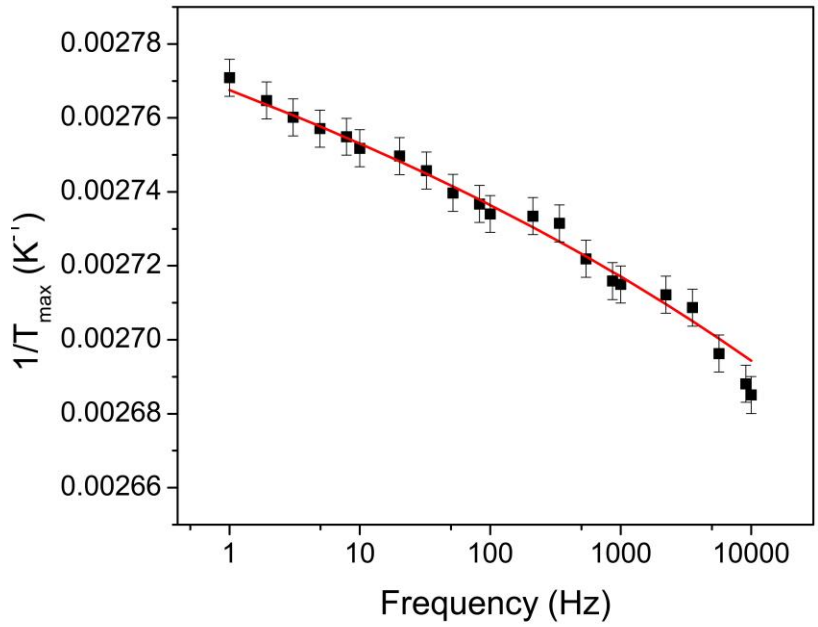

Figure 6.9 Vogel–Fulcher fitting of the dielectric permittivity of unpoled Crystal A (Data from Figure 6.7).

Table 6.1 Vogel-Fulcher Fitting Parameters

Parameter	Value	Standard Error (±)
T_{VF}	336.3 K	5.6
E_a	0.070 eV	0.001
f_0	1.58 x 10^{14} Hz	2.63 x 10^{12}

It is interesting to note that the V-F temperature, T_{VF} = 336 K is close to the depoling temperature, T_d = 56 °C = 329 K. This suggests that upon cooling, the dipole dynamic slows down and freezes out at $T_{VF} \approx T_d$, and a macroscopic ferroelectric phase develops, as revealed by the dielectric behavior of the poled crystal and by the ferroelectric hysteresis loop. The flux inclusions present in Crystal B resulted in defect conduction pathways which prevented dielectric and piezo-/ferroelectric measurements from having meaningful results, however, birefringence analysis can be used in order to determine the nature of the phase transitions for this crystal.

The variation of the optical retardation (proportional to birefringence) with respect to temperature [63] is shown in Figure 6.10 where the rhombohedral line was measured on Crystal A in the area circled in Figure 6.3 and the tetragonal curve was measured on

Crystal B in the area circled in Figure 6.4 upon heating. The retardation of the rhombohedral region shows a dramatic change in slope in the vicinity of 55 – 70 °C, which is close to the temperature at which the induced polarization decays, as shown in Figure 6.8, confirming the phase transition at T_d. It then gradually reduces to zero at 131 °C with a total loss of anisotropy.

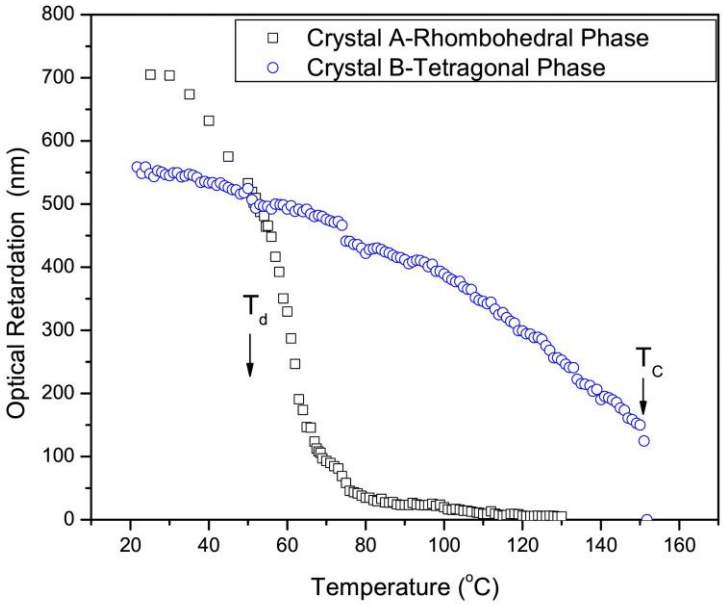

Figure 6.10 Optical retardation vs. temperature measured for Crystals A (339 μm thick) and B (46 μm thick).

In contrast, the apparent tetragonal phase in Crystal Platelet B shows a discontinuous change of domains with optical retardation dropping to zero sharply at T_C = 152 °C corresponding to the transition from the tetragonal phase to the isotropic pseudo-cubic phase. The disappearance of these distinct domains (and reappearance upon cooling) confirms this structural phase transition.

6.4.4 Ferroelectric and Piezoelectric Properties

Polarization-electric field [P(E)] relation of Crystal A was displayed and is shown in Figure 6.11. A maximum field of ± 23 kV/cm was applied to the sample, resulting in a (saturated) P(E) hysteresis loop. From this loop, a coercive field of 3.5 kV/cm and a remanent polarization of 21 $\mu C/cm^2$ can be extracted. The hysteresis loop reveals a

macroscopic ferroelectric state at room temperature, which transforms into the relaxor state, as indicated by the anomaly at T_d = 56 °C at all frequencies in the dielectric permittivity plot in Figure 6.8. The presence of this ferroelectric to relaxor phase transition (and vice versa) makes Crystal A an interesting relaxor ferroelectric material [5], [61], [62].

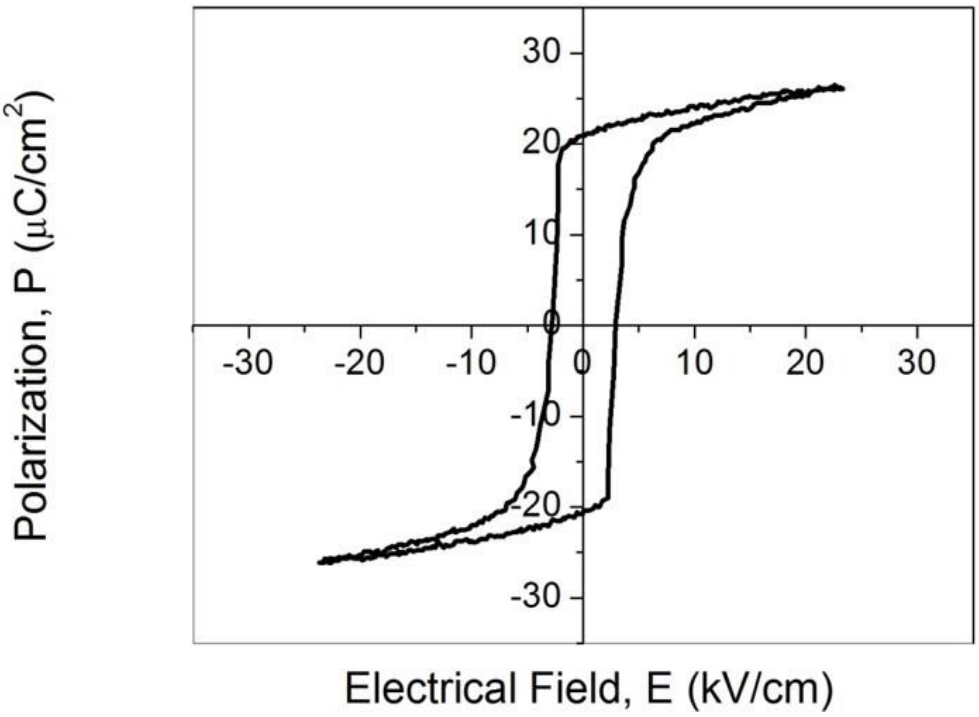

Figure 6.11 Polarization (*P*) vs. electric field (*E*) hysteresis loop displayed for Crystal A, showing ferroelectricity.

The piezoelectric coefficient, d_{33}, of Platelet A measured after poling by a field of 10.5 kV/cm was found to be 825 pC/N. This value is double that of any ceramic counterparts in the established ternary system [55], [56]. By comparing the values of T_C and room temperature ε' of Crystal A with those of the ceramics of the ternary system the composition of the crystals is estimated to be approximately 0.56PMN-0.20PT-0.24BZT, which lies close to the ternary MBP line [57]. Table 6.2 provides the comparison of the properties of Crystal A with those of a ternary ceramic of close composition:

Table 6.2 Comparison of Crystal A with a ceramic of $xPb(Mg_{1/3}Nb_{2/3})O_3$-$yPbTiO_3$-$zBi(Zn_{1/2}Ti_{1/2})O_3$ (d_{33}, E_C and ε' values are at 20 ºC)

Samples	X	Y	Z	T_C (°C)	d_{33} (pC/N)	E_C (kV/cm)	ε'
Ceramics	0.65	0.22	0.13	55	567	5.5	4960
Crystal	0.56*	0.20*	0.24*	56	825	3.5	3400-5130

*Composition estimated from ternary phase diagram [57]

6.5 Conclusions

Single crystals of the PMN-PT-BZT ternary system have been grown by the flux method. Analyses of the crystal morphology and microstructure reveal a layered mechanism for the crystal growth, and the formation of growth striation in the crystals. Varying growth conditions by a slower cooling rate has led to the reduction of growth striation, which is likely due to higher thermal and compositional stabilities within the melt. Nevertheless, compositional segregation still occurred, as attested by the coexistence of the rhombohedral (or pseudo-cubic) and tetragonal phases within the crystal, which is typical of solid solution system with compositions close to the MPB region, like the PMN-PT binary system.

The temperature and frequency dependences of the dielectric properties of Crystal A shows characteristic relaxor behavior, which satisfies the Vogel-Fulcher law, giving a rise to a freezing temperature T_{VF} = 336 K. Poling by an external field reveals a macroscopic ferroelectric phase at room temperature. This poled phase transforms into an ergodic relaxor state upon heating above a depoling temperature, T_d = 56 ºC, as revealed by an anomaly on the temperature dependence of dielectric permittivity at T_d, followed by dispersive relaxor peaks at $T_{max} > T_d$. Ferroelectric hysteresis loops were displayed with a coercive field E_C = 3.5 kV/cm and a remnant polarization P_r = 21 $\mu C/cm^2$. The poled crystal also exhibits a high piezoelectric coefficient, d_{33} = 825 pC/N, much higher than that of its ceramic counterparts.

The PMN-PT-BZT crystals provide a new example of relaxor materials in which, upon cooling, an ergodic relaxor state transforms into a macroscopic ferroelectric phase,

while the dynamics of polar nanoregions freezes (at about the same temperature). The interesting dielectric, piezoelectric and ferroelectric properties indicate that the ternary crystals can constitute a viable class of high-performance piezo-/ferroelectric crystals for a wide range of applications.

Chapter 7. Growth and Characterization of Piezo-/Ferroelectric $Pb(Mg_{1/3}Nb_{2/3})O_3$-$PbTiO_3$-$Bi(Zn_{1/2}Ti_{1/2})O_3$ Ternary Single Crystals II – Insights into the Relationship Between Composition, Structure and Properties

7.1 Abstract

In order to develop new high performance piezo-/ferroelectric materials, single crystals of the nominal composition $0.61Pb(Mg_{1/3}Nb_{2/3})O_3–0.312PbTiO_3–0.078Bi(Zn_{1/2}Ti_{1/2})O_3$ (PMN-PT-BZT) have been grown by high temperature solution (flux) growth in order to attain crystals of morphotropic phase boundary (MPB) type compositions. A large crystal block resulted that has many twinning points that served as separation planes for individual crystals. The individual crystals and the group of crystals as a whole had a high degree of compositional segregation due to changing melt concentration throughout the growth process. This segregation allowed for mechanistic insight into the growth of the PMN-PT-BZT crystal solid solution system, namely that early-stage crystals have a rhombohedral, more PMN-like character, showing relaxor ferroelectric behaviour, and late-stage crystals having more PT- like character, showing normal ferroelectric behaviour. The crystals in the as-grown block cross over the MPB region, due to the presence of rhombohedral, tetragonal and monoclinic phases. Evaluating the ferroelectric behaviour, the incorporation of BZT achieved the goal of “hardening” the PMN-PT binary solid solution system as both remnant polarization, P_r, and coercive field, E_C, showed improvement over the parent system.

7.2 Introduction

Relaxor ferroelectrics of the complex perovskite $A(BB')O_3$ are of increased interest due to their high piezoelectric performance over their ceramic counterparts. Leading research on relaxor ferroelectrics has focused on so-called second generation relaxor materials, e.g. $Pb(Mg_{1/3}Nb_{2/3})O_3–PbTiO_3$ [PMN-PT] and $Pb(Zn_{1/3}Nb_{2/3})O_3–PbTiO_3$ [PZN-PT]-type systems that have been modified with a third component in order to overcome some of the drawbacks of the binary systems, namely low coercive fields (E_c) and low phase transition temperatures (T_C) [2], [10]. Complex perovskites can exhibit

typical relaxor behavior with a diffuse maximum of dielectric permittivity (ε'), the temperature of which (T_{max}) increases with increasing frequency. This phenomenon is thought to arise due to the relaxation of polar nanoregions (PNRs) that form as a result of chemical order/disorder that prevent long-range polar order from developing which would cause a cooperative phase change, as in normal ferroelectric materials.

The (1-x)PMN-xPT relaxor-type ferroelectric materials are the leading high performance ferroelectric materials that are commercially manufactured [2], [15], [36]. Much effort has been put into determining how to refine the crystal growth process and achieve uniform crystals of larger sizes. On the other hand, to overcome the low field-stability and transition temperatures, other perovskite components have been combined with PMN-PT in order to harden the material's Curie temperature, T_C, and coercive field, E_C. Bismuth zinc titanate, $Bi(Zn_{1/2}Ti_{1/2})O_3$ [BZT], is a good candidate to form a solid solution with PMN-PT because Bi^{3+} and Pb^{2+} both have large atomic numbers and contain a stereochemically active $6s^2$ lone electron pair that makes their host lattice more polarizable and thereby introduces a higher degree of asymmetry into the unit cell and causing higher polarization. The addition of BZT has been shown to increase the Curie temperature (T_C) of the canonical ferroelectric $PbTiO_3$ [29], [30], a rare occurrence when forming solid solutions with lead titanate [25], [27]. This can also be seen in other lead-based ferroelectric systems when the addition of the Bi^{3+} ion increased the tetragonal distortion of the unit cell resulting in high tetragonality. However, the high tetragonality also has the disadvantage of increasing the coercive field, sometimes to a value higher than that of dielectric breakdown, making it impossible to pole the material at room temperature and difficult to switch the polarization to realize the potential of the material in devices.

In the previous chapter, exploratory growth of the $Pb(Mg_{1/3}Nb_{2/3})O_3$-$PbTiO_3$-$Bi(Zn_{1/2}Ti_{1/2})O_3$ (PMN-PT-BZT) single crystal system was conducted with an excess of $Bi(Zn_{1/2}Ti_{1/2})O_3$, which allowed the Bi^{3+} ion to be incorporated into the crystal structure. Large crystals were obtained that exhibited mainly rhombohedral symmetry in the bulk part (with a small volume of tetragonal regions at the edge of the grown crystal). The estimated composition falls in the rhombohedral region of the ternary phase diagram. In order to investigate the domain structure, phase symmetry, phase components, phase transitions and properties of the Morphotropic Phase Boundary (MPB)- related features, it is desirable to grow the PMN-PT-BZT crystals with composition around the ternary

MPB regions. After examining the ternary phase diagram shown in Figure 7.1 in this chapter, we chose the nominal composition of $0.61Pb(Mg_{1/3}Nb_{2/3})O_3–0.312PbTiO_3–0.078Bi(Zn_{1/2}Ti_{1/2})O_3$ which is in the tetragonal region of the ternary phase diagram, but close to the ternary MPB area, as the starting point to grow single crystals of compositions around the MPB. It is expected that, due to compositional segregation, the crystals grown in this process would exhibit a spectrum of different phases, symmetries and properties characteristic of the MPB's features. These studies will allow us to gain insights into the relationship between composition, crystal symmetry, domain structure, phase transitions and dielectric and piezoelectric behaviour to provide a better understanding of the nature of the MPB and related phenomena in this interesting ternary piezo-/ferroelectric system.

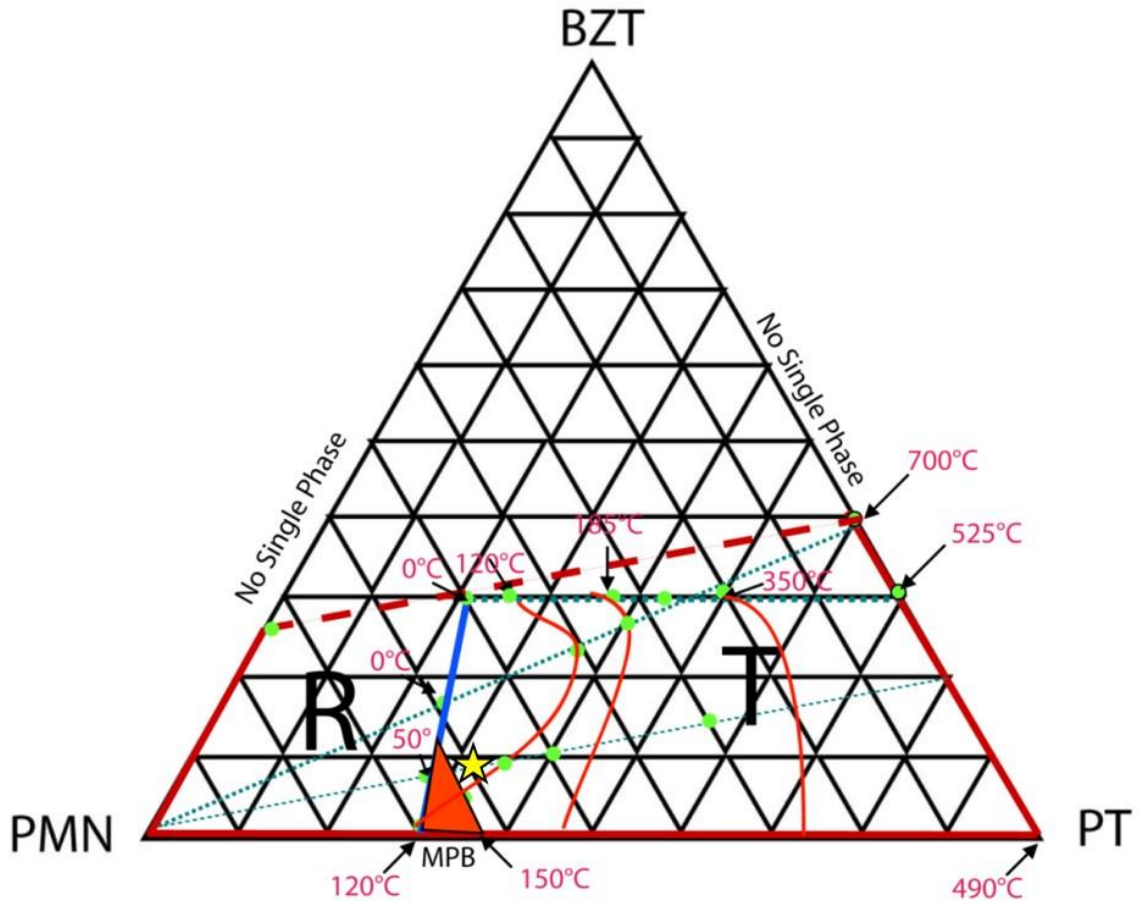

Figure 7.1 Ternary phase diagram of $Pb(Mg_{1/3}Nb_{2/3})O_3$-$PbTiO_3$-$Bi(Zn_{1/2}Ti_{1/2})O_3$ established by Dr H.N. Tailor with a star making the nominal composition ([57]**used with permission).**

7.3 Experimental

7.3.1 Crystal Growth and Sample Preparation

The high temperature solution (flux) method was employed for the growth of the ternary crystals of a nominal charge composition of $0.61Pb(Mg_{1/3}Nb_{2/3})O_3–0.312PbTiO_3–0.078Bi(Zn_{1/2}Ti_{1/2})O_3$. Stoichiometric amounts of high purity constituent metal oxides, PbO, TiO_2, MgO, Nb_2O_5, ZnO, and Bi_2O_3 were mixed in a mortar with a mixture of PbO and H_2BO_3 flux (in a 4:1 mole ratio). The flux:charge molar ratio of 6:1 (total flux + charge = 100g). The resulting mixture was loaded into a 50 cc platinum crucible that was then placed in a cylindrical crystal growth furnace. The growth set up is shown in Figure 7.2. The temperature was raised to 1070 °C over a period of 6 h and held for 24 h to ensure the complete melting of solute. The molten solution was then slowly cooled at a rate of 0.2 °C/h down to 900 °C, followed by natural furnace cooling to room temperature. The melt was visually inspected regularly through and optical hole to observe the formation of nuclei and monitor the progress of growth. The resulting crystals were then leached from the solidified melt using a hot 15% acetic acid solution, monitored at 24 hr intervals.

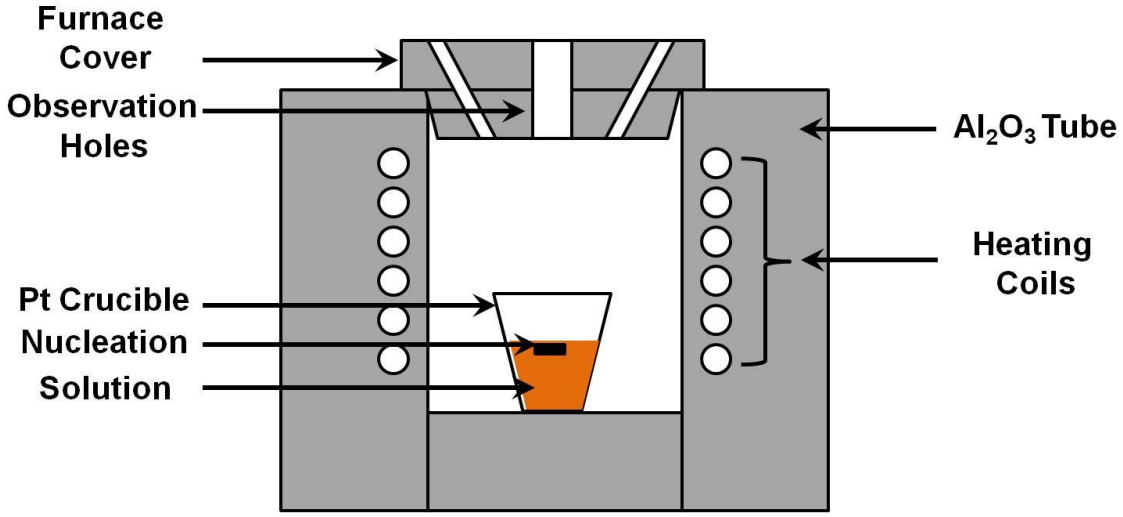

Figure 7.2 Cylindrical muffle set up furnace for single crystal growth from high temperature solid solution.

The as-grown, multinucleated crystal block was divided into 6 separate crystals (labelled A-F see Figure 7.3) which were cut along the interfaces of their twinning facets using a Fine #1 diamond wheel saw (0.006’ width). For optical and dielectric

characterizations, (001)-oriented platelets of the crystals were prepared by cutting parallel to the (001) crystallographic face using the same diamond wheel saw (0.006' width) and then polished with silicon carbide sand paper (220, 400, 600 grit) followed by 3M Al_2O_3 lapping sheets down to 5 to 3 μm to achieve mirror-quality surfaces and optical transparency (400-50 μm thick) for domain observation and optical measurements.

7.3.2 Structural Characterization by X-Ray Diffraction

The crystal structure of the as-grown crystals was examined by X-Ray powder diffraction by grinding a few of the as-grown crystals to a fine powder and recording its diffraction pattern (Bruker D8 Advance Diffractometer, 40 mA, 40 kV, step size = 0.02°/step, 2θ = 10° - 80°) at room temperature. The resulting pattern was analyzed using JADE XRD pattern processing software and TOPAS Academic software to determine the crystal symmetry and refine the lattice parameters.

7.3.3 Optical Domain and Structure Analysis by Polarized Light Microscopy

For optical studies, Polarized Light Microscopy (PLM) was performed using an Olympus BX60 microscope equipped with Olympus UC30 digital camera to study the domain structure, phase symmetry and phase transitions as well as to deduce the growth mechanism. Optical retardation (and thereby the birefringence) of the crystals was measured using an Olympus U-CBE compensator (e - line; λ = 546.1 nm) at varying temperatures (25 - 300 °C, at 0.5°/min) using a Linkham THMS600 heating stage controlled and monitored by Linkham TMS93 and LNP temperature control interfaces and the birefringence was calculated by dividing the optical retardation by the thickness of the platelet.

7.3.4 Dielectric, Piezoelectric and Ferroelectric Characterizations

To perform electrical characterization, the polished, parallel (001) crystal surfaces were first sputtered with gold layers (Anatech Hummer Sputter-Coater 6.2, 12 min., 15 mA plasma discharge current) as electrodes and gold wires were then attached to both surfaces of the samples using colloidal silver paste. The dielectric properties (permittivity, ε', and loss tangent, tanδ) were measured as a function of temperature

(from -50 ºC to 350 ºC at intervals of 3 ºC) at frequencies varying from 1 to 10^6 Hz using a Novocontrol Alpha high-resolution broadband dielectric analyzer. The measurements were performed under both zero-field-cooling (ZFC) and zero-field-heating (ZFH) conditions on both the unpoled samples and the samples poled using an electric field three times the coercive field (E_C) applied at room temperature. Ferroelectric hysteresis loops were displayed using a Radiant Technologies RT66A testing system, connected to a Trek 609E-6 High Voltage Bipolar Amplifier at a scan frequency of 100 Hz. Select samples were subsequently poled in silicon oil using a Stanton PS350 high voltage source prior to piezoelectric measurements by the Berlincourt method using an IACAS Model ZJ-6B d_{33} meter to obtain the piezoelectric coefficient, d_{33}.

7.4 Results and Discussion

7.4.1 Multinucleated Growth and Twinned Crystals

Figure 7.3 shows the images of (a) the as cooled crucible with the grown crystal in the melt and (b) the as-grown crystal after the melt was leached out. The growth yielded a large, as-grown crystal block that was found at the centre of the crucible, submerged in the solidified melt, Figure 7.3a). Careful examination of the morphology of the leached crystal block, Figure 7.3b), shows that it consists of a central crystal (F) with a pseudo-cubic shape, which is surrounded by other pieces of crystals (A, B, C, D, E) with rectangular shapes grown with different heights. Distinct growth steps exist between the different parts of the crystal block, which form the planes of separation for each part. These observations suggest that the large crystal block was grown from multiple nucleations, which have led to the growth of twinned crystals. These crystals were separated and studied individually. In addition to the twinning planes, regular growth steps are visible on the melt side of the crystal block, indicating a 2-dimensional, faceted growth mechanism [36], [64]. The grown crystals are of a light yellow colour, which gives rise to transparent platelets, suitable for optical characterization.

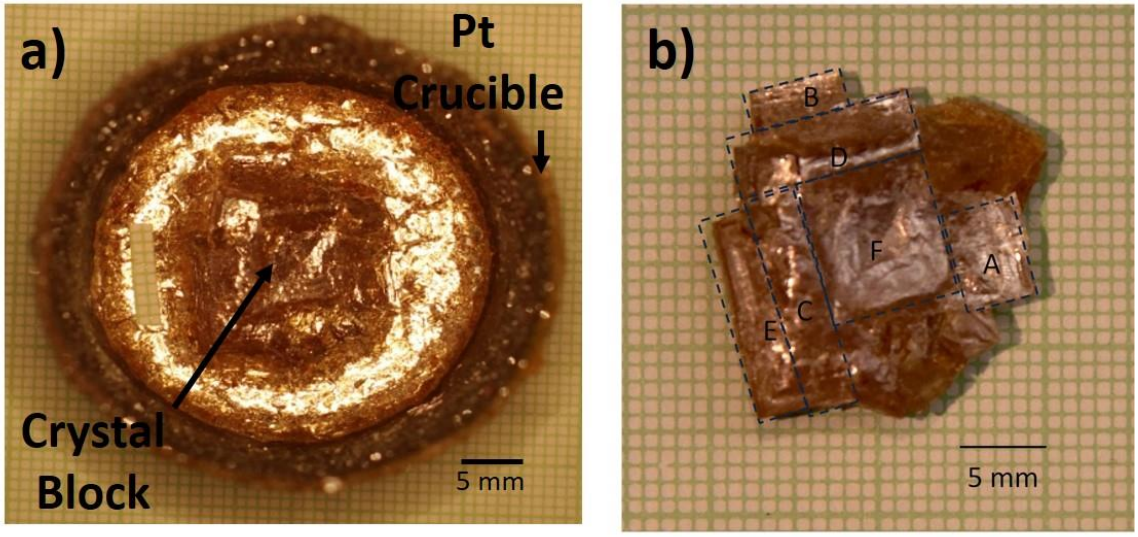

Figure 7.3 **a) As-cooled Pt crucible with as-grown PMN-PT-BZT crystal block in the middle of solidified flux; b) Grown PMN-PT-BZT crystal after leaching, with the growth sections marked by dashed lines and the corresponding crystals named as A, B, C, D, E and F.**

After cutting and polishing, the (001)-oriented platelets of the various crystals (A-F) appeared to be of high quality with uniform composition and very few inclusions. However, due to the changing concentration of the melt throughout the duration of the growth, it is very likely that the twinned crystals may have different actual compositions (as each of them could grow at a different stage), giving rise to compositional segregation, which in turn will affect the phase symmetry and properties of each crystal. Therefore, the twinned crystals will be studied separately in terms of their domain structure and dielectric and ferroelectric properties. Through these studies, trends about the composition variation of the resulting crystal can be concluded based on proximity to the central nucleation point. These conclusions will be utilized to hypothesize optimization of subsequent growths of these ternary single crystals for potential applications as electromechanical transducers.

7.4.2 Rhombohedral Ferroelectric Crystal A

This section reports on the domain patterns, phase symmetry, phase transitions, and dielectric and ferroelectric properties of Crystal A, shown shaded on the crystal sketch in Figure 7.4.

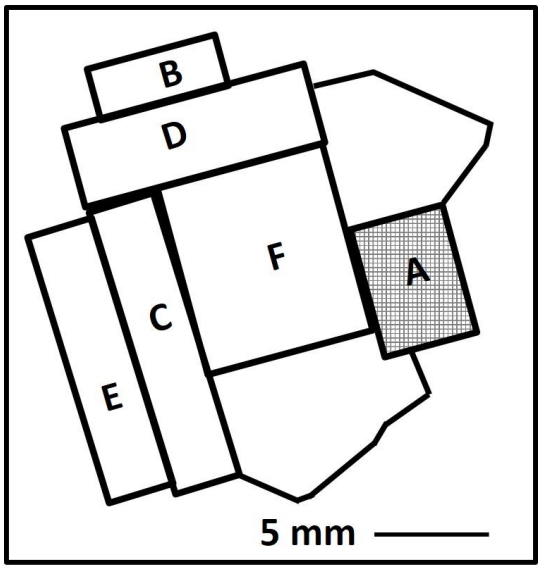

Figure 7.4 Sketch of the as-grown crystal block with Crystal A shaded.

A) Domain Structure and Crystal Symmetry

The domain structure is analyzed by Polarized Light Microscopy (PLM). Figure 7.5 (a-b) shows the PLM images at room temperature of a (001)-platelet of Crystal A with an average thickness of 94 µm, with crossed polarizers (a) parallel to and (b) at a 45° to the $<100>_{cub}$ direction. The majority of the birefringent domains exhibit extinction along the <110> direction (as marked by the red ellipse) which indicates a rhombohedral symmetry according to the optical crystallographic principle [36], thus Crystal A can be considered of rhombohedral symmetry at room temperature.

B) Variations of Domain Structure, Birefringence and Phase Transitions

To study the variations of domain structure and the phase transitions as a function of temperature, the (001) platelet of Crystal A was heated in a Linkham THMS600 stage in which the domain structure was observed and the birefringence measured. Figure 7.5(a-h) shows the domain structure of the crystal at various temperatures upon heating. At room temperature, T = 25 °C, Figure 7.5(a-b), the crystal shows a rhombohedral symmetry throughout the platelet as confirmed by the clear extinction along the <110> direction. It contains fine, overlapping lamella domains. Upon heating to the temperature of T = 72.6 °C, some regions with an extinction direction along the <100> direction start to appear, as well as the faint appearance of mutually perpendicular (90°) domains with domain walls along the <110> direction, as seen in the areas marked with 'T' in Figure 7.5(c-d), which indicate a new phase of tetragonal

symmetry [36]. This is evidence of a phase change from the rhombohedral phase to a tetragonal phase. Upon further heating, the tetragonal phase region grows at the expense of the rhombohedral phase such that at the temperature T = 96 °C, the majority of the platelet now displays domains with extinction parallel to the <100> direction with well defined domain patterns and 90° and 180° domain walls, indicating a complete transition to the tetragonal phase symmetry, shown in Figure 7.5(e-f). As the crystal was further heated to T = 192 °C, as seen in Figure 7.5(g-h), the tetragonal domains are found to transform to an isotropic state as the crystal is in extinction at all angles between crossed polarizers, indicating the transformation from the tetragonal phase to a cubic phase. It is important to note that this transition temperature can be more accurately determined by the measurement of birefringence (see below). Therefore, upon heating, the rhombohedral phase of Crystal A transforms first to the tetragonal phase and then to the cubic phase of the highest symmetry.

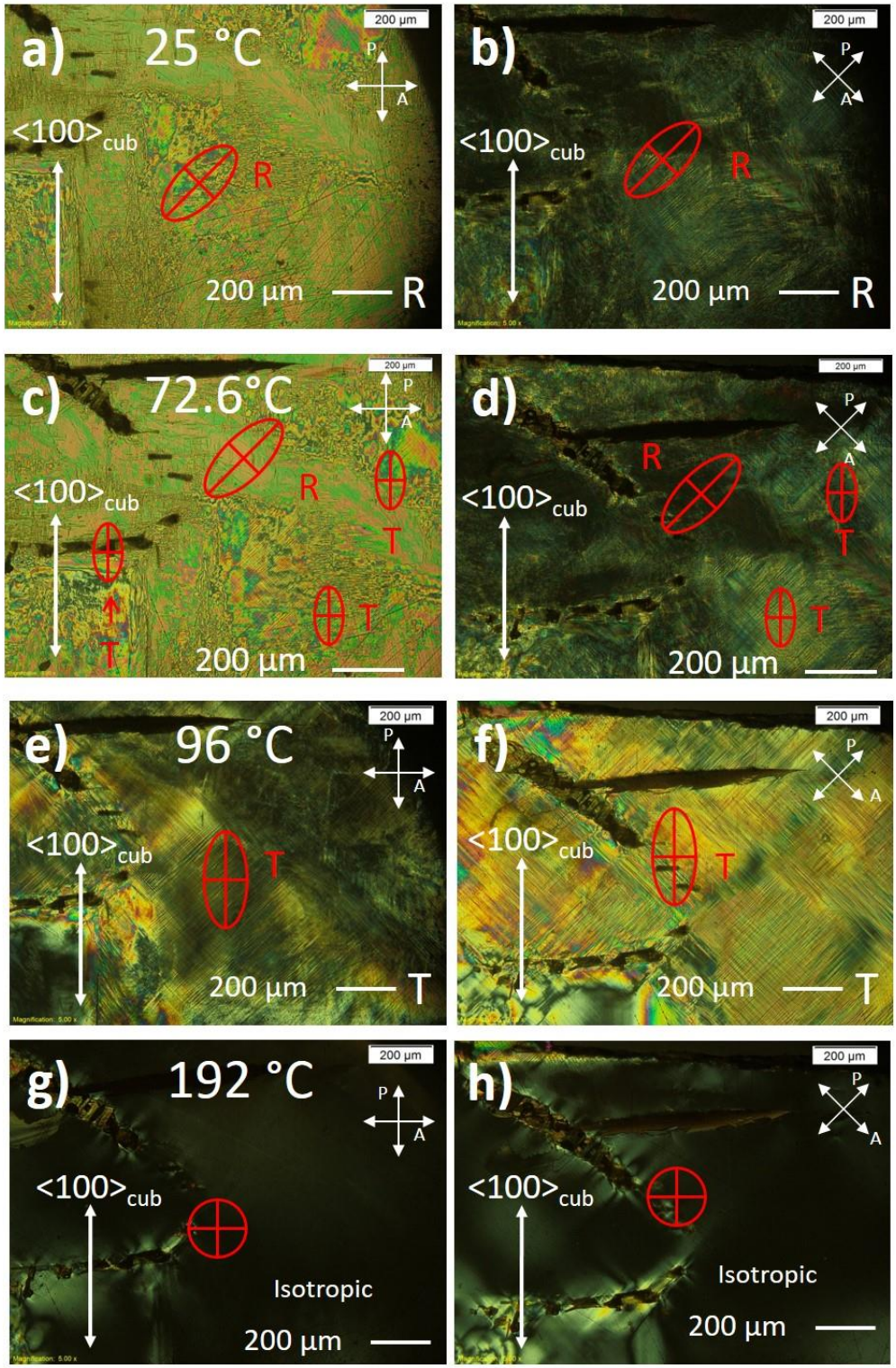

Figure 7.5 **Domain structures of a (001)-platelet of Crystal A observed under PLM with crossed polarizers parallel to (a, c, e and g), and at a 45° angle to (b, d, f and h), the <100> direction, at room temperature (a and b), and upon heating to 72.6 °C (c and d), 96 °C (e and f). and 192 °C (g and h).**

The well-defined domain pattern of the tetragonal phase of Crystal A and reduced birefringence over the rhombohedral phase allows for the measurement of the birefringence, Δn, and its variation with temperature. The results of those measurements are shown in Figure 7.6. Upon heating, the birefringence of the tetragonal domain decreases gradually until 160 °C – 165 °C where it undergoes a steep drop, followed by a slow decline and vanishing to nearly zero. Therefore, the tetragonal to cubic phase transition takes place at $T_C \approx 165$ °C There is residual birefringence that remains at high temperatures which can be attributed to stress-induced birefringence. Upon cooling, birefringence gradually increases until 150 °C where it jumps sharply. This corresponds to the cubic to tetragonal phase transition. Therefore, a thermal hysteresis of 15 °C is observed for the phase transition between heating and cooling. The sudden change in birefringence and thermal hysteresis indicate that the tetragonal ↔ cubic phase transition is of first order.

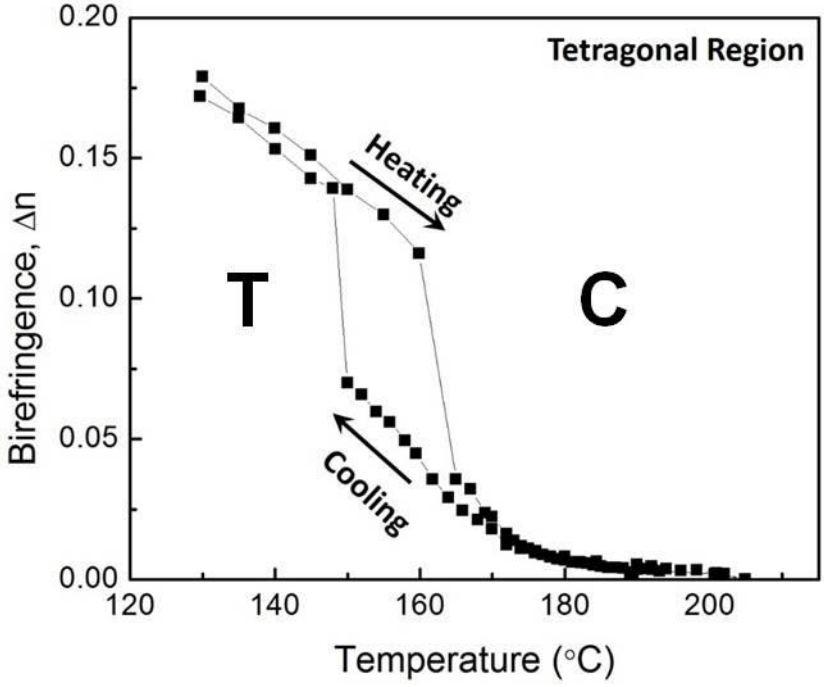

Figure 7.6 **Variation of the birefringence of the tetragonal domain of the (001)-platelet of Crystal A, measured upon heating and cooling, revealing a first-order phase transition between the tetragonal and cubic phases.**

C) Dielectric Properties

The real part of relative dielectric permittivity (dielectric constant), ε', was measured on an unpoled (001) platelet of Crystal A, at different frequencies, as a function of temperature upon cooling and the results are shown in Figure 7.7. It can be seen that with an increase in temperature the dielectric constant increases with significant frequency dispersion occurring at about 95 °C, corresponding to the rhombohedral to tetragonal phase transition temperature (T_{RT}). Further heating gives rise to a sharp dielectric peak at 150 °C, corresponding to the cubic to tetragonal phase transition temperature, T_C. Note that the temperature of the dielectric peaks, T_{max}, does not vary with frequency, indicating a normal ferroelectric phase transition at T_C rather than a relaxor behavior as seen in Figure 7.25. This T_C value is in good agreement with the T_C determined from the variation of birefringence, Δn, upon cooling (150 °C).

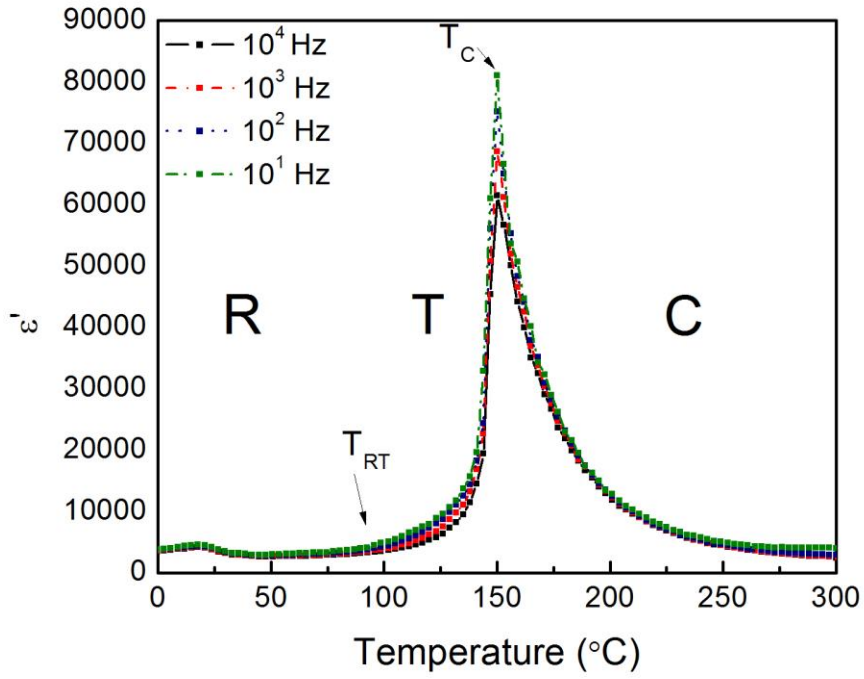

Figure 7.7 Variation of the dielectric permittivity with temperature, measured upon zero-field-cooling at various frequencies for a (001)-platelet of Crystal A.

D) Ferroelectric Properties

The polarization as a function of a bipolar electric field was measured on a (001) platelet of Crystal A, the results of which are shown in Figure 7.8. This measurement

shows hysteresis behavior characteristic of ferroelectric property. The remnant polarization, P_r, of the crystal is found to be 46 μC/cm^2, which is a significant (70%) increase over the property of PMN-PT solid solution (which shows P_r = 27 μC/cm^2 [65]). The coercive field, E_C, which exhibits a value of +3 kV/cm in the forward/positive direction and at -7 kV/cm in the reverse direction of the applied field, giving rise to an asymmetric loop with regard to the field applied (with an off-centering of -4 kV/cm). This off-centering could be due to oxygen vacancies present in the crystal in a gradient that result in domain pinning and an internal bias field that assists bipolar switching in one direction and hinders it in the opposite direction [10], [11].

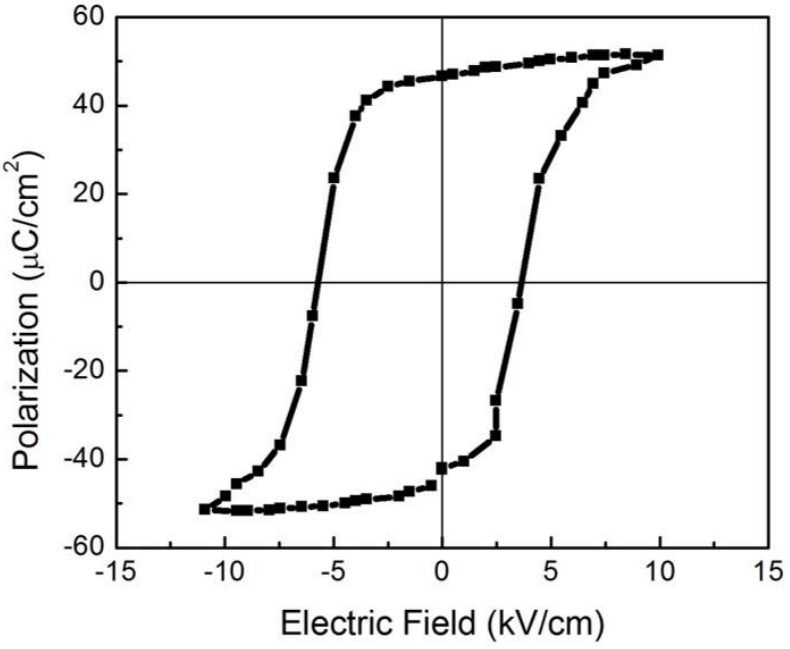

Figure 7.8 Variation of polarization vs. bipolar electric field measured on a (001)-oriented platelet of Crystal A at room temperature.

It is expected that repeated switching (cycling) of the polarization vs. bipolar field could remove the domain pinning effects to some extent. Figure 7.9 displays the measurement of polarization as a function of electric field after n = 7 P(E) cycles (e.g. at the (n + 1)th switch). Notably, the P(E) loop becomes more symmetric while retaining its high remnant polarization from the initial measurement. The bipolar coercive fields are $+E_C$ = +5.5 kV/cm and $-E_C$ = -4.5 kV/cm, with a much smaller off-centering (+1 kV/cm). Interestingly, the loop shifts to the positive field side, suggesting that the internal bias fields have been significantly diminished and the residual field is reversed due to domain wall and/or oxygen vacancy motions upon P(E) switching. This confirms the above

suggestion that internal bias field is due to lattice defects, namely oxygen vacancies that pin domain walls. The resulting average coercive field is larger than +/- ⎪4.5⎪ kV/cm, which is higher than the E_C of PMN-PT single crystals [65].

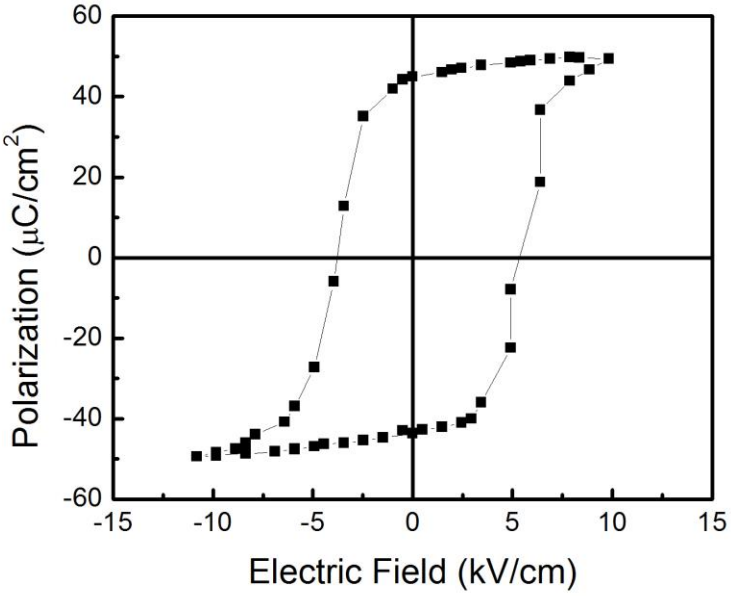

Figure 7.9 Variation of polarization vs. bipolar electric field after n = 7 cycles of bipolar field application, measured on a (001)-oriented platelet of Crystal A at room temperature.

E) Summary of Crystal A

Crystal A crystallizes in a rhombohedral symmetry and experiences phase transitions from a rhombohedral to a tetragonal phase at T_{RT} = 96 °C and then to a cubic at T_C = 150 °C as evidenced by the analysis of domain patterns and the measurements of birefringence, and dielectric permittivity as a function of temperature. The phase transition from tetragonal to cubic is a normal ferroelectric transition with no sign of relaxor behavior. It is found to be of first order character, as characterized by the discontinued variation in birefringence with clear thermal hysteresis. The ferroelectric property of the crystal is confirmed by the polarization – electric field hysteresis loops, which show an increased remnant polarization and enhances coercive field compared with the parent binary system PMN-PT, indicating improvement of the properties by partial substitution of BZT, and confirming the effect of hardening by BZT substitution, as initially envisioned in our research rationale.

7.4.3 Crystals of Mixed Rhombohedral and Tetragonal Phases - B & E

This section reports on the studies of domain patterns, phase symmetry, and dielectric and ferroelectric properties of Crystals B and E, shown shaded in Figure 7.10. For the sake of brevity, only the results on Crystal B will be presented in extensive detail as the properties of Crystal E are similar to Crystal B.

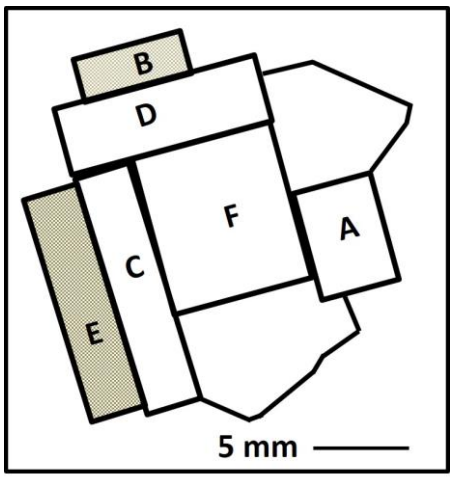

Figure 7.10 Sketch of the as-grown crystal block with Crystals B and E shaded.

A) Domain Patterns and Symmetry

The domain structure is analyzed by Polarized Light Microscopy (PLM). Figure 7.11 shows the PLM images at room temperature, of a (001)-oriented platelet of Crystal B with an average thickness of 107 µm, with crossed polarizers parallel to a) and at a 45° to b) the $<100>_{cub}$ direction. As in Crystal A, there are some regions of Crystal B that show extinction along the <110> direction and have fine, overlapping lamellar domains. These domain features indicate areas of rhombohedral symmetry that is marked with an ellipse and an 'R' for clarity. Different from Crystal A, areas at room temperature, there are significant regions of the crystal that show extinction along the <100> direction and have distinct domain patterns with 90° mutually perpendicular domain walls, indicating a tetragonal phase, marked with an ellipse parallel to the <100> direction and a 'T' for clarity. These analyses indicate that Crystal B contains a mixture of rhombohedral and tetragonal phases and that the composition of Crystals B and E have deviated from that of Crystal A.

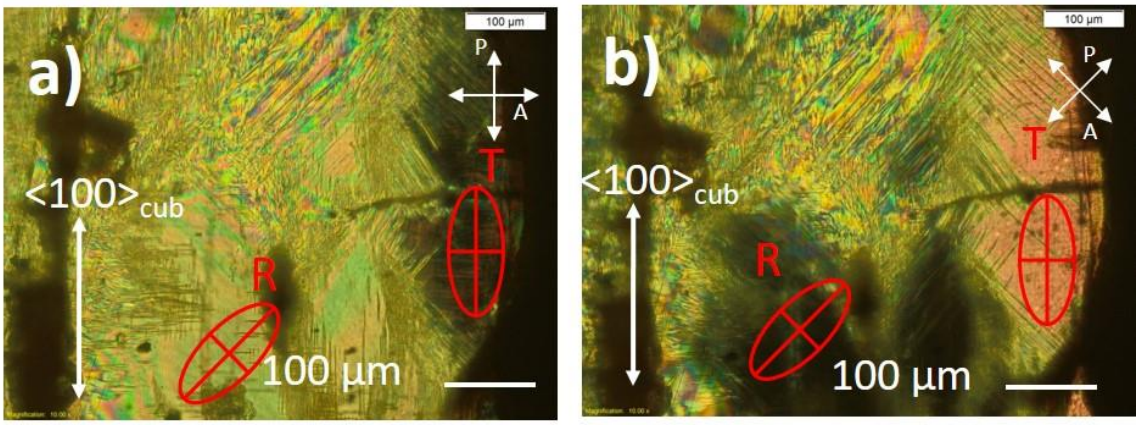

Figure 7.11 Domain structures of a (001)-platelet of Crystal B between crossed polarizers at room temperature parallel to (a), and at a 45° angle to (b), the <100> direction

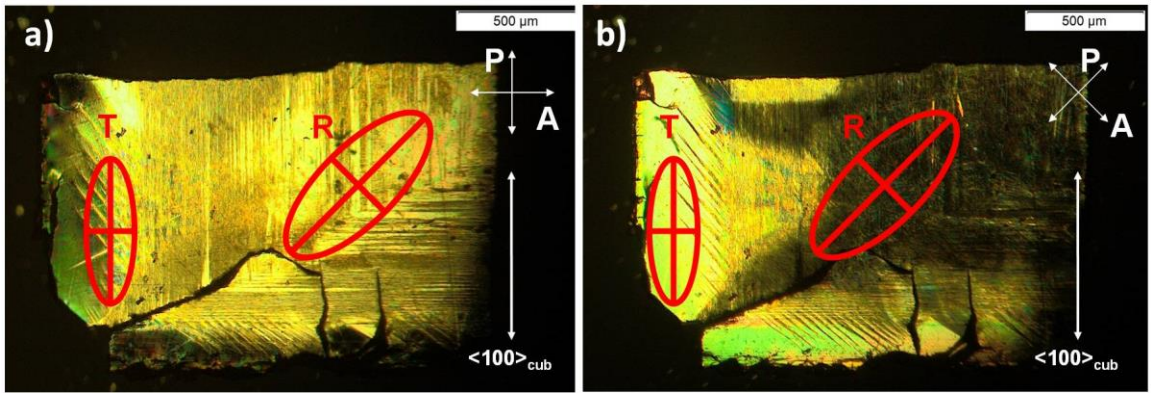

Figure 7.12 Domain structures of a (001)-platelet of between crossed polarizers Crystal E parallel to (a), and at a 45° angle to (b) the <100> direction.

Figure 7.12 shows the PLM images, at room temperature, of Crystal E of (001)-orientation with an average thickness of 80 µm, with crossed polarizers parallel to, a), and at a 45° to, b), the $<100>_{cub}$ direction. As in crystal B, there is a large region that displays extinction along the <110> direction, indicating a rhombohedral symmetry, marked by a 45° ellipse and 'R'. At the same time, the area towards the left edge of the crystal exhibits extinction along the <100> direction, indicating a tetragonal symmetry (T). Therefore, Crystal E also contains coexisting rhombohedral and tetragonal phases. The coexisting R and T phases in Crystal B and E suggests that their compositions are close to the morphotropic phase boundary (MPB) region.

B) Domain Structure, Birefringence and Phase Transitions

The platelet of crystal B was heated in a Linkham THMS600 stage and its domain structure was observed during this process. Figure 7.13 shows the domain patterns imaged at various temperatures upon heating. Figure 7.13(a-b) corresponds to the domain structures at T = 51.2 °C with the crossed polarizers at a 45° angle to, and parallel to, the <100> direction respectively. It can be seen that, compared with the domain patterns at room temperature, (Figure 7.11(a-b)), the volume of the rhombohedral phase has been slightly reduced while the tetragonal phase has gained in area, indicating the gradual transformation from rhombohedral to tetragonal symmetry. As the temperature is increased to T = 66.5 °C, Figure 7.13(c-d), there is still a coexistence of rhombohedral and tetragonal phases, but the tetragonal region has grown substantially at the cost of the rhombohedral phase, as evidenced by more of the platelet showing extinction along the <100> direction, indicating a tetragonal phase. Figure 7.13(e-f) shows that the tetragonal phase persists upon further heating to 91.0 °C, at which the rhombohedral phase has completely transformed to the tetragonal phase, as evidenced by the whole of the crystal showing extinction along the <100> direction.

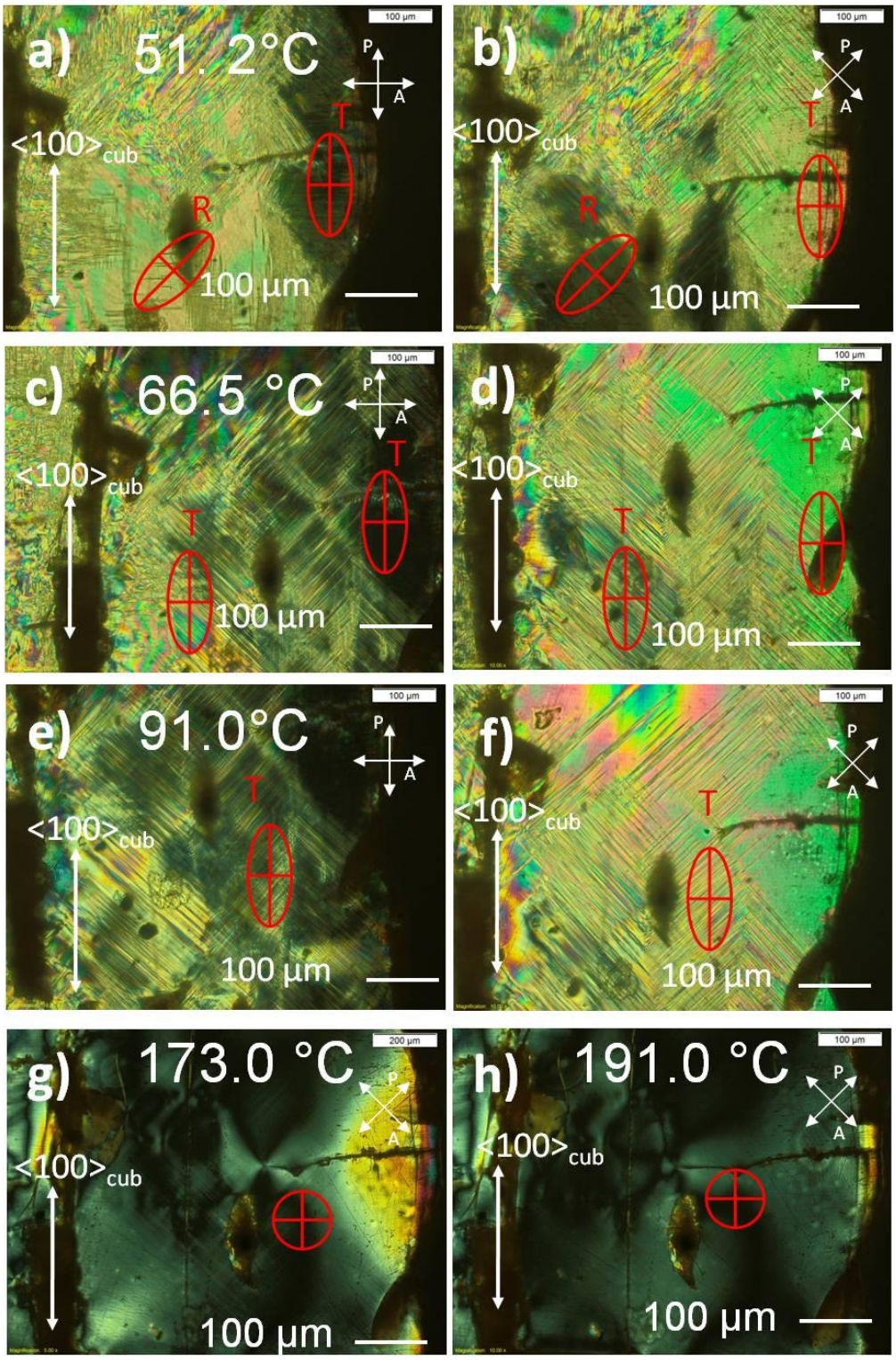

Figure 7.13 **PLM images of the (001) platelet of Crystal B, showing domain patterns observed with crossed polarizers parallel to (a, c, and e), and at a 45° angle to (b, d, f, g and h), the <100> direction at 51.2 °C (a and b), 66.5 °C (c and d), 91.0 °C (e-f), 173.0 °C(g), and 191.0 °C (h).**

At the high temperature of T_C = 173.0 °C, shown in Figure 7.13(g), the crystal transitions from the tetragonal phase to a cubic phase as evidenced by the crystal being in extinction at all angles to the crossed polarizers. There is some weak, seemingly stress induced residual birefringence that disappears upon further heating to T = 191.0 °C, as shown in Figure 7.13(h). Thus, the phase sequence of Crystal B can be described as follows: at room temperature, there is a coexistence of rhombohedral and tetragonal phases. Upon heating, the rhombohedral phase transforms gradually to tetragonal and at T_{RT} = 90 °C it is completely in the tetragonal phase. The tetragonal phase persists to high temperatures until T_C = 173.0 °C, where it transitions to an isotropic cubic phase.

C) Dielectric Properties

The variation of the dielectric permittivity (dielectric constant), ε', measured as a function of temperature at various frequencies, upon zero-field-cooling conditions for a (001)-platelet of Crystal B is shown in Figure 7.14. It can be seen upon cooling there is a broad and major permittivity peak that appears at T_C = 155 °C, which indicates the cubic to tetragonal phase transition. Although the peak values depend on frequency, the peak temperature, T_{max}, does not vary with frequency, indicating a normal ferroelectric phase transition with some degree of diffuseness. Upon further cooling, a similar peak appears at ≅ 82 °C, as a shoulder or kink, corresponding to the onset of the rhombohedral phase, leading to a mixture of tetragonal and rhombohedral phases. Note that this result is in agreement with the phase sequence deduced from the PLM studies and the lower temperatures found here are due to the cooling process, indicating a thermal hysteresis for both transitions.

Looking at the permittivity maximum at T = 155 °C, the peak is diffuse and not as sharp as the normal ferroelectric phase transition of Crystal A. Analysis of the variation of the temperature of maximum permittivity, T_{max}, with frequency indicates that T_{max} stays constant regardless of frequency, indicating that is a Curie temperature, T_C, rather than a frequency dependent T_{max} of a relaxation process. This type of diffuse transition results from chemical disorder and composition inhomogeneity in the solid solution crystal. There are many regions of similar but not uniform composition, each region will have a slightly different T_C, yet that difference is too small to be resolved by the instrument, leading to the overlap of the numerous transitions and thereby, a broadening of the dielectric peak for the paraelectric to ferroelectric transition. This broad transition is in

agreement with the domain transformation observed by PLM in which the tetragonal to cubic phase transition took place over a broad temperature range from T = 140 – 170 °C, before becoming a completely isotropic, paraelectric phase.

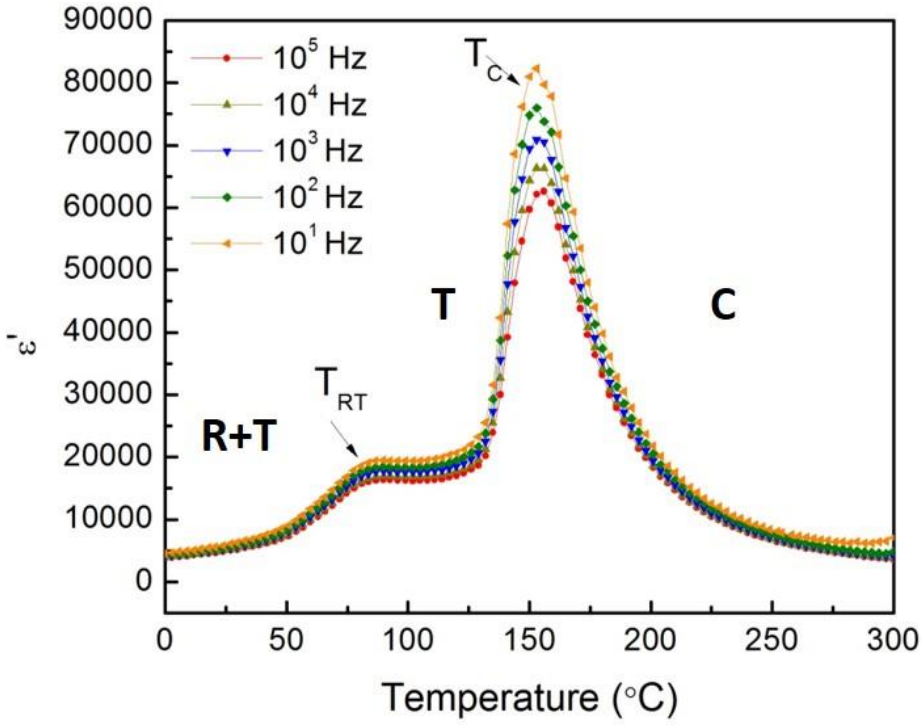

Figure 7.14 Variation of dielectric permittivity with temperature at varying frequencies measured on an unpoled, (001)- platelet of Crystal B upon zero-field-cooling (ZFC).

D) Ferroelectric Characterization

Figure 7.15 shows the variation of polarization (P) with bipolar electric field (E) for a (001) platelet of Crystal B. The measurement shows a well-developed and saturated P(E) hysteresis loop, confirming the normal ferroelectric property for the material. The crystal retains a high remnant polarization, P_r = 37 μC/cm^2, greater than that of the parent binary compound PMN-PT. Additionally, the coercive field is measured to be 4 kV/cm. In comparison to Crystal A, the loop appears to be symmetrical, indicating the absence of any internal bias fields, possibly created by crystal defects, that could influence the dipolar switching behaviour.

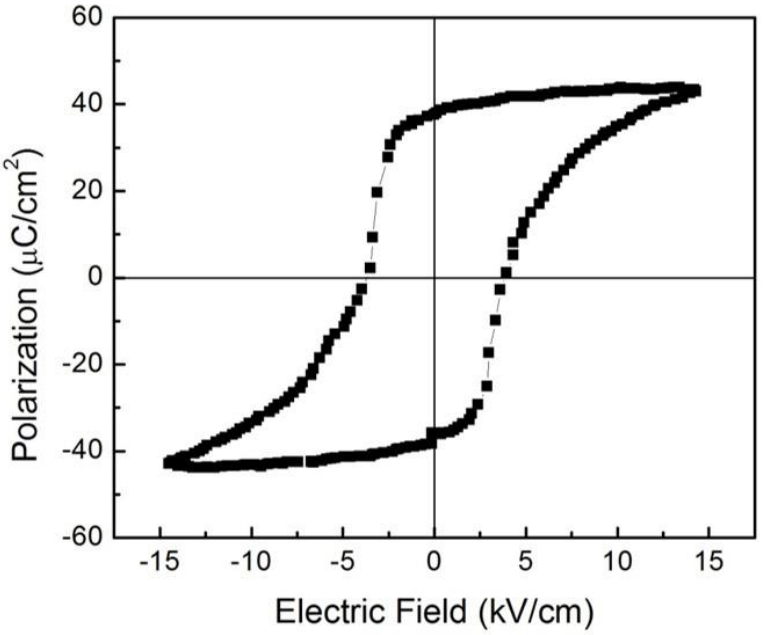

Figure 7.15 Variation of polarization (P) with electric field (E) for a (001)-platelet of Crystal B showing a typical ferroelectric hysteresis loop.

E) Summary on Crystals B and E

Crystal B and Crystal E exhibit the coexistence of rhombohedral and tetragonal phases at room temperature, indicating that the composition is close to the MPB region of the ternary system, with some degree of composition segregation. Upon heating Crystal B, the tetragonal phase takes over the rhombohedral phase gradually and the crystal transforms completely to the tetragonal symmetry at $T_{RT} \approx 90$ °C. Further heating yields a subsequent phase transition from tetragonal to cubic that occurs over a broad temperature range of $T_C = 140 – 170$ °C. The major broad dielectric peak reveals an average $T_C = 155$ °C upon cooling, with no shift in T_{max} with frequency, indicating a diffuse ferroelectric phase transition, possibly resulting from chemical disorder and inhomogeneity in the composition. The crystal shows improved ferroelectric properties over the PMN-PT parent compound, as well as a more symmetrical hysteresis loop than Crystal A.

7.4.4 Crystal of MPB Compositions (C)

This section reports on the domain patterns, phase transitions, dielectric and ferroelectric properties of Crystal C, shown shaded in Figure 7.16.

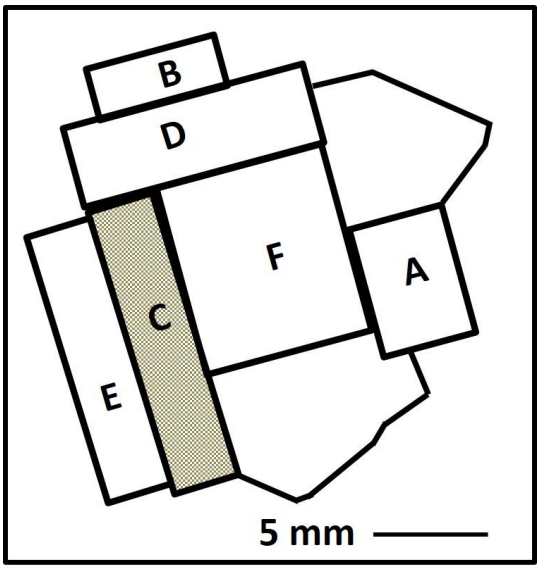

Figure 7.16 Sketch of the as-grown crystal block with Crystal C shaded.

A) Domain Patterns and Phase Symmetry

The domain structure is analyzed by Polarized Light Microscopy (PLM). Figure 7.17 shows the PLM images at room temperature, of a (001)-oriented platelet Crystal C with an average thickness of 88 µm, observed with crossed polarizers parallel to (a), and at a 45° to (b), the $<100>_{cub}$ direction. As seen in Crystals B and E, Crystal C exhibits coexistence of phases. The main part of the crystal shows domains with extinction along the <110> direction, indicating a rhombohedral symmetry, R, marked by the ellipse oriented at a 45° to the <100> direction. The right-side (edge) of the crystal shows extinction along the <100> direction, indicating a tetragonal, T, symmetry, marked by the ellipse that is parallel to the <100> direction. In addition, there is a region that shows extinction neither along the <100>, nor in the <110> directions, but at an angle in between, i.e. at 31° from the <100> direction. This is indicative of the presence of a lower symmetry phase, i.e., a monoclinic phase. The observed coexistence of rhombohedral, tetragonal and monoclinic phases in this crystal suggests that its composition falls in the morphotropic phase boundary (MPB) region.

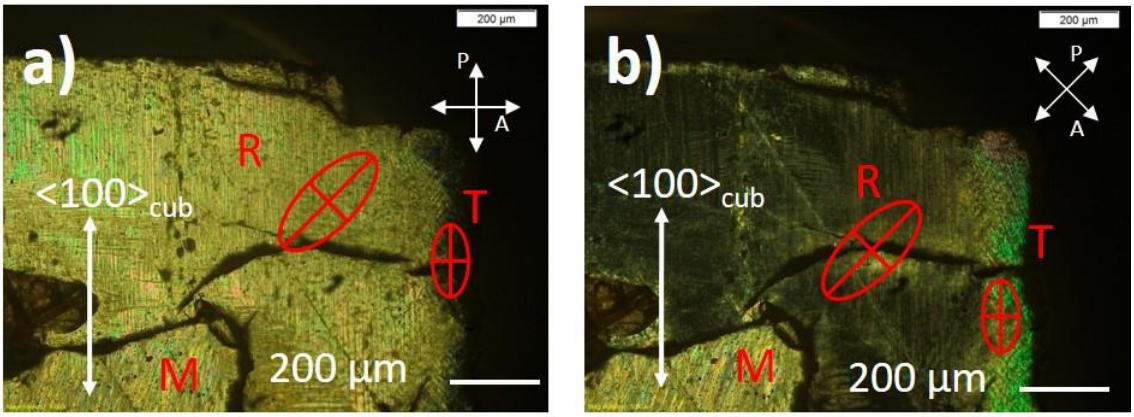

Figure 7.17 Domain patterns for a (001)-platelet of Crystal C at room temperature, between crossed polarizers parallel to (a), and at a 45° angle to (b), the <100> direction.

B) Domain Structure and Phase Transitions

The (001)-platelet of Crystal C is heated in a Linkham THMS600 stage and the domain structure is observed during this process. Figure 7.18 shows the domain structure of the crystal at various temperatures upon heating. Figure 7.18(a-b) shows the crystal platelet at T = 55.0 °C. As the temperature rises above room temperature, the tetragonal phase grows at the expense of the rhombohedral phase, as evidenced by the expansion of the right-hand side region that is in extinction in the <100> direction at the expense of the region in extinction in the <110> direction. In contrast, the apparent monoclinic region appears unchanged. This trend continues upon heating further to T = 80.1 °C, shown in Figure 7.18(c-d), where a larger volume of the crystal has transformed to the tetragonal phase with extinction in the <100> direction, this gradual transformation from rhombohedral to tetragonal phase is evidence of the MPB phase transition, similar to Crystal B. Figure 7.18(e-f) shows that upon further heating to T= 112 °C, the apparent monoclinic phase transitions to the tetragonal symmetry as it now shows extinction in the <100> direction. In addition, the majority of the crystal is in the tetragonal phase with only some areas retaining rhombohedral symmetry with extinction along the <110> direction. Further heating to T = 192 °C leads to the transition from tetragonal phase to an isotropic cubic phase, as evidenced by the crystal being in extinction at all angles between crossed polarizers as shown in Figure 7.18(g-h).

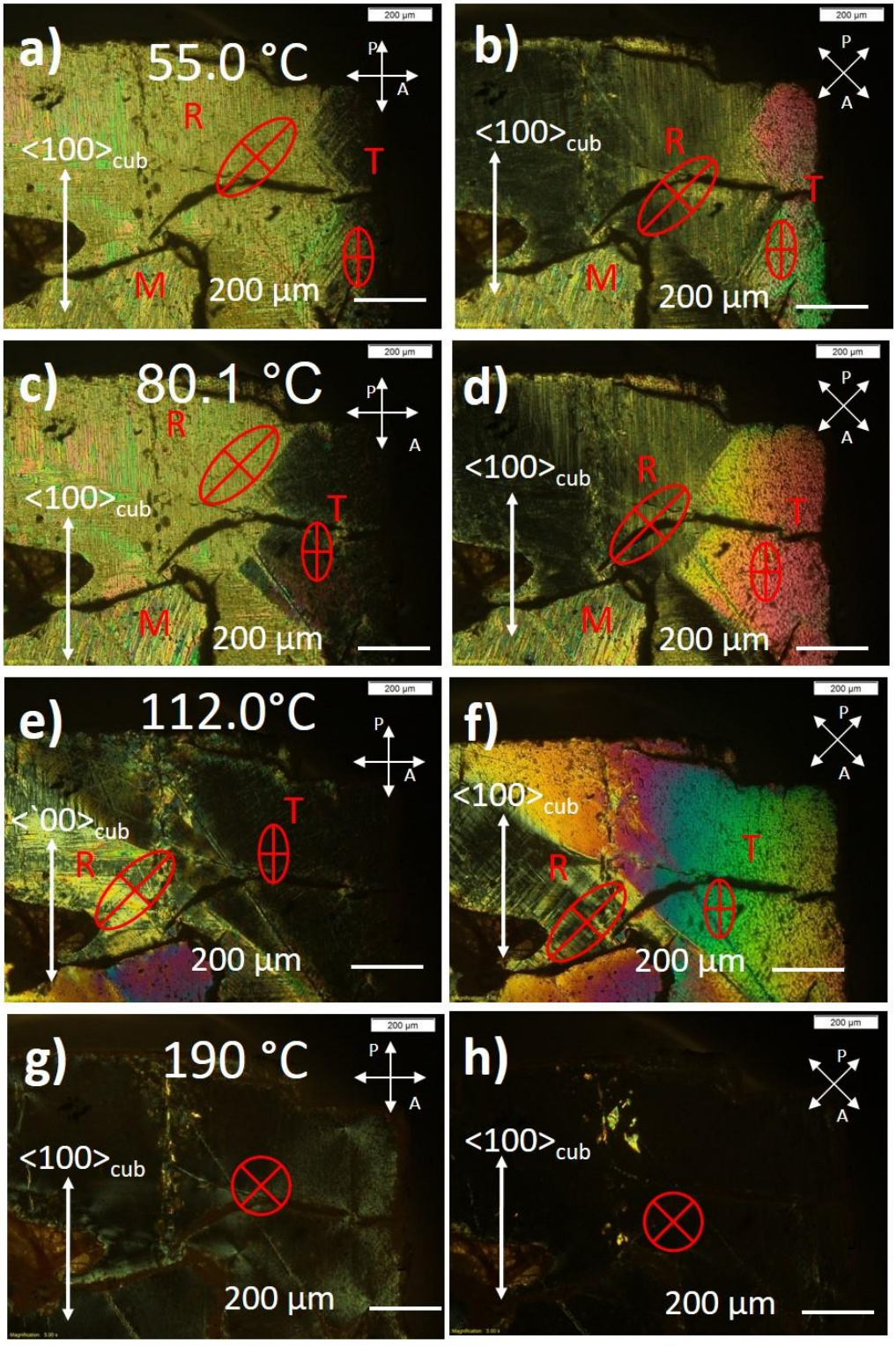

Figure 7.18 **PLM images of the (001)-platelet of Crystal C showing the domain pattern parallel to (a, c, e, and g), and at a 45° angle to (b, d, f, and h), the crossed polarizers at 55.0 °C (a and b), 80.1 °C (c and d), 112.0 °C (e and f), and 190 °C (g and h).**

Further insight into the symmetry of the phases present in Crystal C can be gained from examining the variation of extinction angles with respect to the <100> crystallographic direction as a function of temperature, shown in Figure 7.19. From room temperature to T = 67 °C, all three areas measured retain constant extinction angles, with the extinction of the tetragonal and rhombohedral phases along the <100> and <100> directions respectively, and that of the monoclinic phase at a 31° angle to the <100> direction. Upon heating above 67 °C, two changes occur. First, at T = 71 °C, the extinction angle of the monoclinic phase begins to decrease with respect to the <001> direction. Second, at T = 93 °C, the area of rhombohedral symmetry transforms to tetragonal symmetry, as evidenced by the sudden change in its extinction angle from 45° to 90°/0° with respect to the <100> direction. Upon further heating above 71 °C, the extinction angle of the M phase continues to decrease, resulting from the rotation of its crystallographic axis, which is characteristic of the monoclinic symmetry. At T = 110 °C, the monoclinic phase transforms to the tetragonal phase with its extinction angle sharply changing from 15° to 90°/0° to the <100> direction. Upon further heating, the tetragonal phase persists in the whole of the crystal until T ≅185 °C in which the crystal turns to extinction at all angles between the crossed polarizers, entering a cubic symmetry.

These measurements confirm the coexistence of tetragonal, rhombohedral and monoclinic phases in Crystal C and support the conclusion that the composition of Crystal C is in the morphotropic phase boundary (MPB) region of the ternary phase diagram.

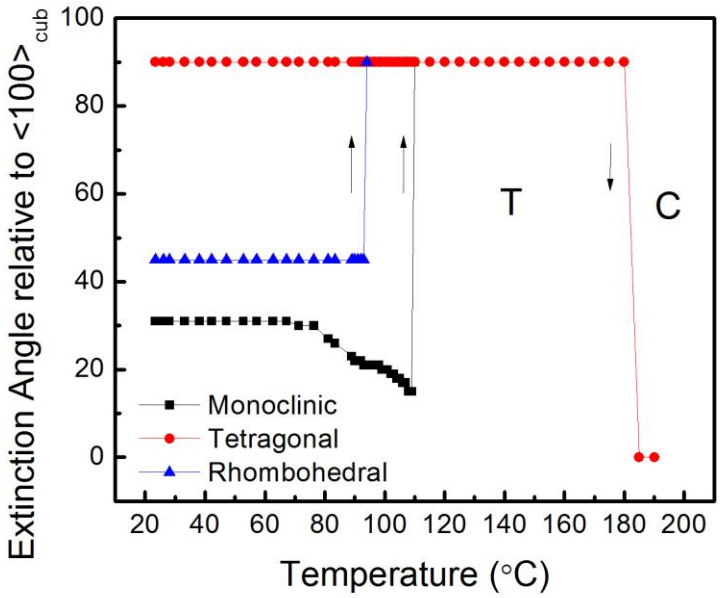

Figure 7.19 Variation of the extinction angle with respect to the <100>$_{cub}$ direction with temperature for the rhombohedral, tetragonal and monoclinic regions of Crystal C.

C) Ferroelectric Characterization

Figure 7.20 shows the variation of polarization (P) with a bipolar electric field (E) for a (001)-oriented platelet of Crystal C. A symmetrical, and saturated P(E) loop is displayed, indicating normal ferroelectric properties at room temperature with a coercive field of E_c = 3.5 kV/cm and a remnant polarization of P_r = 34 μC/cm^2. Both E_c and P_r values are an improvement over the parent compound of PMN-PT, though a decrease from the properties found in Crystal A and B.

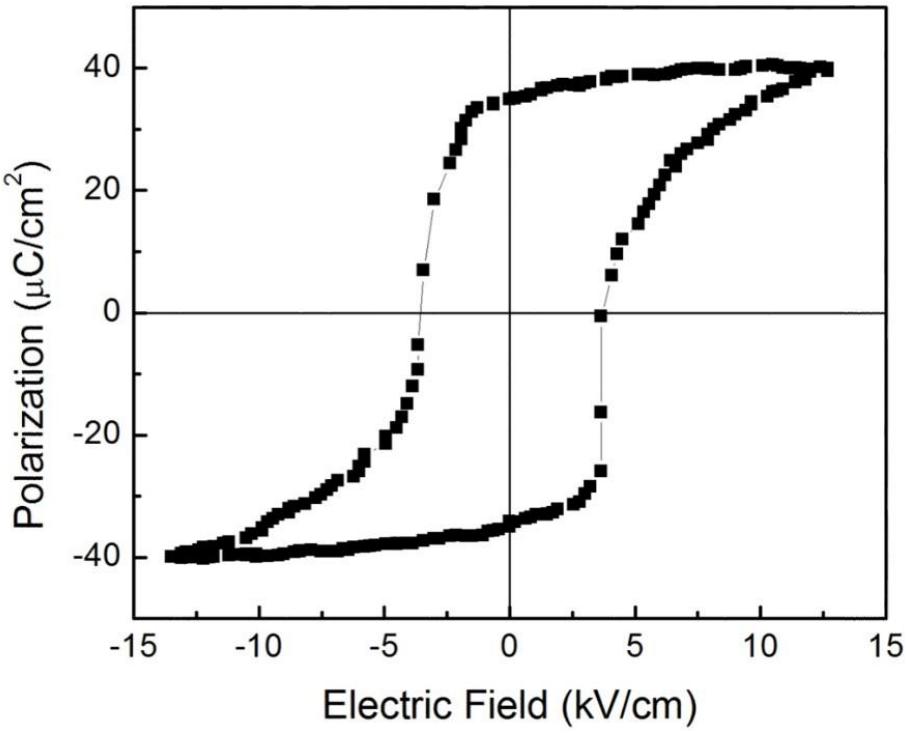

Figure 7.20 Variation of polarization (P) with electric field (E) for a (001)-platelet of Crystal C, showing a typical ferroelectric hysteresis loop.

D) Summary of Crystal C

Crystal C is found to exhibit the coexistence of rhombohedral, tetragonal and monoclinic phases at room temperature, characteristic of a composition that is within the morphotropic phase boundary region. Upon heating, both the rhombohedral and monoclinic phases transition to the tetragonal phase before the tetragonal phase transforms to a high temperature, cubic, paraelectric phase. In addition, Crystal C exhibits normal ferroelectric properties at room temperature, and its P_r and E_c, are improved over those of the parent compound PMN-PT.

7.4.5 Crystal of Relaxor Ferroelectric Behaviour (D)

This section reports on the domain patterns, symmetry, dielectric and ferroelectric properties of Crystal D, shown shaded in Figure 7.21.

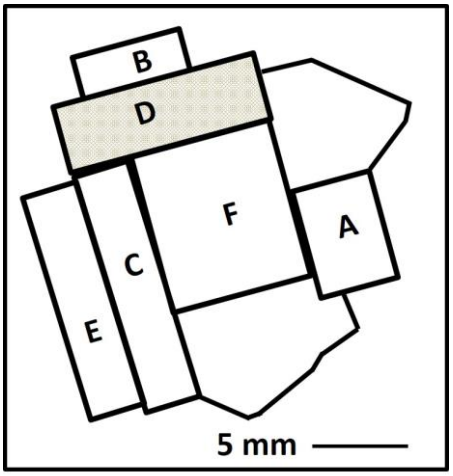

Figure 7.21 Sketch of the crystal block showing crystal D shaded.

A) Domain Patterns and Crystal Symmetry

The domain structure is analyzed by Polarized Light Microscopy (PLM). Figure 7.22 shows the PLM images and domain pattern at room temperature, of a (001)-platelet of Crystal D with an average thickness of 125 µm, with crossed polarizers parallel to (a), and at a 45° to (b), the $<100>_{cub}$ direction. It can be seen that crystal exhibits a uniform extinction along the <110> direction, indicating a single rhombohedral symmetry throughout the crystal.

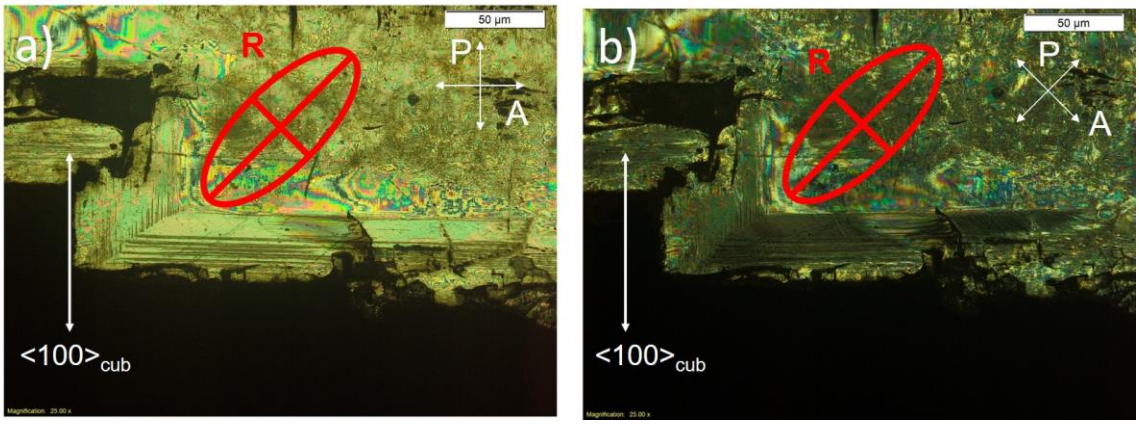

Figure 7.22 Domain patterns for a (001)-platelet of Crystal D at room temperature, between crossed polarizers parallel to (a), and at a 45° angle to (b), the <100> direction.

B) Domain Structure, Birefringence and Phase Transitions

The platelet of Crystal D was heated in a Linkham THMS600 stage in which the domain structure was observed during this process. Figure 7.23(a-b) shows the domain

structure of the crystal at T = 58 °C. The body of the crystal is in extinction along the <110> direction and has a fine, lamellar domain pattern, consistent with rhombohedral symmetry indicated by the ellipse at a 45° to the <100> direction. Upon heating, the extinction angle shifts from the <110> direction to the <100> direction, indicating that the rhombohedral phase is overtaken by a tetragonal phase, Figure 7.23(c-d) shows the crystal at T = 104 °C, at which point the rhombohedral to tetragonal transition is nearly complete. Upon further heating to T = 136 °C, the tetragonal phase transforms to an isotropic cubic phase, as evidenced by the crystal being in extinction at all angles between crossed polarizers with small areas still exhibiting residual, weak birefringence, as shown in Figure 7.23(e-f). At T = 151.0 °C, shown in Figure 7.23(g-h), the transition to cubic is complete and the crystal displays extinction at all angles with the exception of very small areas with weak, stress induced birefringence occurring near the cracks and inclusions in the crystal.

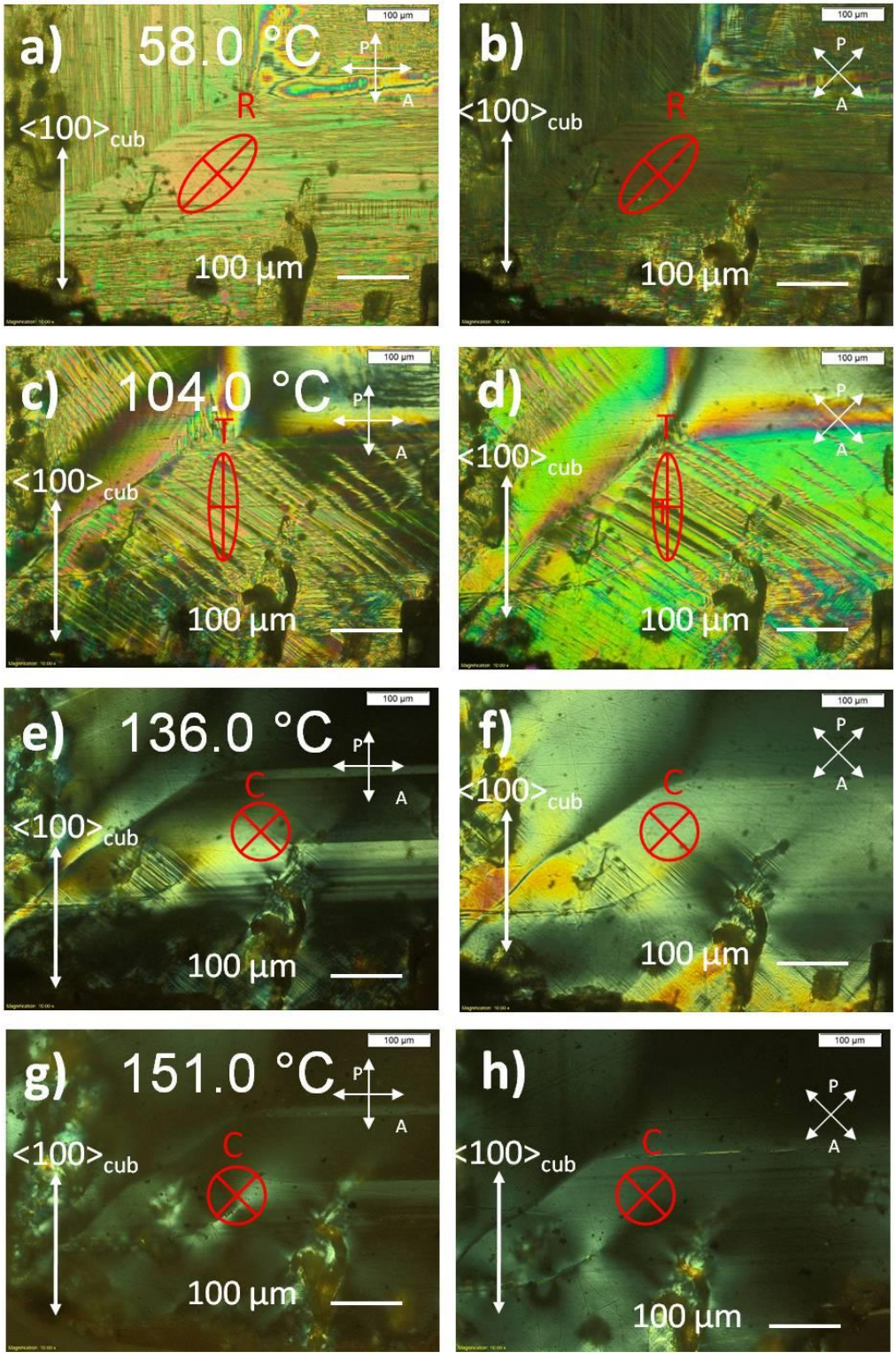

Figure 7.23 **PLM images of a (001)-platelet of Crystal D showing the domain structures observed with crossed polarizers parallel to (a, c, e, and g) and at a 45° angle to (b, d, f and h), crossed polarizers at 58.0 °C (a and b), 104.0 °C (c and d), 136.0 °C (e and f), 151.0 °C (g and h).**

Figure 7.24 shows the birefringence, Δn, as it varies with temperature for the high temperature tetragonal phase of a (001) platelet of Crystal D. As the temperature increases, Δn slowly decreases up to the temperature of T = 134.0 °C at which it undergoes a sharp decrease, and then gradually decreases to zero at high temperatures. This further evidence of the phase transition from tetragonal to cubic symmetry.

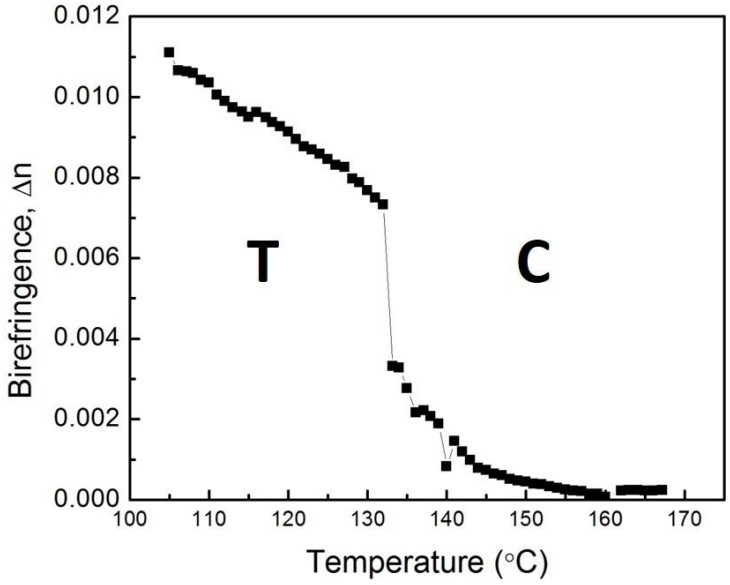

Figure 7.24 Variation of birefringence with temperature for (001)-platelet of Crystal D showing the high-temperature tetragonal to cubic phase transition.

C) Dielectric Properties

The variation of dielectric permittivity (dielectric constant), ε', as a function of temperature measured at various frequencies in zero-field conditions upon cooling is shown in Figure 7.25 for a (001)-platelet of Crystal D. In the dielectric curve a broad, diffuse permittivity maximum can be seen at $T_{max} \approx 130$ °C, which seems to indicate the transition from cubic to tetragonal phases. It is interesting to note that the temperature of maximum permittivity, T_{max}, varies with frequency, indicating some type of dielectric relaxation process that causes a frequency dispersion, potentially displaying some degree of relaxor behaviour. The temperature range of the transition is in agreement with the transition observed by PLM. Upon further cooling, there is a second anomaly in the permittivity curve at T = 90 °C that correlates to the symmetry change from

tetragonal phase to rhombohedral phase. While the dielectric anomaly at this phase transition shows some dispersion, there is no change in the phase transition temperature with frequency, suggesting a transition between two ferroelectric phases.

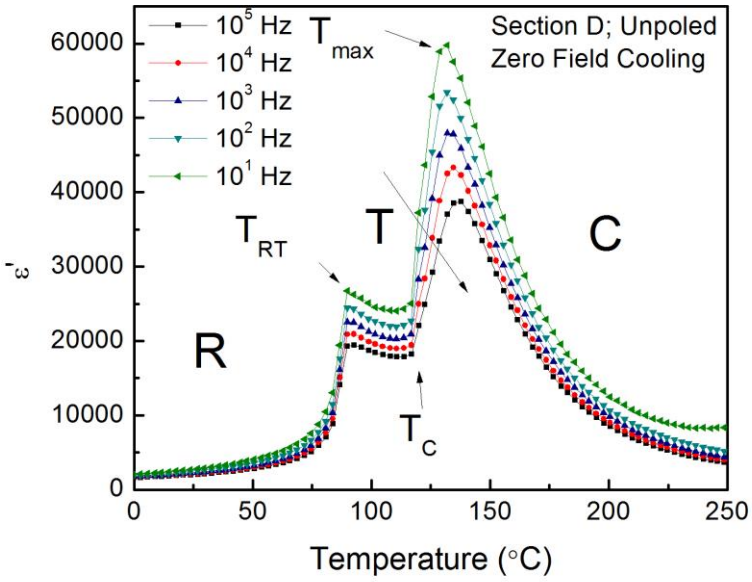

Figure 7.25 Variation of the dielectric permittivity as a function of temperature for an unpoled (001)-platelet of Crystal D, measured at various frquencies in zero-field-cooling conditions.

In order to analyze the dispersion of the high temperature, diffuse permittivity peak, the temperature of maximum permittivity, T_{max}, are plotted against their respective frequencies of measurement, and shown in Figure 7.26. This plot can be fit to the Vogel-Fulcher relationship:

$$f = f_0 exp\left(\frac{-E_A}{k_B(T_{max} - T_{VF})}\right)$$

where f is the frequency, T_{max} is the temperature of maximum permittivity in Kelvin, and f_0, $-E_A$ and T_{VF} are fitting parameters. Satisfactory fitting of T_{max} and f to the Vogel-Fulcher relationship typically indicates relaxor ferroelectric behaviour [5].

Based on this fitting, the following relaxation parameters can be extracted: f_0= 3.924 x 10^{11} Hz, E_a= 0.01923 eV and T_{VF}= 395.048 K. It is notable that the freezing temperature of polar nanoregions, T_{VF}, is in very close agreement with T_C of the

ferroelectric to relaxor phase transition observed in Figure 7.25. The onset frequency of dipolar switching, f_0, is reasonable as it is within the order of magnitude of phonon vibration frequencies [5], [18].

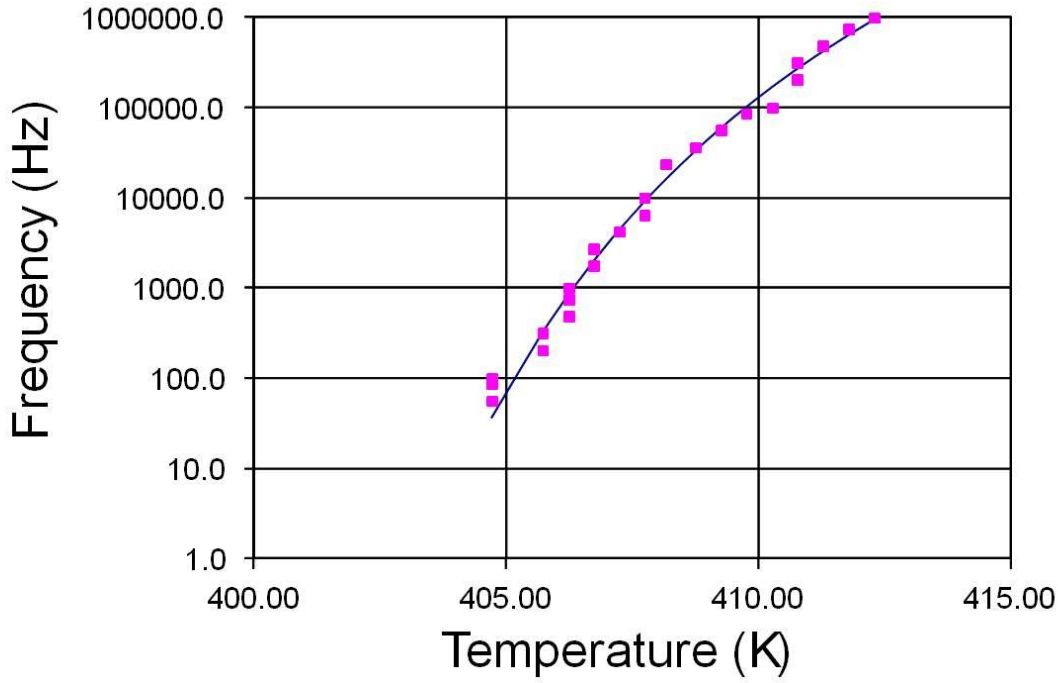

Figure 7.26 Relationship between the temperature of maximum permittivity, T_{max}, and the measurement frequencies, f, for Crystal D, which fits well to the Vogel-Fulcher relation.

D) Ferroelectric Characterization

Figure 7.27 shows the variation of polarization (P) with a bipolar electric field (E) for a (001) platelet of Crystal D, measured at room temperature. The measurements reveal a well saturated, symmetrical hysteresis loop, indicative of normal ferroelectric behavior for the rhombohedral phase. The remanent polarization, P_r = 28 μC/cm^2 is less than the values for P_r obtained for other crystals in the crystal block, but it is still an improvement over the value for PMN-PT32 of P_r = 27 μC/cm^2 [65]. The coercive field, E_c = 3.5 kV/cm again is lower than the that of other crystals in the block but is an improvement over the parent compound, improving the field strength of the material.

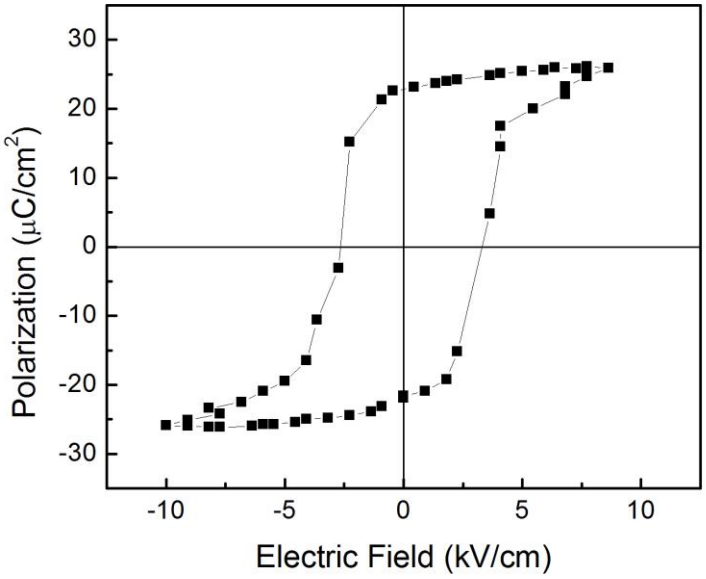

Figure 7.27 Variation of polarization (P) with electric field (E) for a (001)-platelet of Crystal D showing a typical ferroelectric hysteresis loop at room temperature.

E) Summary of Crystal D

Crystal D is found to exhibit rhombohedral symmetry at room temperature. Upon heating, the rhombohedral phase transitions to a tetragonal phase and then an isotropic cubic phase. The dielectric properties of the high temperature, broad phase transition show typical relaxor behavior with the frequency dispersion of the major peaks around $T_{max} \cong 130$ °C. The dispersion of T_{max} can be fit to the Vogel-Fulcher relationship, confirming the relaxor behavior at high temperatures. In addition, Crystal D exhibits well saturated, normal ferroelectric hysteresis loops at room temperature that have a comparable remnant polarization, $P_{r,}$, to PMN-PT and a coercive field, E_c, that is greater than PMN-PT at room temperature, yielding an overall improvement of properties due to increased field stability.

7.4.6 Electric Field Poling and Induced Metastable Phases in Crystal F

This section reports on the domain patterns, symmetry, dielectric and ferroelectric properties of Crystal F, shown shaded in Figure 7.28.

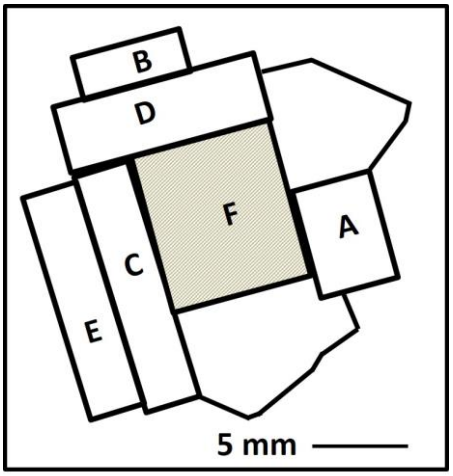

Figure 7.28 Sketch of the as-grown crystal block with Crystal F shaded.

A) Domain Patterns and Phase Symmetry

Figure 7.29 shows the PLM images and domain pattern at room temperature, of a (001)-platelet of Crystal F with an average thickness of 41 µm, with crossed polarizers parallel to (a) and at a 45° to (b) the $<100>_{cub}$ direction. The domains of Crystal F appear to be weakly birefringent, which could result from overlapping domains that partially cancel out the birefringence, and overall extinction along the <110> direction of the crystal, indicating a rhombohedral symmetry throughout the crystal.

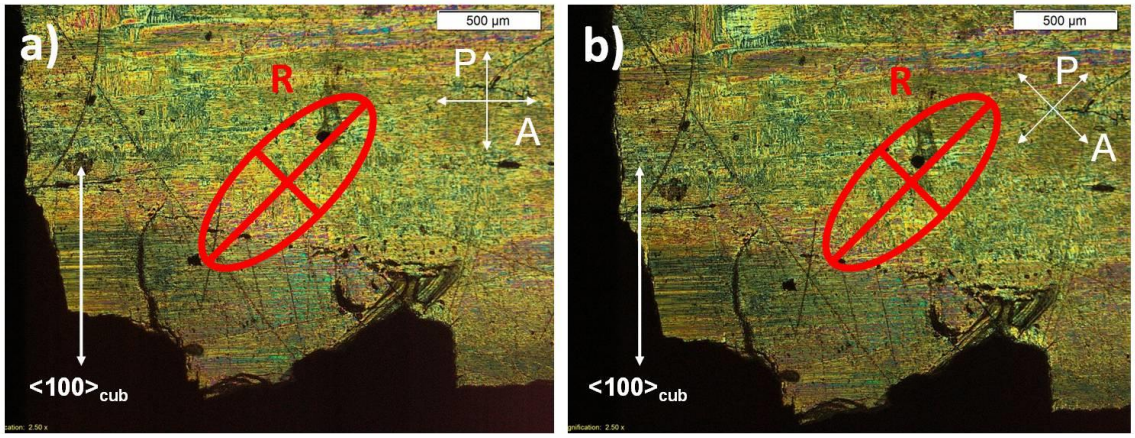

Figure 7.29 Domain structure of a (001)-platelet of Crystal F observed under PLM at room temperature, between crossed polarizers parallel to (a), and at a 45° angle to (b) the <100> direction.

Further insights into the nature of the domain patterning can be revealed by examining changes in the domain pattern upon poling the crystal platelet perpendicular to the (001) polished face. A poled area of Crystal F is shown in Figure 7.30. What is

shown is that with an applied field of 12 kV/cm, the finer, overlapping domains have transformed into a large area with homogeneous extinction along the <110> direction seen in Figure 7.30(a). This domain enlargement arises as a result of electric field poling, which switches 4 of the rhombohedral 'down' domains (polarizations) to 'up' and significantly reduces the number of domains and domain walls, leading to larger R-domains. It is interesting to note from Figure 7.30b that some areas exhibit extinction along the <100> direction, which seems to indicate a tetragonal phase induced from the rhombohedral phase by the electric field applied along the <001>, as circled and marked with 'T'. This process is illustrated in Figure 7.32, step ii). This area will be examined in greater detail below.

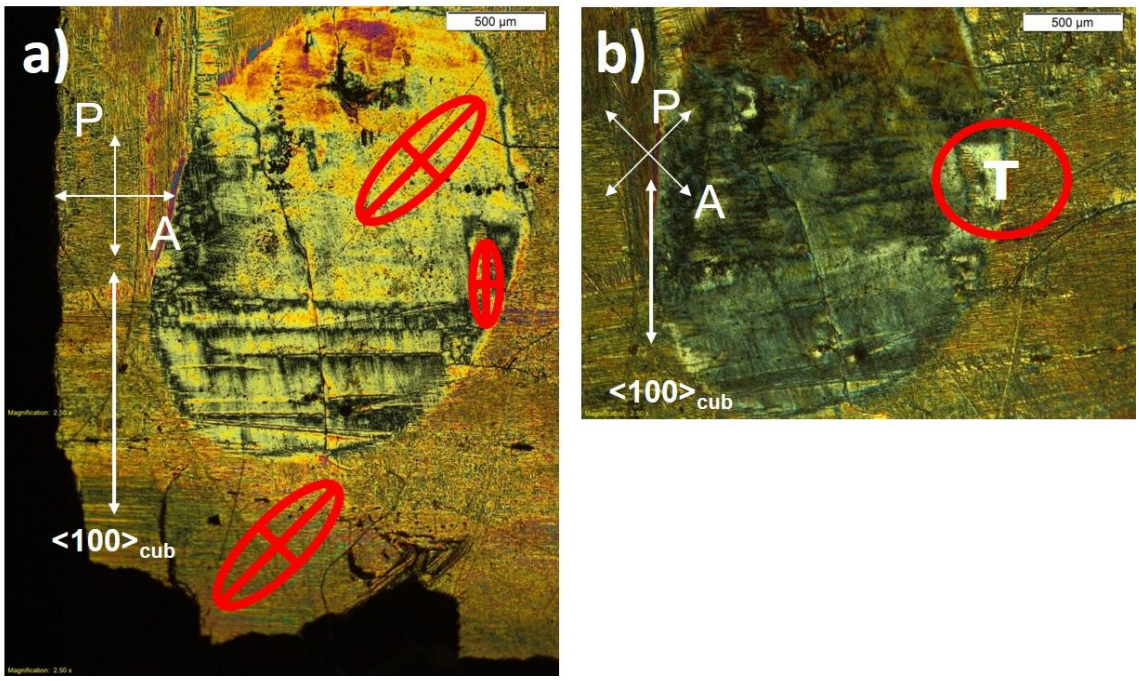

Figure 7.30 Field induced domain states of a (001)-platelet of Crystal F poled along the <001> direction perpendicular to the crystal surface.

An enhanced image of the circled region in Figure 7.30 is shown in Figure 7.31. This is a close-up PLM image utilizing a ¼ wavelength plate to better reveal the contrast of the domain structure. The electrode boundary, as drawn by the red line, creates a clear demarcation between the rhombohedral phase of the unpoled plate and the poled area of tetragonal domains. What can be seen is that in addition to the large 180° domain with extinction parallel to <100> that have developed, there is a pattern of fine domains oriented at a 45° to the <100> direction in between those 180 ° domains, confirming the presence of a tetragonal phase. Figure 7.32 shows a schematic of the

field induced effects in a rhombohedral crystal. In step i), the electric field applied along the <001> switches 4 of the 8 <111> polarization directions of the rhombohedral phase to “up”-ward, significantly reducing the number of domains and domain walls in the poling process. In step ii), some of the <111> polarizations are rotated toward the <001> direction, creating a meta-stable tetragonal symmetry in some areas due to the polarization aligning with the external electric field.

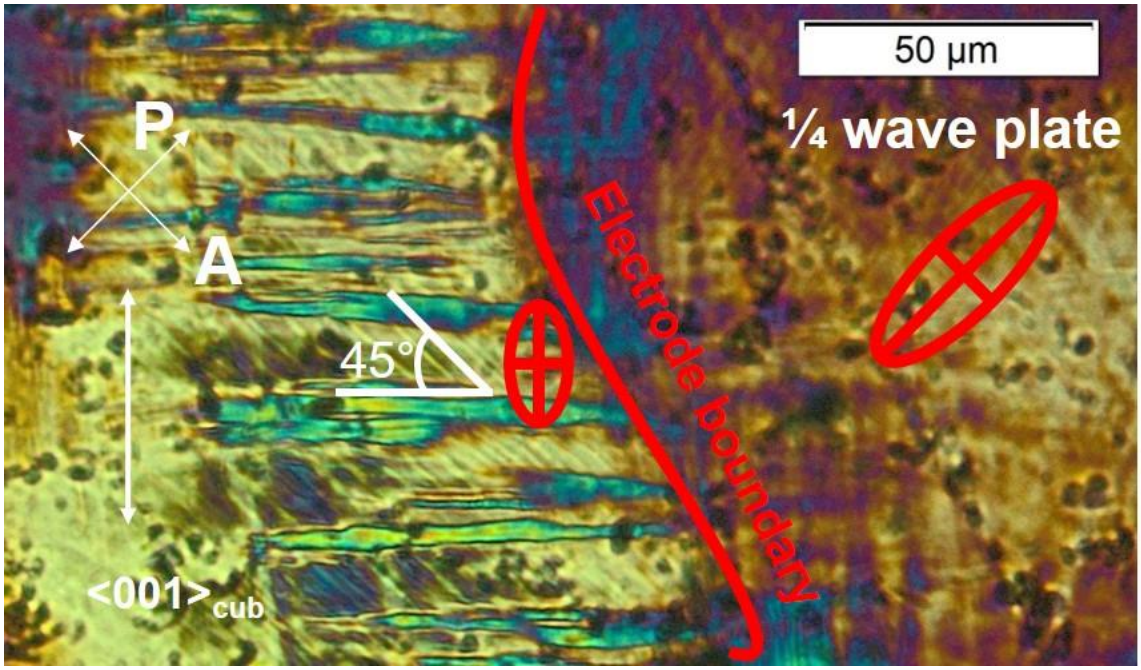

Figure 7.31 Close up image of the electric field induced tetragonal region circled in Figure 7.30 on a (001)-platelet of Crystal F at the electrode boundary, viewed with a ¼ wavelength plate, showing the fine domain pattern.

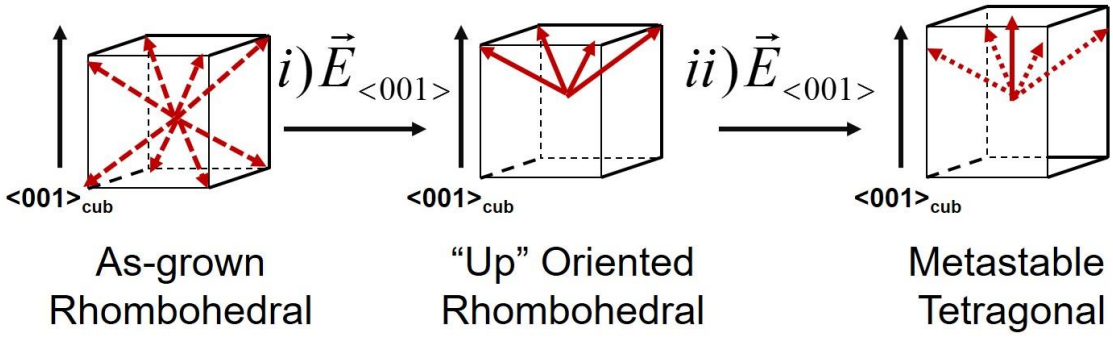

Figure 7.32 Schematic of electric field induced meta-stable tetragonal phase in which the <111> polarization direction first shifts in step i) to orient the 4 "down polarizations" into the "up" configuration of the rhombohedral unit cell, and in step ii) rotating the polarization to be aligned with electric field applied in the <001> direction, causing a change in symmetry to a metastable tetragonal phase.

B) Dielectric Characteristics

The variation of dielectric permittivity (dielectric constant), ε', as a function of temperature measured at various frequencies in zero-field conditions upon cooling is shown in Figure 7.33 for a (001) platelet of Crystal F. Upon cooling from high temperatures, there is a broad phase transition at T_{max} ~ 120 °C that shows dispersion with frequency. In addition, there is an anomaly at T = 90 °C that is frequency independent and is likely a T_C.

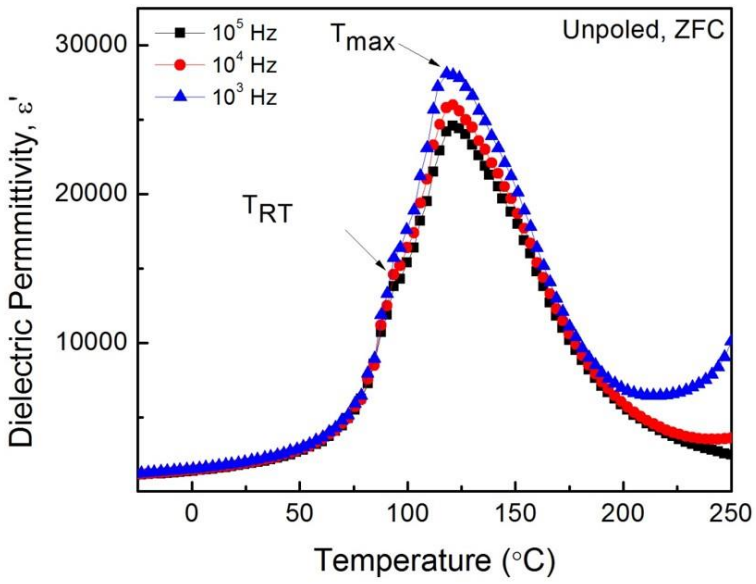

Figure 7.33 Variation of the dielectric permittivity as a function of temperature for an unpoled (001) platelet of Crystal F measured at various frequencies in zero-field-cooling conditions.

The variation of dielectric permittivity (dielectric constant) ε', as a function of temperature, measured at various frequencies for a poled (001) oriented platelet of Crystal F is shown in Figure 7.34. What can be seen in the poled sample, the applied field has enhanced the sharpness of the low temperature phase transition which appears as a clear peak upon heating to T_{RT} = 100 °C. The thermal hysteresis of the transition between heating and cooling runs confirms that it is of first order. The high temperature, diffuse transition occurs at T ≅ 130 °C and it becomes broader, with stronger dispersion at T > T_{RT} due to competing relaxation and charge carrier effects.

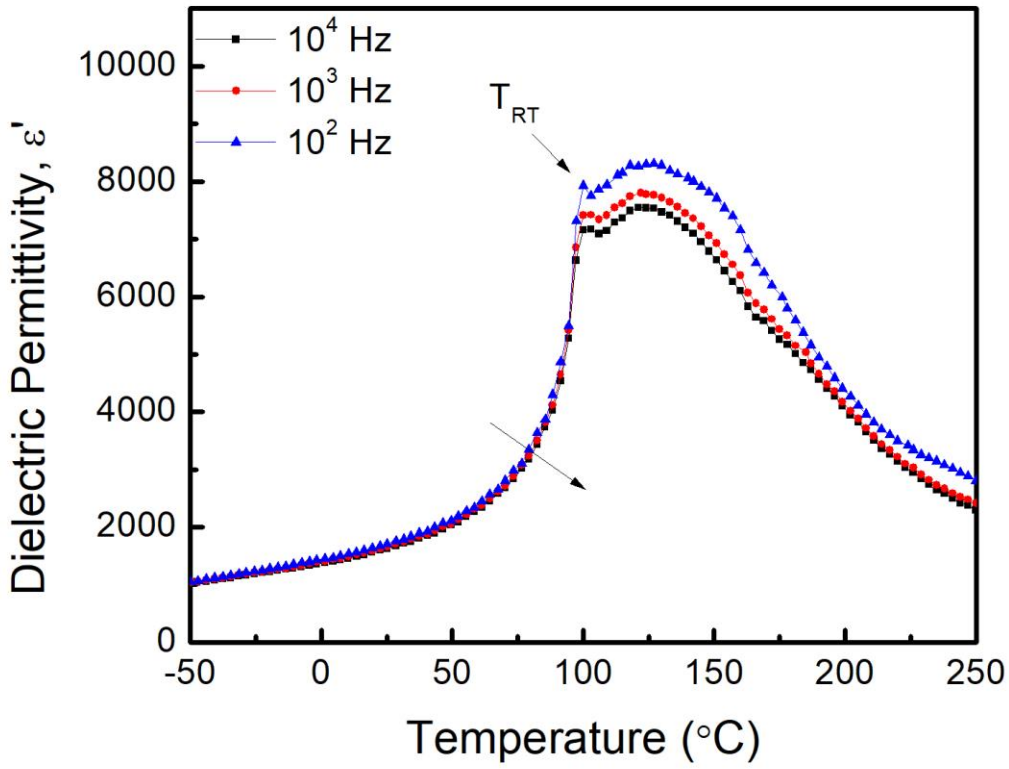

Figure 7.34 Variation of the dielectric permittivity as a function of temperature for an poled (001)-platelet of Crystal F measured at various frequencies in zero-field-heating conditions.

C) Ferroelectric Characterization

Figure 7.35 shows the variation of polarization (P) with a bipolar electric field (E) for a (001) platelet of Crystal F, measured at room temperature. The measurements reveal a well saturated, symmetrical hysteresis loop, indicative of normal ferroelectric behaviour. The remnant polarization, P_r, is found to be 14 μC/cm^2, which is lower than the PMN-PT parent compound. However, the coercive field, E_c, found to be 3.4 kV/cm, is an improvement over PMN-PT.

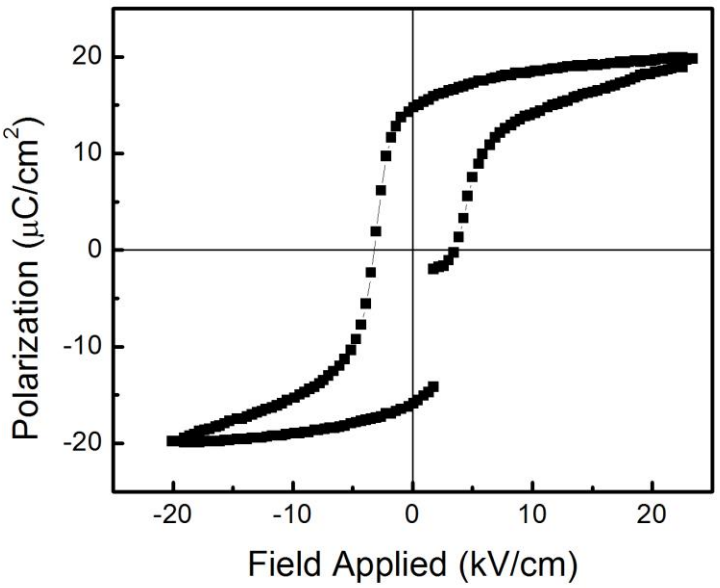

Figure 7.35 Variation of polarization (P) with a bipolar electric field (E) at room temperature for a (001)-platelet of Crystal F showing a typical ferroelectric hysteresis loop.

D) Summary for Crystal F

Crystal F is found to be of rhombohedral symmetry at room temperature, with very weak birefringence due to an overlapping domain pattern. Upon poling by an electric field applied along the <001> direction, the crystal shows larger, rhombohedral domains with stronger birefringence due to growth of the domains after switching. Furthermore, the electric field can induce a rotation of the rhombohedral polarization from <111> towards <001>, giving rise to a metastable, field-induced tetragonal phase. Dielectric measurements yield a broad, and diffuse phase transition at T ~ 130 °C, and a sharper anomaly at T_C = 90 °C that becomes a clear peak in the dielectric spectra after the crystal is poled. This transition shows thermal hysteresis of ~10 ° when measured upon heating. Polarization measurements as a function of bipolar field reveal a saturated hysteresis loop, indicative of normal ferroelectric behavior at room temperature that has improved field stability over the parent compound of PMN-PT, but a lower remnant polarization.

7.5 Composition Estimation

The above studies of the domain structures, phase transitions and dielectric and ferroelectric properties of the various crystals from the same crystal block show strikingly different behaviours, which suggest that these crystals possess different composition because they were grown at different stages of the growth process and formed on different parts of the block. It is, therefore, interesting to try to find out the connections between the formation of the crystals, their compositions and the resulting properties, to deduce the compositional segregation trend, so as to map out the estimate positions of the grown crystals on the phase diagram. To this end, it is necessary first to summarize properties of the crystals and their formation as well as the phase changes that occurred within the crystals, providing a basis to orient the nucleation on the ternary phase diagram. Crystal A is of rhombohedral phase at room temperature and it transitions to a tetragonal phase at T = 96 °C and then undergoes a sharp, first-order ferroelectric to cubic phase transition at T = 147 °C. Crystals B and E show a coexistence of rhombohedral and tetragonal phases at room temperature, and, upon heating, transform to the tetragonal phase at the expense of the rhombohedral phase. They have higher temperature phase transitions from a tetragonal to cubic phase that shows a diffuse permittivity maximum, but does not show any variation in T_{max} with frequency, indicating normal ferroelectric behaviour. Crystal C exhibits a coexistence of rhombohedral, tetragonal and monoclinic phases, indicating this region of the crystal block is of MPB composition. As the crystal is heated, the tetragonal phase gradually consumes the rhombohedral phase as the extinction angle of the monoclinic phase rotates to also transform to tetragonal. Crystal D shows only a rhombohedral phase at room temperature and transitions to tetragonal upon heating. Further heating causes the transformation of the tetragonal phase to cubic, revealing a high temperature, relaxor phase transition that can be fit to the Vogel-Fulcher relationship. Crystal F exhibits rhombohedral phase at room temperature, with a very fine, lamellar domain pattern that becomes more uniform with an applied electric field due to rhombohedral polarization alignment. In addition, further poling can induce polarization rotation from the <111> direction toward the <001> direction, yielding a metastable tetragonal phase that is field induced, as evidenced by 180 ° and 45 ° domains that are in extinction parallel to the <100> direction.

From these results, the key parameters and properties of the Crystals A-F, including Curie temperature, T_C, dielectric constant at room temperature, ε'_{RT}, phase transition temperature from rhombohedral to tetragonal phase, T_{RT}, coercive field, E_c, and remnant polarization, P_r are summarized in Table 7.1 along with piezoelectric coefficient, d_{33}. They are compared with the properties of two PMN-PT binary compositions.

Table 7.1 Compiled Ferroelectric and Piezoelectric Data for the Various Crystals A-F

Section	$T_{C/max}$ (°C)	ε' at Room Temperature (1000 Hz)	T_{RT}	E_c (kV/cm)	P_R (μC/cm^2)	d_{33} (pC/N)
A	147	3150	96	5.7*	46	800
B	153	5060	86	4	37	620
C	116	4224	97**	3.5	34	320
D	132	2241	90	3.5	28	800
E	140	3000	95	-	-	-
F	120	1770	90	3.4	14	-
PMN-0.29PT [10], [54]	135	5400	96	2.3	21	1540
PMN-0.32PT [10], [54]	155	8200	65	2.8	27	2800

*Average due to an asymmetrical P(E) loop; ** Field-induced low-temperature phase

Looking at the T_{max}/T_C values of each crystal in Table 7.1, their transition temperatures are confined to the range of T_C = 116 – 153 °C, indicating the actual compositions of the crystals can be narrowed down to the region circled around the nominal composition, as shown in Figure 7.36. The deviation from the nominal composition results from the compositional segregation inherently occurring in the growth of solid solution crystals of multiple component systems due to the different melting points of the constituent metal oxides, namely, the incongruent melting that drives composition segregation in PMN-PT and PZN-PT [15]. Migration of Ti^{4+}, the primary obstacle to composition uniformity in the Bridgman method, is evident in the crystal growth of this multinucleated block. It is known from the growth of PMN-PT based single crystals that the early-grown crystal exhibits a lower T_C due to a lower concentration of PT. The PT concentration and thereby the T_C, increase as the crystal continues to grow [2], [17]. This trend is expected to have occurred in the PMN-PT-BZT

ternary system. Therefore, it is reasonable to deduce that the crystal growth started from nucleation at the centre of the block, and crystals C and F, were formed first and have the lowest T_C. As the growth process continued, the other crystals nucleated and grew, forming twinned outer crystals D, B and A, which exhibit higher T_C. Thus, the process of the crystals formation could be understood.

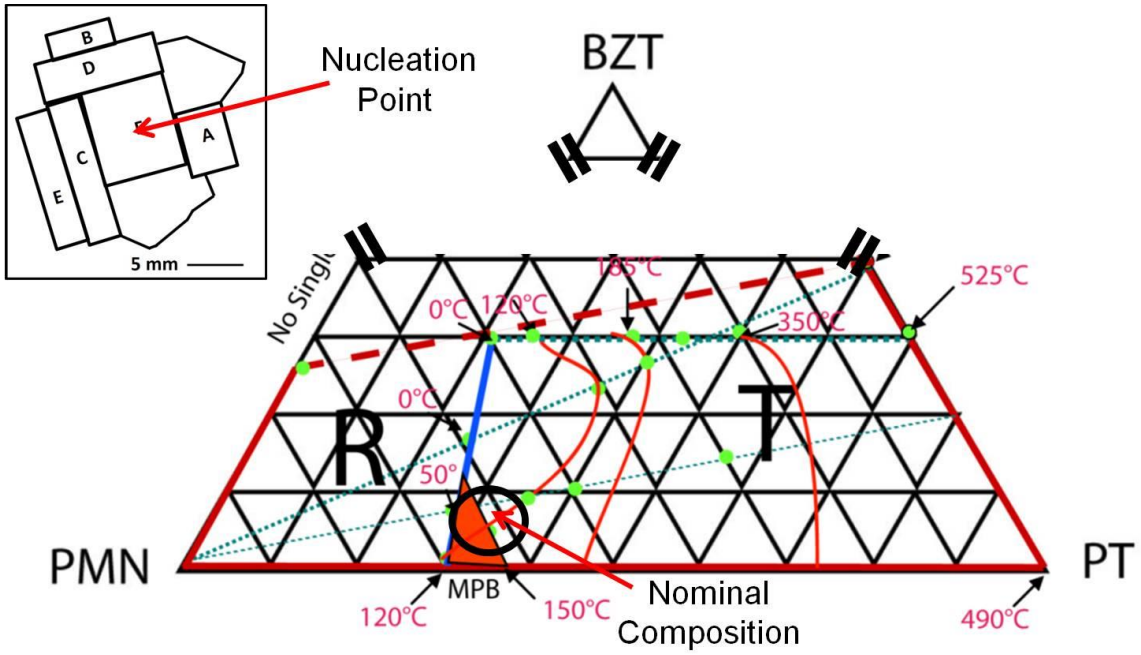

Figure 7.36 Truncated ternary phase diagram of the $Pb(Mg_{1/3}Nb_{2/3})O_3$-$PbTiO_3$-$Bi(Zn_{1/2}Ti_{1/2})O_3$ ternary system. The nominal composition of the grown crystal block marked with the red arrow and the estimated range of the actual composition of the grown crystals marked by the circle.

7.6 Conclusions and Future work

Growth of the nominal composition $0.61Pb(Mg_{1/3}Nb_{2/3})O_3 - 0.312PbTiO_3 - 0.078Bi(Zn_{1/2}Ti_{1/2})O_3$ system yielded a large crystal block that was separated into several crystals that formed at different stages during the growth. Compositional segregation resulted. The crystals of different compositions, which exhibit distinct phase symmetry and phase sequences can be summarized as follows:

i) Crystal A: Rhombohedral $\xrightarrow{T_{RT} = 96\ °C}$ Tetragonal $\xrightarrow{T_C = 147\ °C}$ Cubic, first order phase transition

ii) Crystal B/E: Rhombohedral + Tetragonal $\xrightarrow{T_{RT} = 66-96\ ^{\circ}C}$ Tetragonal $\xrightarrow{T_C = 153\ ^{\circ}C}$ Cubic, diffuse ferroelectric transition

iii) Crystal C: Rhombohedral + Tetragonal + Monoclinic $\xrightarrow{T_{MPB} = 71-110\ ^{\circ}C}$ Tetragonal $\xrightarrow{T_{max} = 116\ ^{\circ}C}$ Cubic

iv) Crystal D: Rhombohedral $\xrightarrow{T_{RT} = 90\ ^{\circ}C}$ Tetragonal $\xrightarrow{T_{max} = 132\ ^{\circ}C}$ Cubic, relaxor ferroelectric phase transition

v) Crystal F: Rhombohedral with fine domain pattern $\xrightarrow{E_{<001>}}$ Larger Rhombohedral domains $\xrightarrow{E_{<001>}}$ Induced Metastable tetragonal phase

This rich variety of phase components, symmetry and transitions reflects the character of the morphotropic phase boundary, and it is quite remarkable to observe these different phase behaviours and properties from one, single growth batch, taking advantage of the normally undesirable composition segregation effects.

All the crystals show an improvement in field stability, E_c, over the MPB compositions of the parent compound of PMN-PT, with greater than or comparable remnant polarization, P_r. The crystals have a reduced room temperature dielectric permittivity, ε', and a reduced d_{33} in comparison with the parent compound of PMN-PT, but are higher than their ceramic counterparts, achieving the objective of hardening the system through chemical substitution and improving upon the properties of the developed ceramic system.

This crystal growth has laid the foundation for subsequent growths to refine the PMN-PT-BZT system. Future work would be to first analyze the composition variation based on proximity from the nucleation point using a technique such as laser ablation - inductively coupled plasma – mass spectrometry (LA-ICP-MS) which can not only quantify the ions present, but can provide a map of the crystal composition across the surface and in a certain depth. Once the composition is quantified, portions of this crystal block can be used as seed crystals for subsequent crystal growths by such methods as top-seeded solution growth, with the aim of reducing the composition segregation and

obtaining more uniform and larger crystals for applications as electromechanical transducers.

Chapter 8. General Conclusions & Future Outlook

8.1 General Conclusions

Relaxor-based piezo-/ferroelectric materials of complex perovskite structure, represented by (1-x)$Pb(Mg_{1/3}Nb_{2/3})O_3$-x$PbTiO_3$ (PMN-PT), that were developed in the last decade, have demonstrated excellent piezoelectric performance potentially useful for high-end electromechanical transducer applications. However, they also exhibit some inherent drawbacks, such as low a Curie temperature, an even lower depoling temperature due to the presence of MPB, a weak coercive field and a high content of lead, which make them unsuitable for high-temperature and high-field (power) applications and raise environmental concerns.

On the other hand, bismuth-based complex perovskites such as $Bi(Zn_{1/2}Ti_{1/2})O_3$ (BZT) seem to be interesting candidate for the replacement of lead-based compounds because, like Pb^{2+}, Bi^{3+} also contains the $6s^2$ lone electron pair which is considered to be essentially needed for the high piezo-/ferroelectric performance in lead-based perovskite. In addition, the solid solution between BZT and PT indeed exhibits larger structural distortion and thereby higher Curie temperature than PT. However, its coercive field is too large for the material to be poled in order to make its potentially high piezo-/ferroelectric properties useful.

Faced with those issues and challenges, the objectives of this thesis work are mainly of two-fold:

1) Use a non-stereochemically active ion and related complex compound, namely $La(Zn_{1/2}Ti_{1/2})O_3$ (LZT) as an end-member to "soften" the structures, chemical bonding and electric properties of "hard" ferroelectric materials, including the canonical ferroelectric PT and the solid solution of PT-BZT, and to achieve improved electric properties such as giant dielectric constant, smaller coercive field, switching polarization and excellent piezoelectricity and ferroelectricity.

2) Use BZT as the third component to "harden" the structures, chemical bonding and electric properties of PMN-PT binary system in order to increase its coercive field and to improve its piezo-/ferroelectricity. In particular, special efforts have been made to

grow the single crystals of the PMN-PT-BZT ternary system. The studies of the single crystals are expected to provide invaluable information on the phase symmetry, domain structures, phase transitions and electric properties and to gain a better understanding of the relationship between crystal formation, chemical composition, phase symmetry and macroscopic properties.

Looking back, it is prudent to say that these objectives have been achieved almost satisfactorily:

The "softening" of the materials has been realized and reported through the studies of three representative systems as reported in Chapters 3, 4 and 5. In Chapter 3, through crystal chemistry concept of softening and the formation of solid solution to create a high dielectric constant material, a new binary solid solution of $(1\text{-}x)PbTiO_3 – xLa(Zn_{1/2}Ti_{1/2})O_3$ has been synthesized with complete and continued solubility for the concentrations of LZT of x = 0.0 – 1.0. At low concentrations of LZT, x = 0.0 – 0.3, the solid solution is of a tetragonal perovskite structure, which transitions to a pseudo-cubic phase for compositions of $0.40 \leq x \leq 0.70$, and at high concentrations of x = 0.8 - 1.0, the solid solution adopts a monoclinic $P2_1/n$ symmetry. A binary phase diagram has been established illustrating these phase regions. It is found from the dielectric characterization that the Curie temperature, T_C, decreases with the increased concentration of x, demonstrating an actual softening of the ferroelectric order and strength. The dielectric peaks become more diffuse, with T_C approaching room temperature for the composition x = 0.30. Giant dielectric constants are found at room temperature for x = 0.30 - 0.40 with low dielectric loss. These enhanced properties demonstrate that the PT-LZT solid solution forms a new family of giant dielectric constant materials very promising for high-density energy storage and MEMS applications.

In the same framework of chemical softening, and through design by crystal chemistry concepts and preparation by solid state reaction and ceramic sintering process, in Chapter 4 a new pseudo-binary system $0.20[(1\text{-}x)Bi(Zn_{1/2}Ti_{1/2})O_3– xLa(Zn_{1/2}Ti_{1/2})O_3] - 0.80PbTiO_3$ (BZT--LZT-PT) has been successfully synthesized with compositions x = 0.0 – 1.0, i.e. complete solubility throughout the series. The highly tetragonally distorted structure in BZT-PT, which had prevented its piezo-/ferroelectricity from being revealed, shows a consistent decrease in tetragonality (c/a) with increasing

mole fraction of LZT (x). This reduction of tetragonal distortion indicates that the structural 'softening', indeed, is realized by the substitution of La^{3+} for Bi^{3+} with a lone electron pair, as evidenced by the decreases in the ferroelectric Curie temperature and coercive field with increasing LZT content. More interestingly, this structural softening also leads to the softening of the polar order. These results demonstrate that the presence of the $6s^2$ lone pair on Bi^{3+} has contributed to the high tetragonality and high Curie temperatures in the BZT-PT binary system in particular, and in other ferroelectric materials in general. The 'softening' effect, realized by the substitution of LZT, allows for the realization of stable, bipolar states as displayed in the polarization vs. electric field hysteresis loops for mole fractions of LZT $x \geq 0.40$. The variations of remnant polarization and piezoelectric coefficients as a function of composition show a peak at compositions $x = 0.6 – 0.7$, making those materials potentially useful for electromechanical transduction applications with high temperature applications.

In Chapter 5, two additional pseudo-binary systems have been prepared and their crystal structures, phase symmetry and solubility limits studied to better characterize the ternary system. Based on the structural and property data obtained in Chapter 3, Chapter 4 and Chapter 5, a preliminary ternary phase diagram is established for the LZT-BZT-PT ternary solid solution system as presented in Figure 5.8. This ternary phase diagram shows the most important structural features and interesting properties of the system. In the region of high PT concentration, a ferroelectric perovskite phase of tetragonal symmetry is formed. Interestingly, this area can be further divided into two sub-regions: hard ferroelectrics with high T_C and high coercive fields, making the material suitable for high-field and high-power applications, and soft ferroelectrics with lower tetragonality, weaker coercive field and lower Curie temperatures, suitable for electromechanical transducers and memory devices. Moreover, room temperature dielectric constants are increased with increasing LZT concentration, leading to giant dielectric constants along the LZT-PT binary side with 30 – 40 mole percent of LZT. Increasing the mole fraction of LZT along the LZT-PT binary line, the pseudo-cubic phase transitions to a $P2_1/n$ monoclinic phase at $x > 0.70$, a dielectric material. On the BZT side of the phase diagram, there is a large area where no single-phase perovskite can be formed under ambient, solid state reaction conditions. This reflects the low chemical stability of the BZT end member. High pressure may be required to prepare a single perovskite phase in that region of the phase diagram.

The concept of "hardening" has been applied to the studies of the ternary PMN-PT-BZT solid solution system in the form of single crystals. In the first part of these studies reported in Chapter 6, single crystals of the PMN-PT-BZT ternary system have been grown from high-temperature solution by the flux method. Analyses of the crystal morphology and microstructure reveal a layered growth mechanism for the crystal growth, and the formation of growth striation in the grown crystals. Varying growth conditions by a slower cooling rate has led to the reduction of growth striation, which is likely due to higher thermal and compositional stabilities within the melt. Nevertheless, compositional segregation still occurred, as attested by the coexistence of the rhombohedral (or pseudo-cubic) and tetragonal phases within the crystal, which is typical of solid solution system with compositions close to the MPB region, like the PMN-PT binary system.

The temperature and frequency dependences of the dielectric properties of Crystal A shows characteristic relaxor behavior, which satisfies the Vogel-Fulcher law, giving a rise to a freezing temperature T_{VF} = 336 K. Poling by an external field reveals a macroscopic ferroelectric phase at room temperature. This poled phase transforms into an ergodic relaxor state upon heating above a depoling temperature, T_d = 56 ºC, as revealed by an anomaly on the temperature dependence of dielectric permittivity at T_d, followed by dispersive relaxor peaks at $T_{max} > T_d$. Ferroelectric hysteresis loops were displayed with a coercive field E_C = 3.5 kV/cm and a remnant polarization P_r = 21 $\mu C/cm^2$. The poled crystal also exhibits a high piezoelectric coefficient, d_{33} = 825 pC/N, much higher than that of its ceramic counterparts.

These preliminary results on the growth and characterization of PMN-PT-BZT crystals provide a new example of relaxor materials in which, upon cooling, an ergodic relaxor state transforms into a macroscopic ferroelectric phase, while the dynamics of polar nanoregions freezes (at about the same temperature). The interesting dielectric, piezoelectric and ferroelectric properties indicate that the ternary crystals can constitute a viable class of high-performance piezo-/ferroelectric crystals for a wide range of applications.

In order to gain more comprehensive knowledge on the relationship between the crystal formation, crystal composition, phase symmetry and macroscopic properties, more systematic studies of the single crystals of the PMN-PT-BZT system have been

performed and reported in Chapter 7. Growth of the nominal composition $0.61Pb(Mg_{1/3}Nb_{2/3})O_3 - 0.312PbTiO_3 - 0.078Bi(Zn_{1/2}Ti_{1/2})O_3$ system yielded a large crystal block that was separated into several crystals that formed at different stages during the growth. Due to inevitable compositional segregation, different crystals exhibit distinct phase symmetry and phase sequences that are summarized as follows:

vi) Crystal A: Rhombohedral $\xrightarrow{T_{RT} = 96\ ^\circ C}$ Tetragonal $\xrightarrow{T_C = 147\ ^\circ C}$ Cubic, with first-order phase transition at T_C;

vii) Crystal B/E: (Rhombohedral + Tetragonal) $\xrightarrow{T_{RT} = 66-96\ ^\circ C}$ Tetragonal $\xrightarrow{T_C = 153\ ^\circ C}$ Cubic, with diffuse ferroelectric transition around T_C (T_{max});

viii) Crystal C: (Rhombohedral + Tetragonal + Monoclinic) $\xrightarrow{T_{MPB} = 71-110\ ^\circ C}$ Tetragonal $\xrightarrow{T_{max} = 116\ ^\circ C}$ Cubic ;

ix) Crystal D: Rhombohedral $\xrightarrow{T_{RT} = 90\ ^\circ C}$ Tetragonal $\xrightarrow{T_{max} = 132\ ^\circ C}$ Cubic, with relaxor ferroelectric behaviour and transition around T_{max};

x) Crystal F: Rhombohedral with fine domain pattern $\xrightarrow{E_{<001>}}$ Larger Rhombohedral domains $\xrightarrow{E_{<001>}}$ Induced metastable tetragonal phase.

This rich variety of phase components, symmetry and transitions reflects the character of the morphotropic phase boundary, and it is quite remarkable to observe these different phase behaviours and properties from one, single growth batch, taking advantage of the normally undesirable composition segregation effects. As expected from the 'hardening" effects, all the crystals show an improvement in field stability, E_c, over the MPB compositions of the parent compound of PMN-PT, with greater than or comparable remnant polarization, P_r, achieving the objective of hardening the system through chemical substitution.

Overall, the research on the growth and characterization of single crystals has laid the foundation for subsequent growths to refine the PMN-PT-BZT system. Future work would be to first analyze the composition variation based on proximity from the nucleation point using an analytical technique such as laser ablation - inductively

coupled plasma – mass spectrometry (LA-ICP-MS, recently available in 4D LABS at SFU) which can not only quantify the amounts of ions present, but can provide a map of the crystal composition across the surface and in a certain depth. Once the composition is quantified, portions of this crystal block can be used as seed crystals for subsequent crystal growths by such methods as top-seeded solution growth, with the aim of reducing the composition segregation and obtaining more uniform and larger crystals for applications as electromechanical transducers.

8.2 Future Outlook

Looking forward, there is much to be done to optimize the systems discussed within this thesis. Additional impedance spectroscopy and analysis should be performed on the new $La(Zn_{1/2}Ti_{1/2})O_3$-$PbTiO_3$ binary solid solution system in order to determine the ideal operation conditions as a giant dielectric constant capacitor, as well as to determine the conditions for industrial processing and scale-up to realize the material's functionality.

The ternary solid solution system of $Bi(Zn_{1/2}Ti_{1/2})O_3$-$La(Zn_{1/2}Ti_{1/2})O_3$-$PbTiO_3$ shows promise as a tunable ferroelectric material. Process and poling conditions should be optimized in order to determine the most suitable applications of the various compositions that have shown stability to both electric fields and temperature. In addition, it would be rewarding to develop the growth conditions to obtain single crystals of the ternary system which are expected to exhibit improved piezo-/ferroelectric properties potentially useful for applications.

The single crystal system of $Pb(Mg_{1/3}Nb_{2/3})O_3$-$PbTiO_3$-$Bi(Zn_{1/2}Ti_{1/2})O_3$ can be optimized by using shorter growth profiles to obtain more uniform compositions. Once crystals with fewer inclusions and a lower degree of composition segregation are obtained, those materials' production can be scaled up using industrial growth methods, for example, the Bridgman growth method. Then, the crystal engineering/fabrication solutions should be developed to utilize the materials in electromechanical devices.

References

[1] G. H. Haertling and G. H. Haertling, “Ferroelectric Ceramics: History and Technology,” *J. Am. Ceram. Soc.*, vol. 82, p. 797, 1999.

[2] Z.-G. Ye, “High-Performance Piezoelectric Single Crystals of Complex Perovskite Solid Solutions,” *MRS Bull.*, vol. 34, no. April, pp. 277–283, 2009.

[3] T. Li and K. Zeng, “Piezoelectric properties and surface potential of green abalone shell studied by scanning probe microscopy techniques,” *Acta Mater.*, vol. 59, no. 9, pp. 3667–3679, May 2011.

[4] D. Damjanovic, “Ferroelectric, dielectric and piezoelectric properties of ferroelectric thin films and ceramics,” *Reports Prog. Phys.*, vol. 61, p. 1267, 1999.

[5] A. A. Bokov and Z. G. Ye, “Recent progress in relaxor ferroelectrics with perovskite structure,” *J. Mater. Sci.*, vol. 41, pp. 31–52, 2006.

[6] A. R. West, *Basic solid state chemistry* Wiley, 2nd ed. 1999.

[7] R. E. Cohen, “Origin of ferroelectricity in perovskite oxides,” *Nature*, vol. 358, no. 6382, pp. 136–138, Jul. 1992.

[8] A. A. Bokov, X. Long, and Z. G. Ye, “Optically isotropic and monoclinic ferroelectric phases in Pb $(Zr_{(1-x)}Ti_x)O_3$ (PZT) single crystals near morphotropic phase boundary,” *Phys. Rev. B - Condens. Matter Mater. Phys.*, vol. 81, pp. 1–4, 2010.

[9] A. Pramanick, D. Damjanovic, J. E. Daniels, J. C. Nino, and J. L. Jones, “Origins of electro-mechanical coupling in polycrystalline ferroelectrics

during subcoercive electrical loading," *J. Am. Ceram. Soc.*, vol. 94, pp. 293–309, 2011.

[10] S. Zhang and T. R. Shrout, "Relaxor-PT single crystals: Observations and developments," *IEEE Trans. Ultrason. Ferroelectr. Freq. Control*, vol. 57, no. 10, pp. 2138–2146, 2010.

[11] D. Damjanovic, *Hystersis in Piezoelectric and Ferroelectric Materials*, vol. 3. 2006.

[12] R. A. Belan, H. N. Tailor, X. Long, A. A. Bokov, and Z.-G. Ye, "Growth and characterization of piezo-/ferroelectric $Pb(Mg_{1/3}Nb_{2/3})O_3$–$PbTiO_3$–

$Bi(Zn_{1/2}Ti_{1/2})O_3$ ternary single crystals," *J. Cryst. Growth*, vol. 318, no. 1, pp. 839–845, Mar. 2011.

[13] A. A. Bokov and Z.-G. Ye, "Universal relaxor polarization in $Pb(Mg_{1/3}Nb_{2/3})O_3$ and related materials," no. April, p. 14, 2002.

[14] B. Noheda, D. E. Cox, G. Shirane, J. Gao, and Z.-G. Ye, "Phase diagram of the ferroelectric relaxor $Pb(Mg_{1/3}Nb_{2/3})O_3$-$xPbTiO_3$" *Phys. Rev. B*, vol. 66, no. 5, p. 54104, Aug. 2002.

[15] S. E. E. Park and W. Hackenberger, "High performance single crystal piezoelectrics: Applications and issues," *Curr. Opin. Solid State Mater. Sci.*, vol. 6, pp. 11–18, 2002.

[16] D. Damjanovic, "Contributions to the piezoelectric effect in ferroelectric single crystals and ceramics," *J. Am. Ceram. Soc.*, vol. 88, pp. 2663–2676, 2005.

[17] Z.-G. Ye, P. Tissot, and H. Schmid, "Pseudo-binary phase diagram and crystal growth of [PMN]," *Mater. Res. Bull.*, vol. 25, no. 6, pp. 739–748, Jun. 1990.

[18] R. E. Newnham, *Properties of Materials Anisotropy, Symmetry, Structure*. Oxford: Oxford University Press, UK, 2004.

[19] C. B. Sawyer and C. H. Tower, "Rochelle salt as a dielectric," *Physical Review*, vol. 35. pp. 269–273, 1930.

[20] K. Uchino, "Glory of piezoelectric perovskites," *Sci. Technol. Adv. Mater.*, vol. 16, no. 4, p. 46001, 2015.

[21] E. Sawaguchi, “Ferroelectricity versus Antiferroelectrucuty in the Solid Solutions of $PbZrO_3$ and $PbTiO_3$,” *J. Phys. Soc. Japan.* --, vol. 8, no. 5, pp. 615–629, 1953.

[22] A. Walsh, D. J. Payne, R. G. Egdell, and G. W. Watson, “Stereochemistry of post-transition metal oxides: revision of the classical lone pair model.,” *Chem. Soc. Rev.*, vol. 40, no. 9, pp. 4455–4463, 2011.

[23] A. A. Bokov and Z.-G. Ye, “Field-induced shift of morphotropic phase boundary and effect of overpoling in $(1-x)Pb(Mg_{1/3}Nb_{2/3})O_3–xPbTiO_3$ piezocrystals,” *Appl. Phys. Lett.*, vol. 92, no. 8, p. 82901, 2008.

[24] P. S. Booklet, “RoHS Guidance.” 2006

[25] I. Grinberg, M. R. Suchomel, P. K. Davies, and A. M. Rappe, “Predicting morphotropic phase boundary locations and transition temperatures in Pb- and Bi-based perovskite solid solutions from crystal chemical data and first-principles calculations,” *J. Appl. Phys.*, vol. 98, 2005.

[26] A. Moure, A. Castro, and L. Pardo, “Aurivillius-type ceramics, a class of high temperature piezoelectric materials: Drawbacks, advantages and trends,” *Prog. Solid State Chem.*, vol. 37, no. 1, pp. 15–39, 2009.

[27] M. R. Suchomel and P. K. Davies, “Enhanced tetragonality in $(x)PbTiO_3$-$(1-x)Bi(Zn_{1/2}Ti_{1/2})O_3$ and related solid solution systems,” *Appl. Phys. Lett.*, vol. 86, pp. 1–3, 2005.

[28] C. J. Stringer, N. J. Donnelly, T. R. Shrout, C. a. Randall, E. F. Alberta, and W. S. Hackenberger, “Dielectric Characteristics of Perovskite-Structured High-Temperature Relaxor Ferroelectrics: The $BiScO_3$–

$Pb(Mg_{1/3}Nb_{2/3})O_3$–$PbTiO_3$” *J. Am. Ceram. Soc.*, vol. 91, pp. 1781–1787, 2008.

[29] I. Grinberg, M. R. Suchomel, W. Dmowski, S. E. Mason, H. Wu, P. K. Davies, and A. M. Rappe, “Structure and dielectric response in the high T_C ferroelectric $Bi(Zn,Ti)O_3$-$PbTiO_3$ solid solutions,” pp. 1–12, 2006.

[30] I. Grinberg, M. R. Suchomel, W. Dmowski, S. E. Mason, H. Wu, P. K. Davies, and A. M. Rappe, “Structure and polarization in the high Tc ferroelectric $Bi(Zn,Ti)O_3$-$PbTiO_3$ solid solutions,” *Phys. Rev. Lett.*, vol. 98, no. March, pp. 2–5, 2007.

[31] L. V. Azaroff, *X-ray diffraction / [by] Leonid V. Azároff [and others].* 1974.

[32] R. Young, “The Rietveld Method,” *by RA Young, Oxford University Press, Oxford*. p. 312, 1993.

[33] W. J. Patzelt, “Polarized Light Microscopy.” 1985.

[34] “Olympus Mircoscopy Resources,” *http://www.olympusmicro.com*. .

[35] “Basics of Polarizing Microscopy, Http://physics.berkeley.edu/research/yildiz/Teaching/PHYS250/Lecture_PDFs/polarization%20microscopy.pdf,” *Olympus*, p. 28. (acessed June 2017)

[36] Z.-G. Ye and M. Dong, “Morphotropic domain structures and phase transitions in relaxor-based piezo-/ferroelectric

(1−x)Pb($Mg_{1/3}Nb_{2/3}$)O_3−x$PbTiO_3$ single crystals," *J. Appl. Phys.*, vol. 87, no. 5, pp. 2312–2319, 2000.

[37] D. V Taylor and D. Damjanovic, "Evidence of domain wall contribution to the dielectric permittivity in PZT thin films at sub-switching fields Evidence of domain wall contribution to the dielectric permittivity in PZT thin films at sub-switching fields," vol. 1973, no. August 1997, pp. 2–5, 2012.

[38] J. S. Blakemore, *Solid state physics / [by] J. S. Blakemore.* 1969.

[39] M. Stewart, M. G. Cain, and D. Hall, "Ferroelectric Hysteresis Measurement & Analysis," *NPL Rep. C.*, no. May, pp. 1–57, 1999.

[40] M. Dawber, I. Farnan, and J. F. Scott, "A classroom experiment to demonstrate ferroelectric hysteresis," *Am. J. Phys.*, vol. 71, p. 819, 2003.

[41] F. Macdougall, J. Ennis, X. Hui, C. Yang, R. A. Cooper, J. E. Gilbert, J. F. Bates, C. Naruo, M. Schneider, N. Keller, S. Joshi, G. Lane, S. Diego, T. R. Jow, J. Ho, C. J. S. Scozzie, P. M. Road, and W. Dc, "High Energy Density Capacitors for Pulsed Power Applications," 2009.

[42] P. Lunkenheimer, T. Götzfried, and R. Fichtl, "Apparent giant dielectric constants, dielectric relaxation, and ac-conductivity of hexagonal perovskites $La_{1.2}Sr_{2.7}BO_{7.33}$" *J. Solid State Chemistry*, vol. 33, pp. 1–8, 2006.

[43] P. Lunkenheimer, T. Götzfried, R. Fichtl, S. Weber, T. Rudolf, A. Loidl, A. Reller, and S. G. Ebbinghaus, "Apparent giant dielectric constants, dielectric relaxation, and ac-conductivity of hexagonal perovskites

$La_{1.2}Sr_{2.7}BO_{7.33}$ (B=Ru, Ir)," *J. Solid State Chem.*, vol. 179, no. 12, pp. 3965–3973, 2006.

[44] B. J. Maier, a. M. Welsch, B. Mihailova, R. J. Angel, J. Zhao, C. Paulmann, J. M. Engel, W. G. Marshall, M. Gospodinov, D. Petrova, and U. Bismayer, "Effect of La doping on the ferroic order in Pb-based perovskite-type relaxor ferroelectrics," *Phys. Rev. B - Condens. Matter Mater. Phys.*, vol. 83, pp. 1–12, 2011.

[45] M. Abba, "The Structure and the Electrical Properties of $Pb_{0.95}La_{0.05}[Zr_xTi_{(0.95-x)}$ $(Mo_{1/3}In_{2/3})_{0.05}]O3$" *Mater. Sci. Appl.*, vol. 2, no. September, pp. 1199–1204, 2011.

[46] R. Ubic, Y. Hu, K. Khamoushi, and I. Abrahams, "Structure and properties of $La(Zn_{1/2}Ti_{1/2})O_3$," *J. Eur. Ceram. Soc.*, vol. 26, no. 10–11, pp. 1787–1790, 2006.

[47] B. Noheda, "Structure and high-piezoelectricity in lead oxide solid solutions," *Curr. Opin. Solid State Mater. Sci.*, vol. 6, no. 1, pp. 27–34, Feb. 2002.

[48] Y. Uesu, M. Matsuda, Y. Yamada, K. Fujishiro, D. E. Cox, B. Noheda, and G. Shirane, "Symmetry of High-Piezoelectric Pb-Based Complex Perovskites at the Morphotropic Phase Boundary: I. Neutron Diffraction Study on $Pb(Zn_{1/3}Nb_{2/3})O_3$-9%$PbTiO_3$," *J. Phys. Soc. Japan*, vol. 71, no. 3, pp. 960–965, 2002.

[49] G. a. Rossetti, a. G. Khachaturyan, G. Akcay, and Y. Ni, "Ferroelectric solid solutions with morphotropic boundaries: Vanishing polarization

anisotropy, adaptive, polar glass, and two-phase states," *J. Appl. Phys.*, vol. 103, pp. 1–15, 2008.

[50] P. Bialo, P. Bigao, A. A. Belik, T. Wuernisha, T. Kamiyama, K. Mori, M. Maie, T. Nagai, Y. Matsui, E. Takayama-muromachi, and O. Kek, "High-Pressure Synthesis , Crystal Structures , and Properties of," no. 7, pp. 133–139, 2006.

[51] D. Damjanovic, "Ferroelectric, dielectric and piezoelectric properties of ferroelectric thin films and ceramics," *Reports Prog. Phys.*, vol. 61, no. 9, p. 1267, 1998.

[52] S.-E. Park, S. Wada, L. E. Cross, and T. R. Shrout, "Crystallographically engineered $BaTiO_3$ single crystals for high-performance piezoelectrics," *J. Appl. Phys.*, vol. 86, no. 5, pp. 2746–2750, 1999.

[53] H. Fu and R. Cohen, "Polarization rotation mechanism for ultrahigh electromechanical response in single-crystal piezoelectrics," *Nature*, vol. 403, pp. 281–3, 2000.

[54] R. E. Eitel, C. a. Randall, T. R. Shrout, and S.-E. Park, "Preparation and Characterization of High Temperature Perovskite Ferroelectrics in the Solid-Solution (1- x)$BiScO_3$ – x $PbTiO_3$," *Jpn. J. Appl. Phys.*, vol. 41, no. 4, pp. 2099–2104, 2002.

[55] H. N. Tailor and Z.-G. Ye, "Structure, Symmetry and Ferroelectric Properties of the Pseudo-Binary System (1-x)(0.65$Pb(Mg_{1/3}Nb_{2/3})O_3$–

0.35PbTiO$_3$)-xBi(Zn$_{1/2}$Ti$_{1/2}$)O$_3$" *Ferroelectrics*, vol. 421, no. November, pp. 9–15, 2011.

[56] H. N. Tailor, a. a. Bokov, and Z.-G. Ye, "Synthesis and Dielectric Characterization of a New Relaxor Solid Solution of (1 − x)Pb(Mg$_{1/3}$Nb$_{2/3}$)O$_3$ -xBi(Zn$_{1/2}$Ti$_{1/2}$)O$_3$," *Ferroelectrics*, vol. 405, no. September 2011, pp. 67–75, 2010.

[57] H. N. Tailor, "Synthesis and characterization of complex perovskite solid solutions," PhD Thesis 2010.

[58] I. Sunagawa, *Crystals : growth, morphology, and perfection / Ichiro Sunagawa.* 2005.

[59] N. Ben Ming, J. F. Hong, and D. Feng, "The growth striations and ferroelectric domain structures in Czochralski-grown LiNbO$_3$ single crystals," *J. Mater. Sci.*, vol. 17, pp. 1663–1670, 1982.

[60] D. Phelan, X. Long, Y. Xie, Z. G. Ye, a. M. Glazer, H. Yokota, P. a. Thomas, and P. M. Gehring, "Single crystal study of competing rhombohedral and monoclinic order in lead zirconate titanate," *Phys. Rev. Lett.*, vol. 105, no. November, pp. 1–4, 2010.

[61] G. a. Samara and E. L. Venturini, "Ferroelectric/relaxor crossover in compositionally disordered perovskites," *Phase Transitions*, vol. 79, no. February, pp. 21–40, 2006.

[62] M. Davis, M. Budimir, D. Damjanovic, and N. Setter, "Rotator and extender ferroelectrics: Importance of the shear coefficient to the

piezoelectric properties of domain-engineered crystals and ceramics," *J. Appl. Phys.*, vol. 101, pp. 1–11, 2007.

[63] D. Zekria, V. a Shuvaeva, and a M. Glazer, "Birefringence imaging measurements on the phase diagram of $Pb(Mg_{1/3}Nb_{2/3})O_3$–$PbTiO_3$," *J. Phys. Condens. Matter*, vol. 17, pp. 1593–1600, 2005.

[64] W. Chen and Z.-G. Ye, "Top seeded solution growth and characterization of piezo-/ferroelectric $(1-x)Pb(Zn_{1/3}Nb_{2/3})O_3$–$xPbTiO_3$ single crystals," *J. Cryst. Growth*, vol. 233, no. 3, pp. 503–511, Dec. 2001.

[65] X. Zhao, B. Fang, H. Cao, Y. Guo, and H. Luo, "Dielectric and piezoelectric performance of PMN-PT single crystals with compositions around the MPB: Influence of composition, poling field and crystal orientation," *Mater. Sci. Eng. B Solid-State Mater. Adv. Technol.*, vol. 96, pp. 254–262, 2002.